On the Propagation and Reflection of Curved Shock Waves

Brendan James Gray

A thesis submitted to the Faculty of Engineering and the Built Environment, University of the Witwatersrand, Johannesburg, in fulfilment of the requirements for the degree of Doctor of Philosophy.

Johannesburg, April 2015

Declaration

I declare that this thesis is my own, unaided work, except where otherwise acknowledged. It is being submitted for the degree of Doctor of Philosophy in the University of the Witwatersrand, Johannesburg. It has not been submitted before for any degree or examination at any other university.

Signed this 21st day of April 2015

Brendan James Gray

“There’s a certain type of brain that’s easily disabled. If you show it an interesting problem, it involuntarily drops everything else to work on it.”

-Randall Munroe, author of *xkcd*

Acknowledgements

I would like to thank Prof B.W. Skews for introducing me to the fascinating field of gas dynamics, and for his advice, assistance and supervision for this thesis. I am also indebted to Mr R.T. Paton for his assistance with both the computational and experimental aspects of the research.

I also acknowledge the work of Mr S. Daya and Mr M. Beharie, who carried out the undergraduate projects which led to this research.

Thanks also go to Mr S. Riekert, and the rest of the laboratory staff. Mr M. van Wyk deserves a special mention for his expertise in manufacturing the apparatus, and providing suggestions which went a long way toward improving the design.

Thanks go to my fellow students for all of the advice and opinions given, particularly in the early stages of the project.

Finally, thanks go to Sandra and my parents, Neil and Karen for their motivation and absolutely unwavering support for all of these years.

This research was funded by the Fluxion bursary scheme through CSIR, Armscor and the South African Department of Defence.

Abstract

Curved shock waves, particularly converging shock waves, have applications in a wide variety of fields, yet they are severely under-represented in the literature. Shock reflection is typically categorised in terms of the shock Mach number and incident angle, but these parameters both vary with time for a curved shock wave.

A facility capable of producing shock waves with an arbitrary two-dimensional profile was designed and manufactured. A planar shock from the end of a conventional shock tube is passed through a narrow slit and turned through a 90° bend, generating a shock with an initial shape matching the profile of the slit.

The facility was first used to study the propagation of shock waves of arbitrary shape. This included a brief computational fluid dynamics (CFD) study of the interaction between straight and concave segments on a shock front, followed by CFD and experimental studies into the propagation of shock waves consisting of both concave and convex segments, with initially sharp and rounded profiles. Shocks with Mach numbers between 1.2 and 1.45 were generated, and the behaviour of the shock waves produced by the experimental facility agreed favourably with the CFD simulations, particularly for the higher Mach numbers.

A detailed study into the reflection of converging cylindrical shock wave segments was then carried out. CFD simulations for Mach numbers at the apex of the wedge varying from 1.2 to 2.1, for wedge angles between 15° and 60°, and experiments with apex Mach numbers between 1.5 and 2.1 and wedge angles between 15° and 50° were carried out. The sonic condition usually used for predicting the planar shock reflection configuration was successful at predicting the initial reflection configuration. If the initial reflection was regular, then the shock was cleanly reflected off the surface, with no discontinuities in the reflected shock front. However, if the initial reflection was a Mach reflection, this would inevitably transition into a transitioned regular reflection, with the residual Mach stem and shear layer still present behind the reflection point. Collision of the Mach stem with the corner at the end of the wedge generated a small region of very high pressure, which lasted for several microseconds.

A simple theoretical model was developed for estimating the Mach stem height and transition point for a converging cylindrical shock segment encountering a straight wedge. The model gives reasonable predictions for shocks of moderate strength and wedge angles below 40°, but deviates from experimental results for wedges at 40° and above.

Scope and Contribution

The primary objective of this research was to investigate the behaviour of shock waves of arbitrary profiles, using experimental and numerical techniques. The contributions to the field of gas dynamics can be summarised as follows:

- The design and testing of a unique facility capable of producing shock waves of an arbitrary two-dimensional profile in a repeatable manner.
- A preliminary investigation into the propagation of various shock wave shapes, including shapes consisting of interacting converging and diverging segments.
- An investigation into the reflection patterns that occur when a propagating cylindrical shock segment encounters an inclined wedge. This includes classification of the initial reflection type and comparison of the later transition points with the conditions currently used with planar shocks. A fast numerical technique for predicting the Mach stem height and transition point was also developed.

Published Work

Aspects of this thesis have been published in the following references:

- Gray, B. J., Skews, B. W. (2012) *Reflection transition of converging cylindrical shock wave segments*; in *Proceedings of the 28th International Symposium on Shock Waves*; Manchester, United Kingdom; Springer Berlin Heidelberg; pp 995–1000.
- Gray, B. J., Skews, B. W. (2012) *Propagation of arbitrarily-shaped shock waves*; in *Proceedings of the 8th South African Conference on Computational and Applied Mechanics*; Johannesburg, South Africa; pp 48–51.
- Gray, B. J., Skews, B. W. (2013) *Experimental investigation into converging cylindrical shock wave reflection*; in *Proceedings of the 29th International Symposium on Shock Waves*; Madison, WI, USA; Springer Berlin Heidelberg (In press).
- Skews, B. W., Gray, B. J., Paton, R. T. (2014) *Experimental production of two-dimensional shock waves of arbitrary profile*; Shock Waves (In press).

Contents

List of Figures

List of Tables

List of Symbols

Gas dynamics:

a	Speed of sound	m/s
A	Cross sectional area	m^2
C	Arbitrary constant	
E	Total error function	
E_i	Image error function	
H_M	Mach stem height	m
M	Mach number	
M_a	Mach number of the shock at the wedge apex	
M_{max}	Maximum shock Mach number	
M_w	Mach number of the Mach stem at the wall	
n	Guderley's power law exponent	
p	Pressure	Pa
p_0	Stagnation pressure / reference pressure	Pa
r	Shock radius	m
r_{min}	Minimum shock radius	m
r_w	Distance of wedge apex from the shock centre	m
R	Specific gas constant	$\mathrm{J\ kg^{-1}\ K^{-1}}$
s	Scale factor	s
t	Time	s
T	Absolute temperature	K
T_0	Stagnation temperature	K
u	Fluid velocity	m/s
$\overline{v}$	Average shock velocity	m/s
$\vec{V}$	Velocity vector	m/s

x, y	Real coordinates relative to the wedge apex	m
x_a, y_a	Pixel coordinates of the wedge apex	px
x_c, y_c	Coordinates of the centre	m
x_e, y_e	Pixel coordinates of the end of the wedge	px
x_i, y_i	Pixel coordinates of a point in an image	px
z	Shock wave strength	
α, β	Alternate coordinates for geometrical shock dynamics	
β	Shock incident angle	rad
γ	Specific heat ratio	
δ	Step size	m
η	Milton's A-M correction factor	
θ	Flow deflection angle / ray direction	rad
θ_C	Complimentary angle / effective wedge angle	rad
θ_t	Image tilt angle	rad
θ_w	Wedge angle	rad
μ	Mach angle	rad
ρ	Density	kg/m^3
χ	Triple point trajectory angle	rad

Mechanics of Materials:

A_t	Tensile stress area	m^2
b	Minimum plate width	m
d	Bolt diameter	m
E	Young's modulus	GPa
F_i	Bolt preload	N
K	Torque coefficient	
K_I	Stress intensity factor	MPa$\sqrt{\text{m}}$
K_{IC}	Fracture toughness	MPa$\sqrt{\text{m}}$
M	Bending moment	N m
n_f	Fatigue safety factor	
P	Applied load	N
q	Load per unit area	N/m^2
S_e	Endurance strength	MPa
S_{ut}	Ultimate tensile strength	MPa
t	Plate thickness	m
T	Torque	N m

α, β_1	Constants for maximum stress formula	
ν	Poisson's ratio	
σ	Stress	MPa

List of Acronyms

CFD	Computational fluid dynamics
CFL	Courant-Friedrichs-Levy number
DiMR	Direct Mach reflection
ESWL	Extracorporeal shock wave lithotripsy
FDS	Flux-difference splitting
GSD	Geometrical shock dynamics
IMR	Inverse Mach reflection
IR	Irregular reflection
LSDST	Large scale diffraction shock tube
MR	Mach reflection
MUSCL	Monotonic upstream centred schemes for conservation laws
NVSL	No visible shear layer
RR	Regular reflection
StMR	Stationary Mach reflection
TRR	Transitioned regular reflection

1. Introduction

This document details an investigation that was undertaken into the propagation and reflection behaviour of curved shock waves. The background and motivation for this research is given below.

1.1 Background

A fluid that experiences significant changes in density when forces are applied to it is referred to as a compressible fluid. One distinctive characteristic of compressible fluids is that information is transmitted through the fluid in the form of waves of finite velocity (Anderson, 2007). The speed at which these waves propagate depends on the fluid's properties, and is referred to as the acoustic velocity, or the speed of sound. If the passing of one of these waves decreases the pressure of the fluid, then it is referred to as an expansion or rarefaction wave. If it leads to an increase in pressure, then it is referred to as a compression wave. A compression wave also leads to an increase in the local speed of sound; thus subsequent waves travel faster. This can lead to a series of compression waves coalescing such that there is a finite discontinuity in the fluid's properties. This discontinuity is called a shock wave (Anderson, 2004).

Fluid passing through a stationary shock wave always experiences a decrease in velocity and an increase in pressure. By changing to an alternate reference frame, it may be deduced that a shock propagating into a stationary fluid accelerates the flow, and results in an increase in pressure (Anderson, 2004). The shock strength is often defined as this change in pressure (Prasad, 1982).

Guderley (1942) investigated the behaviour of cylindrical and spherical shock waves, and found that the strength of a curved shock varied in relation to its radius of curvature. Specifically, he proposed that as a curved shock converges, the shock strength increases according to a simple power law. Because of this, it is possible to generate very high pressures using focussed shock waves.

However, the production of curved shock waves, particularly shock waves with non-uniform curvature, has proved challenging. Recently, conceptual designs for hardware capable of producing a shock wave of arbitrary profile were carried out by Skews and Beharie (2009), and Skews and Daya (2009). The hardware attaches to the end of an existing shock tube and the shock generated by the bursting of the diaphragm travels down the tube and is passed through a curved slit. This shock is then allowed to propagate in a chamber that runs perpendicular to the original shock tube. Using apparatus such as these, it is possible to generate shocks of a wide variety of profiles, and investigate their propagation and reflection behaviour.

1.2 Motivation

Extensive experimental research has been carried out into the behaviour of planar shock waves. However, there is little experimental data available on the behaviour of curved shock waves. In particular, the reflection of curved shock waves is poorly understood.

Accurate methods for predicting of behaviour of such waves are currently limited to computational fluid dynamics (CFD), which is computationally expensive and time-consuming, and geometrical shock dynamics (GSD) which has limited accuracy. A deeper understanding of the mechanisms governing the behaviour of these shock waves would be extremely useful in a range of scientific fields, such as supersonic aerodynamics and blast mechanics, amongst others.

Of particular interest are converging shock waves. Due to the relative ease with which high pressures can be achieved by focusing a shock wave at a point, shock focusing has a wide variety of applications, including the creation of diamonds, production of rare reaction products and the detonation of explosives (Grönig, 1986). Production of precisely shaped curved shock waves with well-behaved post-shock flow is necessary to initiate a reaction an inertial confinement fusion target, which is an important milestone for achieving fusion power (Lindl et al., 1992). There are also several applications of shock waves in medicine, one of which is extracorporeal shock wave lithotripsy (ESWL), which makes use of focused underwater shock waves to break up and remove kidney or gall bladder stones without the need for any invasive surgical procedure (Takayama and Saito, 2004). There is also a possibility that focused shock waves may also be used to aid the delivery of anticancer drugs directly into cancer cells (Kambe et al., 1996).

2. Literature Review

This chapter gives a review of the current state of the field regarding the behaviour of curved shock waves. After an overview of one-dimensional gas dynamics and shock waves, shock wave reflection and curved shock waves will be described separately.

2.1 Overview of gas dynamics

The behaviour of an ideal gas in a one-dimensional channel is well defined in the literature. A summary, largely adapted from Anderson (2004) is given here. The behaviour is governed by the ideal gas law, the continuity equation, the momentum equation, and the energy equation.

If the flow is both adiabatic (i.e. no energy is added or removed from the flow) and reversible (i.e. there is no net change in entropy within the flow), then the flow is known as isentropic flow. The propagation speed a of an acoustic wave in a fluid (assuming no heat addition) is the speed of sound. For an ideal gas with constant specific heats, this is given by

$$a = \sqrt{\gamma R T} \tag{2.1}$$

where γ is the ratio of specific heats, R is the ideal gas constant, and T is the absolute temperature of the fluid. It is convenient to express the velocity of the fluid in a dimensionless form known as the Mach number, which is defined

$$M \equiv \frac{u}{a} \tag{2.2}$$

where u is the fluid velocity.

Any disturbance in the flow will cause a wave to propagate out at the local sound speed. These waves cause a pressure variation in the fluid they pass. A compression wave will cause the pressure in a fluid to increase, whereas an expansion (or rarefaction) wave will cause the pressure to decrease.

Since a compression wave increases the pressure, and therefore temperature of the fluid that it passes, the local sound speed at the rear of the wave will be higher than the sound speed at the wave front. This causes the width of the compression wave to decrease over time. The length of the compression reaches a minimum when viscous effects prevent it from decreasing further. Once this happens, the compression propagates at a speed higher than the sound speed in the fluid in front of it, is no longer isentropic, and has a width that is typically much smaller than other length-scales in the system. Such a compression is referred to as a shock wave.

2.2 Normal and oblique shock waves

Using the laws of one-dimensional gas dynamics, the simple case in which supersonic flow passes through a stationary shock wave may be analysed, and relationships between the thermodynamic properties of the fluid on either side of the shock may be derived. The general case where a normal shock is moving into a non-stationary fluid may be treated by adjusting the reference frame to one in which the shock is stationary. This is achieved by subtracting the velocity of the shock from the velocities of the fluid before and after a shock (Anderson, 2004).

Most relevant to the current study is the case in which a shock wave is moving with some Mach number M_s into stationary flow. In this case, the shock strength is given as

$$z \equiv \frac{p_2}{p_1} = 1 + \frac{2\gamma}{\gamma + 1} \left(M_s^2 - 1 \right) \tag{2.3}$$

where p is the pressure and subscripts 1 and 2 represent the conditions before and after the shock. The Mach number of the flow behind the shock wave is then

$$M_2 = \left[\frac{2 + (\gamma - 1) M_s^2}{2\gamma M_s^2 - (\gamma - 1)} \right]^{\frac{1}{2}} \tag{2.4}$$

If the oncoming flow encounters the shock at some angle, it is referred to as an oblique shock wave. An oblique shock may be analysed using the normal shock relationships by changing the reference frame. Consider the general case of a plane shock moving into a fluid moving with an angle of incidence to the shock. By applying a Galilean transformation (by rotating and imposing a velocity vector on the reference frame) one can change to a reference frame in which the shock is stationary and the flow is perpendicular to the shock. The normal shock relations may then be applied.

The pressure ratio across the shock, Mach number of the flow behind the shock, and the angle through which the flow is deflected, θ, are then given by Anderson (2004) as:

$$\frac{p_2}{p_1} = \frac{2\gamma}{\gamma+1} M_1^2 \sin^2\beta - \frac{\gamma-1}{\gamma+1} \tag{2.5}$$

$$M_2^2 sin^2\left(\beta-\theta\right) = \frac{\gamma+1+(\gamma-1)\left(M_1^2\sin^2\beta-1\right)}{\gamma+1+2\gamma\left(M_1^2\sin^2\beta-1\right)} \tag{2.6}$$

$$\tan\theta = 2\tan\beta\left[\frac{M_1^2\cos^2\beta-\cot^2\beta}{2+M_1^2(\gamma+\cos 2\beta)}\right] \tag{2.7}$$

where β is the angle of incidence between the shock and the oncoming flow.

2.3 Shock tubes

In experimental gas dynamics, a common apparatus for studying the behaviour of shock waves is the shock tube. There are a number of means by which a shock tube may generate a shock wave, including the rapid motion of a piston, the opening of a quick acting valve, or the bursting of a diaphragm. A schematic diagram of this last case is shown in in Figure 2.1. A high pressure driver section (region 4) is separated from the low pressure driven section (region 1). Rapid removal of the diaphragm will allow the high pressure gas to flow out of region 4, which will drive a shock wave through region 1.

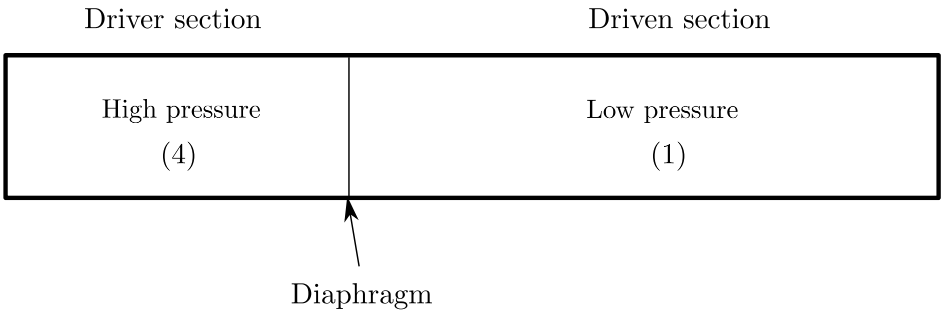

(a) Initial conditions in the shock tube

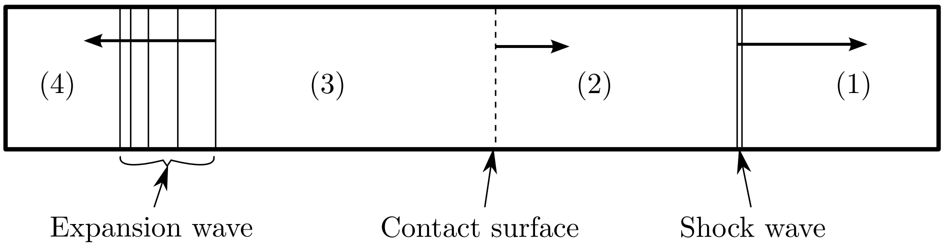

(b) Conditions at some time after the removal of the diaphragm

FIGURE 2.1: Formation of a shock wave in a shock tube

Typically, the diaphragm is broken either by some external trigger (such as a mechanical device or an electric current) or by natural failure. When this happens, an expansion wave propagates into the driver section. The wave front will propagate at the sound speed of region 4, whereas the rear of the wave will propagate at the sound speed of region 3 (which is lower than that in region 4), thus the length of the expansion wave will increase with time. A compression is generated over the length of time it takes for the diaphragm to break. This rapidly steepens into a shock wave, which propagates into region 1 at some speed higher than the sound speed in region 1. The speed at which this shock propagates is entirely a function of the initial pressure ratio across the diaphragm, p_4/p_1. A contact surface separating regions 2 and 3 follows the shock wave at the local gas velocity. The gas in region 2 is gas that was originally in the driven section, where as the gas in region 3 was originally in the driver section. Even though the gases in regions 2 and 3 have the same pressure and velocity, the fact that they have different stagnation pressures means that there is a significant temperature and density difference across the contact surface. If regions 1 and 4 are both initially at the ambient room temperature (which is often the case), region 2 will be at a temperature higher than this, and region 3 will be at some temperature lower than this.

It is a simple matter to calculate the conditions in each region. However, of primary interest to the current research is the initial pressure ratio across the diaphragm required to generate a shock of a given strength. This is given by Anderson (2004) as

$$\frac{p_4}{p_1} = \frac{p_2}{p_1} \left\{ 1 - \frac{(\gamma_4 - 1)(\frac{a_1}{a_4})(\frac{p_2}{p_1} - 1)}{\sqrt{2\gamma_1 \left[2\gamma_1 + (\gamma_1 + 1)(\frac{p_2}{p_1} - 1) \right]}} \right\}^{\frac{-2\gamma_4}{\gamma_4 - 1}} \tag{2.8}$$

where the shock strength $\frac{p_2}{p_1}$ may be calculated from the desired shock Mach number using equation (2.3).

2.4 Shock wave reflection

If flow travelling parallel to a surface (or a symmetry plane) encounters an oblique shock, then the flow will be deflected toward the surface. However, since no fluid can actually flow through the surface, the flow behind the shock must also be parallel to the surface in order to meet boundary conditions. If, in a shock-fixed reference frame, the flow behind the shock is supersonic, then at least one additional shock wave (referred to as a reflected shock wave) must form in order to deflect the flow and meet these conditions.

Depending on the flow conditions, several types of reflection are possible. Some of these are discussed in this section.

2.4.1 Types of shock reflection

In the simplest case, a single reflected shock which meets the incident shock at the surface deflects the flow so that it is parallel to the wall, as in Figure 2.2(a). Such a two shock system is referred to as a regular reflection (RR) (Ben-Dor, 2007).

However, it is often the case that no shock wave exists that is capable of turning the flow through the necessary angle (Hornung, 1986). In these cases, the reflected shock intersects the incident shock some distance away from the wall. A third shock (which is approximately normal to the oncoming flow) referred to as the Mach stem forms between this intersection point (now referred to as the triple point) and the wall. Since the velocities of the fluid behind the reflected shock and Mach stem are not equal, a shear layer is also present. This shear layer seperates two regions of equal pressure in which the fluid is flowing in the same direction, but with different velocities, densities and temperatures. This three shock system is referred to as a Mach reflection (MR), and is shown in Figure 2.2(b). von Neumann (1943a) analysed the flow through regular and Mach reflections, leading to the two and three shock theories.

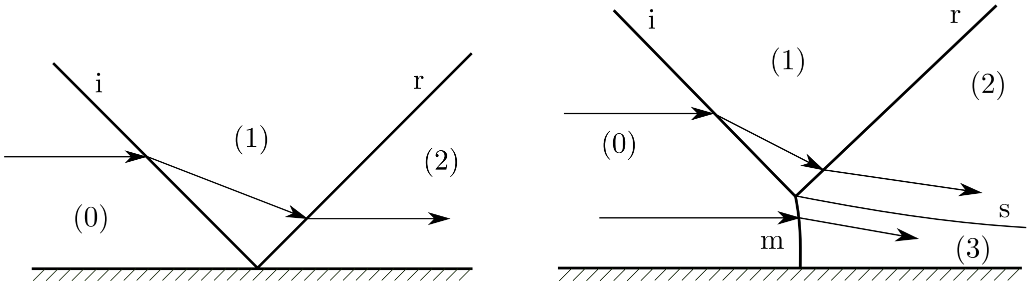

(a) Regular Reflection

(b) Mach Reflection

FIGURE 2.2: Diagram showing types of reflection possible in steady flow. The incident shocks (i), reflected shocks (r), Mach stem (m) and shear layer (s) are shown. In a shock-fixed reference frame, the flow is moving through the system from left to right, and the arrows represent streamlines

In steady and pseudosteady flows, the Mach stem is concave toward the oncoming flow, and the shear layer is furthest from the reflection surface at the triple point. In the case of a shock moving into a stationary medium that encounters a wedge, the reflection is self-similar, and the triple point follows a linear trajectory away from the wedge. This type of MR is referred to as a direct Mach reflection (DiMR). Smith (1945) carried out a thorough experimental study of shock reflection in a shock tube and measured various geometric parameters of DiMRs, including the angle between the triple point trajectories and the surface for a range of Mach numbers and wedge angles. These trajectory angles are summarised in Figure 2.3.

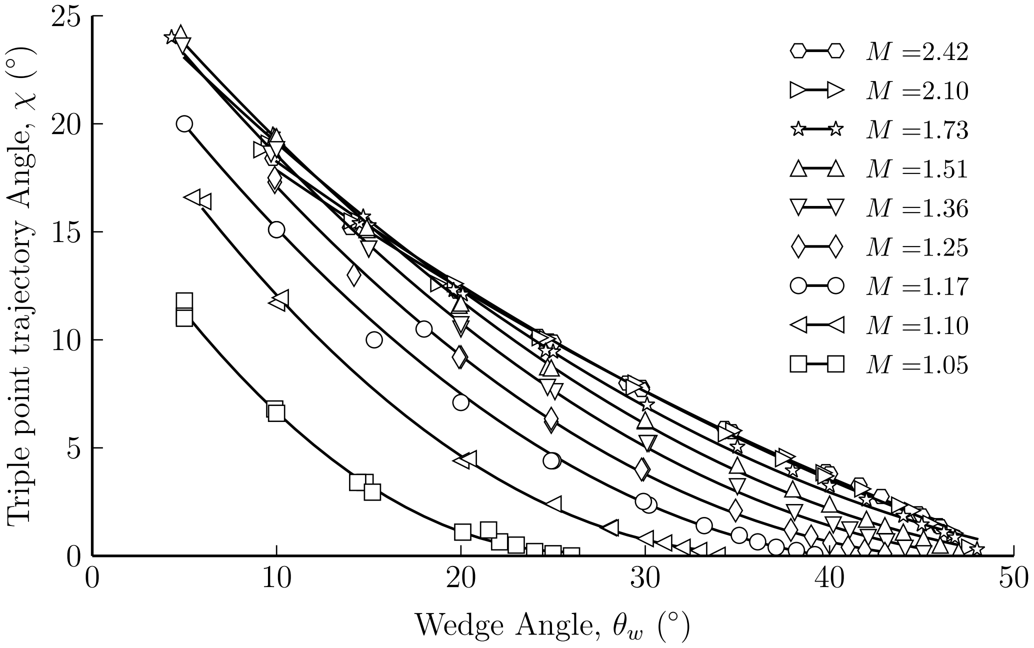

Figure 2.3: Triple point trajectory angles in Mach reflections measured by Smith (1945)

In unsteady flows, it is possible for changes in flow conditions to cause the triple point trajectory to be directed back toward the wedge. In these cases, the Mach stem becomes convex. This is referred to as an inverse Mach reflection (IMR), as shown in Figure 2.4(a).

Since the triple point in an IMR moves back toward the reflection surface, it will eventually reattach, resulting in an RR. The shear layer is still present, however, and interacts with the reflected shock, forming a Mach stem and a new triple point on the reflected shock. This structure is referred to as a transitioned regular reflection (TRR), as shown in Figure 2.4(b).

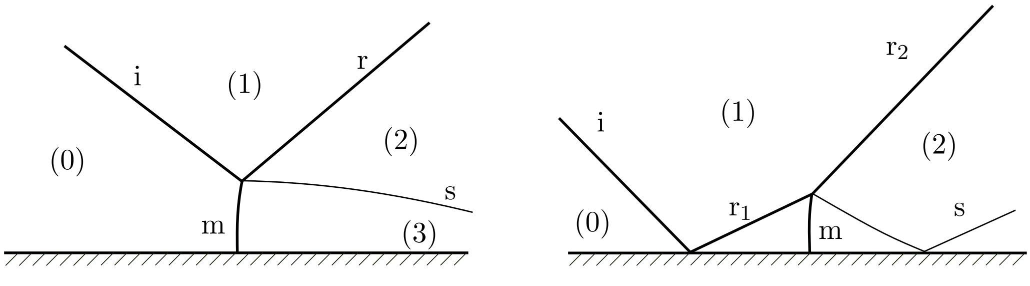

(a) Inverse Mach Reflection

(b) Transitioned Regular Reflection

Figure 2.4: Some reflection configurations possible in unsteady flow. The incident shocks (i), reflected shocks (r), Mach stems (m) and shear layers (s) are shown. In a shock-fixed reference frame, the flow is moving through the system from left to right

It should be mentioned that many other reflection types are possible. These include those reflections associated with weak shock waves and small wedge angles (namely the von Neumann, Guderley, and Vasilev reflections), and those associated with strong shocks in pseudosteady flows (including transitional and double Mach reflections). These are beyond the scope of this text.

2.4.2 Reflection transition criteria for planar shocks

Several criteria have been proposed for predicting whether specific conditions will give rise to RR or MR in steady and pseudosteady flows. Most notable are the detachment, sonic, and mechanical-equilibrium criteria, all of which were originally put forward in some form by von Neumann (1943a,b), and are summarised by Ben-Dor (2007). Unsteady flow (such as that which occurs when the reflection surface is curved) introduces new factors which need to be considered. These cases are discussed below.

2.4.2.1 Transition criteria in steady and pseudosteady flows

The maximum-deflection condition

As mentioned in section 2.4.1, RR cannot occur if no reflected wave exists that is capable of reflecting the flow so that it is parallel to the boundary. This is referred to as the maximum-deflection condition, or detachment condition, and represents the largest incident angle at which a RR is possible.

The sonic condition

The sonic condition states that MR will occur if corner signals travelling at the local sound speed are able to catch up to the reflection point. This is only possible if the flow behind the reflected shock is subsonic relative to the reflection point. If the flow is supersonic, then the reflection point is isolated from the corner, and RR will occur.

Since the detachment and sonic points lie relatively close to each other, it is difficult to distinguish between the two experimentally. However, experiments designed by Lock and Dewey (1989) to distinguish between the two cases suggest that in pseudosteady reflection, the sonic criterion is the one that applies.

The mechanical-equilibrium condition

Experiments by Henderson and Lozzi (1975) showed several cases where the above two criterion were violated. In order to address this, they proposed the mechanical-equilibrium condition to account for this difference. In many cases, the maximum-deflection or sonic criteria require there to be a discontinuous pressure change in the region behind the reflected shock. Such a discontinuous pressure change would need to be supported by additional pressure waves in order to maintain mechanical equilibrium, but such waves had never been experimentally observed. To account for the absence of these pressure waves, the mechanical-equilibrium condition requires that transition occurs at the critical angle at which the two and three shock theories coincide. In order for this to occur, the shear layer in the vicinity of the triple point must be parallel to the reflection surface, and the Mach stem must be straight and perpendicular to the surface.

A number of criticisms of the mechanical-equilibrium condition have been raised (Hornung, 1986; Ben-Dor, 2007). Firstly, there is a critical Mach number below which the mechanical equilibrium condition cannot be satisfied. For a diatomic gas with $\gamma = 1.4$, this occurs for Mach numbers below 2.202. Secondly, the basis of the transition criterion — that there cannot be a discontinuous pressure change during transition — is unfounded, and such discontinuous pressure changes during transition, especially in MR to RR, are in fact commonly observed, and give rise to the Mach stem in the TRR shown in Figure 2.4. Finally, experimental results for pseudosteady reflections do not agree with the mechanical-equilibrium condition. Henderson and Lozzi (1975) proposed that this was because many RRs observed in pseudosteady flows were actually underdeveloped MRs that were not resolved, but experiments involving very long wedges (allowing the MR ample time to grow) do not support this hypothesis.

However, the mechanical-equilibrium condition does have some use. The point at which the two- and three-shock theories coincide also predicts the smallest possible incident angle at which a DiMR is possible. For any incident angle below the mechanical-equilibrium condition, any MR that occurs must be an IMR. This is significant for the length-scale condition described below.

The length-scale condition

Hornung et al. (1979) introduced the length-scale condition, or information condition. The basis of this criterion is that an RR has no length scale, whereas the Mach stem of an MR inherently does. The length-scale condition states that in order for an MR to form, it requires some information regarding the length scale of the system as a whole. This condition differs from the others in that it applies differently in steady and pseudosteady flows. In pseudosteady flows, corner signals are generated as the flow turns at the wedge apex. If these waves catch up to the reflection point, then they transmit information about the length scale from the corner, and MR can occur. This can only happen if the flow behind the reflected shock is subsonic relative to the reflection point, which corresponds with the sonic condition.

In steady flows, however, the information about the length scale does not come from the wedge apex, but rather from the end of the wedge. Expansion waves will be generated by the trailing edge of the wedge, and these will be refracted by the reflected shock and strike the wall some distance behind the reflection point. MR can occur only if a path exists between this point and the reflection point. Hornung et al. (1979) argue that in an MR, the flow between the shear layer and the wall is always subsonic, so a path always exists if MR is possible. In other words, if MR is possible in a steady flow, then it will occur. The earliest point at which an MR is possible is given by the mechanical-equilibrium condition. At low Mach numbers for which the mechanical-equilibrium condition cannot be satisfied, the length scale condition predicts transition at the sonic condition.

In summary the length-scale condition states that transition is predicted by the mechanical-equilibrium condition in steady flows above a critical Mach number, and the sonic criterion in pseudosteady flows, and steady flows below that critical Mach number. This hypothesis is well supported by experimental evidence (Ben-Dor, 2007).

2.4.2.2 Transition criteria in unsteady flows

The analytical treatment of unsteady shock reflection is a little more complicated, as the variation of flow conditions over time need to be considered. In the above section, transition criteria were determined as a function of the shock Mach number and incident angle. If either of these varies with time, then the shock is unsteady, and additional factors need to be taken into account for the transition. The first of these cases — that of a shock with non-constant velocity — corresponds to a curved shock wave, and this will be discussed in section 2.5.4. The case in which the incident angle varies as a shock of constant velocity propagates past an obstacle will be considered here. This corresponds to a planar shock in a shock tube encountering a curved surface, which may be either concave or convex.

Concave cylindrical walls

For concave surfaces, the conditions may pass from the MR domain into the RR domain. In this case, the pressure behind the reflected wave is not continuous during transition, and the Mach stem of the TRR discussed in section 2.4.1 forms as a result. Because of this discontinuity, it is clear that the conditions proposed by Henderson and Lozzi (1975) for the mechanical-equilibrium condition are not applicable in this case.

Ben-dor and Takayama (1985) proposed applying the length-scale criterion of Hornung et al. (1979) in order to analytically predict the MR→TRR transition over a concave cylindrical wedge. As in the pseudosteady case, they proposed that the MR would terminate once corner signals from the start of the wedge could no longer reach the reflection point.

The transition point depends on the path that the corner signals take. Without doing a full computation, there is no simple way of knowing what path the corner signals follow. Ben-dor and Takayama (1985) propose two possibilities. The first possibility is that the corner signals follow a path that closely approximates the wall shape. This may be justified by assuming that the signal propagates along the side of the slip stream, and observing that the Mach stem is typically short compared to the radius of curvature of the wall.

The resulting transition criteria is thus

$$\frac{\sin\theta_w}{\theta_w} = \frac{M_s}{U_{10} + A_{10}} \tag{2.9}$$

where θ_w is the effective wedge angle at which transition takes place, M_s is the shock Mach number, and U_{10} and A_{10} are the flow velocity and speed of sound behind the incident shock, normalized by the speed of sound ahead of the shock, and are given by the following relations:

$$U_{10} = \frac{2\left(M_s^2 - 1\right)}{(\gamma + 1)\, M_s} \tag{2.10}$$

$$A_{10} = \frac{\gamma - 1}{\gamma + 1}\frac{1}{M_s}\left[\frac{2\gamma}{\gamma - 1}\left(M_s^2 - 1\right)\left(M_s^2 + \frac{1}{\gamma - 1}\right)\right]^{\frac{1}{2}} \tag{2.11}$$

The second possibility is that the corner signals propagate along a straight path. Using the same method, one may obtain the criteria

$$\cos\frac{\theta_w}{2} = \frac{M_s}{U_{10} + A_{10}} \tag{2.12}$$

Comparison with experimental results by Ben-dor and Takayama (1985) and numerical results by Taieb et al. (2010) show that equation 2.9 gives reasonable predictions in the range of Mach 1.25 to Mach 2.0. Equation 2.12 gives good predictions in the range of Mach 1.0 to Mach 1.1, but becomes wildly inaccurate for larger Mach numbers.

Ben-dor and Takayama (1985) do note that these models have several limitations. Both models predict that the radius of curvature of the wall does not affect the transition point, but experimental results show that it does play a role. Ben-Dor (2007) states that attempts at developing a more accurate model that takes radius into account require more information about the reflection, and have not yet been successful. Skews and Kleine (2007) point out that the model only takes into account disturbances produced at the inlet, and does not account for the disturbances generated along the rest of the wall.

Skews and Kleine (2007) studied the reflection of shock off a concave cylindrical wall using a high-speed video camera. They used a test piece with a small ramp at the entrance to produce a corner signal, which follows behind the reflected shock at the local sound speed. They identified that the corner signal falls behind the reflection point before transition occurs. This implies that the actual transition will occur slightly later than predicted by Ben-dor and Takayama (1985), and this is likely because of the effect on the wall shape on the triple point trajectory. Skews and Kleine (2009) tracked perturbations generated along the wall, and found that some of the disturbance waves generated along the wall intersect the incident shock above the triple point, implying that the incident shock's strength is not constant near the triple point. This raises questions as to whether three-shock theory is applicable in these cases.

In another analysis by Ben-dor et al. (1987), three shock theory is used with a number of assumptions that are only applicable to very weak shocks to predict the trajectory of the triple point of a shock wave reflecting off a concave cylindrical wedge. The Mach reflection terminates once the triple point trajectory intersects the reflecting surface. The predicted triple point trajectories match those measured from experiments for a Mach 1.10 shock, but deviate at higher Mach numbers.

Convex cylindrical walls

For a convex wall, the shock passes from the RR domain into the MR domain. The primary assumption made when treating concave walls — that the reflected shock is very weak — is not valid in the case of a convex cylinder. As such, no direct analytical models exist yet. However, several numerical methods have been applied to predict transition lines (Ben-Dor, 2007).

Some of the more successful models use geometrical shock dynamics (see section 2.5.3) in order to predict the transition point. One such model is that of Itoh et al. (1981), who proposed that the transition line would be given by

$$\frac{M_w}{M}\sin\theta_w = \tan\theta_w \tag{2.13}$$

where θ_w is the wedge angle at transition, M is the Mach number of the incident shock, and M_w is the Mach number of the Mach stem at the wall, which may be calculated using geometrical shock dynamics. This model shows reasonable agreement with experimental results for lower Mach numbers, but disagreement becomes significant for Mach numbers greater than 2.

Experimental studies (Skews and Kleine, 2009) suggest that visible MR begins at angles about 10° greater than the angle at which corner signals reach the reflection point. Kleine et al. (2014) attempt to estimate the transition point by extrapolating the triple point trajectory back to the wedge from both experimental and numerical data. Although they do acknowledge that this approach may not be accurate, they do find that the angle at which transition occurs for inviscid flows matches that of a straight wedge, but is delayed by between 1° and 3° for Reynolds numbers in the order of 10^5 and 10^6, and up to about 10° as the Reynolds number is decreased to 10^3.

2.4.2.3 Summary of transition criteria

Figure 2.5(a) shows the transition lines for some of the above conditions in steady flows as a function of Mach number and complementary angle (given by $90° - \beta$, where β is the incident angle of the shock). Between the maximum-deflection condition (the point below which which RR is no longer possible) and the mechanical-equilibrium condition (the point at which MR first becomes possible), there exists what is referred to as the "dual solution domain". Usually, an MR will occur in this region, however, if conditions change such that the flow moves into the RR domain and back, an RR will occur in the dual solution domain (Ben-Dor, 2007).

Figure 2.5(b) shows the transition criteria for unsteady flows, with the Mach number transformed from a shock fixed reference frame to a lab fixed frame Although the mechanical-equilibrium criterion is not typically used in pseudosteady flows, it is included here as it predicts the theoretical transition between DiMR and IMR. Ben-Dor's concave wall model, given by equation (2.9) is included for comparison.

2.5 Curved shock waves

The above mentioned criteria consider a shock wave of a specific Mach number. Introducing curvature along a shock front will cause the speed of the shock to vary as it propagates. In addition, as a curved shock wave propagates along a straight surface, the angle of incidence of the shock varies. These factors have a significant effect on the behaviour of the shock wave. Some previous work on the behaviour of such shock waves is discussed in the following sections.

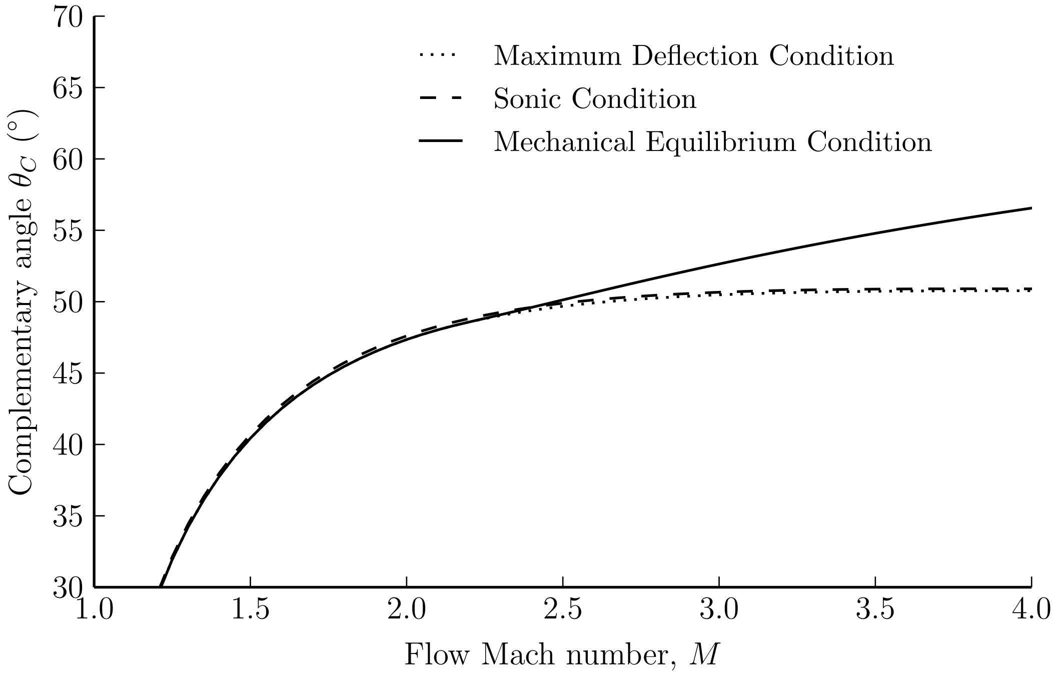

a) Steady transition criteria

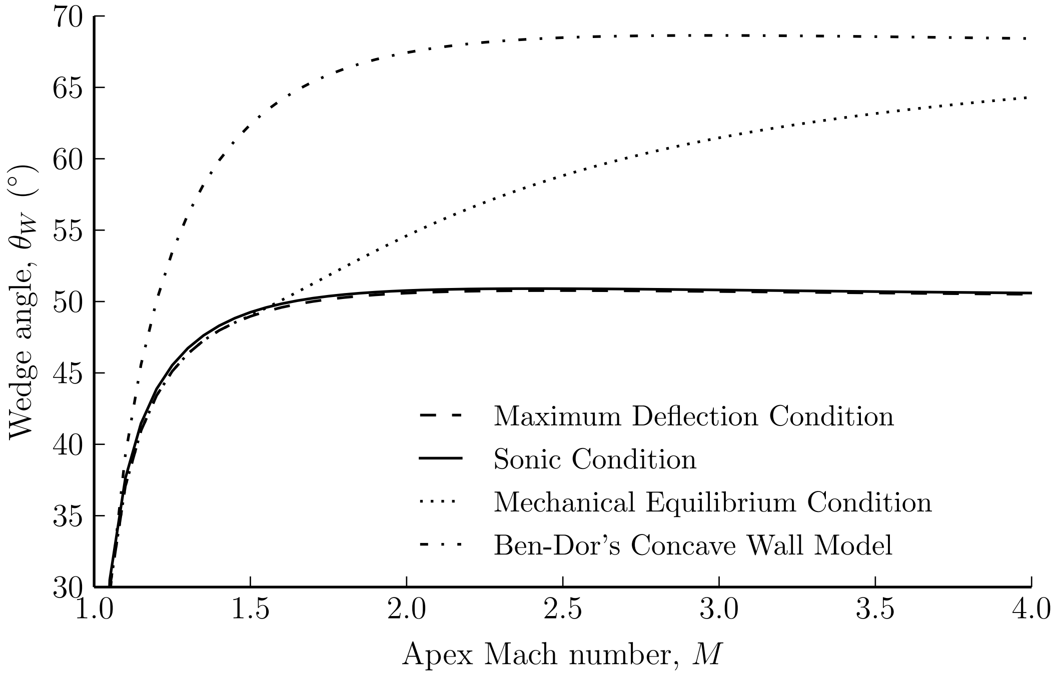

b) Pseudosteady and unsteady transition criteria

Figure 2.5: Theoretical transition lines for steady and unsteady flows. Mach number and incident angle combinations that lie above the transition lines fall in the RR domain, whereas points below the transition lines fall in the MR domain

. The maximum deflection and mechanical equilibrium conditions, while not criteria in pseudosteady and unsteady flows, are included for reference and comparison

2.5.1 Production of curved shock waves

There have been a number of attempts at producing curved shock waves, which have acheived varying levels of success. One of the simplest methods is to reflect the blast waves generated by a detonation off concave reflectors, but this has the major disadvantage that the flow through which the resulting wave propagates is not uniform, and it does not allow for any investigation into the interaction between the shock wave and solid objects.

The method used by Perry and Kantrowitz (1951), whereby the planar wave from a standard shock tube was directed through an axisymmetric chamber which turned the flow inward to form a converging cylindrical wave (see Figure 2.6), proved effective, but compromises had to be made in flow visualisation. The method has been used with some success in studies into the stability of converging cylindrical shocks such as that carried out by Watanabe and Takayama (1991). An improvement to the design was implemented by Wu et al. (1980), who replaced the tear-drop shaped centre body with a segmented axisymmetric contraction, made up of three straight segments, to turn the shock wave through 90°. While each corner initiates an MR, the angles are specially chosen so that these MRs partially cancel each other out as the shock enters the convergence chamber.

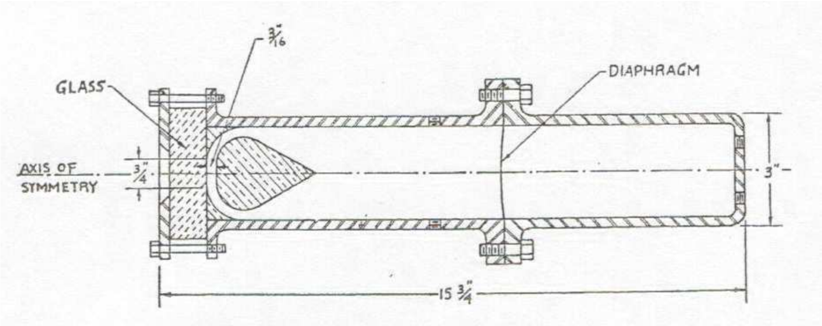

Figure 2.6: Converging shock generation using an annular chamber (Perry and Kantrowitz, 1951)

Similar annular facilities have also been used to produce shock waves with a non-circular shape. Eliasson et al. (2006) replaced the circular outer wall of the convergence chamber with octagonal and pentagonal boundaries to modify the shape of the converging shock wave. Further work by Eliasson et al. (2007) kept the circular boundary, but modified the shape of the shock wave using various inserts inside the convergence chamber to produce polygonal and other converging shock wave shapes. This work was taken further by Kjellander et al. (2011), who carried out numerical simulations into the formation of a two-dimensional converging shock front in the convergence chamber of the facility, the results of which are shown in Figure 2.7. The shock wave is reflected back and forth between the walls of the chamber. The primary shock front strengthens and becomes plane, while the reflected shock waves behind it diminish in strength. A standing shock system is formed some distance from the corner.

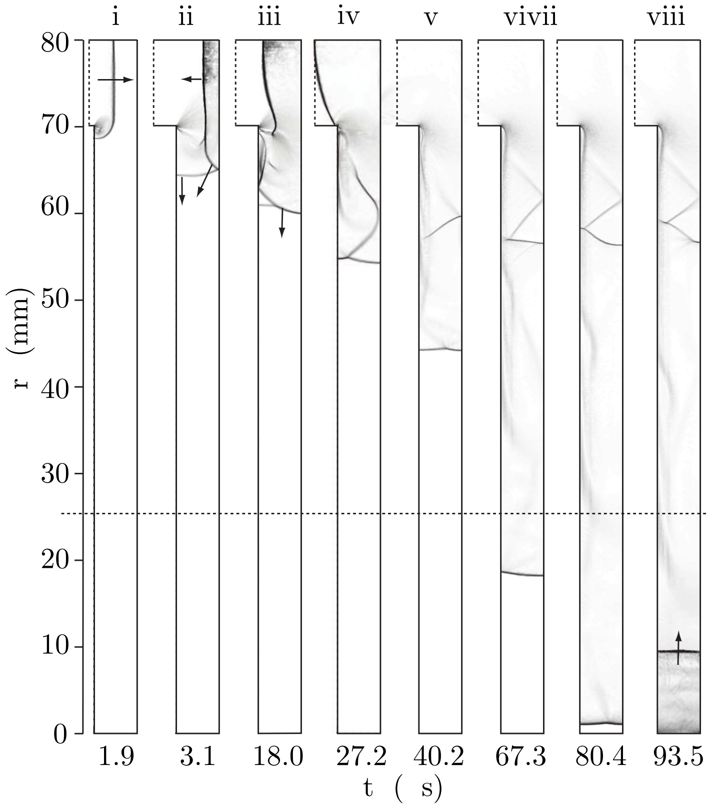

FIGURE 2.7: Numerical schlieren of the formation of a two-dimensional shock front after an axisymmetric corner (Kjellander et al., 2011)

In order to address some of the stability problems with the above design, Dumitrescu (1992) proposed applying geometrical shock dynamics (see section 2.5.3) to determine the wall shape required to bend the shock into the desired shape, as in Figure 2.8. The primary disadvantage of this design is that a different wall shape is required for each initial shock velocity. Nonetheless, this method has been applied with some success to produce converging cylindrical shocks (Zhai et al., 2010) and spherical shocks (Apazidis et al., 2013).

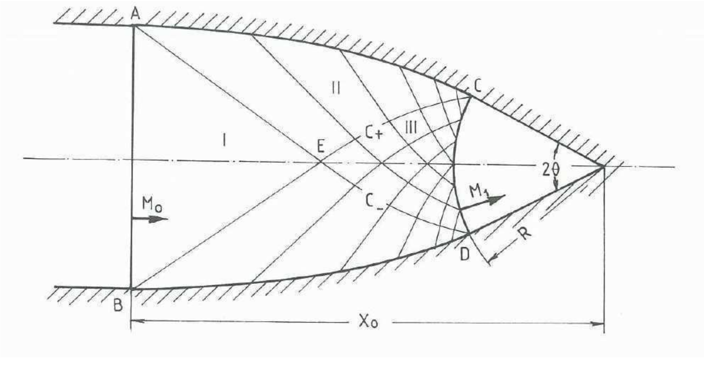

FIGURE 2.8: Generation of a converging shock by means of wall shaping (Dumitrescu, 1992)

Another method for producing shock waves of arbitrary shape is to use the rapid motion of a specially shaped piston to generate the shock wave, as proposed and studied analytically by Van Dyke and Guttmann (1982), although this method would require relatively complex machinery, and is difficult to implement.

The gas lensing technique developed by Dimotakis and Samtaney (2006) provides a repeatable means of producing a converging shock wave of arbitrary shape (see Figure 2.9). A thin membrane of a certain shape separates two gases of different densities. When a planar shock passes through the membrane, its shape is deformed. However, this technique is extremely challenging to implement. One major challenge lies in finding a membrane that is rigid enough to maintain its shape before the arrival of the shock wave, yet flexible enough to allow transmission of the shock wave without significantly impeding its passage. Biamino et al. (2013) have experimented with using a thin wire mesh to hold the membrane in place. This does maintain the membrane shape, but has a detrimental effect on the quality of the post-shock flow.

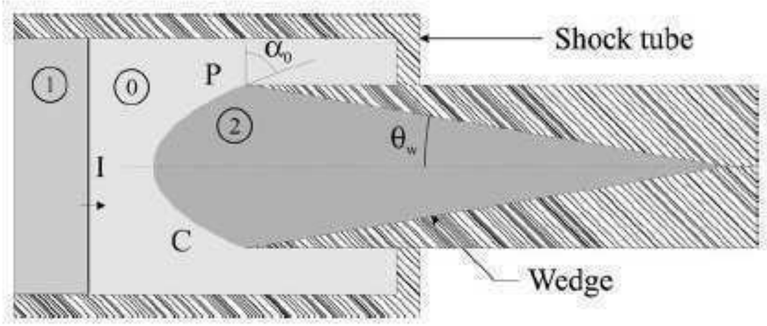

FIGURE 2.9: Converging shock generation by means of gas-lensing (Dimotakis and Samtaney, 2006)

2.5.2 Propagation of curved shock waves

Curved shock waves are unsteady phenomena, and it is not possible to reduce the problem into a pseudosteady problem by applying a Galilean transformation, since the strength of the shock wave varies with time. One of the first attempts at mathematically describing the behaviour of a cylindrical shock wave was made by Guderley (1942), who proposed a power law as a first order approximation for the propagation of a converging shock wave. This may be expressed as

$$r = Ct^n \tag{2.14}$$

where r is the distance from the centre, C is an arbitrary constant that depends on the initial conditions, t is the duration of time before the shock reaches the centre, and n is a constant exponent which depends on the shape of the shock. Several studies have used analytical, numerical and empirical approaches to obtain values for the exponent n. A review of several of these studies by Ponchaut et al. (2006) gives values of 0.835 for cylindrical shocks and 0.717 for spherical shocks.

This relation may be rewritten with the time variable redefined such that it runs forward as the shock wave propagates. The equation may be manipulated in order to determine how the shock Mach number, M, varies as the shock propagates, by taking the time derivative of both sides, and dividing through by the speed of sound a. The variation in the Mach number of the shock front at any given position is thus

$$\frac{M}{M_0} = \left(\frac{r}{r_0}\right)^{\frac{n-1}{n}} \tag{2.15}$$

Where M_0 and r_0 are the Mach number and radius of the shock wave at some previous point in time.

The stability of these converging shocks has been of much interest. Experiments by Perry and Kantrowitz (1951) showed that converging cylindrical shock waves are inherently unstable, and any disturbance along the shock front will result in a local increase in curvature, and eventually cause the formation of reflected waves behind the original shock front. Schwendeman and Whitham (1987) determined both analytically and numerically that such a disturbance would form an MR, and showed that a converging cylindrical shock wave exposed to a series of regularly spaced disturbances would eventually result in a series of repeating polygons. This unstable behaviour was confirmed by experiments carried out by Watanabe and Takayama (1991). Figure 2.10 shows the resulting shape of a converging cylindrical shock wave some time after encountering four small, evenly-spaced disturbances. Schwendeman (2002) later showed that this behaviour also occurs in three dimensions, and that imploding spherical shocks exposed to regular disturbances would result in a series of repeating polyhedra.

The majority of the research that has been carried out into the propagation of shocks of non-constant curvature has been into the focusing of shocks of various shapes, produced by reflecting a planar shock off of a concave cavity at the end of a shock tube. Grönig (1986) gives a summary of the earlier works in this field. One of the first of such studies was carried out by Sturtevant and Kulkarny (1976), who investigating the focus of shock waves produced by planar incident shocks of Mach 1.005 to Mach 1.5 reflected off shallow cavities. Five of their six models had sharp corners at the cavity inlet, and their study found that the flow in these profiles was dominated by the interaction between the converging incident shock, and what Sturtevant and Kulkarny (1976) termed diffracted expansions, which were actually most likely the Mach stems of a TRR pair (MacLucas, 2012).

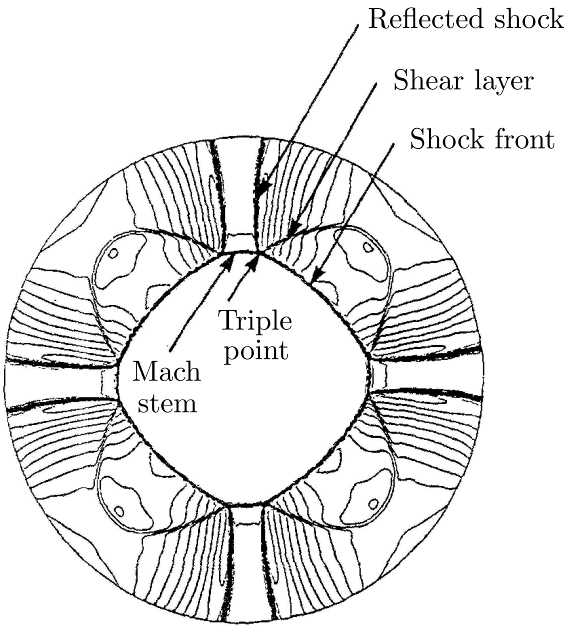

FIGURE 2.10: A converging cylindrical shock some time after encountering four small, evenly-spaced disturbances (Watanabe and Takayama, 1991)

The sixth profile of Sturtevant and Kulkarny (1976) was designed with a curved entry with flat ends, so that the reflected shock front would not contain any discontinuities. Results obtained from these profiles at various Mach numbers are shown in Figure 2.11.

Each of the four cases shown undergo distinctly different behaviour. As the shock propagates, two points along the shock front undergo a local increase in curvature, forming a pair of kinks which develop into the triple points of an MR. At the acoustic limit, this occurs on the symmetry axis at the geometrical focal point of the cavity profile. For strong shocks, the triple points follow divergent trajectories. For weak and moderately weak shock waves, the triple points converge, and for initial incident Mach numbers of about 1.2 and below, the triple points cross, resulting in what Sturtevant and Kulkarny (1976) referred to as a “crossed and folded” shock front, which resembles the reflection pattern that was later named TRR.

Several studies have expanded the work of Sturtevant and Kulkarny (1976), such as those of Izumi et al. (1994), Skews and Kleine (2007), Taieb et al. (2010) and MacLucas (2012). It is important to note that the curved wave propagates into flow that has already been disturbed by the incident shock, and for all but the shallowest profiles, the shock will interact with reflected shocks from the cavity entrance. This limits the insight that these studies can provide into the propagation of a curved shock into stationary flow.

There exist some means of treating the propagation of an arbitrarily-shaped shock front analytically, and these will be described in the next section.

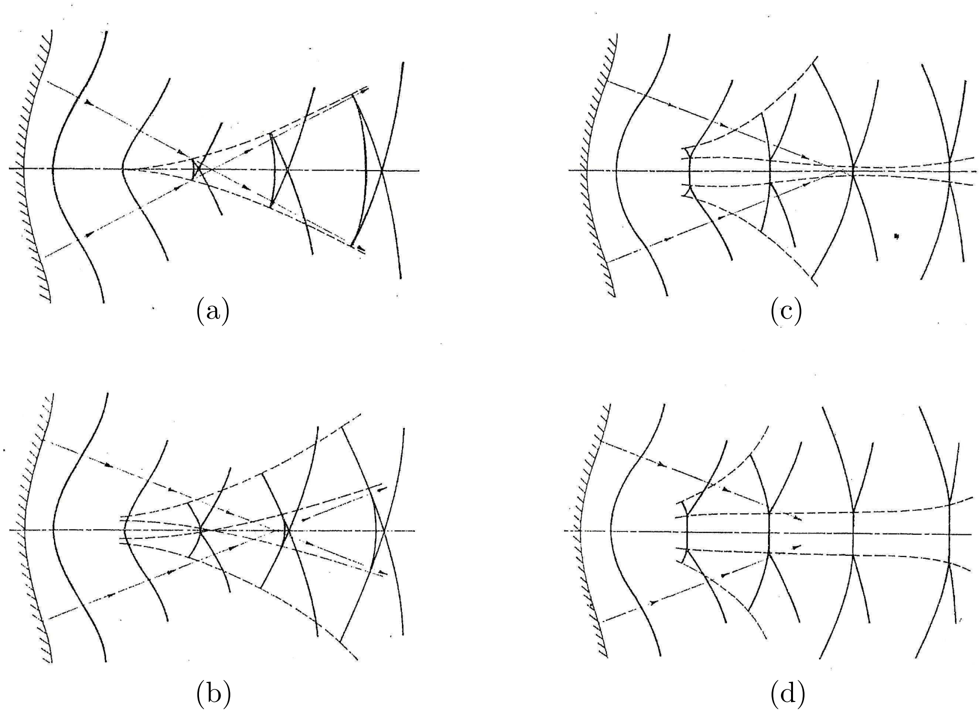

FIGURE 2.11: Schematic of shock positions at various times after reflecting off a shallow concave cavity for (a) sound pulses, (b) weak shocks ($M \sim 1.1$), (c) moderately weak shocks ($M \sim 1.3$), and (d), moderate shocks ($M \sim 1.5$) (Sturtevant and Kulkarny, 1976)

2.5.3 Geometrical shock dynamics

Whitham (1957, 1959) developed an approximate theory of shock propagation, referred to as geometrical shock dynamics (GSD), by treating disturbances in the flow as waves propagating along the shock front. The theory considers a set of successive shock positions as a shock moves into a uniform medium. It then introduces a set of orthogonal trajectories, called "rays" between the shock positions, as shown in Figure 2.12. Chester (1954) developed an expression for the strength of a shock undergoing a small area change, which was later expanded by Chisnell (1957). Whitham applied these expressions to each ray to determine the propagation of the shock front. The summary below is primarily adapted from Whitham (1974).

The change in Mach number of the shock as it propagates along a ray may be found by solving the so-called A-M relation

$$\frac{A}{A_0} = \frac{f(M)}{f(M_0)} \tag{2.16}$$

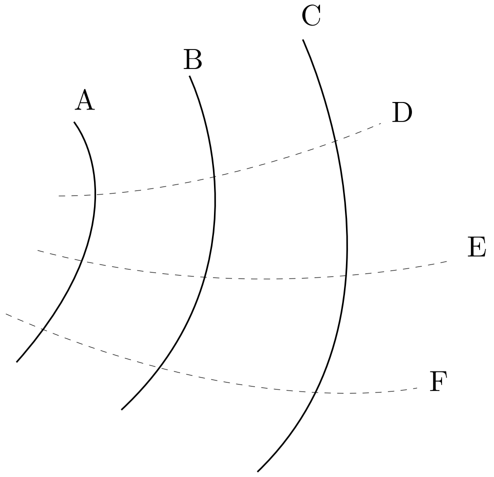

FIGURE 2.12: A sketch showing successive shock front positions A, B, and C, and orthogonal rays D, E, and F

where A_0 and M_0 represent the initial cross-sectional area of the ray and Mach number respectively. The function $f(M)$ is given by

$$f(M) = \exp\left(-\int \frac{M\lambda(M)}{M^2-1} dM\right) \tag{2.17}$$

with

$$\lambda(M) = \left(1 + \frac{2}{\gamma+1}\frac{1-\mu^2}{\mu}\right)\left(1 + 2\mu + \frac{1}{M^2}\right) \tag{2.18}$$

and

$$\mu^2 = \frac{(\gamma-1)M^2+2}{2\gamma M^2-(\gamma-1)} \tag{2.19}$$

Note that equation (2.19) is equivalent to equation (2.4), so μ represents the Mach number of the flow behind the shock wave, measured relative to the shock wave.

While a few problems do have analytical solutions, the equations of GSD usually need be solved numerically. Popular approaches include the method of characteristics, as used by Bryson and Gross (1961), front tracking methods, such as the one proposed by Henshaw et al. (1986), and finite-difference schemes, such as the one developed by Cates and Sturtevant (1997).

GSD does have some limitations, and many of these arise when dealing with the reflection of a shock by a wedge. GSD predicts MR at all angles (Henderson, 1980). In addition, it only predicts the behaviour of the incident shock, although the presence of a reflected shock and shear layer may be inferred from discontinuities along the shock front — what Whitham (1957) referred to as shock-shocks. Whitham believed that tracking the trajectory of these shock-shocks would give the triple point trajectory of an MR. However, the predicted trajectory angles severely under- or overestimate the actual trajectory angle for most wedge angles and Mach numbers.

One likely reason for this is that GSD neglects the effect of disturbances behind the shock on the shape of the shock front, yet such disturbances play a significant role in the formation of an MR. In order to address this, Milton (1975) proposed modifying the area change function in equation 2.17, by including an additional term as follows:

$$f(M) = \exp\left[-\int \left(\frac{M\lambda(M)}{M^2-1} + \frac{\eta}{M}\right) dM\right] \tag{2.20}$$

where

$$\eta = \frac{1}{2\gamma}\left[\sqrt{\frac{\gamma(\gamma-1)}{2}} + 1\right]\left[1 - \frac{M_0^2}{M^2}\right] + \frac{1}{2}\ln\frac{A_0}{A} \tag{2.21}$$

Duong and Milton (1985) give the following approximate expression for this integral

$$\frac{A}{A_0} = \left(\frac{M_0-1}{M-1}\right)^2 \left(\frac{M_0+1}{M+1}\right)^{\alpha} \left(\frac{M_0-\delta}{M-\delta}\right)^{\beta} \left(\frac{M_0}{M}\right)^{\eta} \tag{2.22}$$

where $\alpha = 2.719$, $\beta = 0.354$, and $\delta = 0.493$ for a gas with $\gamma = 1.4$.

This modification gives better predictions for the triple point trajectory angle for strong shocks for wedge angles below 40°, after which it begins to deviate as the RR domain is approached. For weaker shocks, the range of Mach number over which the model gives reasonable predictions is reduced. At a Mach number around 1.7, Milton (1975) shows that the range of good agreement with experiment is reduced to wedge angles between 30° and 40°, and at Mach 1.5, the range reduces to just 32° to 37°. However, Milton does note that strong shock approximations were made when calculating these ranges, and that slightly more accurate results could possibly be obtained using exact relations.

2.5.4 Reflection of curved shock waves

There has not been much previous work into the reflection of curved shock waves. Very little research into the behaviour of two-dimensional shock waves could be found, and the majority of research into spherical waves involved the reflection of blast waves off the ground.

Some of the original work into blast wave reflection was carried out by Dewey et al. (1977). Their results show a reflection that is initially regular, but transitions to an MR as the incident angle increases. A theoretical treatment of blast wave reflection transition was developed by Hu and Glass (1986), and is shown in Figure 2.13. Their analysis shows that the initial reflection will fall into the RR domain, but as the blast wave expands, the Mach number and effective wedge angle decrease, moving through the double Mach reflection, and transitional Mach reflection domains, and finally into the single Mach reflection domain. Once the instantaneous Mach number, wedge angle and reflection configuration are known, the flow properties behind the blast wave may be calculated using standard shock relations.

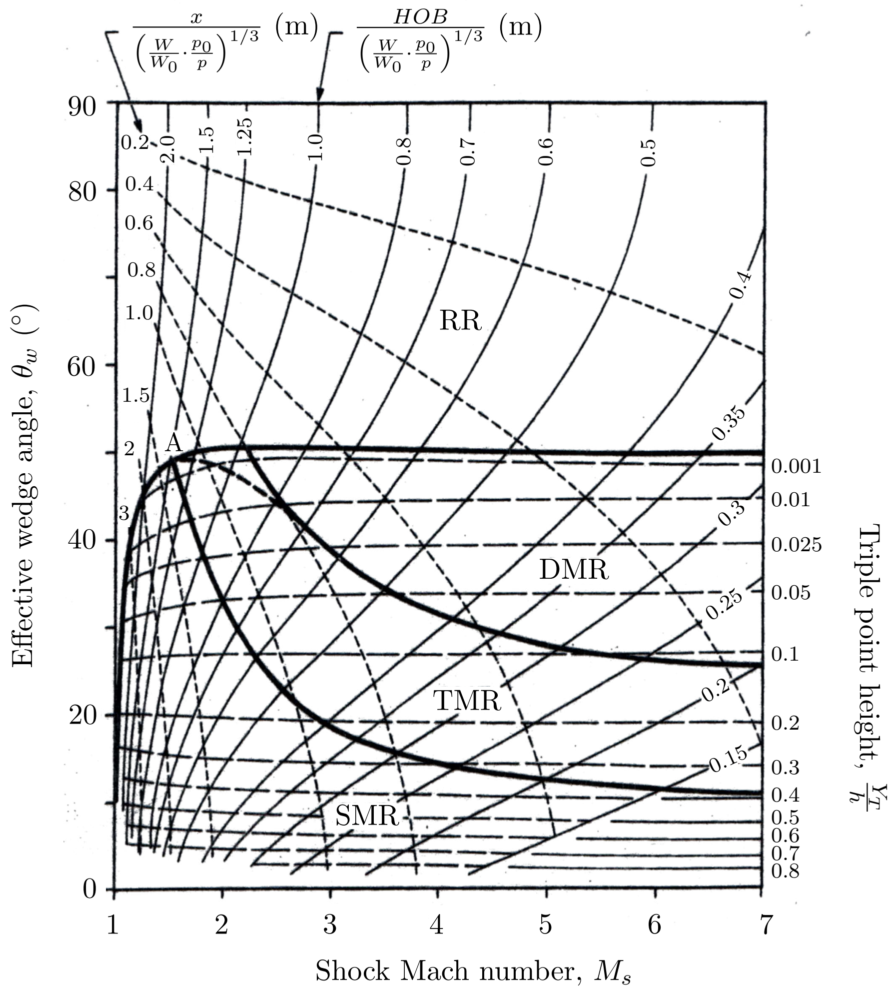

FIGURE 2.13: Incident angle and Mach number locii for a spherical blast wave encountering a planar surface (Hu and Glass, 1986). x and HOB are the horizontal distance from the centre of the blast and height of burst, non-dimensionalised by a reference weight of TNT W_0, and reference pressure p_0. The height of the triple point Y_T is also predicted

Comparison with experiments by Wisotski et al. (Ben-Dor, 2007) show that the transition angle predicted by theory may be out by as much as 10° in some cases, and in fact, the theory predicts that the transition angle will decrease with Mach number, whereas experimental results show an increasing trend.

Takayama and Sekiguchi (1981a,b) generated spherical shock waves from the end of a shock tube and studied the reflection of these shocks over flat surfaces and cones. They developed a simple analytical method for predicting the triple point trajectory of the resulting MR, which showed good agreement with their own experiments, as well as experiments involving blast waves by Dewey et al. (1975).

Numerical simulations have also been carried out on cylindrical (Liang et al., 2001) and spherical (Liang et al., 2002) blast waves encountering a flat plate. In the case of cylindrical and weak spherical blast waves, the initially regular reflection transitioned directly into a single Mach reflection for all cases simulated. However, in strong spherical blast wave reflection, the initial reflection can be a double Mach reflection if the height of burst is low enough. This results in a complex system of shocks behind the wave front as the Mach number slows and effective wedge angle decreases, which persists into what Hu and Glass (1986) predicted would be the single Mach reflection domain.

3. Research Objectives

Following on from the introduction given, the objectives for the investigation may be defined. The primary objective of this research was the design, manufacture and validation of a new facility for the production of shock waves of an arbitrary two-dimensional profile. Additional objectives are as follows:

- Investigate the propagation of shock waves of arbitrary profiles.
    - To use the newly constructed facility to experimentally produce and photograph successive positions of shock waves with various two-dimensional profiles.
    - Compare the wave shapes and speeds produced by the experiments to computational results.
- Investigate the reflection behaviour of converging shock wave segments of constant curvature.
    - Carry out experimental, computational and analytical studies into the interaction between converging cylindrical shock wave segments and an inclined wedge.
    - Determine the effect of the shock Mach number, initial radius of curvature and wedge incidence angle on the type of reflection and the transition conditions.

4. Facilities

The research involved both computational and experimental aspects. The facilities used for these are described in the following sections.

4.1 Computational facilities

Various analysis, post-processing and graph plotting tasks were carried out by means of scripts written in Python 2.7.5 using the NumPy 1.7.0 extension, and the Matplotlib 1.3.0 plotting library (Hunter, 2007).

Computational Fluid Dynamics (CFD) simulations were used to analyse the flow behaviour for various cases. Two solvers were readily available, namely ANSYS® Fluent and Wits University's Flow Research Unit's in-house Euler solver. In both cases, post-processing was carried out using TecPlot 360™. More details of each of these solvers are given in the following sections.

4.1.1 Simulations using the in-house solver

The University of Witwatersrand's in-house solver is a vertex centred finite volume flow solver written in C++ by Felthun (2002), and has been adapted and added to by a number of authors in subsequent years. Since the code was developed for use with moving boundaries, it includes a very robust meshing scheme that is ideally suited for resolving transient flow features. The primary advantage of using the in-house solver is that the source code may be readily edited, and the workings of the solver are transparent.

The geometry is specified by a series of edges, which may be straight, or defined by piecewise cubic splines. The solver then uses a built-in robust meshing scheme to generate an unstructured triangular mesh across the domain. This mesh is then adapted and refined throughout the simulation if the normalised density gradient within a cell exceeds a specified limit. Near the boundaries, the adapted mesh is adjusted to conform to the curves specifying the original geometry, rather than the mesh that it was adapted from. This ensures that the shape of the domain is maintained, even in regions where the initial mesh may have been relatively coarse. Typical initial and adapted meshes are shown in Figure 4.1.

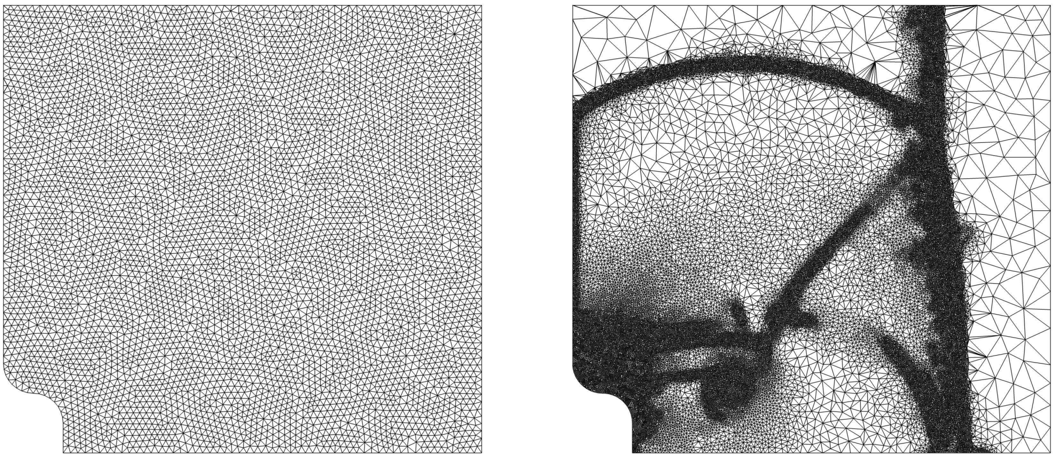

(a) Initial mesh

(b) Adapted mesh

FIGURE 4.1: Typical meshes used by the in-house Euler solver

The initial shape of the shock wave was configured as a pressure inlet, with the conditions at the inlet set to match the velocity and stagnation pressure and temperature behind the shock wave to be generated. For straight sections of the inlet, the direction of the flow was defined to be perpendicular to the inlet. Curved inlets were divided into segments defined by cubic splines, with each segment having a locally defined flow direction that was normal to the boundary. The limitation of this approach is that the flow direction will not be exactly normal to the boundary at any specific point, but will be normal to the boundary when averaged over a small region, and there are finite changes in flow direction where two splines meet. However, this should not significantly affect results as long as the change in flow direction between two adjacent nodes on the boundary is of similar or smaller magnitude to changes in flow direction between two adjacent nodes away from the boundary. All other boundaries were treated as solid walls.

Specific configuration of the solver varied from simulation to simulation. Where necessary, these will be discussed in the relevant sections.

4.1.2 Simulations using ANSYS Fluent

Three-dimensional and two-dimensional axisymmetric numerical simulations were carried out for the facility design, and pure two-dimensional simulations were carried out for the case of a curved shock impinging on a wedge. These simulations were carried out in ANSYS Fluent using an inviscid, density-based finite difference solver, with second order implicit time formulation. The flow was modelled using the third order Monotonic Upstream Centred Schemes for Conservation Laws (MUSCL) with Roe's Flux-Difference Splitting (FDS) scheme, and least squares, cell-based spatial discretisation.

The meshes were generated using ANSYS Meshing. For the 2D cases, mapped face meshing was used to generate structured quadrilateral mesh conforming to the domain. The size of the cells were controlled by specifying the number of divisions along each edge, with a slight bias to smaller cells closer to the wedge apex. In the 3D cases, the mesh was generated based on proximity and curvature, with a curvature normal angle of 10°, a minimum of five cells across gaps, and a growth rate of 1.06.

During all of the simulations, cells with normalised density or Mach number gradients exceeding certain limits were refined up to five times, and cells in regions of approximately uniform flow were combined to optimise the computation time needed. The thresholds for determining whether to coarsen or refine the mesh in a region depended on Mach number. For a weak initial shock, features in the flow are more difficult to resolve, and thus the threshold needs to be set lower. Much higher gradients occur for a stronger initial shock, and these simulations are susceptible to noise if the threshold is set too low, resulting in excessively long computation times. To overcome this, cells were refined if the normalised density or Mach number gradient exceeded 2% for initial shocks less than Mach 1.7, 3% for shocks between Mach 1.7 and 1.9, and 8% for shocks stronger than Mach 1.9, and cells were coarsened if these gradients were less than 1%, 3% and 12% in each of the above Mach number ranges.

Typical initial and adapted meshes for the 2D and 3D simulations are shown in Figure 4.2.

The air inside the domain was modelled as an inviscid ideal gas, and initialised with a pressure of 101325 Pa and a temperature of 300 K. The inlet was set as a pressure inlet, with the flow conditions set to the conditions behind the shock of the desired strength, and the flow direction was set to be normal to the boundary. This produces an initial shock wave that closely conforms to the shape of the inlet. For the cases where the inlet was curved, the shock wave needed to be resolved sufficiently within a small distance, which required a relatively small initial time step. A time step of 1×10^{-7}s was found to be suitable, and is equivalent to a CFL number less than 0.1 for a Mach 2.0 shock wave, based on the initial cell size.

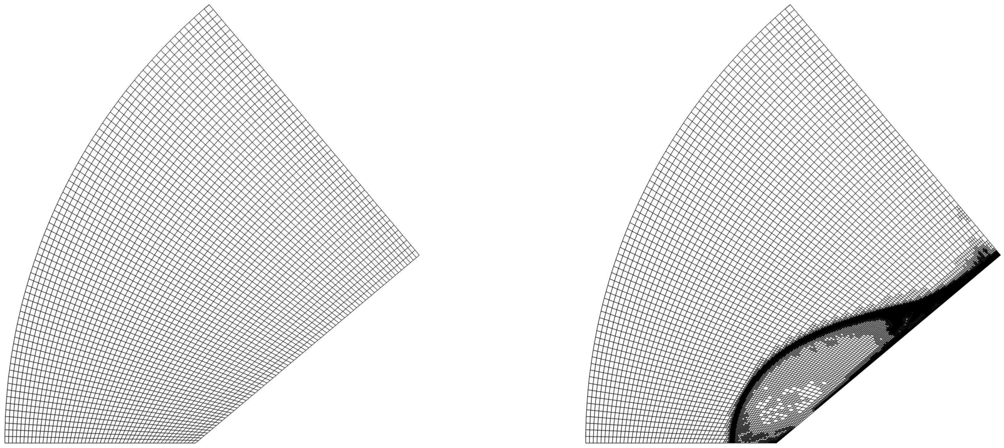

(a) Initial 2D mesh (b) Adapted 2D mesh

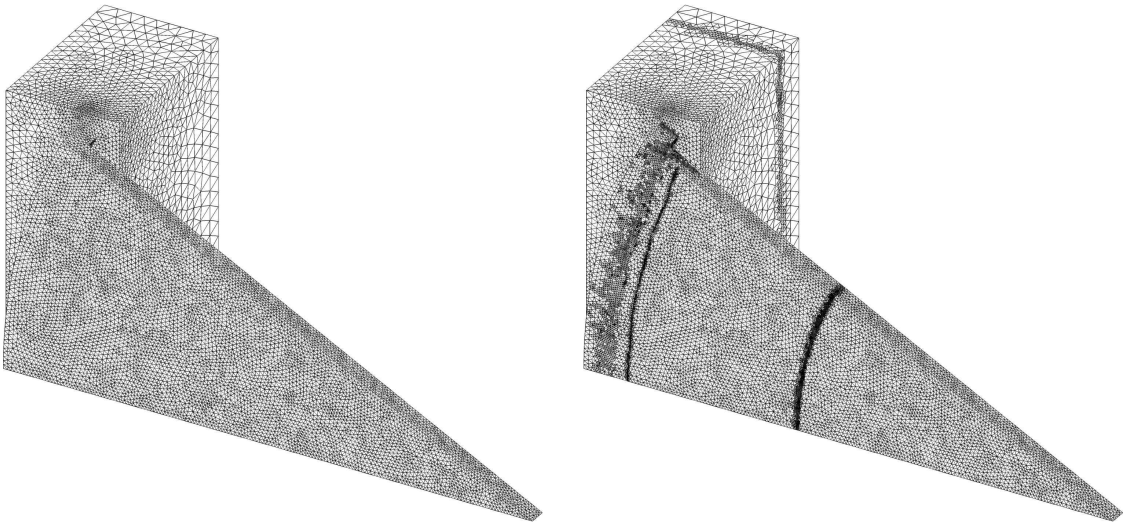

(c) Initial 3D mesh (d) Adapted 3D mesh

Figure 4.2: Typical meshes used by ANSYS Fluent

4.2 Experimental facilities

Experiments were carried out in the Flow Research Unit, located in the Barloworld Laboratories at the University of the Witwatersrand, Johannesburg.

An experimental apparatus for the production of curved shock waves was designed. Rather than designing and building a complete new facility, a device which may be attached to the end of a conventional shock tube was designed. The design of this apparatus is covered in more detail in Chapter 5, but descriptions of the rest of the equipment used are given below.

4.2.1 Shock tube

The shock tube used was the Large Scale Diffraction Shock Tube (LSDST), colloquially referred to as the "Blue Tube". The shock tube was originally designed by Lacovig (2011) and consists of:

- a cylindrical driver section, approximately 2m long, capable of reaching pressures of up to 10 bar (shown in Figure 4.3(a)),
- a plastic diaphragm, and
- a driven section consisting of three 2m long sections with a rectangular internal cross section with internal dimensions of 450mm and 100mm, held together with M14 bolts (shown in Figure 4.3(b)).

The research apparatus consists of an end-piece which attaches to the end of the expansion chamber of the above shock tube. Due to the small size of the test section compared to the driver capacity, modifications were made to the driver in order to reduce its capacity in the interests of safety. Details of these modifications are given in Appendix A.

4.2.2 Flow visualisation

Schlieren flow visualisation was used to capture the behaviour of the shock waves. The schlieren technique takes advantage of the fact that the refractive index in a medium increases approximately linearly with density (Settles, 2001). The system is configured such that parallel light passes unaffected through a flow field of uniform density. This parallel light is then focused onto a knife edge, such that approximately half of the light is cut off uniformly across the flow field. If a density variation is introduced in the flow field, then the path of the light through the density variation is deflected toward the side with the higher density. Depending on the orientation of the knife edge, this may result in the light being deflected slightly away from or toward the knife edge, resulting in a brighter or darker region at a point in the image. As a result, the intensity of light reaching any point on the image is directly proportional to the density gradient in the direction perpendicular to the knife edge of the corresponding point in the flow field.

In this particular study, a Z-configuration schlieren system such as the one in Figure 4.4 was used. The system was made up of the following components:

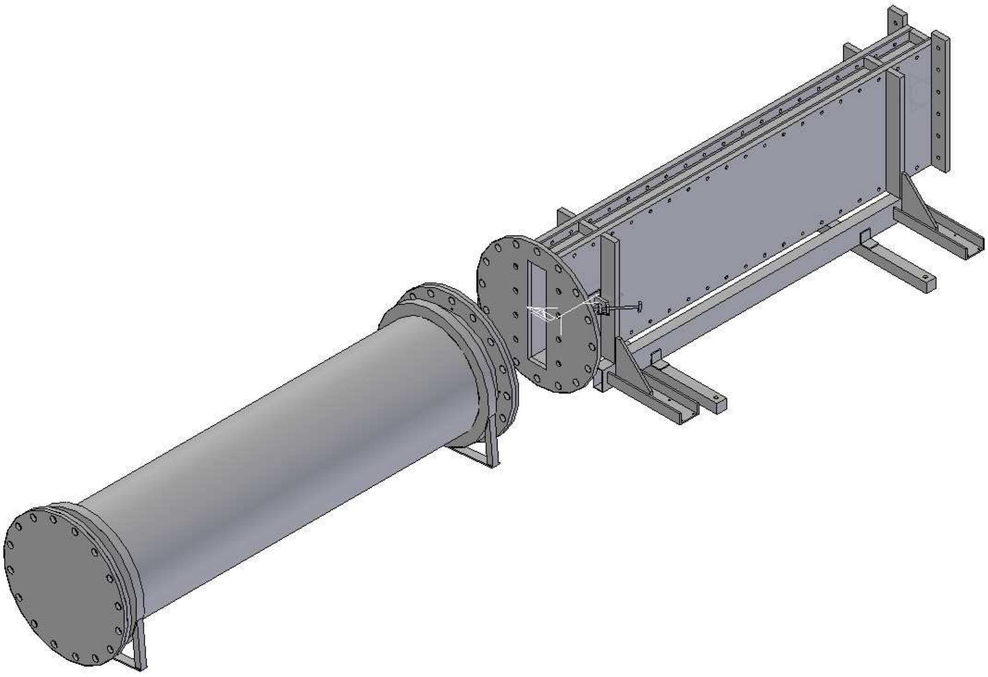

(a) Driver and first driven section of the LSDST

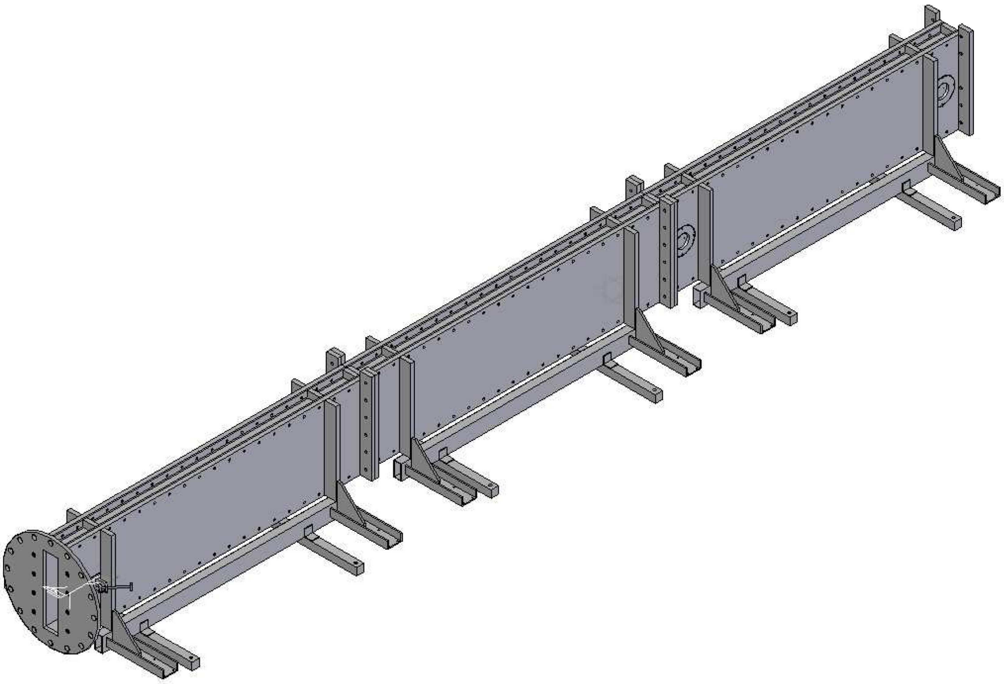

(b) All three driven sections of the LSDST

Figure 4.3: Isometric view of existing shock tube driver and driven sections (Lacovig, 2011)

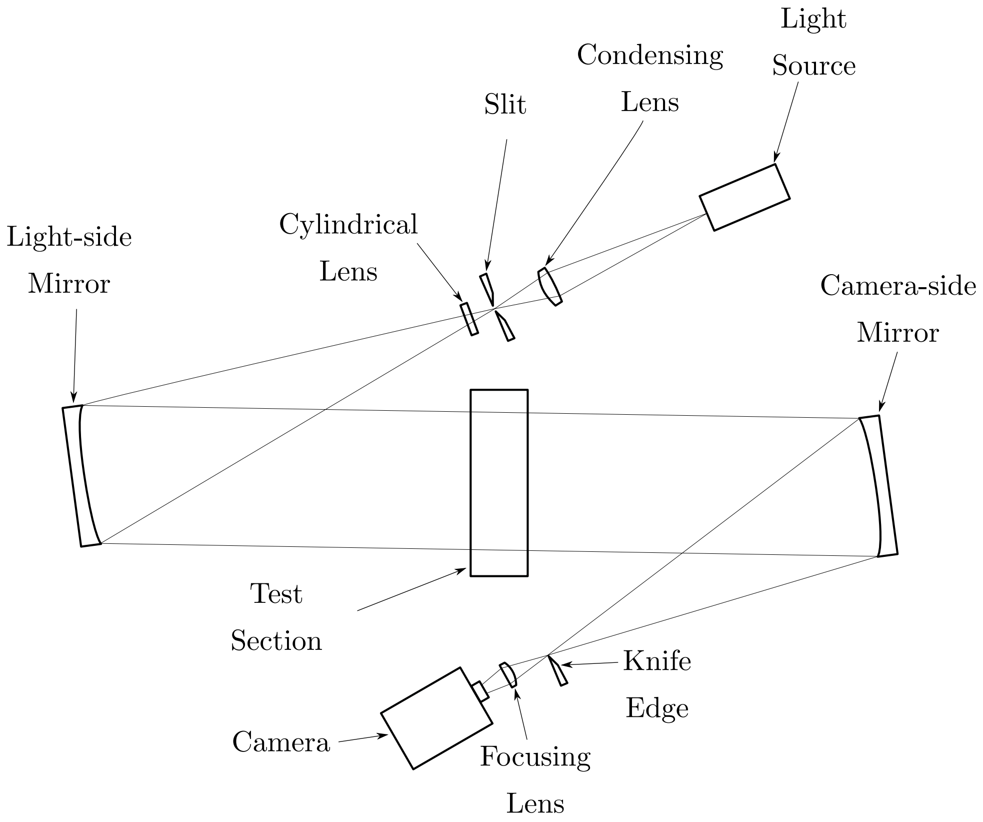

Figure 4.4: Schematic diagram of the schlieren configuration used

- A light source — For single shot photography, a xenon flash lamp was used, with an equivalent exposure time of approximately 1.5 μs. For high speed photography, a Canon Speedlite 430EX II camera flash served as the light source.
- Condenser lens with a focal length of approximately 85 mm.
- Slit — A pair of adjustable knife edges served as the slit. Black insulation tape was applied on either side of the slit to ensure that a circular beam of uniform intensity emerged on the other side.
- Cylindrical lens — This was necessary to correct astigmatism and ensure a point focus on the camera-side knife edge.
- Schlieren mirrors — Two 350 mm diameter parabolic mirrors with focal lengths of 1836 and 1841 mm respectively were used. Parabolic mirrors ensure that the light passing through the test section is truely parallel, however, using parabolic mirrors off axis inherently introduces coma into the system. Using two almost identical mirrors in a Z configuration effectively cancels this coma (Merzkirch, 1987).

- Knife edge — A razor blade mounted on an adjustable stand served as the knife edge. The orientation of the knife edge varied between tests, depending on the features that needed to be resolved.
- Focusing lens with a focal length of approximately 75 mm for low magnification, or 165 mm for higher magnification.
- Camera — For single shot photography, a Nikon D40X 10.2 megapixel camera was used. High-speed photography was carried out using a Photron FASTCAM SA5 camera running at either 20 000 or 100 000 frames per second and the minimum shutter speed of 1 μs.

4.2.3 Instrumentation and facility layout

The layout of the instrumentation used to operate the shock tube is shown in Figure 4.5.

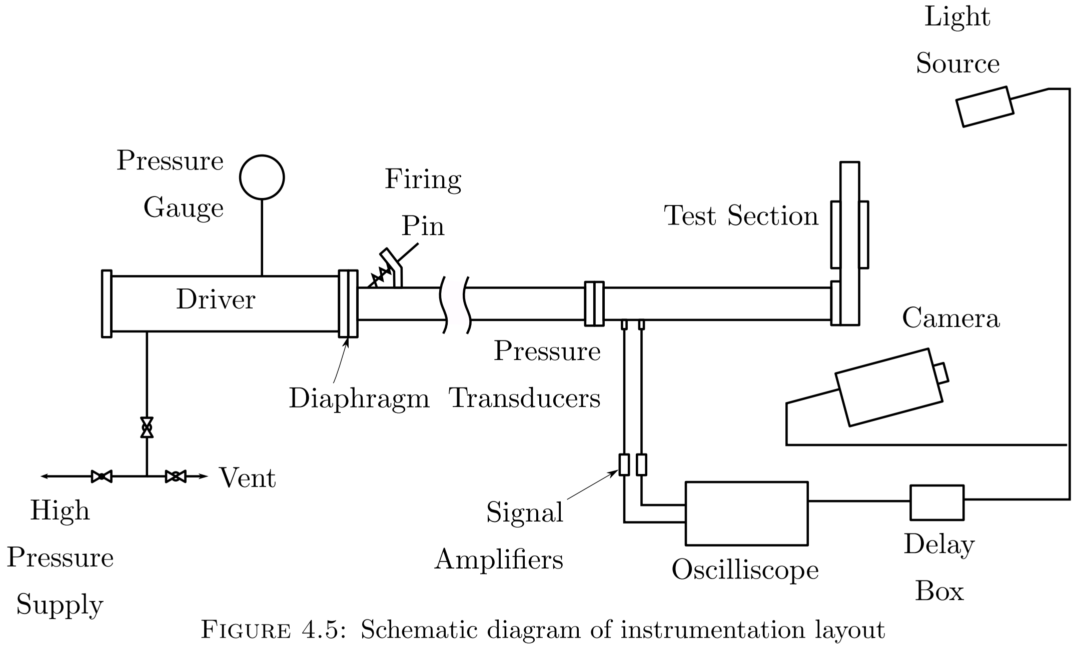

Figure 4.5: Schematic diagram of instrumentation layout

A 15 bar air supply was used to pressurise the driver. A pair of ball valves mounted onto the control board allowed switching between pressurising and venting the driver. A pressure gauge was also mounted to the control board, and this gave a reading of the pressure inside the driver.

Controlled bursting of the diaphragm was achieved by means of a spring loaded pin. A catch was used to hold the pin in place while the driver was pressurised. When the driver reached the desired pressure, the operator could release the catch using a pull cord to fire the pin into the diaphragm. By leaving the pin latched, a natural burst could also be achieved.

Pressure measurements were taken by a pair of PCB pressure transducers embedded in the wall of the driven section. The signal from these transducers was recorded by an oscilloscope, which was used to generate a trigger signal when the shock reached the transducers, and also measure of the time taken for the shock to pass between the two transducers. The signal was first passed through a delay box, and then sent to trigger the light source, and, in the case of high-speed photography, the camera. For single shot photography, the lights in the room were switched off, and the shutter was manually held open for the duration of the test, with the length of the pulse from the light source determining the effective exposure time.

5. Test Facility Design

The design of the apparatus used to generate the curved waves is largely based on previous conceptual work. The existing concepts were combined and adapted to produce a suitable design which is capable of producing waves of an arbitrary shape and strength in a repeatable manner, but without overly complicating the manufacture, assembly and operation of the facility. The design process is described in the following sections.

5.1 Summary of previous design work

Two conceptual designs were carried out at the University of the Witwatersrand, Johannesburg in 2009. The first of these designs (Skews and Daya, 2009) is shown in Figure 5.1. The facility develops a cylindrical wave by passing the planar shock wave from the end of the shock tube through a curved slit of constant radius, and allowing the resulting wave to propagate in a chamber that runs perpendicular to the original shock tube. The concept was developed using a CFD study into the effect of various configurations on the shape and stability of the resulting wave. Results for one case are shown in Figure 5.2.

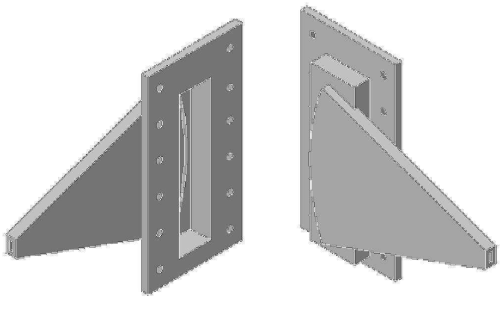

FIGURE 5.1: The design concept of Skews and Daya (2009)

The study found that the most stable shock for a variety of inlet curvatures occurred when the walls of the propagation chamber were perpendicular to the curve profile. This prevented unwanted expansion which interfered with the shape of the shock. The shock also stabilised

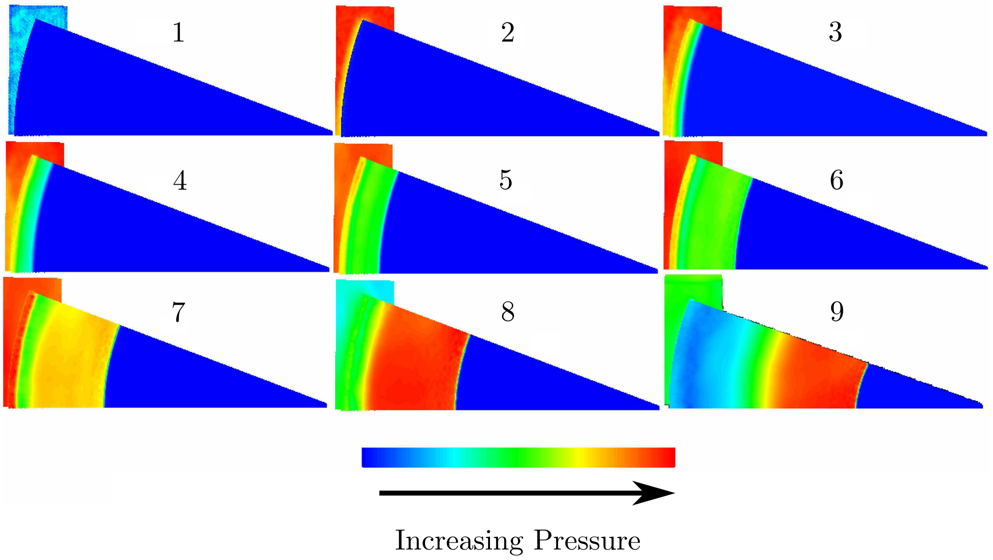

Figure 5.2: CFD results for a shock turning through a cylindrical slit - quality of transmitted shock (Skews and Daya, 2009)

into an approximately two-dimensional wave faster as the thickness of the propagation chamber was decreased. However, while decreasing the thickness of the slit improved the overall quality of the shock, it had a negative effect on the quality of the wave at the edges.

The design of Skews and Beharie (2009) follows on from the previous design. The principle of its operation is the same, but the design takes manufacture and customisability concerns into account. The design, shown in Figure 5.3(a), consists of three plates that are attached to the end of the shock tube. The first and third plates make up the side walls of the propagation chamber, while the second plate makes up the profile of the expansion chamber. The first plate has a slit cut out that determines the initial profile of the shock wave, and the third can be modified to include rails which accommodate removable sliding panels, which may be used to position viewing windows or pressure transducers wherever necessary, as in Figure 5.3(b).

Once the shock passes through the slit, it is turned through a 90° angle. The study considers the effect of the shape of this corner on the resulting shock wave. Low resolution CFD simulations were carried out for three cases: the original case had both the inside and outside edges of the corner as sharp 90°bends, and then the effect of having a gentle radius as first the inside corner only, and then both corners was considered. A selection of the results from this study are shown in Figure 5.4. It was found that having both walls as sharp corners resulted in the formation of both low and high pressure regions as the shock was transmitted through the corner. Adding a radius to the inside corner reduced the low pressure region, resulting in a slight increase in the strength of the transmitted shock. However, adding a radius to both walls reduced the high pressure region as well, resulting in no increase in shock

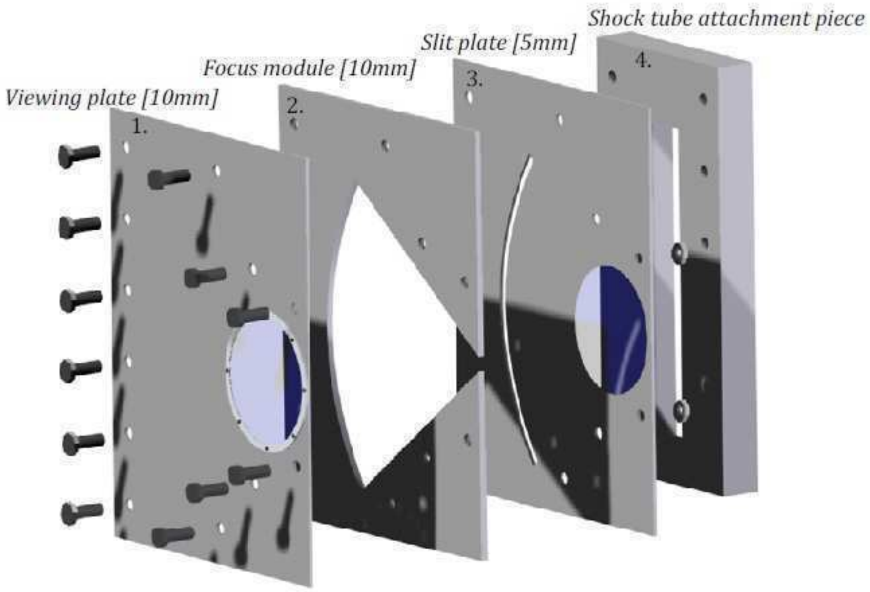

(a) Original three plate design

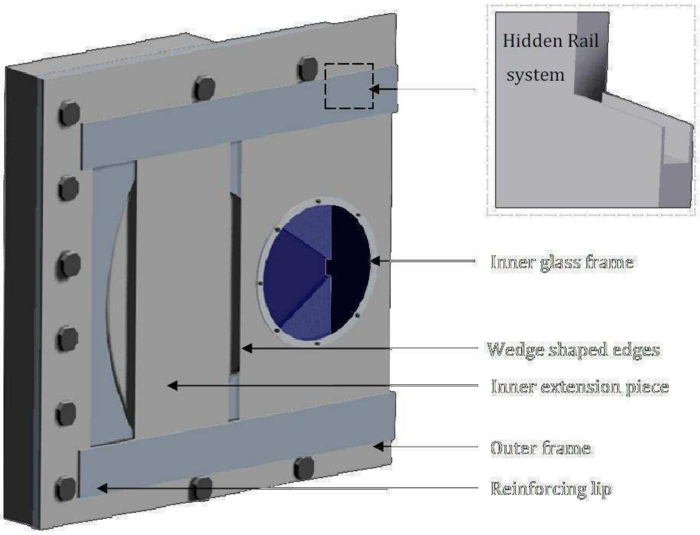

(b) With modifications for a variable viewing port.

Figure 5.3: The design concept of Skews and Beharie (2009)

strength. However, curving both walls did help the shock to maintain it's shape around the corner, and the resulting wave stabilised within a slightly shorter distance.

Figure 5.5 shows the formation of the shock wave after turning the corner. The original incident shock that passes through the slit is reflected off the back wall. The shock strengthens, and appears to form a planar shock front, which strengthens as it propagates into the test section. One point of concern is the low resolution of the simulations. The shock is relatively thick compared to the width of the test section, and flow features in the vicinity of the corner are not very well resolved. These results do however show that a shock wave is transmitted

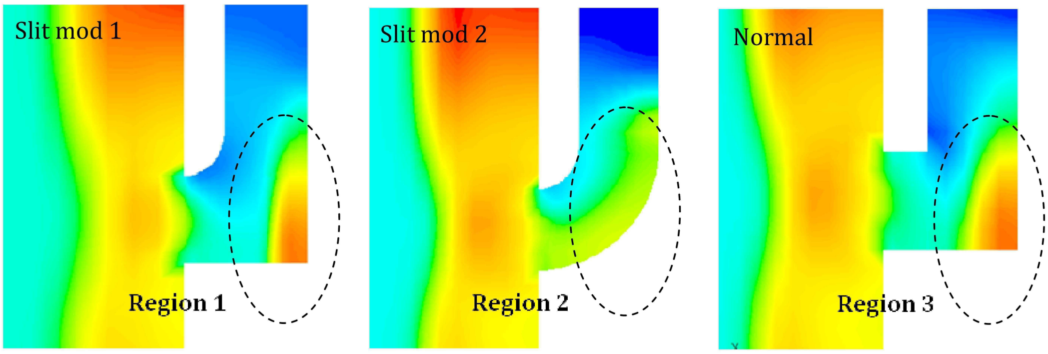

FIGURE 5.4: CFD results for a shock turning through a cylindrical slit - effect of corner shape (Skews and Beharie, 2009)

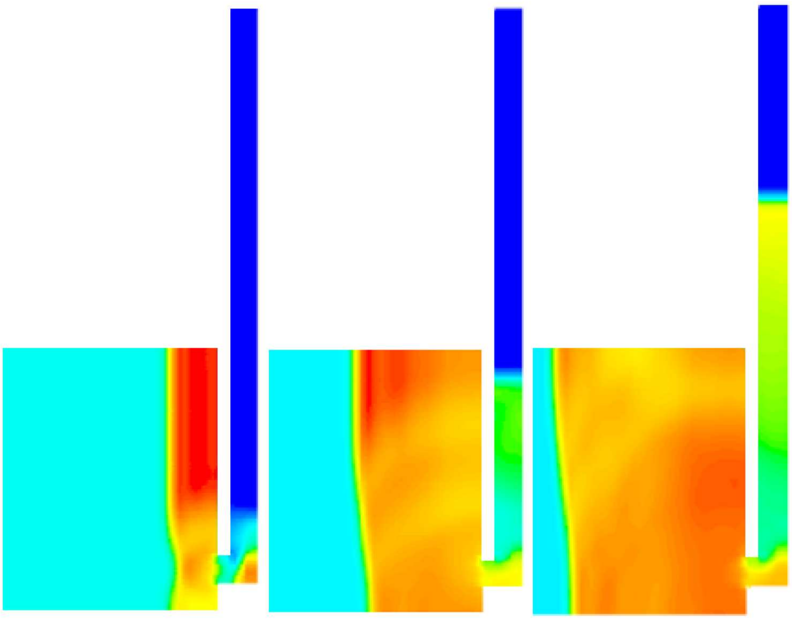

FIGURE 5.5: CFD results for a shock turning through a cylindrical slit - formation of the shock front (Skews and Beharie, 2009)

around the corner into the test section, and this shock appears to strengthen as expected for a converging cylindrical shock wave.

The findings of these two projects provide enough information to begin the detailed design of the facility to be used in the current investigation. Further numerical analysis, the design process, and a description of the configuration of the final facility are discussed in the following sections.

5.2 Preliminary design concept and sizing

In order to accommodate future research that may be undertaken into the behaviour of waves of arbitrary profile, a modular design was used for the apparatus. The concept of arranging a series of plates to form the necessary shape for the facility was borrowed from Skews and Beharie (2009). It was decided that rounding the corners of the slit would make the apparatus unnecessarily complicated to manufacture, with no noticeable affect on the later shock quality, and so it was decided that the sides of the slit would be sharp 90° corners.

The apparatus consists of a profiled propagation chamber sandwiched between two outer plates, in which windows are embedded. The outer plate on the side of the shock tube's expansion chamber (referred to as the back of the apparatus for convenience) is cut short to make space for a fourth removable plate which contains the profiled slit. This plate sits between the end of the expansion chamber of the shock tube and the focusing apparatus.

Various calculations were carried out to ensure that the components of the apparatus would be able to withstand the loading of a passing shock wave. In particular, the thickness of the profile plate and viewing windows needed to be determined, and the bolts between the apparatus and the shock tube needed to be sized. Details of these calculations are described in Appendix B.

A profile plate thickness of 15 mm was chosen, and it was concluded that the facility would be attached to the shock tube by seven M14 bolts. Viewing windows with a thickness of 33 mm and a diameter of 350 mm were used, but would be held in place by a clamping ring, leaving a effective viewing region 330 mm in diameter.

5.3 Extension of numerical analysis

Before deciding on a final design configuration, some further numerical work was carried out into the behaviour of the flow inside the facility. Using the configuration and sizing information in the previous section, it is possible to set some of the dimensions of the final design, such as the width and depth of the slit.

There are also some issues arising in the results of Skews and Daya (2009) and Skews and Beharie (2009), which warrant further investigation. In frames 7 to 9 of Figure 5.2, a contact surface is visible some distance behind the shock wave. This contact surface has little effect on the flow ahead of it, but it does affect the accuracy of the solution in the region behind it. It is caused by a stagnation temperature mismatch between the inlet and the flow behind the shock wave, and can be avoided by ensuring that the stagnation temperature at the inlet is set correctly. In addition, the shock in the results of the three-dimensional simulations shown in Figure 5.4 is not very well resolved, and it is likely that other flow features present as the shock turns the corner would not be resolved by these simulations. A higher resolution simulation is required to ensure that the flow is modelled as accurately as possible.

Two further sets of simulations were carried out using ANSYS Fluent. The first simulation was a full three-dimensional analysis of a planned geometry for the facility, and the second was a higher resolution two-dimensional axisymmetric simulation of the flow through the slit. The solver configuration described in section 4.1.2 was used, and the results obtained in these simulations are discussed in following sections.

5.3.1 Low resolution 3D model

In order to save on computational time, only half of the facility was modelled, and the lower boundary of the geometry was set as a symmetry plane. The geometry consisted of three sections. The first was a 225 mm high by 100 mm wide by 150 mm long rectangular section representing the final portion of the shock tube's driven section. This was followed by a 15 mm wide arc with an internal radius of 450 mm spanning the height of the test section, which extends 15 mm from the end of the shock tube, making up the slit. Finally, there was a 15 mm wide cylindrical segment, which represents the propagation chamber. These dimensions are shown in Figure 5.6.

Simulations were carried out for an initial shock in the shock tube moving at Mach 1.4. Contours of constant pressure are shown in Figure 5.7 at six different times. A preliminary qualitative analysis of the results show that the initial front is reflected off of the end wall of the shock tube, which forms a high pressure supply region at the entrance of the slit. The shock front that enters the propagation chamber initially has a similar strength to that of the original shock in the shock tube, as in Figure 5.7(b). From Figure 5.7(b) to (c) we see that the strength of the shock front increases rapidly as the shock front forms. After this initial formation period, the shock increases in strength only gradually between Figure 5.7(c) and (e), but the strength begins to increase at a much greater rate as the shock approaches the centre of the arc.

The first rapid strengthening phase as the shock enters the chamber is caused by compressions generated as the initial shock reflects back and forth between the walls of the propagation chamber. The strength of these compressions diminish rapidly as the shock moves further into the propagation chamber. The second phase of rapid strengthening occurs as the shock approaches the geometric centre of the slit, and is caused by gas dynamic focus as the radius of

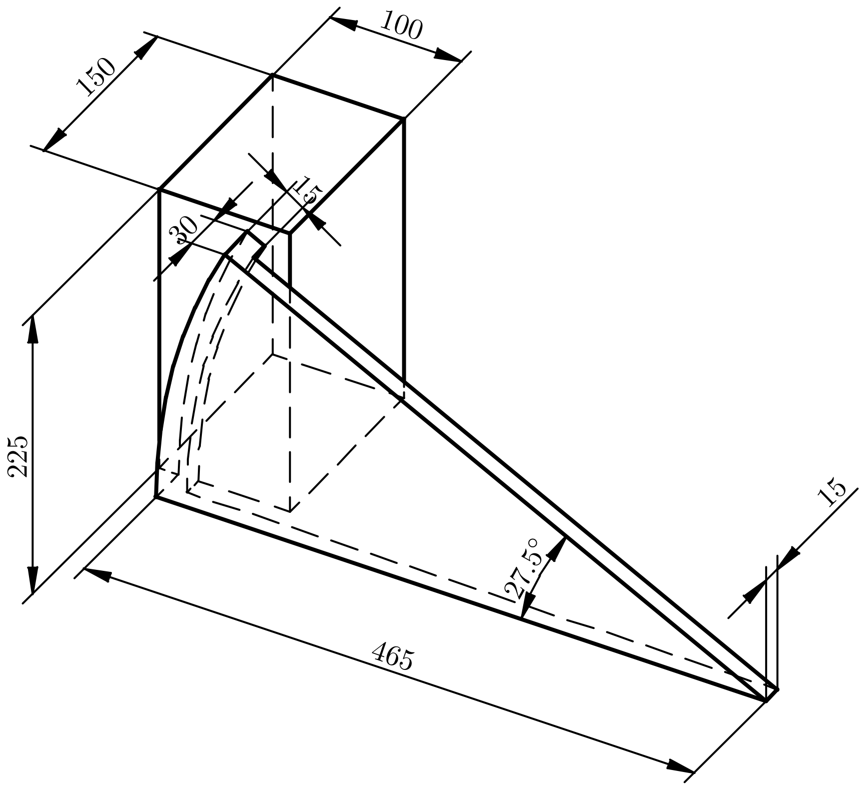

Figure 5.6: Dimensions of the domain used for 3D CFD simulations

the shock decreases. This second phase resembles the behaviour expected for a 2D converging cylindrical shock according to Guderley's power law given in equation (2.14).

The distance of the shock from the geometric centre of the slot at various times may be directly measured from the CFD and compared with Guderley's power law, which allows a more direct quantitative comparison to be made. An exponent n of 0.835 was used, which corresponds to a cylindrical shock wave. The shock reached the focal point at 1123 μs after the start of the simulation, which was 813 μs after entering the slit. The constant C was calculated at eight intermediate points between the times t = 240 μs and t = 590 μs after the shock entered the slit, and the average of these was used in the equation. This gave a value for C of 1.80. The shock radius in the CFD results is compared to the curve predicted by equation (2.14) in Figure 5.8(a).

The increasing pressure across the shock that is observed in Figure 5.7 should cause the shock to accelerate, introducing some curvature into the radius-time plot, but this is not very apparent until the last two data points. To ensure that the shock was indeed accelerating, the Mach number was calculated by numerically differentiating the radius with respect to time using a central difference formula. The resulting Mach number is shown together with

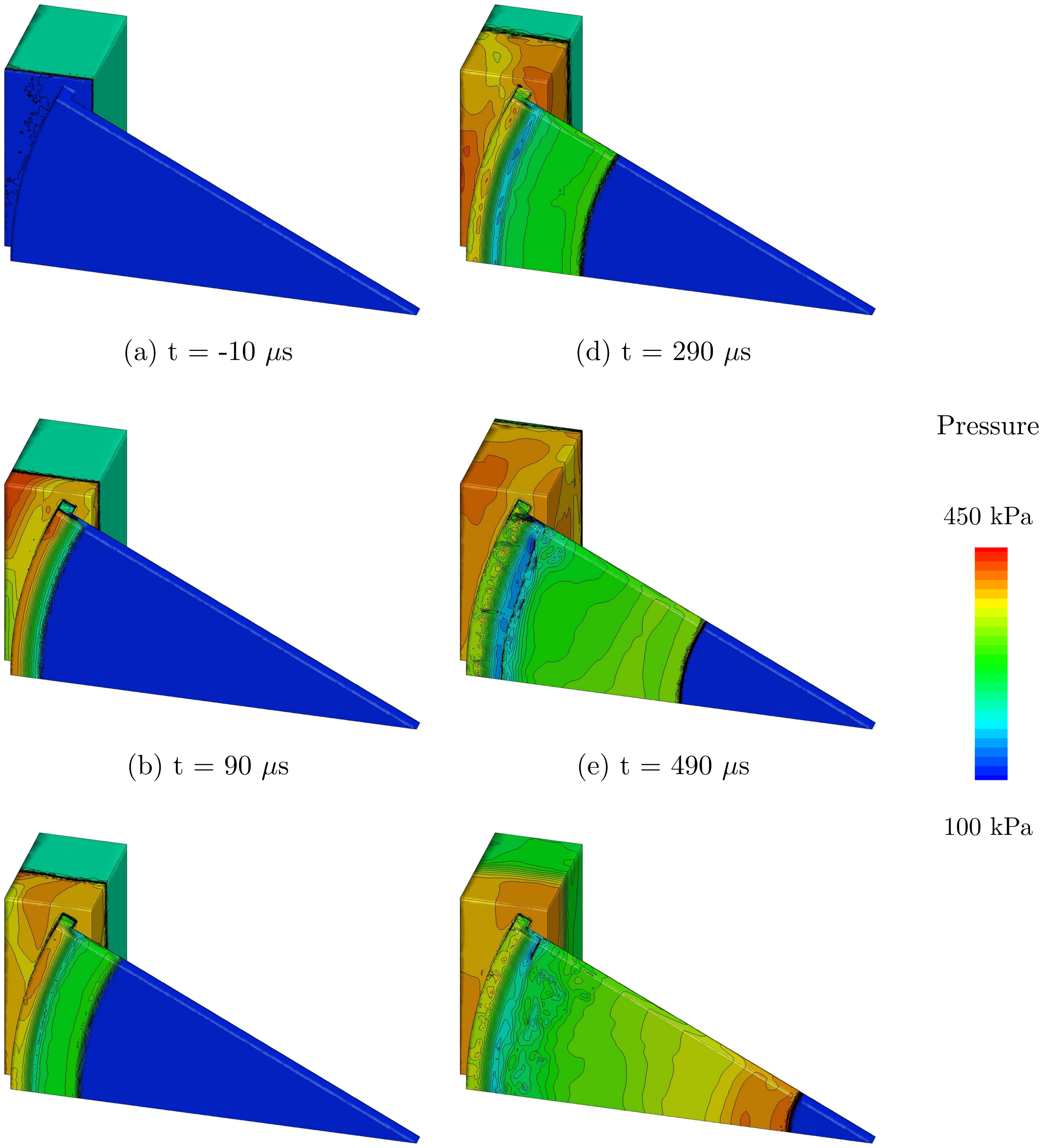

(a) t = -10 μs

(d) t = 290 μs

(b) t = 90 μs

(e) t = 490 μs

(c) t = 190 μs

(f) t = 690 μs

FIGURE 5.7: Results from a 3D simulation of a converging cylindrical shock wave segment with an initial radius of 450 mm, generated from an initial Mach 1.4 planar shock wave. The time is measured from the instant at which the shock front first reaches the end wall of the shock tube and enters the slit

the Mach number predicted by equation (2.15) in Figure 5.8(b). In this figure, both the initial strengthening due to reflected compressions catching up to the shock, and the later strengthening caused by the shock curvature are apparent, and for times greater than 300 μs after entering the slit, adhere closely to the expected power law behaviour. This suggests that the resulting shock front closely approximates the behaviour of a two-dimensional converging cylindrical shock wave.

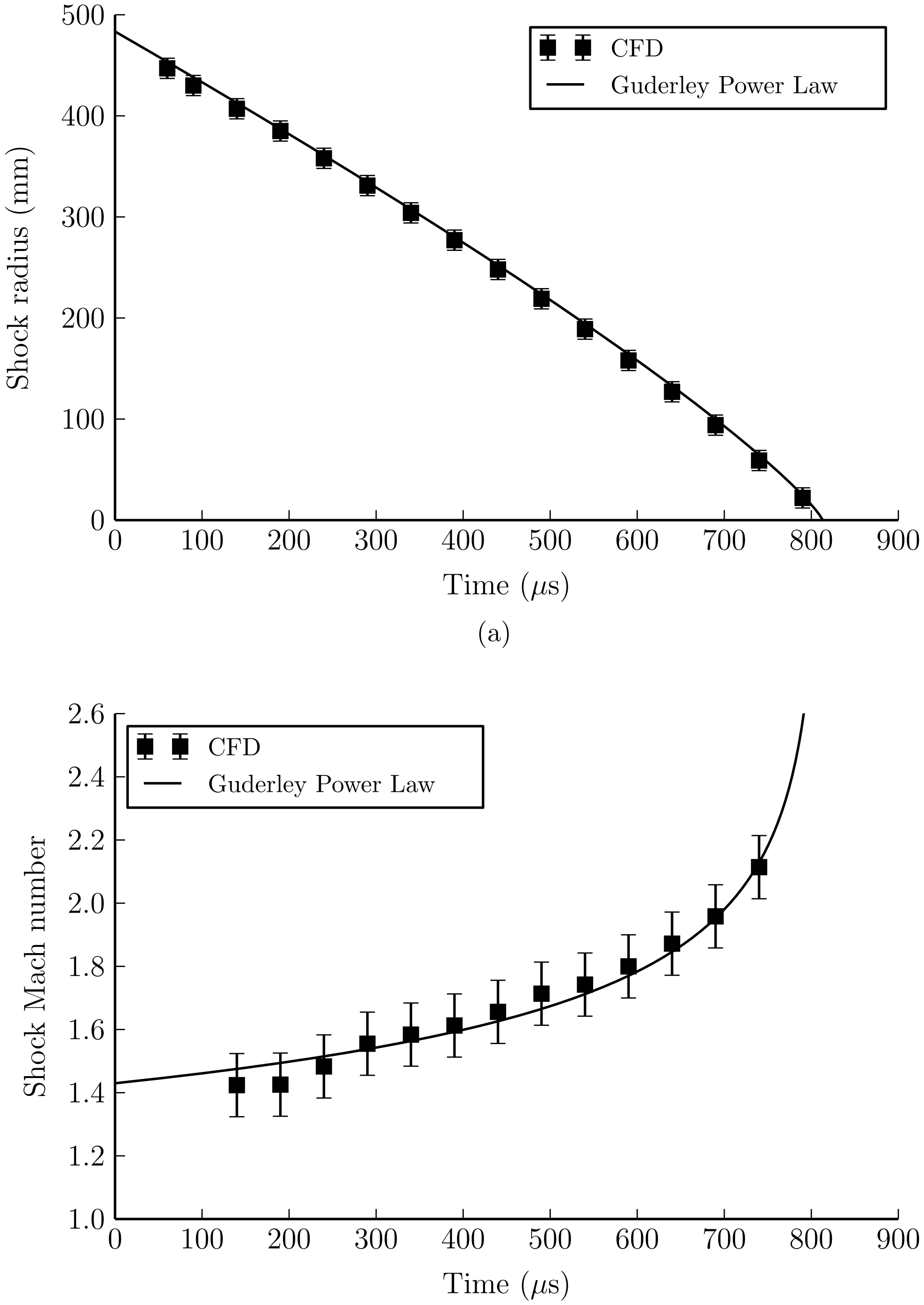

(a)

(b)

FIGURE 5.8: Comparison of the variation of shock radius (a) and Mach number (b) with time to the 3D simulations. The time is measured from the moment the shock first enters the slit

Although the initial formation of the shock front was modelled by the 3D simulation, some of the features responsible for this were not very well resolved. Since a higher resolution 3D simulation would require additional computational resources, and provide little more information than a high resolution 2D simulation, it was decided that a 2D simulation would be carried out instead. Details of this simulation are given in the following section.

5.3.2 High resolution 2D axisymmetric model

Instead of modelling the slit as an arc, it was modelled as an axisymmetric domain with the axis located at the geometric centre of the slit. One disadvantage of this approach is that it fails to account for the edges of the slit, and that the rectangular cross section of the shock tube is not taken into account. However, since much higher resolutions can be achieved at a fraction of the computational cost of a full 3D model, and since the previous 3D simulations showed that these effects are minimal, 2D axisymmetric simulations were deemed sufficient.

The domain was set up as shown in Figure 5.9, with the shock initially generated by the pressure inlet on the left. The shock is allowed to propagate along the 150 mm length of a hollow cylinder with a thickness 100 mm. The shock then passes through a 15 mm wide circular slit with a 400 mm inner radius, and then turns through the 90° corner, and is allowed to propagate toward the centre of a disk shaped propagation chamber.

Density contours of the simulation of a shock initially moving at Mach 1.4 at six different times are shown in Figure 5.10. From Figure 5.10(b), it can be seen that the shock strength is not significantly affected as it passes through the slit. However, a pair of vortices are formed as the shock diffracts around the corners of the slit. A third vortex is formed as the shock passes the inside edge of the 90° bend in Figure 5.10(c), and the shock front, and the signifficantly weaker curved portion of the diffracted front begins to propagate into the propagation chamber. When the original front reaches the opposite wall, it is reflected back, producing a region of very high pressure. A regular reflection is formed on the wall, but this very quickly transitions to a Mach reflection, which propagates through the propagation chamber, as in Figure 5.10(d). The triple point of this Mach reflection is reflected back and forth between the walls, and the shock front gradually strengthens and straightens as transverse waves catch up. By the time shown in Figure 5.10(f), the converging shock front has reached a strength close to that of the original shock, and is very close to plane. The quality of the shock front improves further as it strengthens and propagates inward.

The diffraction vortices are still present with trapped shocklets, and do follow behind the shock, but at a much slower velocity. This leaves a large region of approximately uniform flow immediately behind the shock. This phenomenon is analogous to the contact surface of a diaphragm burst, in that there is a uniform region of the fluid for some distance behind the shock that was originally in the propagation chamber, and did not have to turn the corner. Following behind this is fluid that was originally upstream from the slit, which turned through

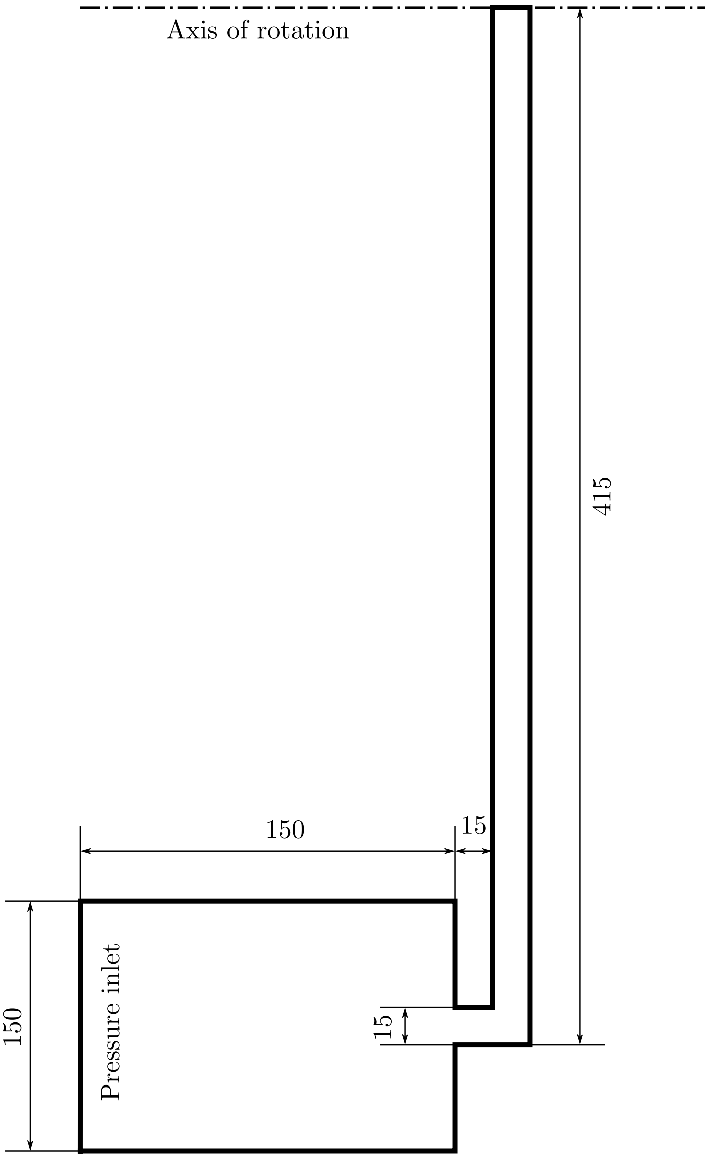

Figure 5.9: Domain used for CFD of a shock turning a 90° corner after passing through a circular slit

the corner, gaining a rotational component, resulting in non-uniform flow in the propagation chamber.

Figure 5.11 shows Mach number contours and velocity vectors for the time shown in Figure 5.10(f). Although there are large variations in flow direction and velocity immediately after the corner, the flow in the upper portion of the propagation chamber is uniform, and flowing in the correct direction.

The simulations show that within a distance of 120 mm, the shock stabilises to an acceptable level (that is, the density change across the transverse waves was less than 1% of that across

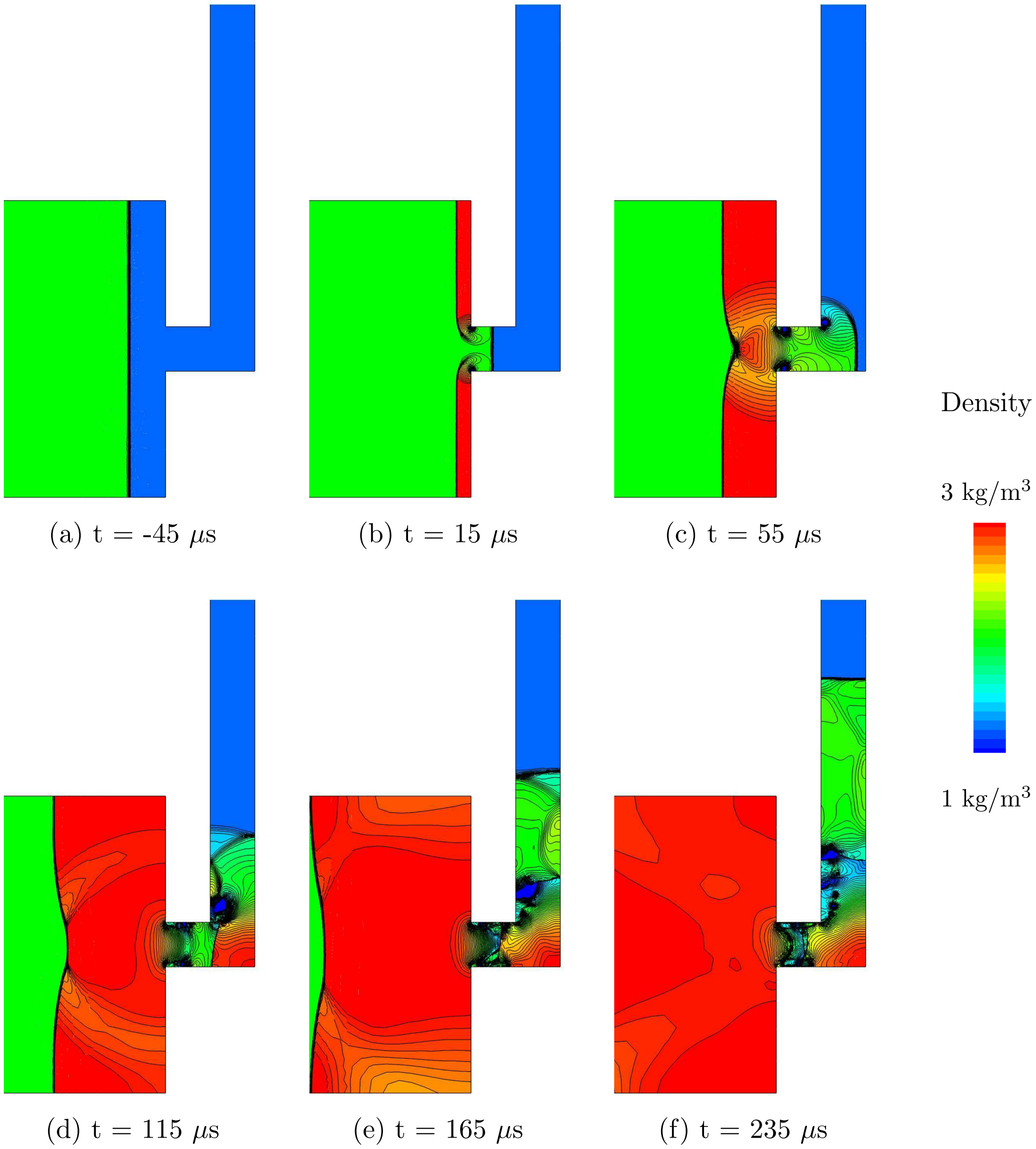

(a) t = -45 μs (b) t = 15 μs (c) t = 55 μs

(d) t = 115 μs (e) t = 165 μs (f) t = 235 μs

FIGURE 5.10: Density contours for for a Mach 1.4 incident shock turning a 90° corner after a 15 mm circular slit with an inner radius of 400 mm. The time is taken such that the shock first enters the slit at $t = 0 \mu s$

the shock front). After this distance, the shock front is a close approximation of a two-dimensional shock wave.

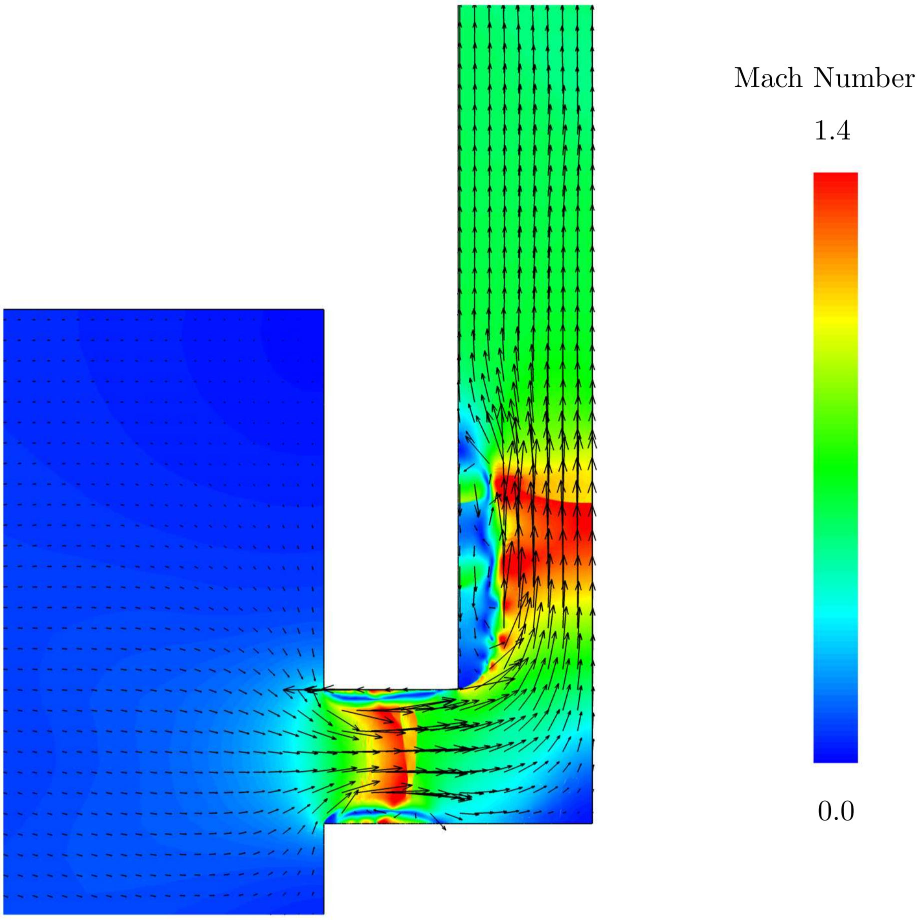

FIGURE 5.11: Mach number contours and velocity vectors for a Mach 1.4 incident shock turning a 90° corner after a 15 mm circular slit with an inner radius of 400 mm, $235\mu s$ after the shock passed through the slit

5.4 Description of final design

An exploded view of the final design is shown in Figure 5.12, and a photograph of the facility attached to the end of a shock tube is shown in Figure 5.13. Detailed engineering drawings of this design may be found in Appendix C, and instructions for assembly and disassembly are included in Appendix D.

In summary, the apparatus consists primarily of four main plates arranged in three layers. Starting from the side opposite the shock tube, the first layer is the large outer plate, with an embedded glass window. The second layer is the propagation plate, and an optional test model. The third and final layer contains the back plate, in which the second window is embedded, and the profile plate.

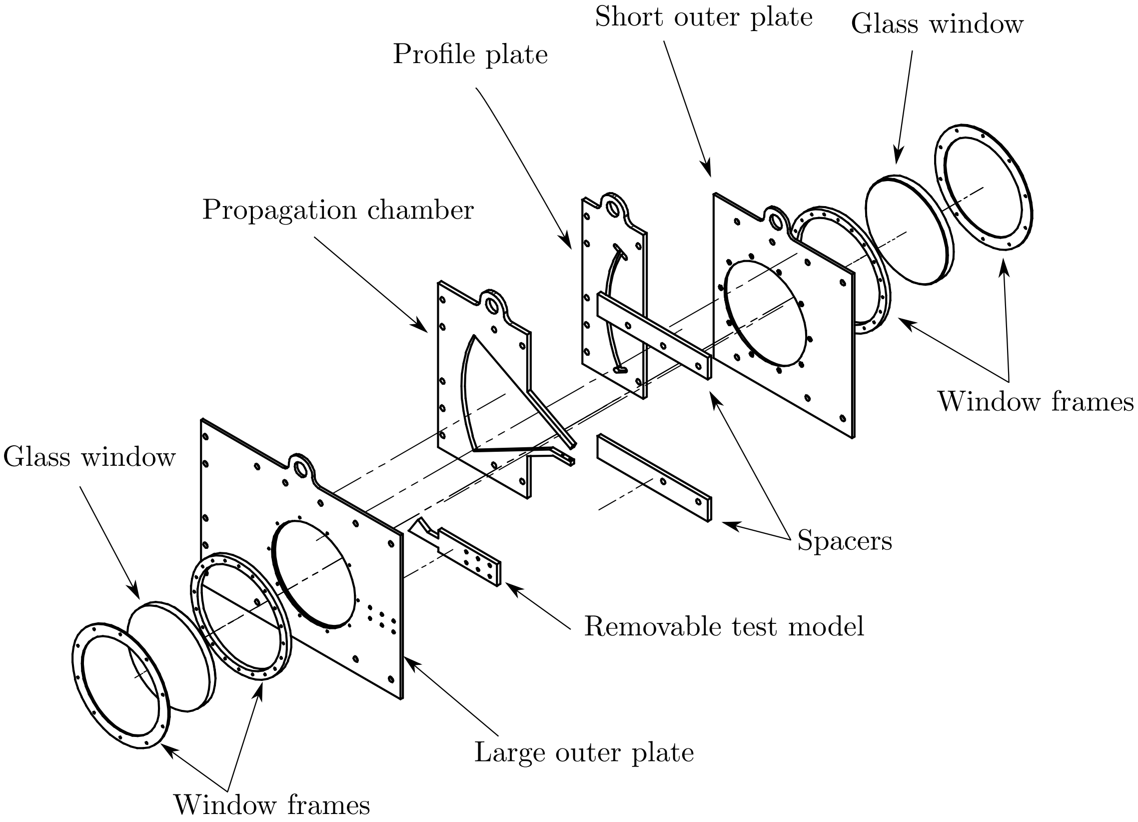

FIGURE 5.12: Exploded view of the final design, with a profile plate, propagation plate, and test wedge for studying the reflection of a converging cylindrical shock wave segment

An adequate seal between the profile and the back plate is obtained using a 4 mm O-ring cord, which is fitted into a 3 mm deep by 5 mm wide groove cut in the side of the profile plate. Paper gaskets are also inserted where necessary between each layer, and between the profile plate and the end of the shock tube.

The removable test model may be bolted with six M6 bolts to the front plate only. This allows just the back plate to be removed to clean out pieces of trapped diaphragm without having to disassemble the entire apparatus. With the back plate removed, the wedge piece may be changed with relative ease.

Although all of the components are light enough to be lifted, the combined mass of the outer plates is great enough that this cannot be done without some difficulty. In order to aid with adjusting the configuration of the apparatus, tabs were included so that a hook from an overhead gantry may be attached to prevent the plates from falling. This allows the configuration to be changed by a single operator (although it may be considerably faster with the aid of an assistant).

FIGURE 5.13: Photograph of the facility attached to the shock tube

The windows are fixed in place, and were were sized and positioned so as to maximise the viewing area. The diameters of the window frames are oversized by 4 mm, allowing space for epoxy, and to aid in installing the windows so that they lie flush with the inner surface of the outer plates. The inside rim of the window has a 3 mm chamfer, which ensures that the window will be unable to fall into the propagation chamber. A steel frame on the outside clamps the window in place and prevents the internal pressure from pushing the window out of position. The 2 mm gap between the window and the frame was filled with 3M Scotch-Weld™ 2216 B/A epoxy adhesive.

6. Propagation of Shock Waves of Arbitrary Profiles

This chapter describes a general overview of the propagation of shock waves of arbitrary two-dimensional profile. In particular, it focuses on shock waves with an initial shape consisting of a combination of straight segments, and convex and concave cylindrical arcs.

Purely convex shock waves will be considered only briefly, followed by a short numerical investigation into the propagation of purely concave shock waves. The chapter will be concluded with a comparison between an experimental and purely two-dimensional numerical investigation into the behaviour of two compound shock wave profiles — that is, profiles consisting of both concave and convex segments. This will establish to what degree the experimental facility models the propagation of a two-dimensional shock wave.

It is important to note that all of the shock waves considered in this chapter contain at least one discontinuous jump in the radius of curvature along the shock front. By equation 2.15, this implies that there will be a discontinuous jump in shock speed along the shock. This will distort the shock wave's shape in the region of the curvature discontinuity, possibly forming additional shock waves and shear layer in the flow behind the shock wave.

6.1 Propagation of convex shock waves

In general, any convex shock wave propagating into an open space will tend toward a spherical shape (Takayama and Sekiguchi, 1981a). When constrained to two dimensions, the shape of the shock wave will tend toward a cylindrical shape. Unless discontinuities are present when the shock wave is formed, no additional discontinuities in the shock shape will be introduced, and the shape of the shock front will remain smooth and continuous.

Consider a shock wave profile that initially consists of a convex arc and a straight segment. The convex section of the shock wave slows down as it propagates, and the pressure behind it decreases. If the curved segment were not present, the straight section would propagate at a constant speed, and the pressure behind it would remain constant. This generates a pressure imbalance immediately behind the shock front at the point where the two segment meet. This results in a series of expansion waves which propagate into the flow behind the straight segment of the shock, and slow that part of the shock down. This causes the straight section to gradually curve into a convex shape. At the same time, a series of compression waves propagate into the flow behind the segment of the shock that was initially convex. These prevent the shock from slowing down as much as it would have in the absence of the straight segment, and cause the radius of curvature to increase at a greater rate.

The net result is that the sharp discontinuous jump in the radius of curvature of the initial shock wave becomes a gradual rise in radius of curvature as one moves from the curved segment into the straight segment, as shown in Figure 6.1.

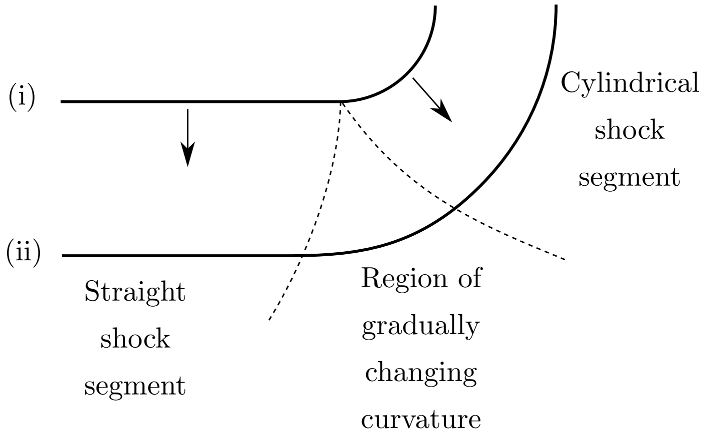

Figure 6.1: Schematic diagram showing the shape of an initially straight-convex shock wave (i) in it's original position, and (ii) after having propagated some distance

A shock front consisting of two straight shock segments meeting with an initially sharp convex corner may be considered to be the extreme of the above case, for which the initial radius of curvature of the cylindrical segment is zero. Complications that shock waves of this shape introduce will be discussed in section 6.3.1.2, but a preliminary consideration could be arrived at using same argument used above. The resulting shock shape will consist of a curved shock segment between the two straight segments, and the radius of curvature will vary along the length of the curved segment. The radius will reach a minimum on the symmetry line, which will bisect the angle formed by the two original straight segments.

6.2 Propagation of concave shock waves

For a concave shock wave, the simplest case to consider is that of two straight shock segments that meet at a sharp concave corner. Using symmetry, it may be argued that a sharp concave 90° corner on a shock front is analogous to a shock encountering a 45° wedge. As a result, the shock will reflect off of the symmetry plane, forming a pair of Mach reflections (MRs) (although a regular reflection could form if the Mach number of the shock is very low, or if the angle is much smaller than 90°). The MR would expand, but remain approximately self-similar, with the triple points following diverging straight paths, as in Figure 6.2(a).

If the corner is rounded with some radius, then the shock front will briefly undergo focusing before the MR pair forms. In this case, the curved portion of the shock increases in strength (as described in section 2.5.2), whereas the fluid behind the straight portion of the shock front does not. This produces compressive waves which move into the region behind the straight shock. These compressive waves gradually distort the shock front, producing a kink in the shock front on either side of the symmetry plane at which the curvature of the shock front is higher than at those points around it. As the shock propagates, this effect is magnified, until the compressive waves coalesce into a pair of reflected shocks, and the kinks form a pair of finite discontinuities along the shock front, which become the triple points of an MR pair. After this point, the MR pair expands self-similarly, as in the case with a sharp corner. This behaviour is shown in Figure 6.2(b).

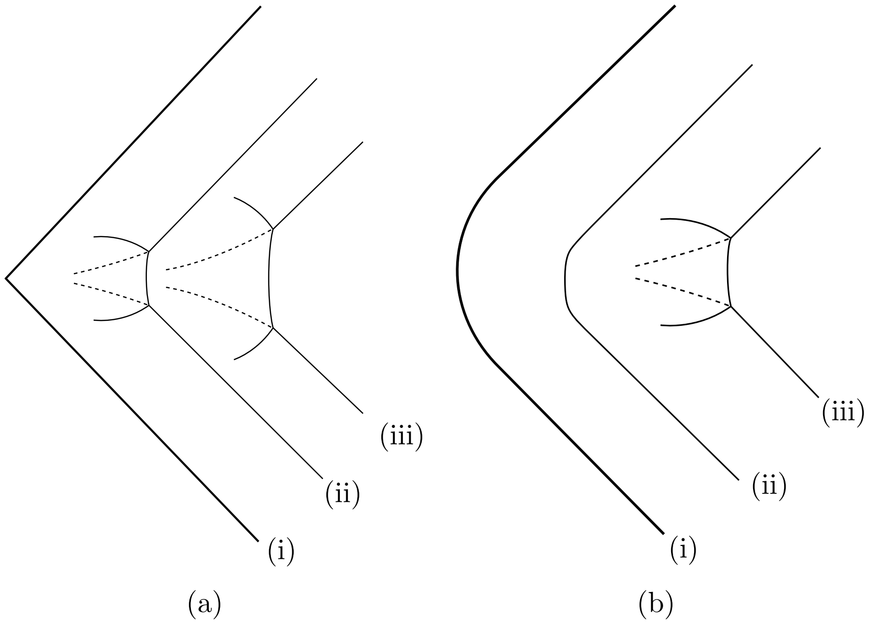

Figure 6.2: Schematic diagrams showing the shape of initially sharp (a) and rounded (b) converging shock waves at three times

In order to gain some insight into the formation of these reflections, a brief numerical investigation into the interaction between straight and curved shock segments were carried out. These are discussed in the following section.

6.2.1 Interaction between concave and straight shock segments

The CFD simulations were carried out in ANSYS Fluent using the configuration described in section 4.1.2. These simulations aimed to further investigate the interaction between the concave and straight segments of a shock front.

A total of four initial shock wave shapes were tested, which each consisted of a cylindrical arc spanning some angle, placed in between a pair of straight shock segments. These shapes were chosen so that they would fit within the constraints of the experimental facility designed in Chapter 5. The radii of the cylindrical segments were chosen so that the estimated location of the transition from compression waves to reflected shocks would occur within or close to the viewing region of the experimental facility. The straight section was then selected so that it would be as long as possible, whilst still fitting within the geometrical constraints set by the shock tube exit. Table 6.1 gives a summary of the geometries used. To reduce the required computational time, the region that would fall to the right of the viewing windows was truncated from the domain.

Table 6.1: Cases used for numerical simulation of straight-concave compound shocks

Convergence angle	Radius of concave segment	Length of straight segments	Mach number
50°	145 mm	130 mm	1.40
37°	235 mm	145 mm	1.40
35°	175 mm	160 mm	1.40
20°	185 mm	175 mm	1.40

In all cases, a Mach 1.4 initial shock was generated, and allowed to propagate between a pair of straight converging walls. Figures 6.3 to 6.6 show contours of constant density taken from the results of the simulations for the four cases at various points in time.

While a concave shock front on its own tends to decrease in radius, the results show that the opposite behaviour occurs in the presence of an adjacent straight section. A series of compressions forms behind the curved section, which propagate outward, distorting the straight segments into slightly concave shapes. These compressions gradually coalesce in the region where the curved and straight shocks meet, eventually forming an additional shock wave, and a sharp kink in the shock front (see Figure 6.3(b)). When this shock wave forms, the resulting

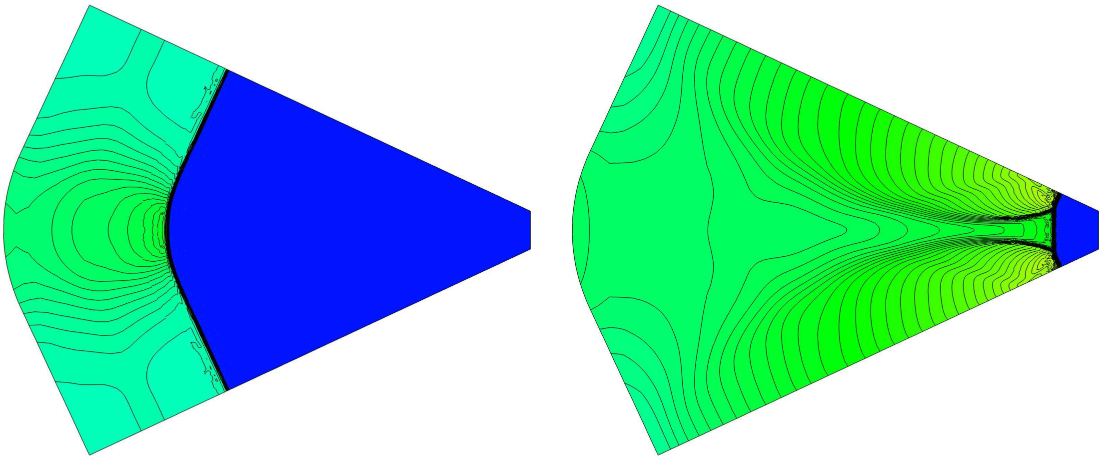

(a) 250 μs

(d) 700 μs

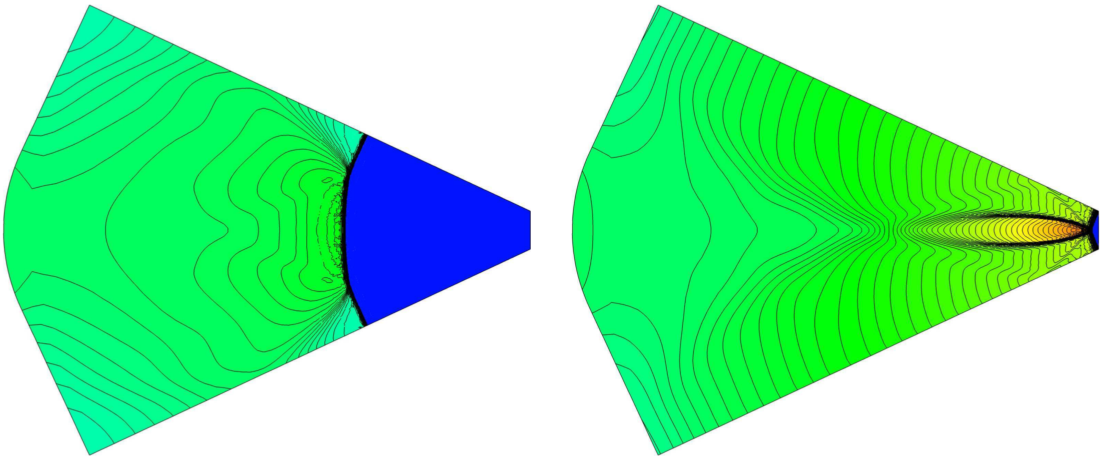

(b) 500 μs

(e) 750 μs

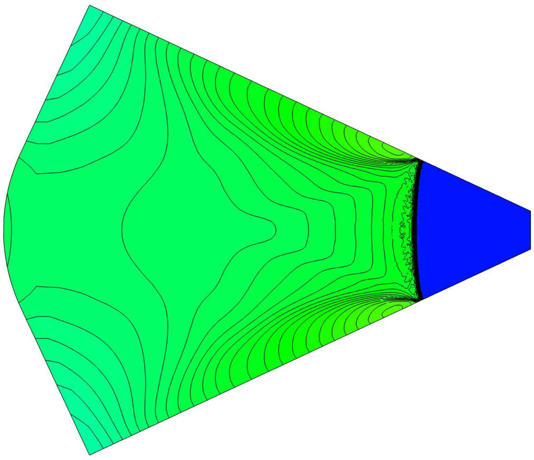

(c) 600 μs

Figure 6.3: Numerical results for the propagation through a 50° converging channel, for an initially Mach 1.4 compound shock front with a straight-concave-straight initial shape. The radius of the cylindrical arc is 145 mm, and the straight segments are each 130 mm long

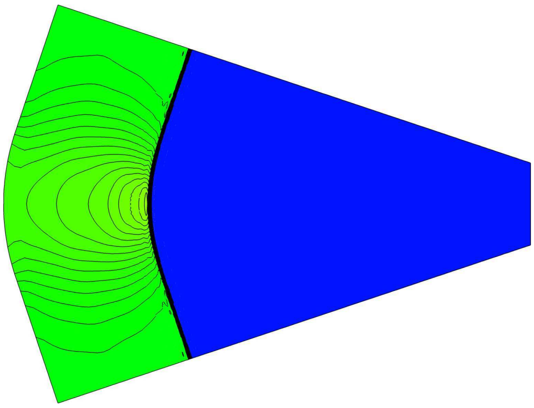

(a) 299 μs

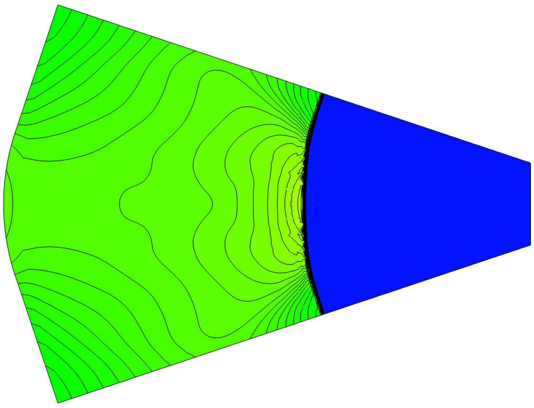

(b) 599 μs

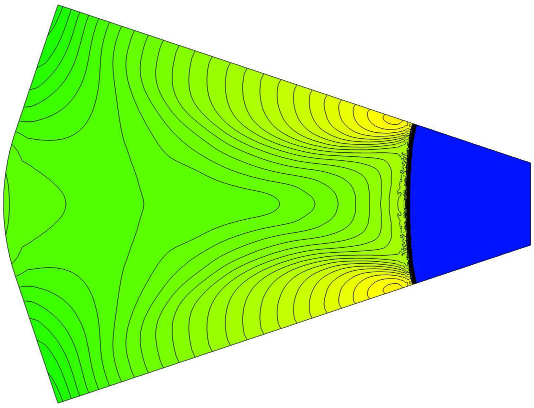

(c) 799 μs

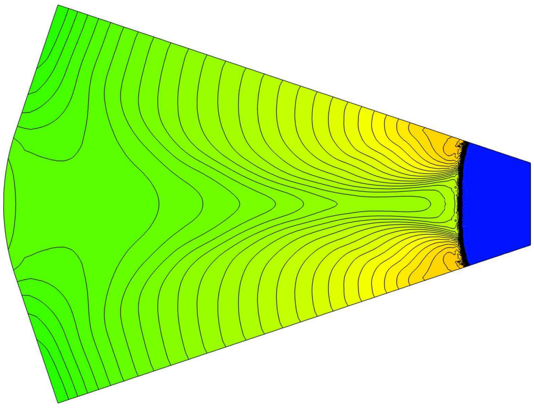

(d) 899 μs

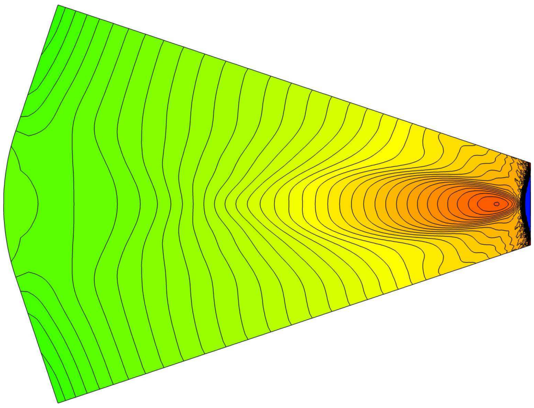

(e) 1019 μs

FIGURE 6.4: Numerical results for the propagation through a 37° converging channel, for an initially Mach 1.4 compound shock front with a straight-concave-straight initial shape. The radius of the cylindrical arc is 235 mm, and the straight segments are each 145 mm long

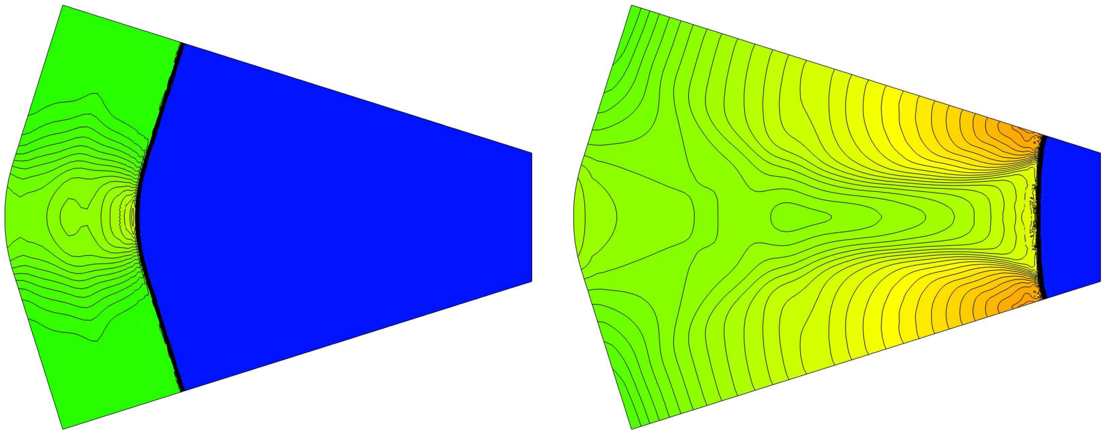

(a) 250 μs

(d) 850 μs

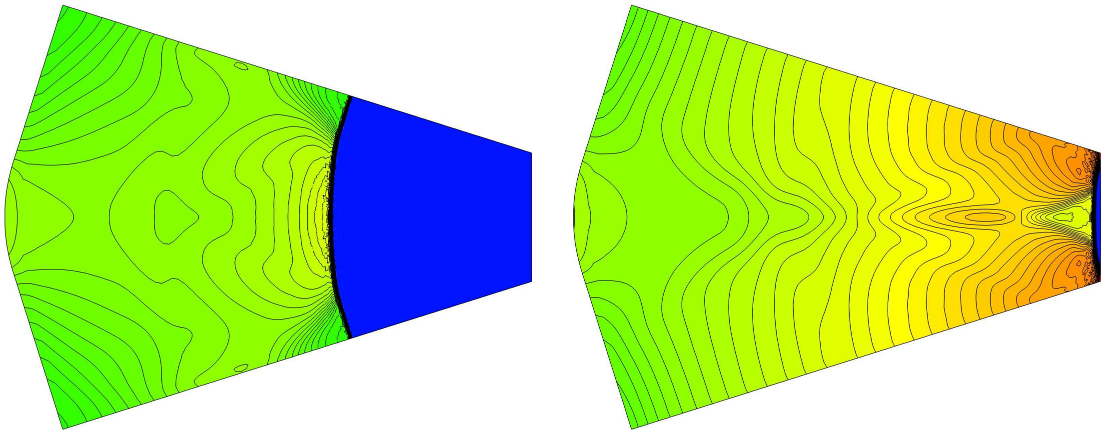

(b) 600 μs

(e) 950 μs

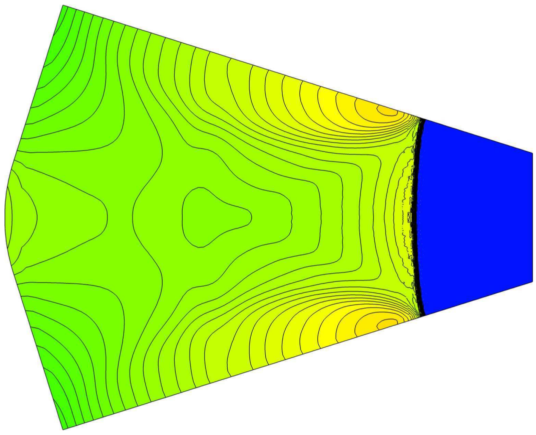

(c) 750 μs

FIGURE 6.5: Numerical results for the propagation through a 35° converging channel, for an initially Mach 1.4 compound shock front with a straight-concave-straight initial shape. The radius of the cylindrical arc is 175 mm, and the straight segments are each 160 mm long

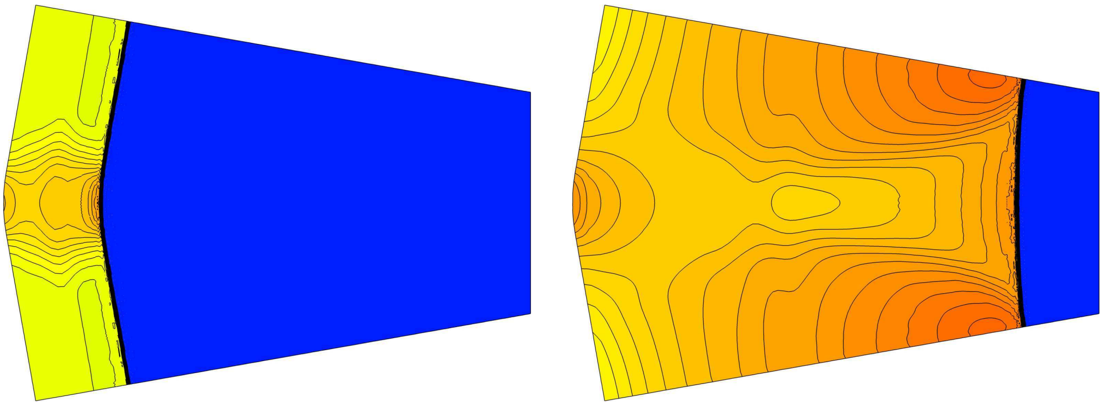

(a) 200 μs

(d) 900 μs

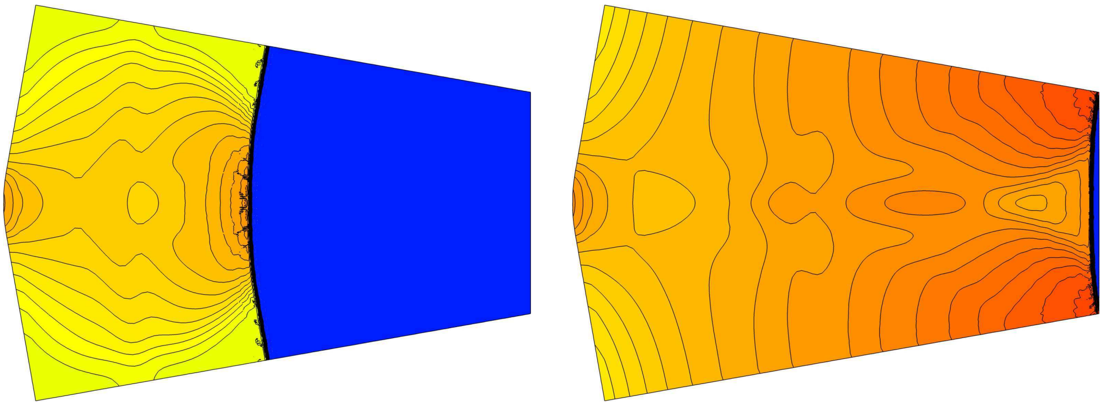

(b) 500 μs

(e) 1050 μs

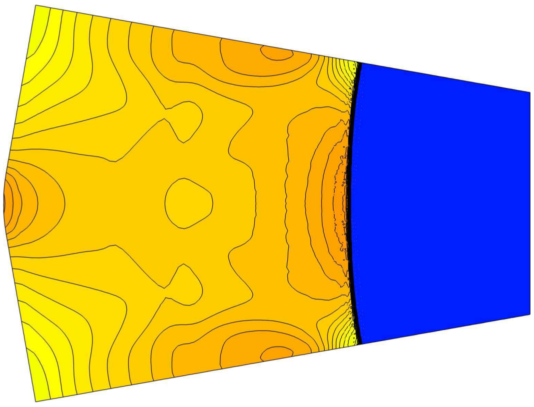

(c) 700 μs

FIGURE 6.6: Numerical results for the propagation through a 20° converging channel, for an initially Mach 1.4 compound shock front with a straight-concave-straight initial shape. The radius of the cylindrical arc is 185 mm, and the straight segments are each 175 mm long

mismatch in flow properties between the original and new shock waves causes a shear layer to form behind the kink (visible in Figure 6.3(d) and 6.5(d)). Meanwhile, the originally curved shock straightens and its velocity tends toward a constant value. This new configuration is essentially a symmetric pair of MRs, with the original straight segments forming the incident shock waves, and the original curved segment forming the Mach stem. Eventually, the triple points and reflected shocks reflect off the walls of the domain. When the reflected shocks intersect, this produces a localised high pressure region in the flow along the symmetry plane at some distance behind the shock front (see Figure 6.5(e)). This high pressure region expands, eventually catching up to the shock front when the triple points meet (as in Figure 6.4(e)). The maximum pressure reached in this high pressure region increased as the angle of convergence of the initial shock was increased.

With this basic qualitative understanding of some of the mechanisms involved in the propagation of shock waves with both curved and straight segments, it is possible to begin to study shock waves that consist of both concave and convex segments mixed with straight segments. This is dealt with in the following section.

6.3 Propagation of compound shock waves

Although the preliminary computational studies mentioned in the previous chapters suggested that the shock would take on any shape defined by the slit, this needed to be verified experimentally. In order to evaluate the sensitivity of the apparatus to the slit shape, an investigation was carried out into the propagation of shocks of compound profiles - that is, profiles consisting of both a converging and a diverging section. This involved carrying out CFD simulations into the behaviour of shock waves with two similar initial shapes, identifying the similarities and differences between the two shapes, and noting whether or not these similarities and differences are also present in experimental results.

The profiles consisted of three straight sections, separated by one converging and one diverging section. It would be preferable that the propagation chamber have parallel walls, as this plate would be useful for a wide variety of studies. In order to maintain a symmetry between the converging and diverging sections, it was decided that these would each span an angle of 90°.

The first chosen profile chosen consisted of a pair of concave and convex arcs, arranged in an S shape. The second profile was obtained by replacing the two arcs with sharp 90° corners, forming a step shape. However, the problem of determining the size and position of the profile relative to the shock tube exit and viewing windows remained.

This was done by considering the behaviour of the converging and diverging sections separately, and then estimating the combined effect. The behaviour of the combined effect was then confirmed using CFD, and this information was used to design the profile plates for the experimental study.

6.3.1 Preliminary numerical investigation

If a shock front initially consists of both concave and convex segments, then there will be some interaction between the two segments. Prior to any analysis, the results of these interactions for a pair of 90° corners may be considered qualitatively.

When a triple point of the MR from the concave segment first encounters the convex segment, the incident angle for the MR will increase slightly in magnitude, which will result in a weaker incident shock, and a steeper triple point trajectory. This will cause the triple point to move even further into the convex segment, and the Mach stem will be longer than in the case of a purely concave initial shock. The curved triple point trajectory will also cause the slope of the Mach stem to move toward that of the planar wave segment, and alter the curvature of the Mach stem, taking it from its initial concave shape into a slightly convex shape. Over time, the entire shock front is expected to tend toward a planar shape.

In order to validate this analysis, CFD simulations were carried out for each of the two shock shapes, arbitrarily using a step length of 100 mm for the sharp profile, and radii of 50 mm for the rounded profile. The simulations were run using the in-house solver, using the configuration described in section 4.1.1. Several difficulties were encountered, particularly with the sharp profile, which limited the maximum time that could be reached by the simulations. The results obtained from the preliminary model are given in section 6.3.1.1, and the challenges encountered are discussed in section 6.3.1.2.

6.3.1.1 Results

In spite of these challenges, results were obtained for early times for shock waves with initial Mach numbers of Mach 1.4 and 1.8. These are shown in Figure 6.7 and 6.8.

Although the mechanism of the initial formation of the MR differs between the sharp and rounded profiles, the shape of the shock fronts begin to resemble each other after a relatively short distance (within about 1.5 times the step length).

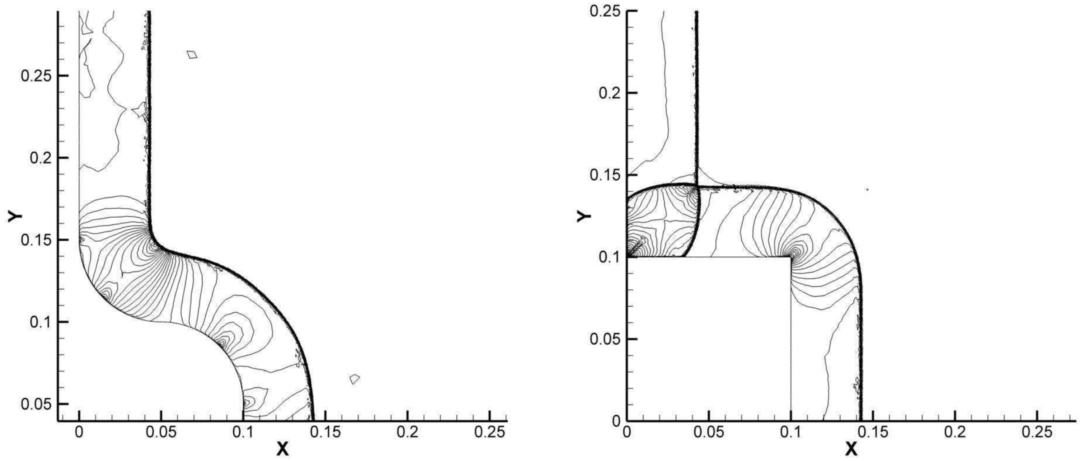

(a) $t = 90\mu$s (d) $t = 90\mu$s

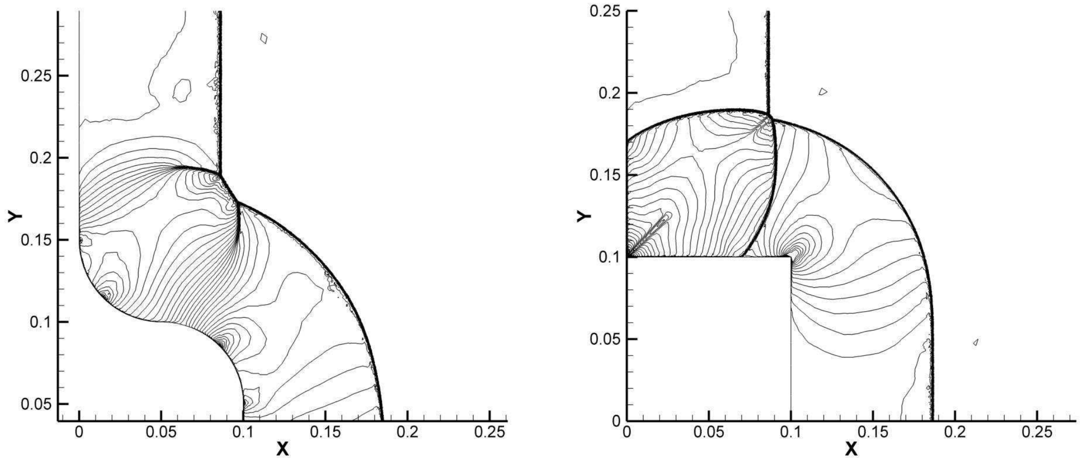

(b) $t = 180\mu$s (e) $t = 180\mu$s

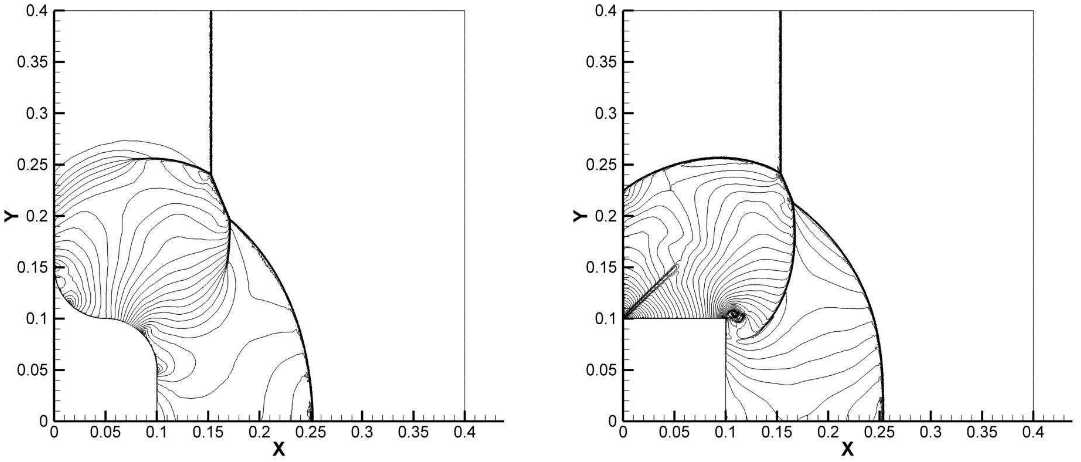

(c) $t = 320\mu$s (f) $t = 320\mu$s

FIGURE 6.7: Preliminary CFD results for the behaviour of a compound shocks with rounded (a-c) and sharp (d-f) initial profiles. The shocks are moving from left to right in a 400 mm high section, with an initial Mach number of 1.4

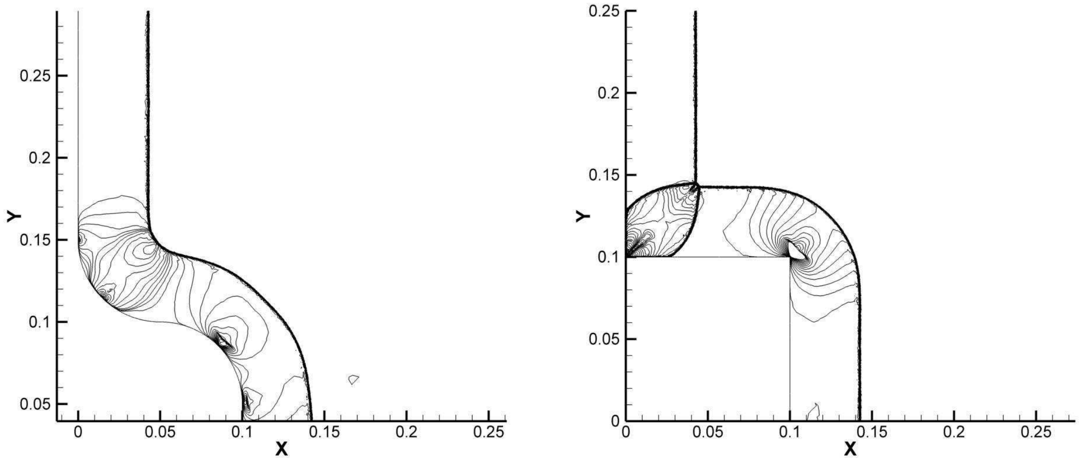

(a) $t = 70\mu\text{s}$ (d) $t = 70\mu\text{s}$

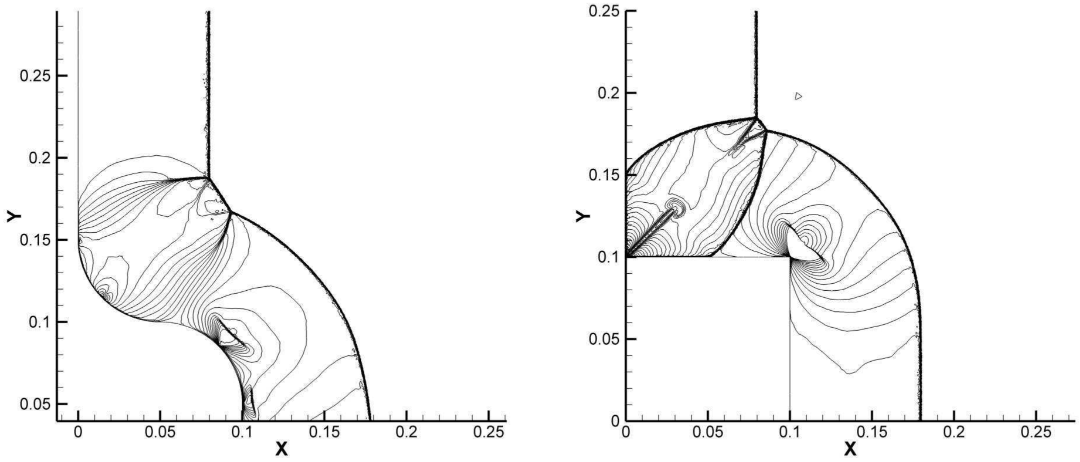

(b) $t = 130\mu\text{s}$ (e) $t = 130\mu\text{s}$

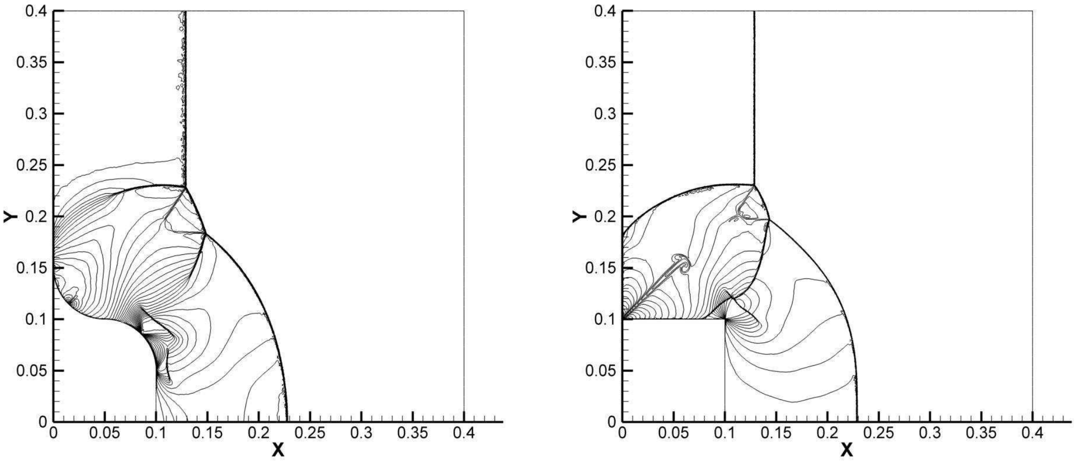

(c) $t = 210\mu\text{s}$ (f) $t = 210\mu\text{s}$

FIGURE 6.8: Preliminary CFD results for the behaviour of a compound shocks with rounded (a-c) and sharp (d-f) initial profiles. The shocks are moving from left to right in a 400 mm high section, with an initial Mach number of 1.8

For both profiles, the Mach stem bows slightly outwards, and gradually changes in angle toward the vertical. The upper triple point follows a trajectory that is directed at just above 45° to the horizontal, which curves very slightly downward as the shock propagates. The curvature of the lower triple point trajectory is initially much more severe, and although it is also initially directed at just below 45° to the horizontal, the expanding convex section deflects it downward, so that it the trajectory is almost horizontal by the time the shock has travelled 1.5 step lengths. As the convex section straightens out, the effect on the lower triple point diminishes.

6.3.1.2 Challenges in the simulation of convex corners

When modelling a sharp convex corner, a discontinuity in flow direction along the inlet causes a relative vacuum region around a singularity in the vicinity of the corner. Initial attempts at modelling the propagation of compound shocks in ANSYS Fluent using the configuration described in section 4.1.2 failed due to rapid temperature divergence within this singularity. Several attempts at tweaking the model were made in order to overcome this, including refining the mesh around the corner, rounding the corner slightly, and modelling a small trip wire just before the corner. All of these came at a great cost in computational time, and only served to delay the divergence.

The in-house Euler solver features a more robust numerical method than ANSYS Fluent, although this comes at a small cost of increased numerical noise. The flow was modelled using the in-house solver in the hopes that the solution divergence would be delayed sufficiently long that useful results would be obtained. However, a major disadvantage of the Euler solver is that it requires a single velocity vector with a constant direction to be specified along the length of an inlet. This is overcome by specifying multiple inlet curves. Initially, the sharp inlet was specified by three individual curves, and the rounded inlet was specified as six individual curves.

In the Euler solver, the discontinuity at the corner generated a shocklet, which delayed the onset of the temperature divergence long enough to get some useful results. This shocklet expands to a significant size, and is visibly interfering with the reflected shock emanating from the lower triple point in Figure 6.8(f). A closer investigation showed that, in a reference frame fixed relative to the shocklet, flow passing through it was being accelerated from locally subsonic speeds to supersonic speeds. Although the Euler equations do allow this behaviour (since they are time reversible), these flows are not physically possible as they violate the second law of thermodynamics (Anderson, 2004). This is a clear indication that this shocklet and vacuum region are numerical artefacts, and would not be present in a physical flow.

Due to the discrete manner in which velocity vectors were applied to the curved inlet, shocklets are also present near the inlet in the results for the rounded profile. The same argument applies in this case. As a result, all of the results in the preliminary study have limited accuracy. However, they are still somewhat useful for gaining a qualitative understanding of the behaviour of the shock front, which was used in the design of the profile plate for the experimental investigation.

A change in approach was required to overcome these challenges for later simulations. The methods used for this are described in section 6.3.4.1, but these preliminary results were still useful for drawing some simple qualitative conclusions regarding the shock behaviour. These were used to aid in the design of the profile plates.

6.3.2 Profile plate design

The biggest challenge in selecting a profile is to position the slit such that as many significant features as possible are visible in the viewing window. The most obvious feature in the results shown in section 6.3.1 is the triple point pair, and the shear layers that follow them. Although the actual trajectories vary with Mach number, general qualitative trends may be identified. The upper triple point follows a trajectory that starts off just above 45° from the horizontal, but quickly curves to a trajectory below 45°. From the preliminary results, the lower triple point trajectory is initially directed upward at an angle just below 45° from the horizontal, but turns to follow an approximately horizontal trajectory.

Using this information, it is possible to set very rough limits for the trajectories of the triple points — a horizontal line and a 45° originating from the concave corner. These can be used to position the slit such that these limits lie within the window, as shown in Figure 6.9. Using the slit width of 15 mm as chosen in chapter 5, the final slit dimensions were chosen to be those shown in Figure 6.10. More detailed drawings of the profile plates, including the precise position of the slit, are included in section C.4 of Appendix C.

6.3.3 Experimental results

The two profiles were manufactured, and experiments were carried out at various Mach numbers between Mach 1.2 and 1.4 for each of the two profiles. There was little discernible difference between the images captured under different conditions, so further analysis was limited to the tests shown in Table 6.2. These tests were chosen as they were at opposite ends of the Mach number range tested, and similar Mach numbers were obtained for both profiles. The results from these four experiments are shown in Figures 6.11 to 6.14.

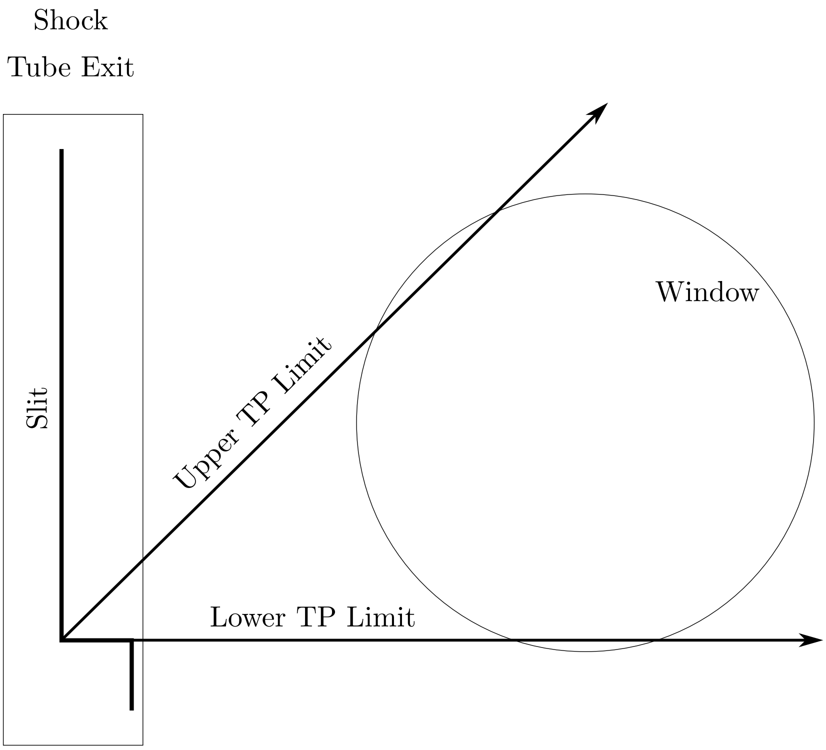

FIGURE 6.9: Positioning the slit based on expected limits for the upper and lower triple point trajectories

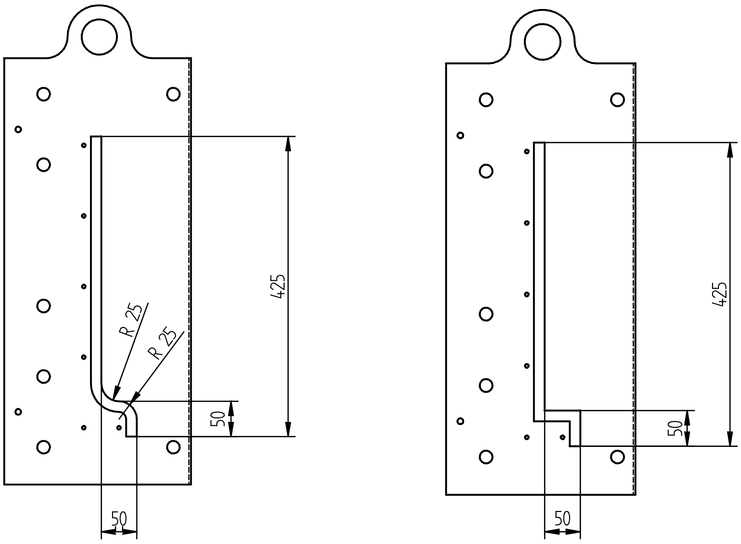

(a) (b)

FIGURE 6.10: The profile plates used to produce the sharp (a) and rounded (b) compound profiles in the facility

Although the preliminary CFD results were for much earlier times, the experimental results reveal that the basic shock structure - at least in the vicinity of the upper triple point, remains stable as the shock wave propagates. As the shock front first enters the viewing window, the shear layer and reflected shock of the upper MR are clearly visible, and the triple point

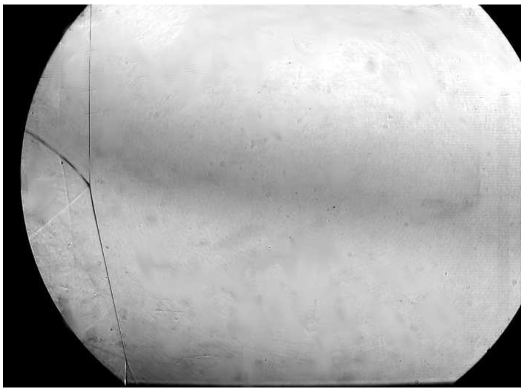

(a) 390 μs after passing through the slit

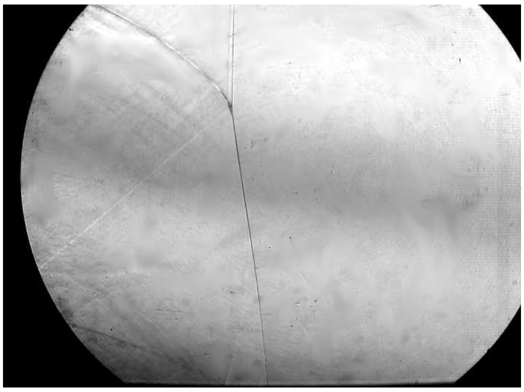

(b) 590 μs after passing through the slit

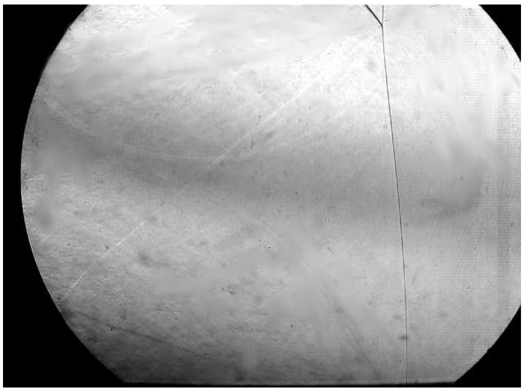

(c) 790 μs after passing through the slit

FIGURE 6.11: Schlieren photographs of the shock front generated by the rounded profile with an initial Mach number of 1.21

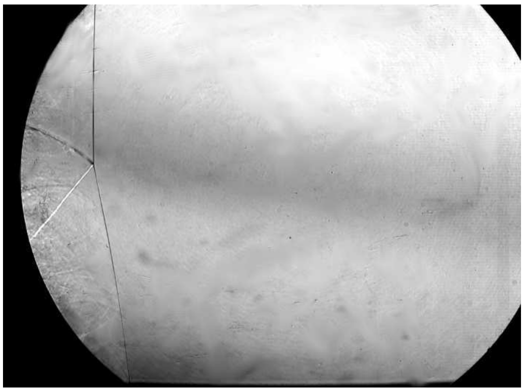

(a) 430 μs after passing through the slit

(b) 580 μs after passing through the slit

(c) 680 μs after passing through the slit

FIGURE 6.12: Schlieren photographs of the shock front generated by the rounded profile with an initial Mach number of 1.41

(a) 430 μs after passing through the slit

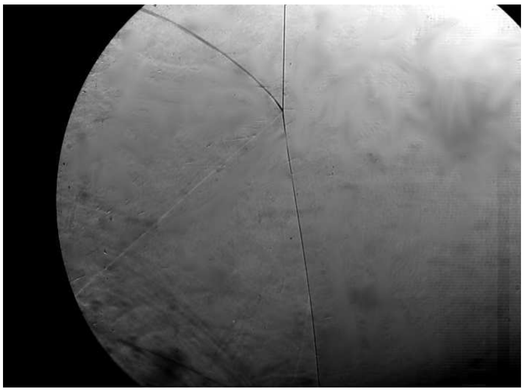

(b) 630 μs after passing through the slit

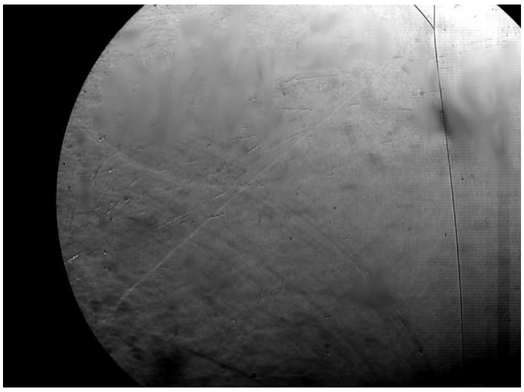

(c) 830 μs after passing through the slit

FIGURE 6.13: Schlieren photographs of the shock front generated by the sharp profile with an initial Mach number of 1.20

(a) 430 μs after passing through the slit

(b) 630 μs after passing through the slit

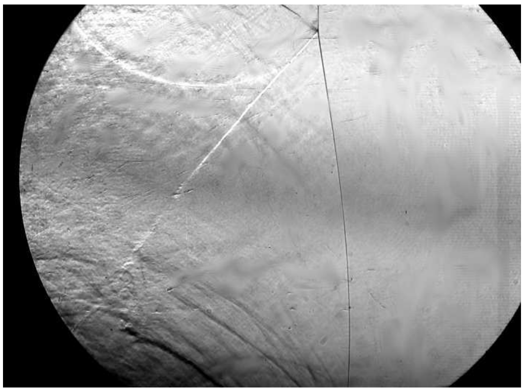

(c) 730 μs after passing through the slit

FIGURE 6.14: Schlieren photographs of the shock front generated by the sharp profile with an initial Mach number of 1.42

Table 6.2: Conditions for the compound shock propagation experiments

Case number	Profile	Driver Pressure	Mach number
4	Sharp 50 mm step	150 kPa	1.20
9	Sharp 50 mm step	410 kPa	1.42
11	Rounded 25 mm radius	150 kPa	1.21
14	Rounded 25 mm radius	410 kPa	1.41

propagates toward the upper right corner of the viewing window. The triple point of the lower MR was not visible in any of the images captured.

In the tests carried out at the higher Mach number ($M \approx 1.4$), the flow behind the inital shock front is significantly more disturbed than at lower Mach numbers ($M \approx 1.2$), and for the upper portion of the incident shock wave in the same position, the triple point is lower at lower Mach numbers.

In the $M \approx 1.2$ tests, the upper MR is the only clearly discernible flow feature, although some weak acoustic disturbances are present, and a discontinuity of some sort is visible in the lower left corner at later times. At $M \approx 1.4$, two distinct flow discontinuities are present in the lower left corner of the images, most obvious in Figures 6.12(b) and (c). These would appear to be the reflected shock and shear layer emanating from the lower MR, but it is not entirely clear which is which. A vortex structure is present where one of these discontinuities interacts with the shear layer of the upper MR, which would suggest that this discontinuity is the shear layer of the lower MR. However, the triple point of the lower MR would need to be visible in order to confirm this.

Further interpretation of the experimental results were made with the aid of more detailed CFD simulations. These simulations are described in the following section.

6.3.4 Computational results

Further CFD simulations were carried out using the Euler solver, as described in section 4.1.1. However, before these simulations could be carried out, the issues raised in section 6.3.1.2 needed to be addressed. The measures taken are described below.

6.3.4.1 Handling the convex corner

Three changes were made to the model in order to overcome some of the difficulties outlined in section 6.3.1.2. For the rounded profile, the inlet was broken up into a total of eighteen segments (as opposed to six used previously), reducing the difference between the flow directions at the joints, and more accurately describing the actual flow.

The cell size of the initial mesh was greatly reduced. Although the usual approach in simulating shock waves is to start with a coarse initial mesh, and then refine it in the vicinity of the discontinuities in the flow, it was found that a much finer initial mesh resulted in a more stable solution at the start. Once the shock front was established, the mesh was coarsened in regions of approximately uniform flow. It was found that a much finer mesh was required for a stable solution for the sharp profile than for the rounded profile. The mesh was refined in regions where the density gradient exceeded 2% of the maximum density gradient in the flow.

Finally, the Courant number was reduced to less than 0.1. Although a Courant number close to 1 is preferred for an accurate solution and fast convergence, reducing the Courant number to such an extent ensures that the initial time step remains very small (in the order of 5×10^{-8} s). This allows the solution in any given cell to be affected by the conditions at points outside of the domain of influence for that cell (Anderson, 1995). Although this is usually undesirable in supersonic or shock-dominated flows, as it reduces the accuracy of the solution, it is acceptable here because all points lie either on the inlet or in the undisturbed flow field, and the flow conditions are known exactly at both of these locations. The net result is that it introduces a significant degree of numerical smoothing in the solution which eliminates any discontinuities which would have formed along the inlet. Once the shock was established, the Courant number was increased to 0.3, and was later increased to 0.6 once it had propagated roughly one step length (in this case, 50 mm) from the inlet.

These changes resulted in a significant increase in running time for the simulations, with the simulations for the sharp profile taking an order of magnitude longer to cover the same distance as the simulations for the preliminary investigation. The simulations for the rounded profile took approximately two weeks to reach completion, whereas those of the sharp corner profile took approximately eight weeks.

6.3.4.2 Results

Figure 6.15 shows the progression of an initially Mach 1.4 shock front for both profiles. It is immediately apparent that the shock is better resolved for the sharp profile, due to the finer mesh size required to handle the sharp corner. However, the sharper shock leads to higher density gradients, which make weaker features (such as the shear layer) more difficult to resolve.

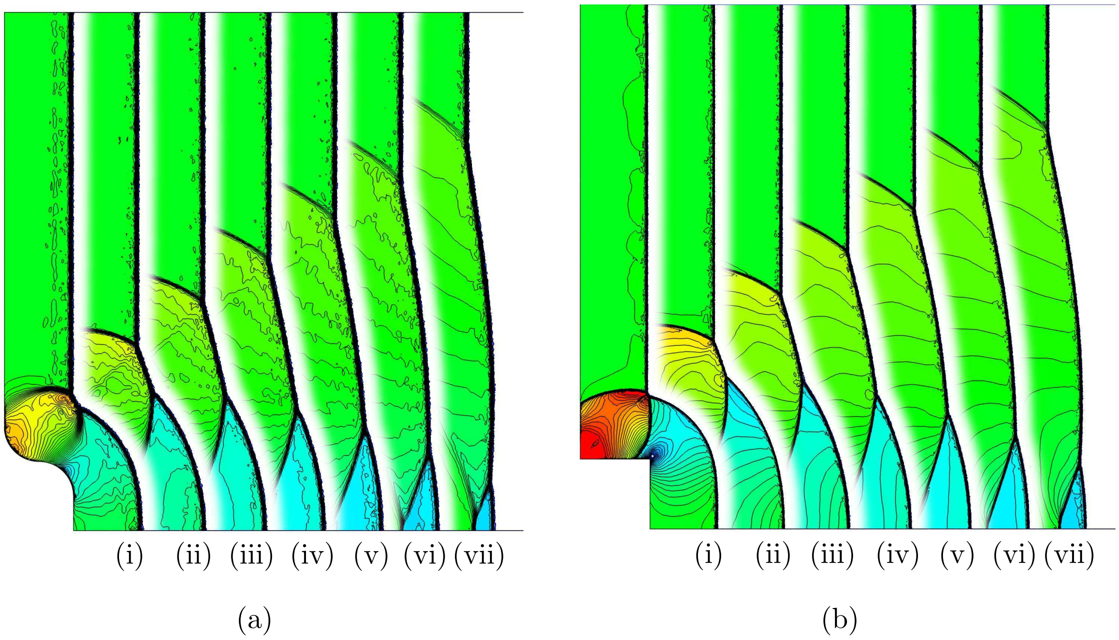

(a) (b)

FIGURE 6.15: Contours of constant density in the vicinity of the shock front from 2D numerical simulations from Mach 1.4 shocks with initially rounded (a) and sharp (b) profiles. The images show times at 100 μs intervals up to 700 μs after being generated at the slit

The shapes of the two shock fronts tend toward each other with time. One difference is that the reflected shocks for the sharp profile extend all the way toward the inlet, whereas the reflected shocks for the rounded profile break down some distance behind the shock front. The trajectories of the upper triple points appear similar, but the triple point for the rounded profile appears to be slightly lower than that of the sharp profile.

Contours of constant density are shown for the entire domain for the rounded profile in Figure 6.16 and for the sharp profile in Figure 6.17. For reference, the location of the viewing windows are indicated by a dashed circle of radius 165 mm with a centre 342 mm horizontally and 207 mm vertically from the lower left corner of the domain.

Several notable features appear in these results. A shear layer and diffraction vortex form after the lower reflected shock wave passes over the convex corner on the inlet, and these are visible to the right and slightly above the corner in both profiles. The shear layers from the MRs formed on either side of the concave portion of the shock meet at the inlet, and form a high speed jet. This jet is present even for the sharp profile, for which the shear layers were not well resolved. At later times, the shear layers break away from the jet, and end in what appears to be a double vortex structure.

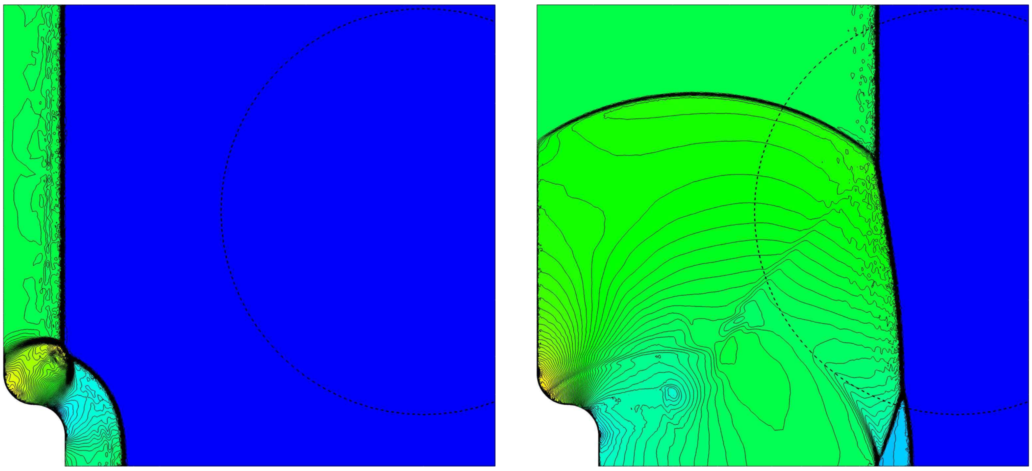

(a) t =100 μs

(d) t =580 μs

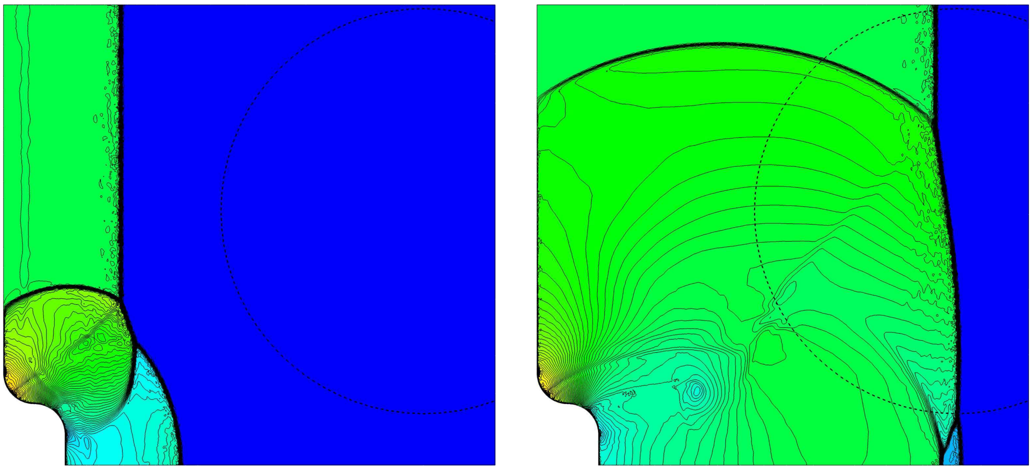

(b) t =200 μs

(e) t =680 μs

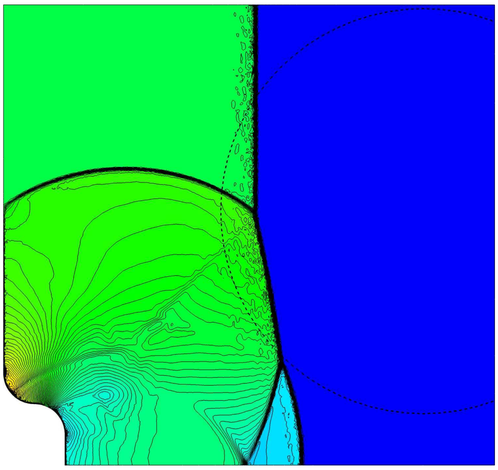

(d) t =430 μs

FIGURE 6.16: Contours of constant density from numerical simulations of a Mach 1.4 shocks with an initial profile containing a 50 mm rounded step. The dashed circle indicates the location of the viewing window

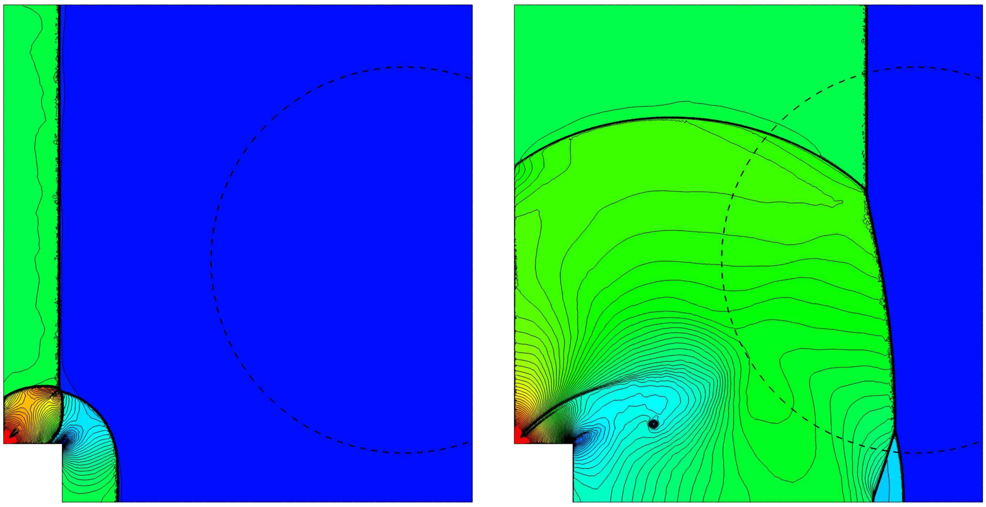

(a) t =100 μs

(d) t =630 μs

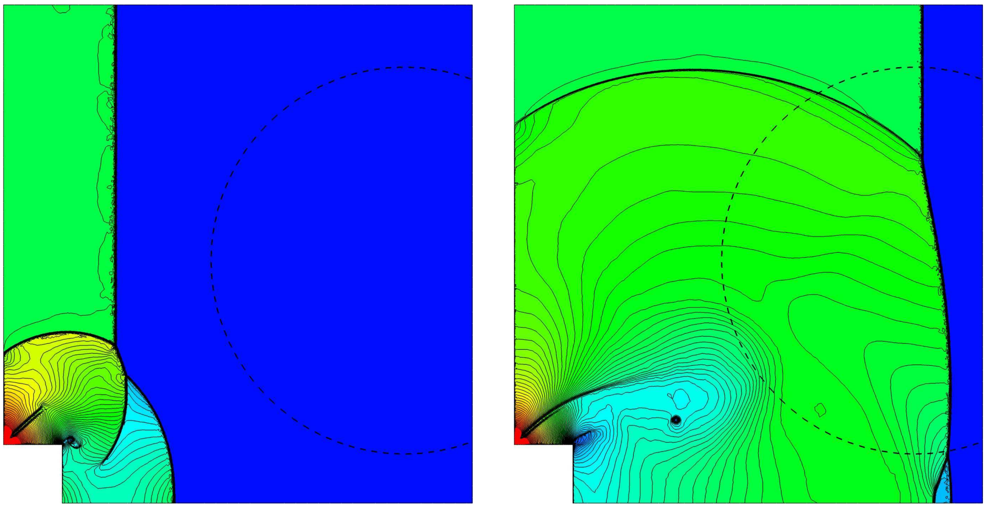

(b) t =200 μs

(e) t =730 μs

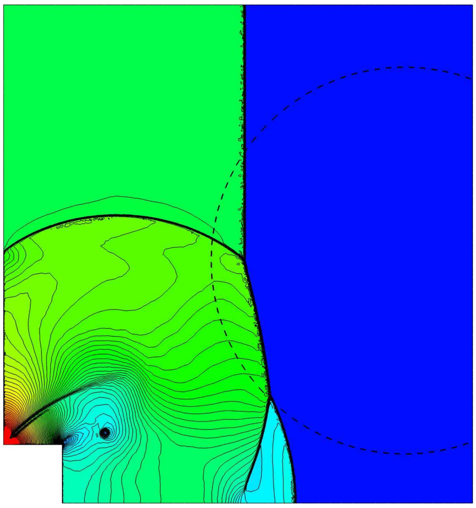

(d) t =430 μs

Figure 6.17: Contours of constant density from numerical simulations of a Mach 1.4 shocks with an initial profile containing a 50 mm sharp step. The dashed circle indicates the location of the viewing window

6.3.5 Comparison and discussion

A direct comparison between the numerical and experimental results show very close agreement to the extent that the numerical results may be used to fill in details in regions that fall outside of the viewing windows, at least for the Mach 1.4 cases. Figure 6.18 shows a schlieren photograph from the experiments inset in a numerical schlieren image from the CFD results for the same time and Mach number. This allows some of those features that could not be identified form the experimental results alone (such as the structures in the lower left corner of the photographs) to be identified. The most prominent features are labelled in Figure 6.19.

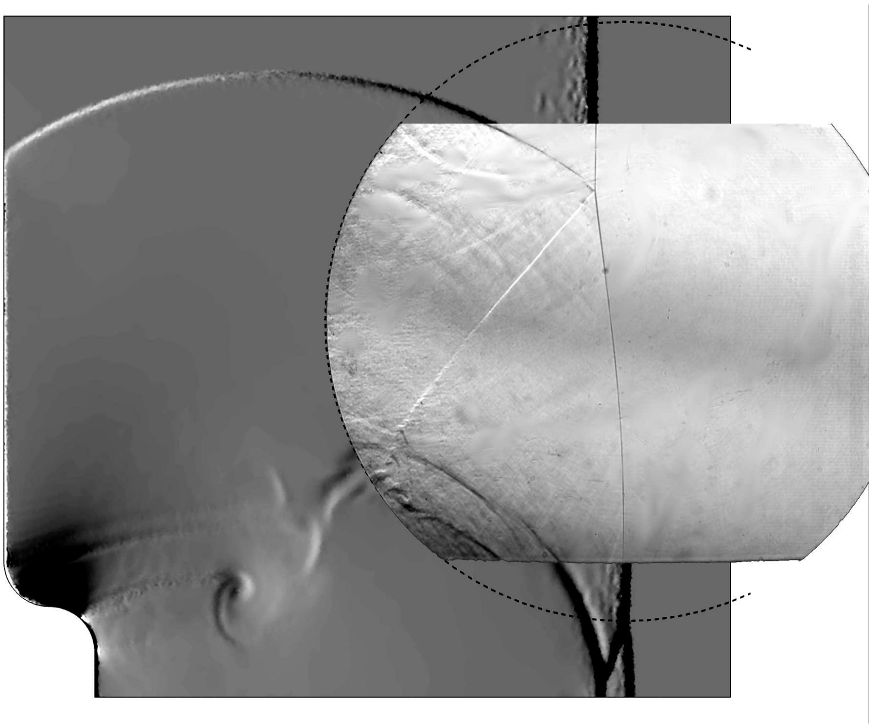

FIGURE 6.18: Schlieren photograph from experimental results (inset) and numerical schlieren from CFD results for a Mach 1.4 shock from the rounded profile after 680 μs

There are three notable mechanisms which generate features in the flow. The first is the initial concave segment of the shock front, which gives rise to the MR pair, producing the two reflected shocks and two shear layers in the flow. It also gives rise to the jet originating on the inlet. The second mechanism is the diffraction of the lower reflected shock around the convex corner of the inlet. This generates a shear layer which originates at the corner, and a diffraction vortex, which propagates into the flow. The third mechanism is the reflection of the lower reflected shock off bottom wall of the propagation chamber. This is an MR, which produces a short Mach stem attached to the wall, and a another shear layer.

The trajectories of the upper triple point from the CFD and experiments are compared in Figure 6.20 for two Mach numbers. In the CFD results, the triple point location was

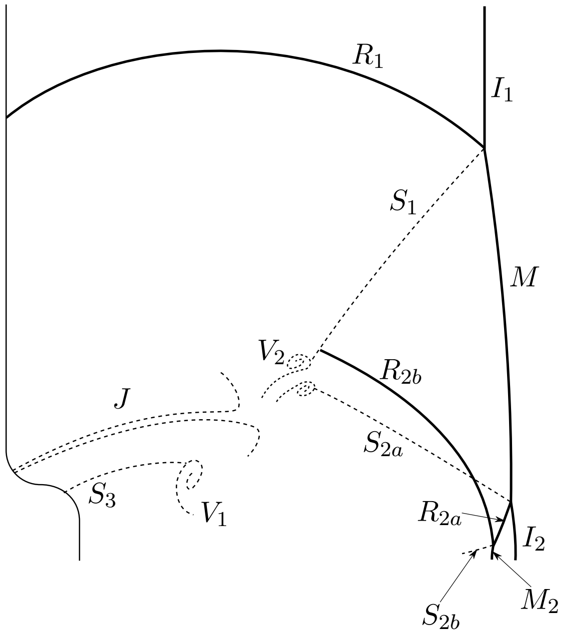

I_1	Upper incident shock wave
I_2	Lower incident shock wave
R_1	Upper reflected shock wave
R_{2a}	Lower reflected shock wave
R_{2b}	Lower re-reflected shock wave
M	Primary Mach shock wave
M_2	Lower reflected shock's Mach stem
S_1	Upper shear layer
S_{2a}	Lower shear layer
S_{2b}	Lower reflected shock's shear layer
S_3	Diffraction shear layer
V_1	Diffraction vortex
V_2	Shear layer interaction vortices
J	High speed jet

FIGURE 6.19: Schematic diagram of the features produced behind a compound shock wave

measured vertically from the bottom edge of the domain, and horizontally from the upper straight segment in the inlet. For the experimental results, the dimensions of the window outline were measured, and using the fact that the viewing window had a diameter of 330 mm, and its centre was known to lie 240 mm vertically from the bottom wall of the facility and 330 mm horizontally from the centre line of the upper portion of the profile slit, the coordinates of the triple point relative to the slit were calculated.

The initial shape of the shock wave appears to have very little effect on the trajectory of the triple point for both the experimental and CFD results. The triple point for the stronger shock wave followed a slightly higher trajectory, as expected from typical behaviour observed in previous experiments (refer to Figure 2.3).

For the Mach 1.4 shocks, the agreement between the CFD and experiment is excellent, even though the origin of the shock for the experiments lay on the centreline of the slit, whereas the leading edge of the slit was used as the origin for the CFD. This suggests that the effective two-dimensional profile that the facility simulates lies within the slit, rather than at the leading edge.

The trajectory obtained from experiments for the Mach 1.2 shock lies significantly higher than that obtained in the CFD simulations. The reason for this is uncertain, but it may have

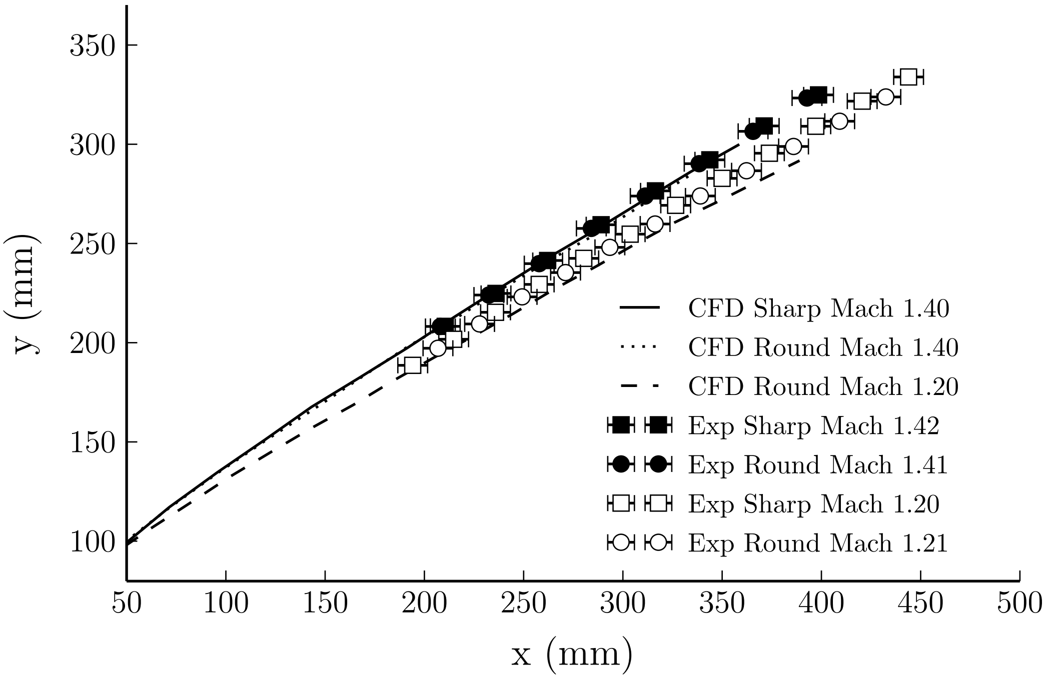

Figure 6.20: Comparison of the upper triple point trajectory for experimental and CFD results. The error bars on the experimental results indicate the slit width

been caused by the fact that the strength of the transverse waves generated as the shock turns the corner in the facility remain significant for a longer period for weaker shock waves.

A deeper understanding of the effect of Mach number and profile shape on the shape of the shock front may be obtained by making a direct comparison of the shock shape when the undisturbed upper straight segment of the shock front is in the same position. Figure 6.21 compares the shapes of the shock fronts produced by the sharp and rounded profiles.

The lower triple point of the rounded profile follows a slightly lower trajectory than that of the sharp profile, and the lower incident shock of the round profile lags slightly behind that of the sharp profile. This may be because the diverging segment of the sharp profile has a slight head start. This will be offset slightly by the fact that the velocity of the sharp profile's diverging segment decays at a slightly faster rate at early times.

Although the shock fronts produced by both profiles tends toward a planar shape, this occurs slightly faster for the rounded profile than for the sharp profile.

Even though the upper triple points are in approximately the same location for both profiles, the upper reflected shock produced by the rounded profile lies slightly below that of the sharp profile. However, the lower reflected shocks for the two profiles appear to coincide, and reflect

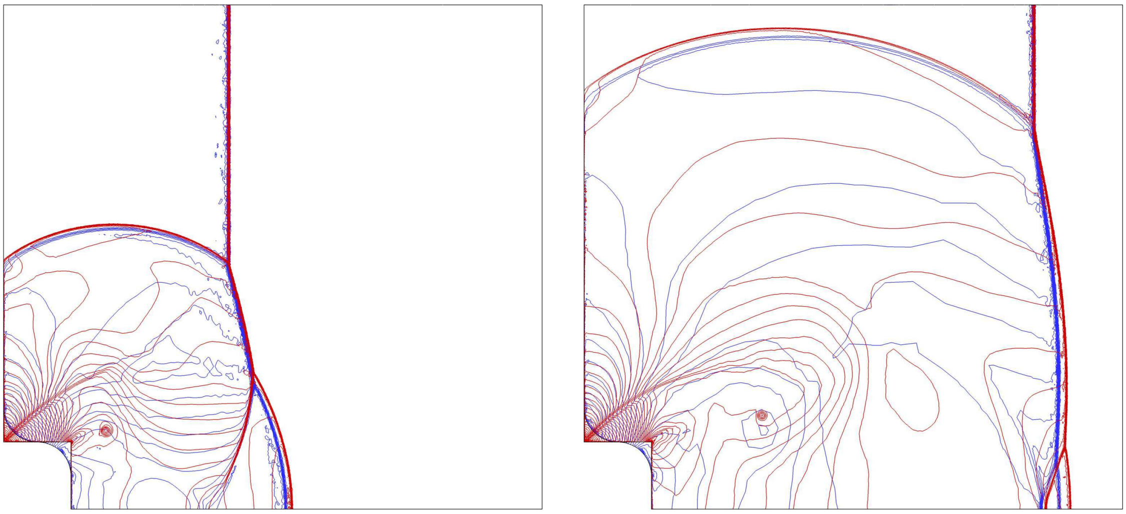
(a) t =350 μs

(b) t =700 μs

FIGURE 6.21: Effect of initial profile on the shape of the shock front for a Mach 1.4 shock wave. The images show lines of constant density for the rounded (blue) and sharp (red) profiles at two different times

off the lower wall at approximately the same place, even though they originate at different points.

Figure 6.22 shows the effect of Mach number on the shock front shape. The lower trajectory of the upper triple point for the lower Mach number is apparent. The lower triple point, however, follows a higher trajectory for the lower Mach number. This is in line with the fact that the triple point trajectory angle for a planar shock encountering a straight wedge tends to increase with Mach number.

The velocity of the diverging section for the higher Mach number slows more rapidly, which causes it to cover a shorter distance than the diverging section of the lower Mach number, when the upper straight section has covered the same distance. Once again, the lower reflected shock appears to reflect off the bottom wall of the facility at approximately the same point for both Mach numbers.

6.3.6 Comment on sharp convex corners on a shock front

The sharp convex corner proved to be rather challenging to model. Theoretically, a sharp convex point along a two-dimensional shock front would require a finite flow rate to emerge from an infinitesimal volume, and is thus not possible in practice.

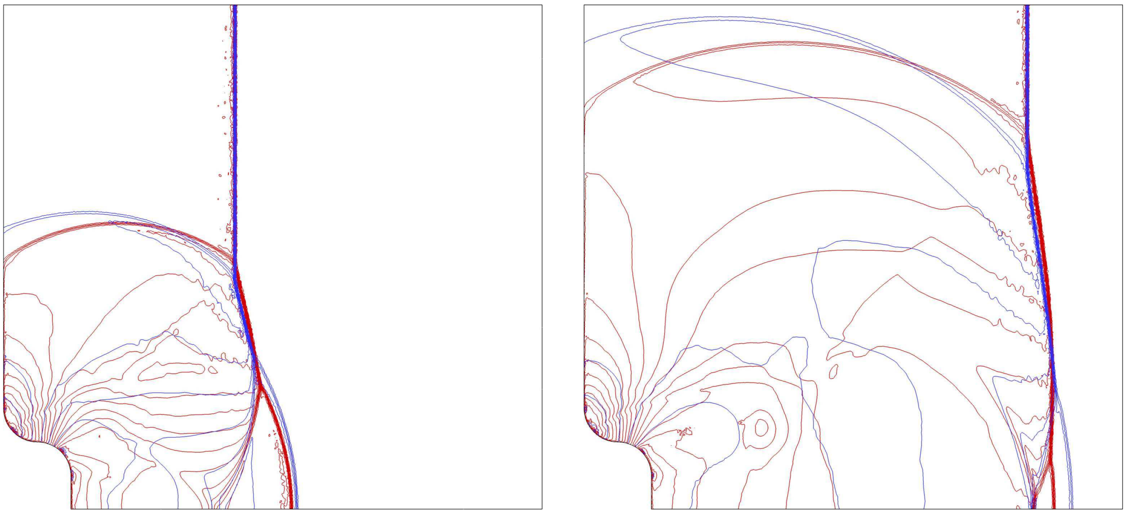

(a) t =420 μs for $M = 1.2$ (blue), and t =360 μs for $M = 1.4$ (red)

(b) t =805 μs for $M = 1.2$ (blue), and t =690 μs for $M = 1.4$ (red)

Figure 6.22: Effect of Mach number on the shape of the shock front for the rounded profile. The images show lines of constant density at the same shock positions for two Mach numbers

Sharp convex corners are however of interest from a theoretical point of view, as some three-dimensional flows do come close to approximating a flow that would be generated by such a shape. The three-dimensional flow through the slit of the very apparatus used in this investigation is one such example.

The results obtained suggest that it is indeed possible to model these three-dimensional flows using a simplified two-dimensional model, but care needs to be taken so as not to introduce numerical artefacts in the vicinity of the corner.

7. Reflection of Converging Cylindrical Shock Wave Segments

The facility designed in the previous chapters provides an ideal means for a broad investigation into the reflection of curved shock waves. As mentioned in section 2.5, the reflection of planar shock waves is typically categorised based on the Mach number and incident angle of the shock, but both of these parameters vary with time in the case of curved shock waves.

In the case of a converging cylindrical shock wave, the Mach number increases, and the incident angle decreases. This means that conditions may pass from the Mach reflection (MR) domain to the regular reflection (RR) domain. This chapter describes a computational and experimental investigation into both the initial reflection type, and the transition between MR and RR as converging cylindrical shock wave segments encounter wedges inclined at various angles.

The type of shock wave considered in this chapter is one for which the radius varies with time, but is constant along the shock at any given time. In two dimensions, the shock is in the shape of a circular arc, which forms a segment of a cylinder when extruded into the third dimension. The ends of this shock wave are initially perpendicular to two straight converging walls, which would intersect at the geometric centre of the shock wave. At some distance from the centre, one of the walls has a sharp corner, and a new wall, or wedge, continues at some angle θ_w to the original wall. This is illustrated in Figure 7.1. It is clear that the incidence angle β changes between times (ii) and (iii). This will be dealt with in the following section.

7.1 Analytical treatment

A planar shock wave encountering a straight wedge will correspond to a single point on the plot in Figure 2.5(b), whereas a cylindrical shock wave segment will trace a curve as the

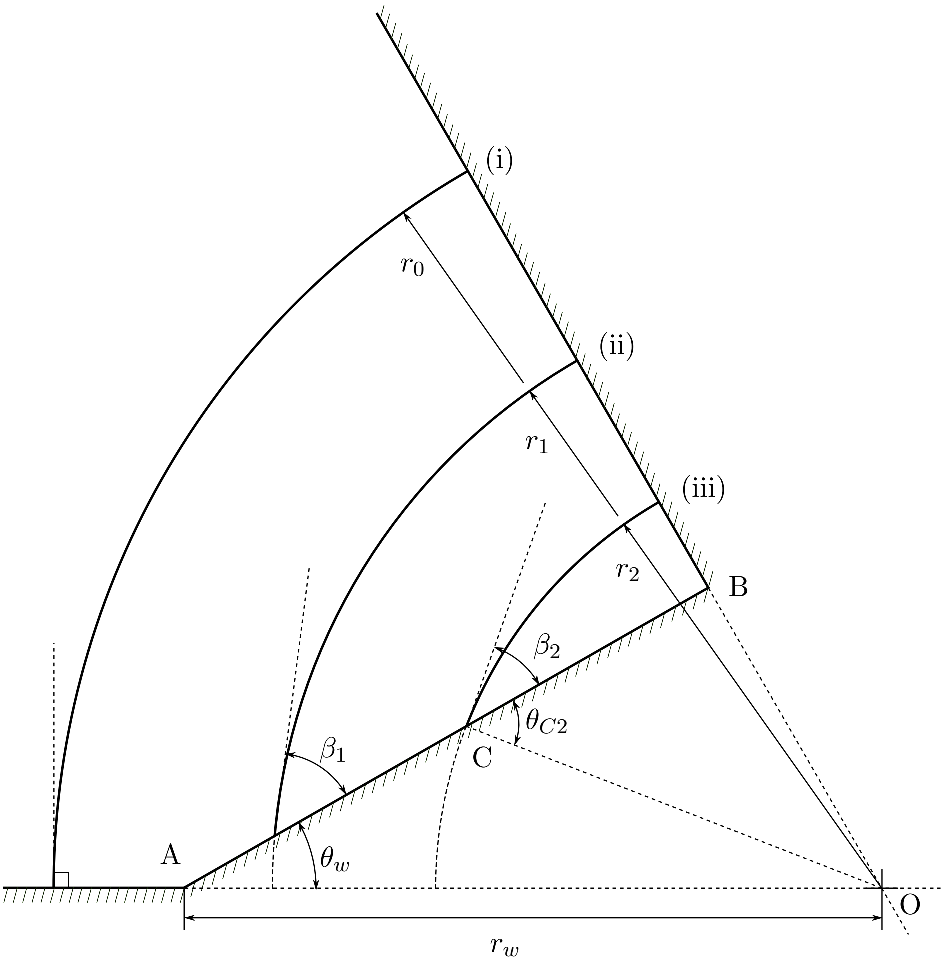

FIGURE 7.1: Schematic diagram of a converging cylindrical shock wave segment encountering a straight wedge at three different times. The wedge apex (A), end of the wedge (B), a reflection point (C), and the geometric centre of the shock (O) are labelled.

shock propagates along the wedge. Equations (2.14) and (2.15) give the radius $r(t)$ and Mach number $M(t)$ of the shock wave at any time t. It is possible to use these equations and the geometry in Figure 7.1 to calculate the locus of the incident angle $\beta(t)$ and Mach number for any given wedge angle θ_w, initial radius r_w and Mach number M_w.

The radius of the shock wave is given by equation (2.14) when it is within the limits of the wedge:

$$r_{min} \leq r(t) \leq r_w \tag{7.1}$$

where r_w is the distance of the wedge apex from the geometric centre, and r_{min} is the radius of the shock when it reaches the end of the wedge, which is equal to the length of the line segment OB, and may be calculated from the geometry of the wedge:

$$r_{min} = r_w \sin \theta_w \tag{7.2}$$

Since the length of OB is known from the wedge geometry, and the length of OC is simply the radius of the shock when it reaches C, The angle of incidence β is given by

$$\beta(t) = \arccos\left(\frac{r_w}{r(t)}\sin\theta_w + \frac{H_m(t)}{r(t)}\right) \tag{7.3}$$

where $H_m(t)$ is the height of the Mach stem (which is equal to zero for RR). The Mach stem height may be calculated iteratively using geometrical shock dynamics (as in the following section), but no simple analytical expression may be derived.

However, progress may be made by assuming that the Mach stem is short compared to the shock radius. If that is the case, then the $\frac{H_m(t)}{r(t)}$ term in the above equation may be neglected. This assumption is always true for RR, and it will be shown later that it is reasonable for wedge angles greater than about 30°. However, the assumption is certainly not valid for wedge angles below this, and this must be considered when interpreting the results of this derivation.

Since the length of OB is known, and the length of OC is simply the radius of the shock when it reaches C, The angle of incidence β is given by

$$\beta(t) = \arccos\left(\frac{r_w}{r(t)}\sin\theta_w\right) \tag{7.4}$$

Equation (2.15) provides a relation between the Mach number and radius of the shock for a given set of initial conditions:

$$M(t) = M_a\left(\frac{r(t)}{r_w}\right)^{\frac{n-1}{n}} \tag{7.5}$$

where M_a is the Mach number of the shock when it reaches the wedge apex, and $n = 0.835$, which is Guderley's exponent for a cylindrical shock wave.

The maximum Mach number that may be reached for a given wedge angle is

$$M_{max} = M_a\left(\sin\theta_w\right)^{\frac{n-1}{n}} \tag{7.6}$$

which occurs when the shock reaches the end of the wedge, point B.

Equation (7.4) may be expressed in terms of Mach number:

$$\beta(M) = \arccos\left[\left(\frac{M_a}{M}\right)^{\frac{n}{n-1}}\sin\theta_w\right] \tag{7.7}$$

The complimentary angle, or effective wedge angle θ_C is defined as the angle between the shock and a normal to the wedge, which is simply

$$\theta_C = \frac{\pi}{2} - \beta \tag{7.8}$$

or

$$\theta_C = \arcsin\left[\left(\frac{M_a}{M}\right)^{\frac{n}{n-1}} \sin\theta_w\right] \tag{7.9}$$

Note that $\theta_C = \theta_w$ at the wedge apex, but tends toward 90° as the shock approaches the end of the wedge.

By substituting equation (7.6) into (7.9), the following expression may be obtained:

$$\theta_C = \arcsin\left[\left(\frac{M_{max}}{M}\right)^{\frac{n}{n-1}}\right] \tag{7.10}$$

This shows that the locus of Mach number and effective wedge angle is independent of the initial conditions of the shock, and depends only on the maximum Mach number that the incident shock reaches at the end of the wedge.

Figure 7.2 (a) shows these loci for various final Mach numbers (dotted curves) together with the regular (RR) and Mach reflection (MR) domains predicted by the sonic criterion (solid curve). When the shock first encounters the wedge, the location on the plot will be given by the initial conditions. As the shock propagates up the wedge, the conditions will move upward and to the right on the figure, following the locus passing through the initial point. Eventually, the Mach number will reach M_{max} when the effective wedge angle reaches 90°, after which the shock wave is completely reflected, and the incident shock no longer exists.

If the initial conditions fall within the RR domain, then the reflection will remain regular throughout the reflection process. However, if the initial conditions fall within the MR domain, then the reflection will transition from MR to a TRR at some point along the wedge. It is unlikely that this would happen at exactly the angle predicted by the sonic transition line, as the sonic transition line only considers a pseudosteady process, and does not consider unsteady effects.

An exception to the above may occur in the small region that exists for weak shock waves encountering wedges at angles below 30° at speeds below about Mach 1.05. The initial conditions for such a shock wave may fall into the shaded region in Figure 7.2 (b), which lies in the RR domain. However, the locus of Mach number and incidence angle for such a shock wave would take it into the irregular reflection (IR) domain (as conditions will fall into the weak shock reflection domain), and then back into the RR domain. The reflection would need to undergo two transitions — first from RR to IR, and then from IR back to RR. This behaviour still needs to be verified by experiment, but this may pose some challenges. Firstly, producing such weak converging shock waves is difficult as the shock waves strengthen rapidly as the radius decreases, and some distance is required for the shock waves to stabilise

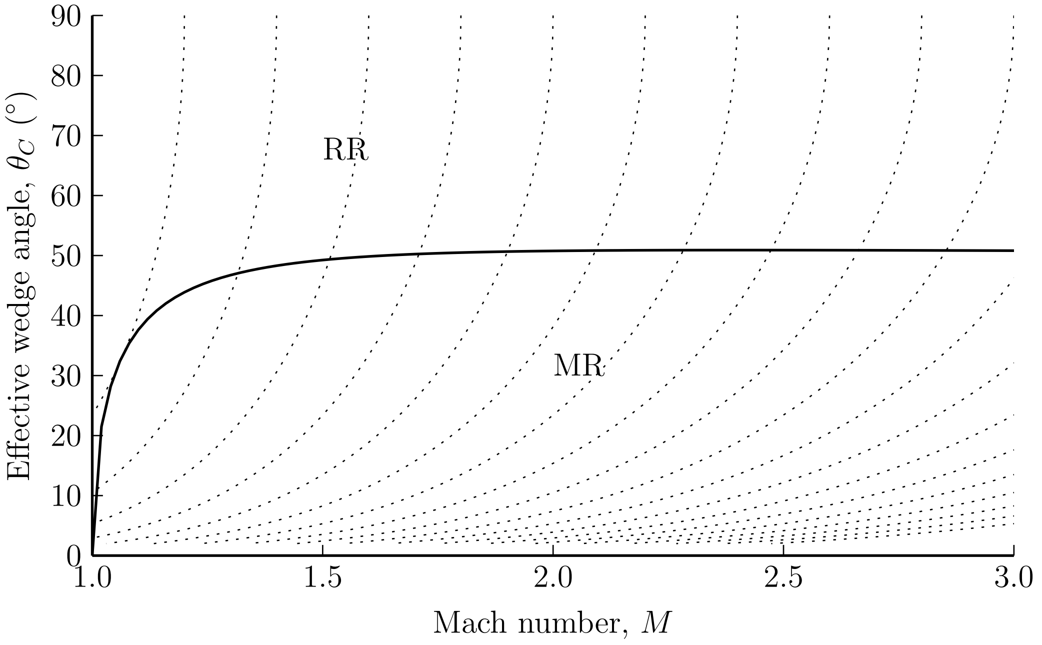

(a) For most Mach numbers, RR occurs for initial conditions above the transition line, and MR→TRR transition occurs for initial conditions below the transition line

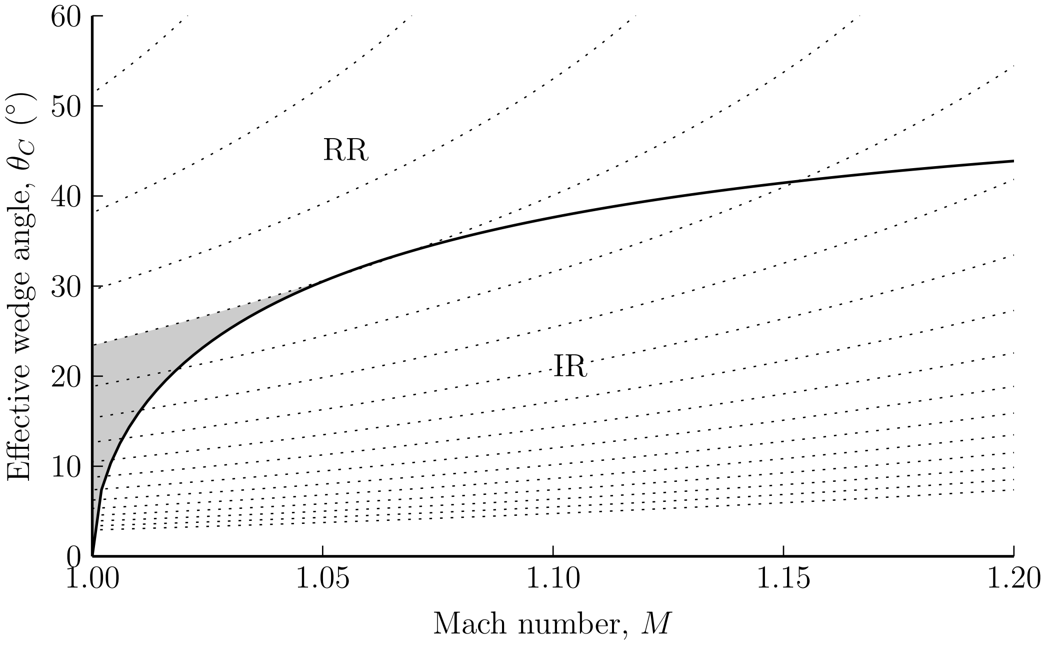

(b) For initial conditions within the shaded region, RR→IR→RR transition may be possible

Figure 7.2: Theoretical loci of Mach number and incident angle for a converging cylindrical shock wave segment (dotted lines), compared to the sonic transition criterion (solid line)

to a two-dimensional form in the current facility. Secondly, it will be difficult to resolve features that occur, and many of the difficulties that have been encountered in the past with resolving features in weak shock reflection of planar shock waves (both numerically and experimentally) are likely to be encountered. Such an investigation is beyond the scope of the current investigation.

7.2 Predicting the Mach stem height

It is not possible to predict the height of the Mach stem analytically, but a simple iterative procedure using GSD has been developed. Itoh et al. (1981) derived an expression for the derivative of Mach stem height of a planar shock encountering a concave wall, and used GSD to find the unknown terms in the expression. The triple point trajectory was obtained by integrating this expression. A similar approach is described here for a converging cylindrical shock wave segment reflecting off a straight wedge.

Assume that the curvature of the Mach stem is negligible, so that the Mach stem may be treated as if it were straight and perpendicular to the wedge. If this is the case, then the Mach number may be assumed constant along the length of the Mach stem.

In a coordinate system measured relative to the wedge apex, as shown in Figure 7.3, the geometric centre of the shock wave is located at the point $(x_0, -y_0)$ where

$$x_0 = r_0 \cos\theta_w \tag{7.11}$$

$$y_0 = r_0 \sin\theta_w \tag{7.12}$$

If the triple point is located at the point (x, y), then the radius of the shock is the distance from the centre to the triple point:

$$r^2 = (x_0 - x)^2 + (y_0 + y)^2 \tag{7.13}$$

This may be rearranged to give an expression for the Mach stem height.

$$y = \sqrt{(r^2 - (x_0 - x)^2} - y_0 \tag{7.14}$$

The derivative of this expression is then

$$\left(\frac{dy}{dx}\right) = \frac{r\left(\frac{dr}{dx}\right) + (x_0 - x)}{(y_0 + y)} \tag{7.15}$$

Integration of the above expression would give the Mach stem height y as a function of x, but this requires the radius derivative $\left(\frac{dr}{dx}\right)$ to be known at all points along the trajectory. This

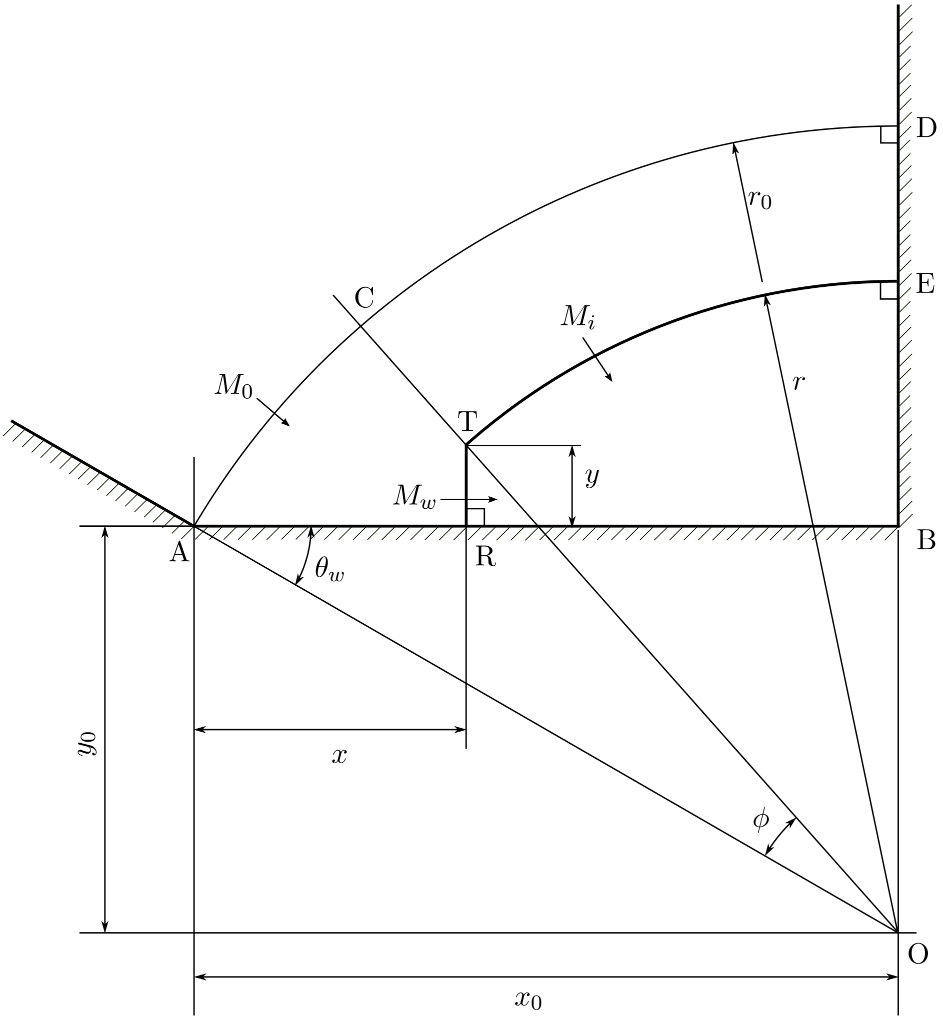

FIGURE 7.3: Schematic diagram showing dimensions used in predicting the Mach stem height

derivative may be calculated from the shock wave properties. The velocity of the incident shock may be found from the Mach number:

$$\left(\frac{dr}{dt}\right) = -M_i a_0 \tag{7.16}$$

where Mi is the Mach number of the incident shock, and a_0 is the sound speed in the undisturbed gas ahead of the shock. Note that the velocity is negative, because the shock wave is converging. Similarly, for the Mach stem:

$$\left(\frac{dx}{dt}\right) = M_w a_0 \tag{7.17}$$

where M_w is the Mach number of the Mach stem.

These two give enough information to determine the unknown derivative.

$$\left(\frac{dr}{dx}\right) = \frac{\left(\frac{dr}{dt}\right)}{\left(\frac{dx}{dt}\right)} = -\frac{Mi}{M_w} \tag{7.18}$$

The incident Mach number M_i depends on the current radius of the shock, and is given by equation (2.15). The Mach number of the Mach stem may be calculated using Whitham's theory, equation (2.16). The line segment CT is a ray, and since rays cannot intersect, the incident shock TE originated from the portion CD of the original shock, and the Mach stem RT originated from the portion AC of the original shock. Therefore, all rays originating on the arc AC, which has a total area of A_0, must intersect RT, which has a total area of A_w. These areas may be calculated per unit width from the geometry.

$$A_w = y \tag{7.19}$$

$$A_0 = r_0 \phi \tag{7.20}$$

where ϕ is the angle between the ray CT and the x-axis, and is given by

$$\phi = \arctan\left(\frac{y_0 + y}{x_0 - x}\right) - \theta_w \tag{7.21}$$

The Mach number at the wall may then be calculated using the A-M relation.

$$\frac{A_w}{A_0} = \frac{f(M_w)}{f(M_0)} \tag{7.22}$$

In this case, the approximate formula for Milton's modification of $f(M)$ given by Duong and Milton (1985) given in equation (2.22) was used, as this incorporates a correction for reflected disturbances behind the shock wave.

A complication that arises is the case for which $\phi = 0$, which occurs at the beginning of the wedge. In this case, A_w and A_0 are both zero, which leads to an indeterminate form for the area ratio. In order to resolve this, the initial triple point trajectory angle was set to be that of a planar shock wave at a Mach number M_0 and wedge angle of θ_w.

Equation (7.15) may be integrated numerically using a forward marching scheme to obtain the triple point trajectory. Triple point trajectories for three Mach numbers and wedge angles that were predicted using this method are shown in Figure 7.4.

7.3 Experimental results

A profile plate and propagation chamber were manufactured to produce converging cylindrical shock wave segments with initial radii of 450 mm (see Figures C.5 and C.7 of Appendix C for drawings). Straight wedges with angles varying between 15° and 50° were mounted to

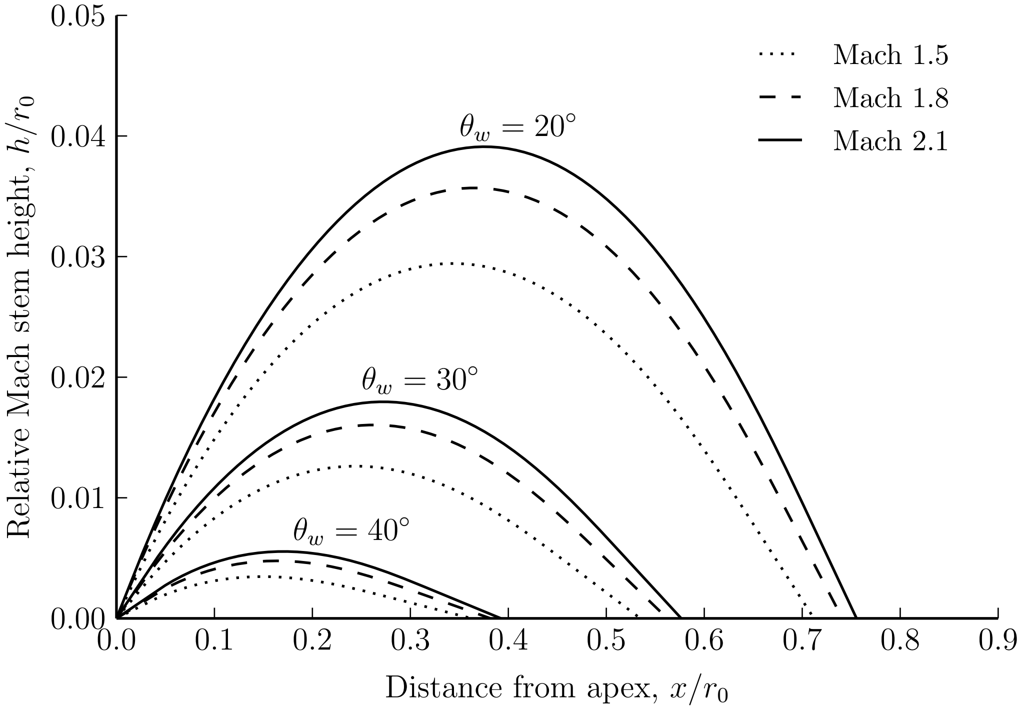

FIGURE 7.4: Predicted trajectories of the triple points for three different Mach numbers and wedge angles

the lower wall of the propagation chamber such that the apex lay a distance of 100 mm from the geometric centre of the slit.

All of the wedges were 72 mm long, which left a small exhaust area for air to escape, preventing the build up of extremely high pressures that shock focussing could potentially produce at the end of the wedge. The disadvantage of this is that the final portion of the reflection process could not be visualised, but this was necessary as the walls and windows of the facility would need to be considerably thicker to withstand these pressures. Having a fixed length for all of the wedges simplifies the calculation of the scaling factor for each image captured.

A series of tests were carried out in the shock tube described in section 4.2.1. Initially, single shot photography was used to capture images of the shock reflection at a single instant for a 30° wedge and a limited range of Mach numbers. This was followed by a more detailed investigation involving more wedge angles and a greater range of Mach numbers, using a high speed camera to capture images of multiple shock positions for each test.

7.3.1 Single shot photography

The initial study used a Nikon D40X 10.2 megapixel camera, and a xenon flash lamp with an approximate effective exposure time of 1.5 μs to capture an image of the shock wave in a single position for each test. The schlieren system described in section 4.2.2 was used with the knife edge oriented perpendicular to the wedge.

Planar shock waves with Mach numbers varying between 1.2 and 1.3 were produced in the shock tube, corresponding to estimated Mach numbers between 1.5 and 1.7 at the wedge apex. Figures 7.5 to 7.9 show schlieren photographs taken of different shock positions in five separate tests carried out under the same conditions, but using different delays. The wedge angle is 30°, and the Mach number and radius of the shock at the apex were approximately Mach 1.5 and 100 mm. A 3.3x zoomed image of the reflection pattern is shown to the right of each photograph. The shock wave is moving from left to right, and the time since the shock passed the apex was estimated from the delay.

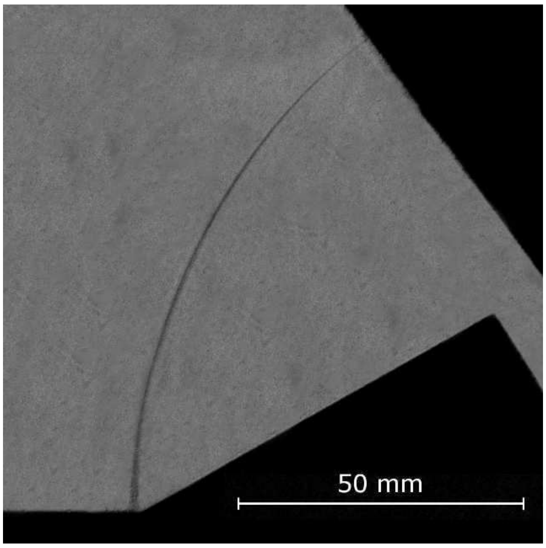

Figure 7.5: Schlieren photograph of the shock wave shortly before encountering the wedge apex

Figure 7.5 shows a well formed cylindrical shock segment, with relatively uniform flow behind it. The shock appears much thicker toward the bottom of the test section, and even seems to disappear toward the top. The disappearance of the shock wave toward the top of the image is due to the knife edge orientation. At this point, the density gradients through the shock wave are parallel to the knife edge, so they don't cause any shadows in the image. The thicker shock wave at the bottom of the image is due to motion blur. For the conditions under which these tests were carried out, a Mach 1.5 shock wave moves at a velocity of 515 m/s, and covers a distance of about 0.77 mm within the exposure time of the light source. This corresponds to the observed shock thickness in the photographs. Features that are stationary or move

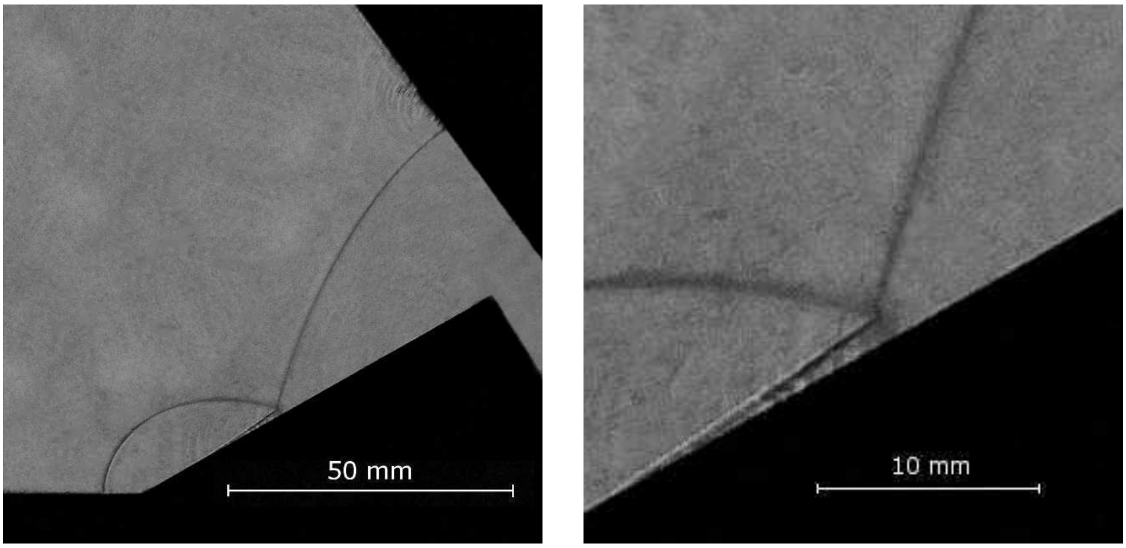

Figure 7.6: A direct Mach reflection (DiMR) $40\mu s$ after the apex

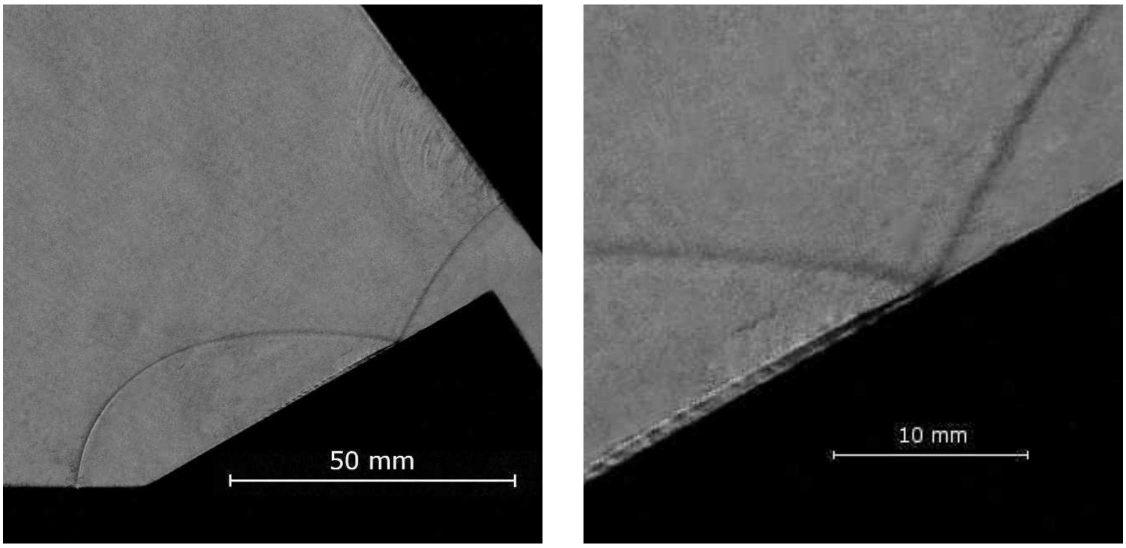

Figure 7.7: The triple point starts moving toward the wedge forming an inverse Mach reflection (IMR) $60\mu s$ after the apex

slowly (such as the wedge surface and shear layers) are sharper, as they are not affected by motion blur.

For all cases, the initial reflection was an MR, but as the shock propagated up the wedge, the decreasing incident angle caused the triple point to turn back toward the surface. Toward the top of the wedge, the triple point collided with the wedge, resulting in a TRR.

A regular periodic disturbance is clearly visible in the shear layers of Figures 7.7 to 7.9. This is most likely a Kelvin-Helmholtz instability, although images with a higher resolution and shorter exposure time are necessary in order to confirm this. It is worth noting that

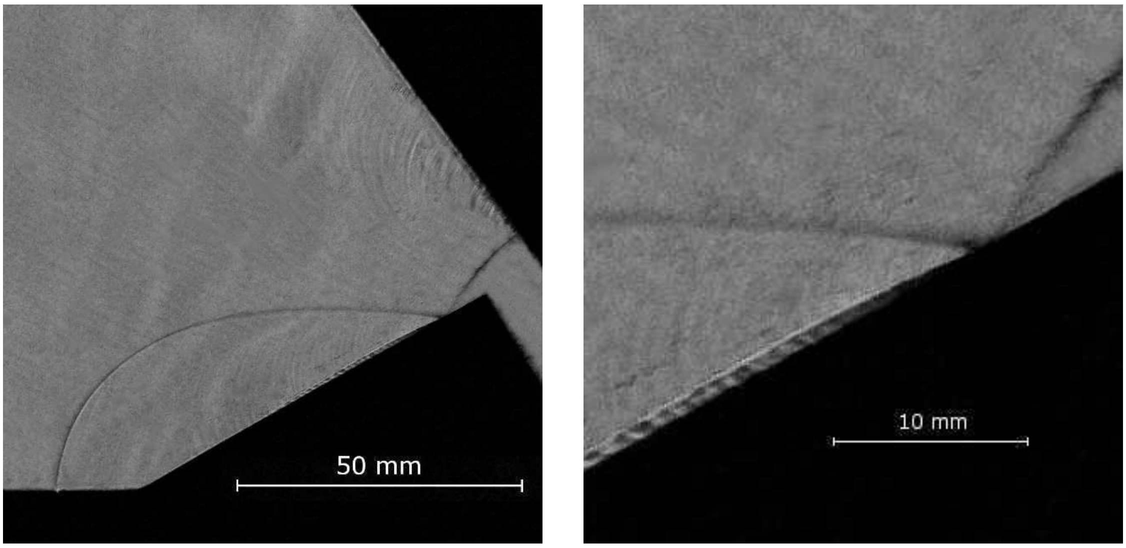

Figure 7.8: The triple point collides with the wedge, causing the onset of transitioned regular reflection (TRR) 65μs after the apex

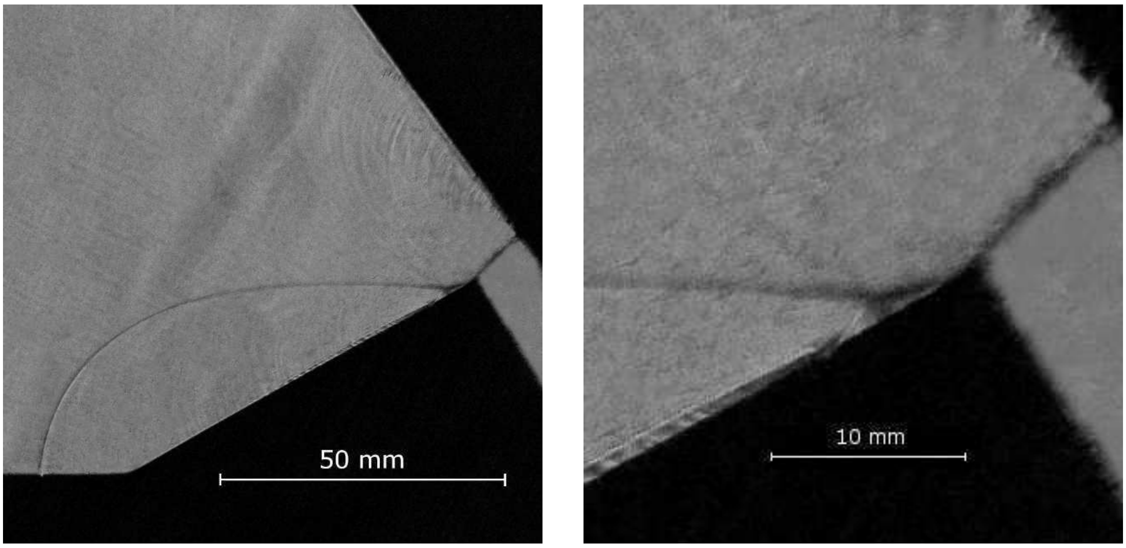

Figure 7.9: Transitioned regular reflection (TRR) is well established by the end of the wedge 70μs after the apex

the instability appears to be significantly more pronounced than in shear layers resulting from the MR of planar waves, and this is likely due to the fact that the triple point of a converging shock reflection is accelerating along a curved trajectory, rather than propagating at a constant velocity along a straight trajectory, as is the case for the reflection of a planar shock wave.

Estimated incidence angles at which MR→TRR transition occurred are shown in Table 7.1. The trend observed in the results is that transition occurs at a lower incident angle (which occurs higher up the wedge) for higher Mach numbers. However, there is a significant degree of uncertainty in the measured angles for two reasons. Firstly, the previously mentioned motion blur leads to a slight ambiguity in the shock position. Secondly, it is challenging to determine the exact point at which the triple point collides with the wedge surface. In many cases, the angle was obtained by interpolating between two images, such as Figures 7.7 and 7.8. Since these two images were obtained in separate tests, the conditions may not have been identical between the two tests, introducing further uncertainty into the measurements.

Table 7.1: Estimated incident angles at TRR transition for a 100mm radius shock reflecting off a 30° wedge

Mach number at apex	Incident angle at TRR transition
1.5 ±0.1	30° ±2.5°
1.6 ±0.1	27° ±2.5°
1.7 ±0.1	25° ±2.5°

The Mach number of the incident shock wave was estimated based on the set delay and shock positions in successive tests. The resulting Mach numbers were found to fluctuate by approximately 10% depending on which tests were used in the calculations. The values reported in Table 7.1 are median values calculated for each set of tests.

Due to the large uncertainties, the results of the single shot experiments are primarily useful only for a qualatative understanding of the reflection process. The images clearly show that the shock wave encountering a 30° wedge forms an DiMR, which gradually inverts, and eventually transitions to TRR

In order to improve the uncertainty of the results, another series of tests was carried out using a high speed camera to capture multiple photographs of the same experiment. This is described in the following section.

7.3.2 High speed photography

A Photron FASTCAM SA5 high speed camera was used with the same schlieren optics as in the previous section, except with the knife edge oriented horizontally. Tests were carried out for six wedge angles, and at least five different Mach numbers for each wedge. The driver pressure was set to produce planar shock waves with Mach numbers varying between 1.2 and 1.5. These resulted in cylindrical shock wave segments at the wedge apex with Mach numbers varying between 1.5 and 2.1.

Table 7.2 gives a summary of the conditions tested and the resulting Mach numbers and radii at the wedge apex. Although the facility was designed to produce shock waves with a radius of 100 mm, the actual measured shock radii were slightly larger. Possible reasons for this will be discussed in section 7.5.1.

Table 7.2: Conditions for experiments for converging cylindrical shock wave reflection

Wedge angle	Driver pressure	Shock Tube Mach number	Mach number at apex	Radius at apex
15°	150 kPa	1.23	1.52	113.8 mm
15°	250 kPa	1.31	1.72	120.4 mm
15°	350 kPa	1.35	1.81	117.9 mm
15°	450 kPa	1.43	1.94	118.1 mm
15°	550 kPa	1.48	2.03	122.0 mm
25°	150 kPa	1.22	1.55	113.3 mm
25°	250 kPa	1.31	1.75	120.2 mm
25°	350 kPa	1.37	1.88	122.9 mm
25°	450 kPa	1.43	1.98	120.0 mm
25°	550 kPa	1.48	2.08	125.4 mm
30°	150 kPa	1.22	1.55	111.6 mm
30°	250 kPa	1.31	1.76	120.8 mm
30°	350 kPa	1.38	1.84	123.7 mm
30°	450 kPa	1.44	1.96	122.5 mm
30°	550 kPa	1.47	2.05	120.5 mm
40°	150 kPa	1.21	1.55	108.3 mm
40°	250 kPa	1.32	1.74	121.1 mm
40°	350 kPa	1.37	1.86	124.4 mm
40°	450 kPa	1.44	1.97	124.3 mm
40°	550 kPa	1.47	2.04	125.3 mm
45°	150 kPa	1.22	1.55	107.4 mm
45°	250 kPa	1.32	1.78	127.9 mm
45°	350 kPa	1.37	1.88	125.0 mm
45°	450 kPa	1.44	2.01	127.8 mm
45°	550 kPa	1.47	2.07	123.3 mm
50°	150 kPa	1.19	1.53	105.1 mm
50°	250 kPa	1.32	1.79	121.6 mm
50°	350 kPa	1.37	1.88	122.3 mm
50°	450 kPa	1.43	2.01	121.2 mm
50°	550 kPa	1.48	2.08	125.5 mm

Photographs were captured at 100 000 frames per second (corresponding to one frame every 10 μs), with an exposure time of 1 μs for each frame. At these speeds, the maximum resolution at which the camera was capable of operating was 320x192 pixels. A total of 635 photographs were captured for various conditions and shock wave positions, and a number of these are shown in Figures 7.10 to 7.17. In these tests, the camera was tilted to match the inclination of the wedge in order to optimise the usage of the limited resolution available. In each of the images, the wedge apex is just visible in the lower left corner of the images, and the end of the wedge is visible on the far right of the image.

For the 15° and 25° wedges, the initial reflection was an MR, which persisted until the end of the wedge. In the case of the 25° wedge, the triple point trajectory turned back toward the wedge surface, but transition to TRR did not occur before the Mach stem reached the exhaust area. For the 30° wedge, the initial reflection is also MR, but this transitions to TRR just before the end of the wedge, and the transition occurs slightly earlier for slower Mach numbers (which agrees with the behaviour observed from the single shot photography). It is difficult to discern the Mach stem of the reflection for the 40° wedge, as the triple point remains close to the surface. However, careful examination of frames around that shown in Figure 7.14(a) suggest that the reflection is indeed an MR. Transition to TRR appears to occur between half and three quarters of the way up the wedge, depending on the Mach number. The Mach stem is too small to be seen for the 45° and 50° wedges, and transition occurs low down on the wedge. The shear layer of the TRR is very weak, but is just discernible on some of the images, for example Figure 7.17(c)

The possible Kelvin-Helmholtz instability observed in the single shot photography is not as clearly resolved. This may be because of the change in the knife edge orientation, and the reduced resolution of the photographs. There is, however, still a clear breakdown in the shear layers in several of the images, particularly for stronger shock waves and lower wedges angles. This is most noticeable in Figure 7.11.

7.4 Computational results

Simulations were carried out for a range of wedge angles between 15° and 60° in ANSYS Fluent using the configuration described in section 4.1.2. For each wedge angle, a range of radii between 50 mm and 400 mm, and apex Mach numbers ranging from 1.24 to 2.13 at the apex were simulated. A summary of all of these cases is given in Table 7.3.

For all cases, the domain was bounded by three straight walls and a curved inlet, as shown in Figure 7.18. The top and bottom walls were both perpendicular to the inlet. The wedge

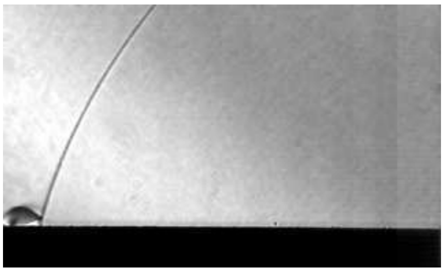

(a) $t = 10.7$ μs

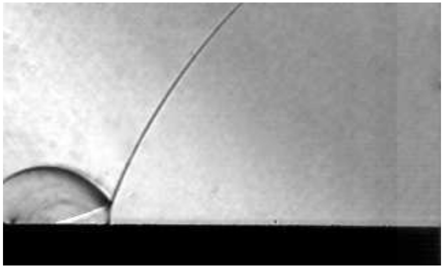

(b) $t = 30.7$ μs

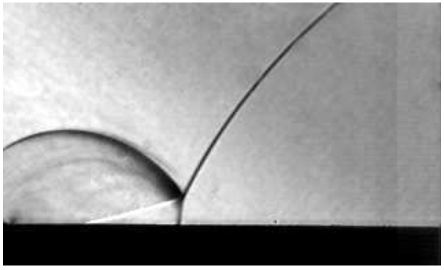

(c) $t = 50.7$ μs

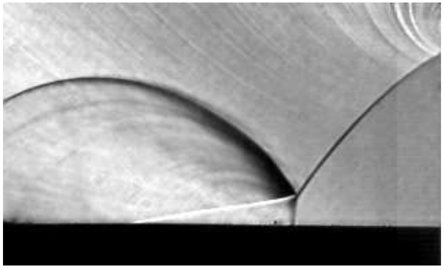

(d) $t = 80.7$ μs

(e) $t = 110.7$ μs

FIGURE 7.10: Schlieren photographs of a Mach 1.52, 113.8 mm radius converging cylindrical shock wave segment reflecting off a 15° wedge

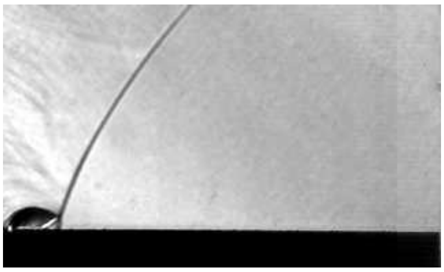

(a) $t = 11.3$ μs

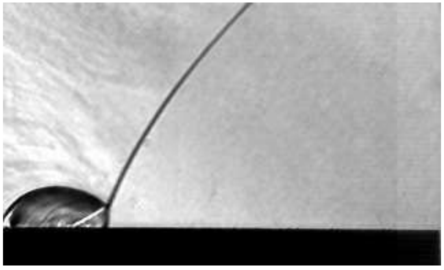

(b) $t = 21.3$ μs

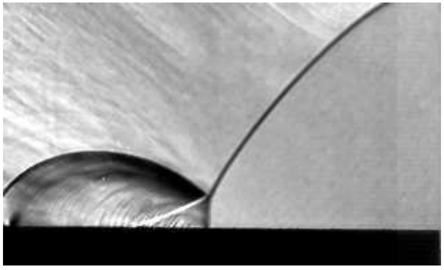

(c) $t = 41.3$ μs

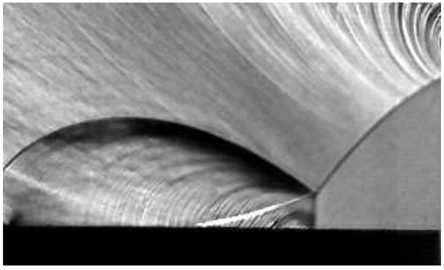

(d) $t = 61.3$ μs

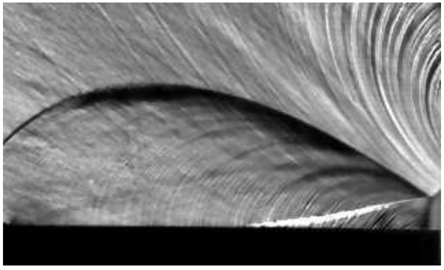

(e) $t = 81.3$ μs

FIGURE 7.11: Schlieren photographs of a Mach 2.03, 122.0 mm radius converging cylindrical shock wave segment reflecting off a 15° wedge

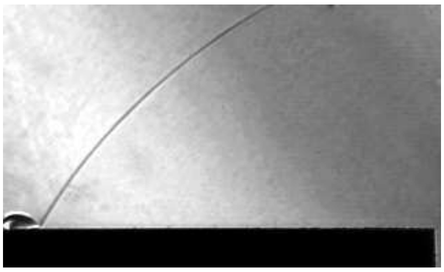

(a) t =8.4 μs

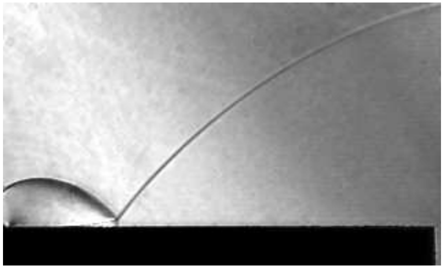

(b) t =28.4 μs

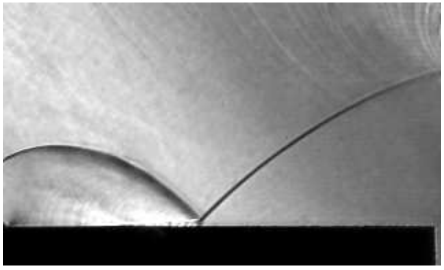

(c) t =48.4 μs

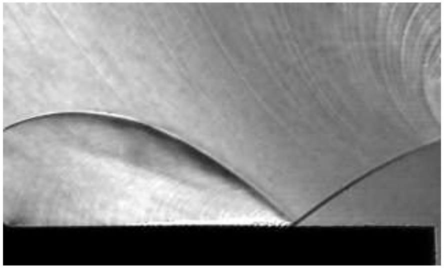

(d) t =68.4 μs

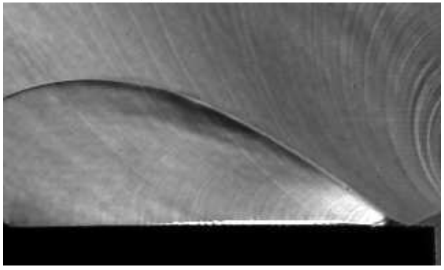

(e) t =88.4 μs

FIGURE 7.12: Schlieren photographs of a Mach 1.55, 111.6 mm radius converging cylindrical shock wave segment reflecting off a 30° wedge

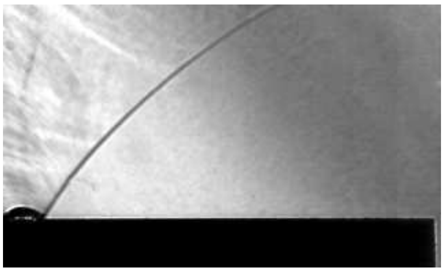

(a) t =6.9 μs

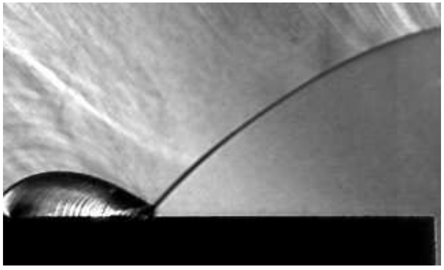

(b) t =26.9 μs

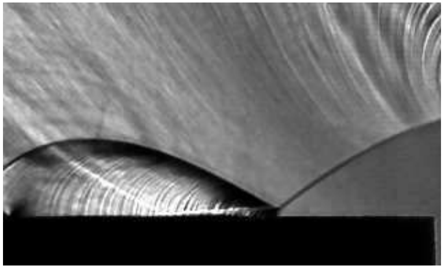

(c) t =46.9 μs

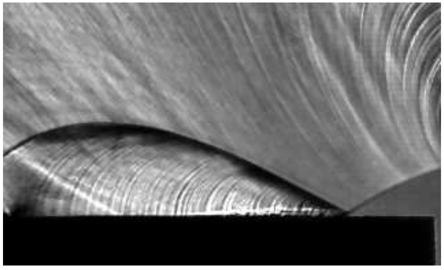

(d) t =56.9 μs

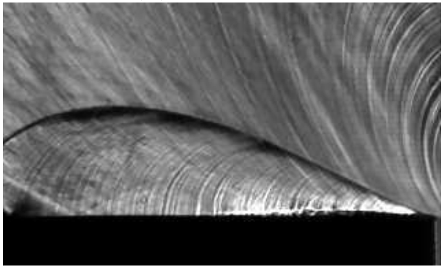

(e) t =66.9 μs

FIGURE 7.13: Schlieren photographs of a Mach 2.05, 120.5 mm radius converging cylindrical shock wave segment reflecting off a 30° wedge

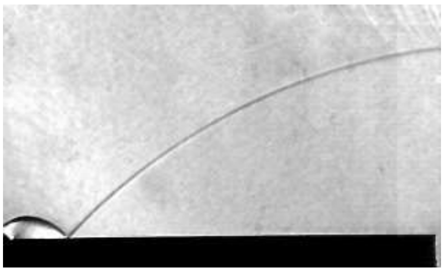

(a) $t = 12.8$ μs

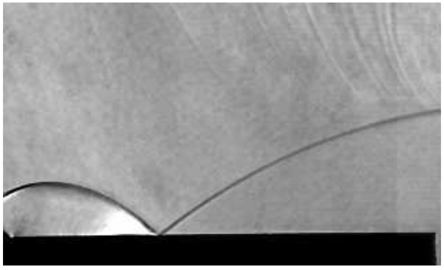

(b) $t = 32.8$ μs

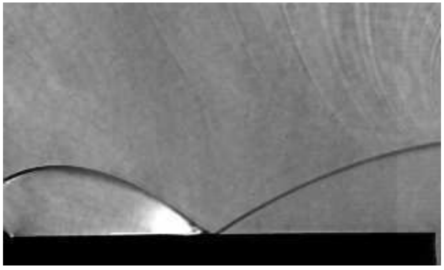

(c) $t = 42.8$ μs

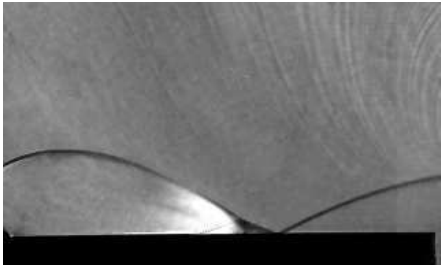

(d) $t = 52.8$ μs

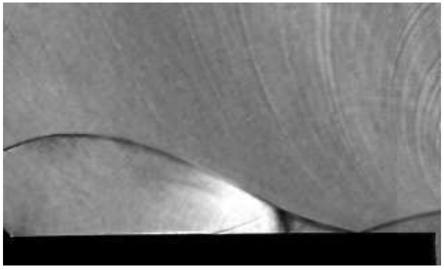

(e) $t = 62.8$ μs

FIGURE 7.14: Schlieren photographs of a Mach 1.55, 108.3 mm radius converging cylindrical shock wave segment reflecting off a 40° wedge

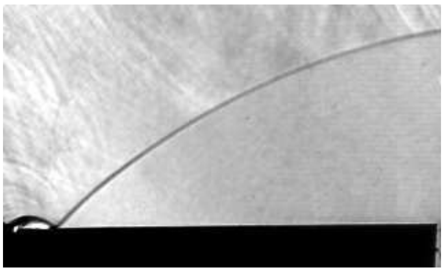

(a) $t = 6.1$ μs

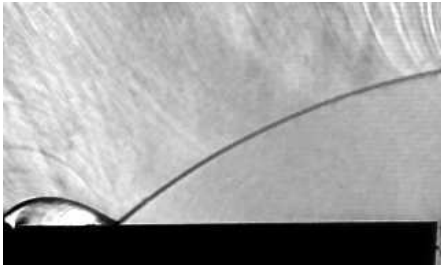

(b) $t = 16.1$ μs

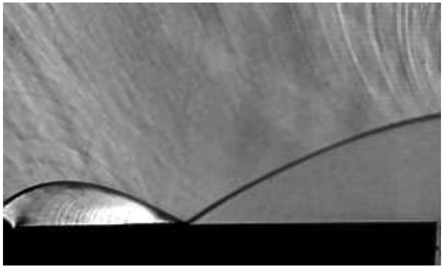

(c) $t = 26.1$ μs

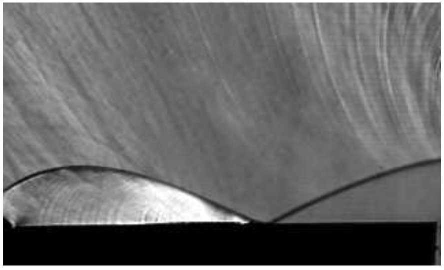

(d) $t = 36.1$ μs

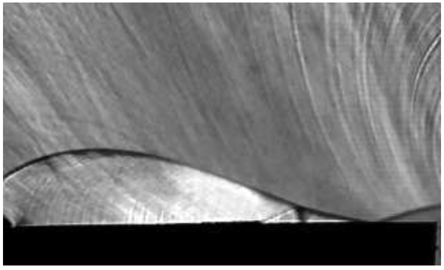

(e) $t = 46.1$ μs

FIGURE 7.15: Schlieren photographs of a Mach 2.04, 125.3 mm radius converging cylindrical shock wave segment reflecting off a 40° wedge

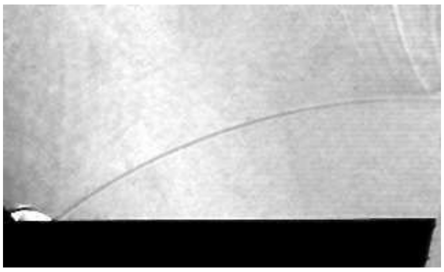

(a) t =7.8 μs

(b) t =27.8 μs

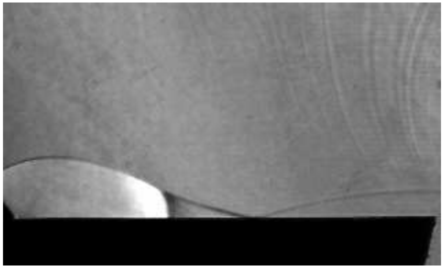

(c) t =37.8 μs

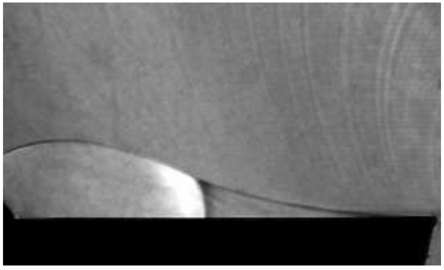

(d) t =47.8 μs

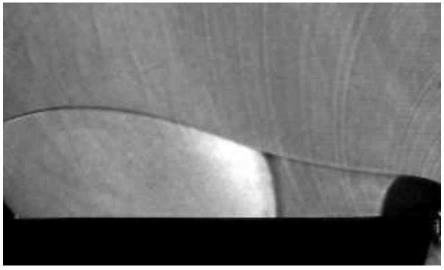

(e) t =67.8 μs

FIGURE 7.16: Schlieren photographs of a Mach 1.53, 105.1 mm radius converging cylindrical shock wave segment reflecting off a 50° wedge

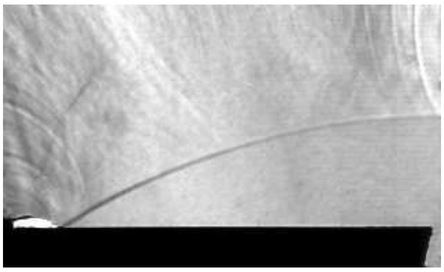

(a) t =6.7 μs

(b) t =17.7 μs

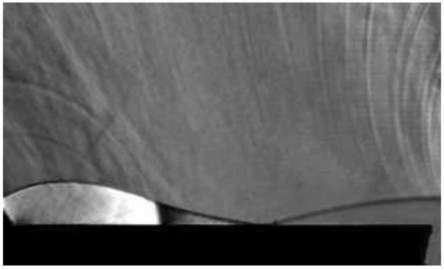

(c) t =27.7 μs

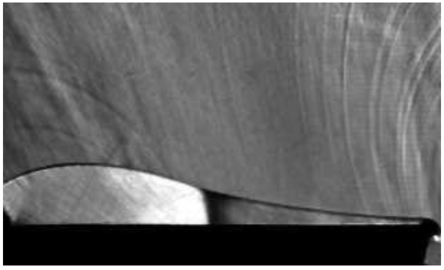

(d) t =37.7 μs

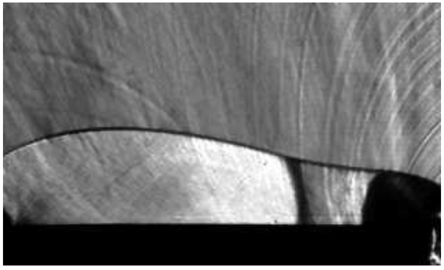

(e) t =57.7 μs

FIGURE 7.17: Schlieren photographs of a Mach 2.08, 125.5 mm radius converging cylindrical shock wave segment reflecting off a 50° wedge

Table 7.3: Summary of CFD simulations for converging cylindrical shock wave reflection

Radius at apex	Apex Mach number	Wedge angles
50 mm	1.24	15°, 30°, 45°, 60°
50 mm	1.69	15°, 30°, 45°, 60°
50 mm	2.13	15°, 30°, 45°, 60°
100 mm	1.24	15°, 25°, 30°, 35°, 40°, 45°, 50°, 55°, 60°
100 mm	1.46	15°, 25°, 30°, 35°, 40°, 45°, 50°, 55°, 60°
100 mm	1.69	15°, 25°, 30°, 35°, 40°, 45°, 50°, 55°, 60°
100 mm	1.91	15°, 25°, 30°, 35°, 40°, 45°, 50°, 55°, 60°
100 mm	2.13	15°, 25°, 30°, 35°, 40°, 45°, 50°, 55°, 60°
200 mm	1.24	30°, 35°, 40°, 45°, 50°, 55°, 60°
200 mm	1.46	30°, 35°, 40°, 45°, 50°, 55°, 60°
200 mm	1.69	30°, 35°, 40°, 45°, 50°, 55°, 60°
200 mm	1.91	30°, 35°, 40°, 45°, 50°, 55°, 60°
200 mm	2.13	30°, 35°, 40°, 45°, 50°, 55°, 60°
400 mm	1.24	15°, 30°, 45°, 60°
400 mm	1.69	15°, 30°, 45°, 60°
400 mm	2.13	15°, 30°, 45°, 60°

was inclined at the desired angle to the bottom wall, and the angle of convergence between the top and bottom walls was adjusted so that the angle between the top wall and the wedge would always be 90°. Because the flow was modelled as inviscid, the top wall could also be considered a symmetry plane. The radius of the inlet was set to 1.5 times the desired shock radius at the wedge apex, resulting in an inlet length of half the apex radius. Typical meshes used are shown in Figure 4.2 (a) and (b).

Figures 7.19 to 7.23 show contours of constant density at selected times for shock waves with a radius of 100 mm and Mach number of 1.46 at the wedge apex, for five different wedge angles. The initial shock wave is moving from left to right, and the images have been rotated so that the wedge surface is horizontal. The time is measured from the moment that the shock passes the wedge apex.

There are two phases in the reflection process. The first is the initial reflection phase, in which the initial cylindrical shock segment is propagating into undisturbed air. The second phase is the post-reflection behaviour, in which the reflected shock waves propagate back into the post-shock flow.

For the 15° wedge, the shock wave initially forms an MR with a weak shear layer. As the shock propagates, the shear layer strengthens, and the triple point of the MR begins to turn

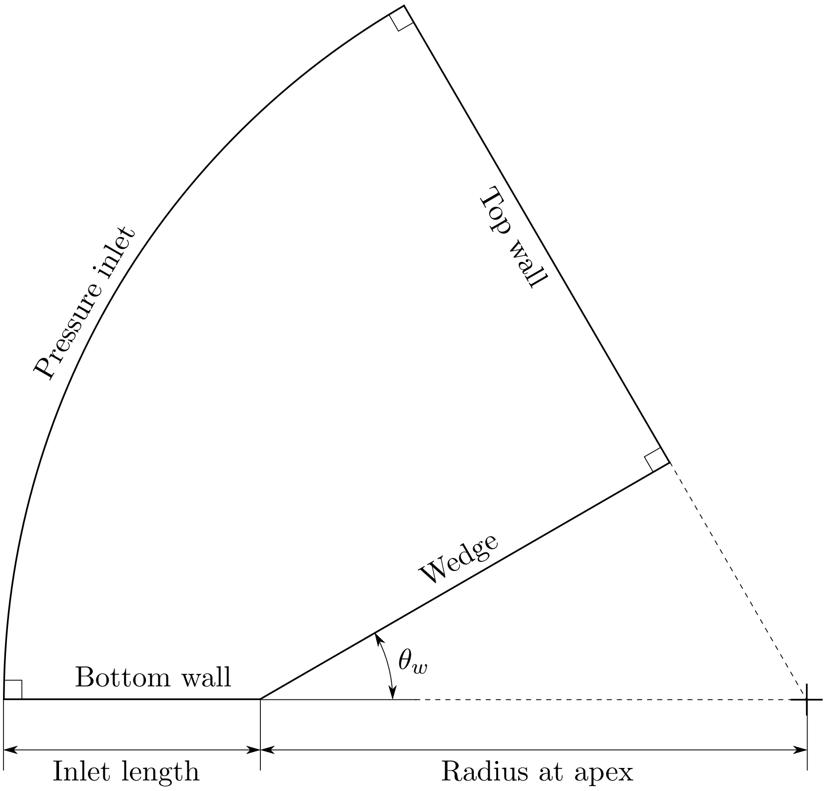

Figure 7.18: Domain for CFD simulations into reflection of converging cylindrical shock segments

back toward the wedge. The Mach stem is significantly tilted by the time the shock wave is halfway up the wedge. The triple point collides with the wedge about 134 μs after the shock passed the apex, and for a very brief time, a TRR is formed. Almost immediately after this, the incident shock reaches the end of the wedge.

At a wedge angle of 30°, the triple point remains close to the wedge, and transition to TRR occurs lower down the wedge than for the 15° wedge. For the 40° wedge, the Mach stem is extremely short, and the shear layer from the initial MR remains very close to the wall. Transition to TRR occurs approximately halfway up the wedge. The shear layer emanating from the triple point of the TRR is relatively weak.

No shear layers or Mach stems are visible in the results for the 50° and 60° wedges at Mach 1.46, although a barely discernible shear layer and Mach stem was present for the 50° wedge at higher Mach numbers. The absence of these features suggest that the reflection is initially regular, and remains regular throughout. The final reflected shock is a smooth curve with no discontinuities, as seen in Figure 7.23 (f).

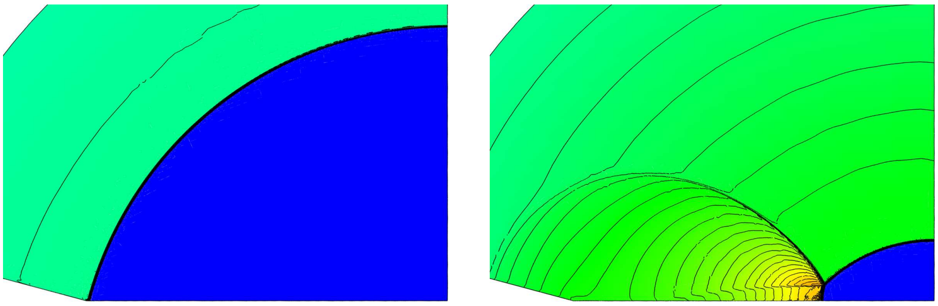

(a) t = 2 μs (d) t = 110 μs

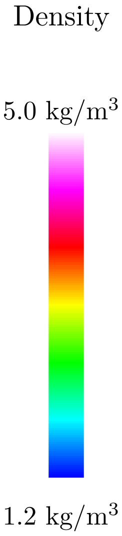

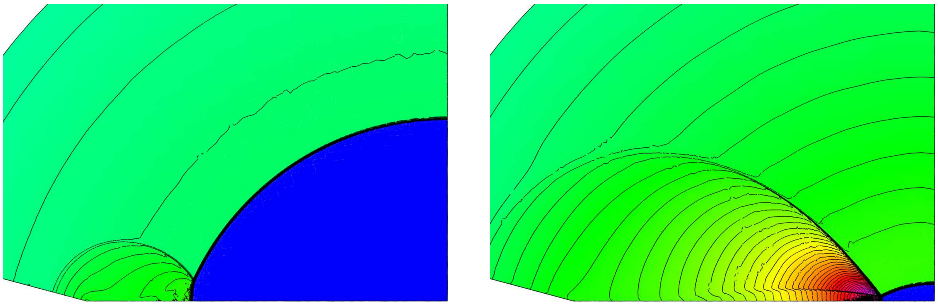

(b) t = 50 μs (e) t = 130 μs

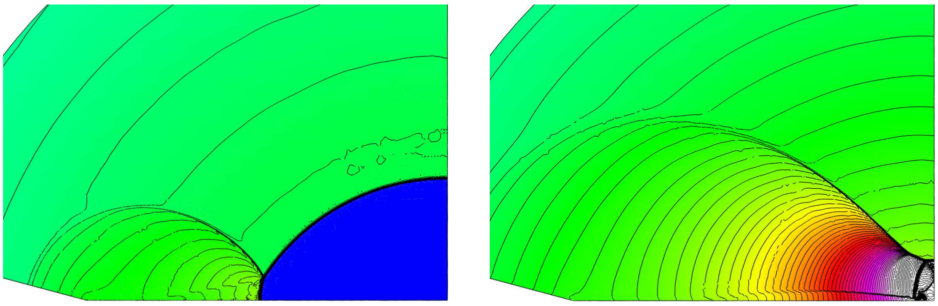

(c) t = 80 μs (f) t = 160 μs

FIGURE 7.19: Contours of constant density for a shock encountering a 15° wedge with a radius of 100 mm and Mach number of 1.46 at the apex. Note that the areas shaded white briefly exceed 5.0 kg/m^3, reaching a maximum of 8.7 kg/m^3 at t = 150 μs after passing the wedge apex

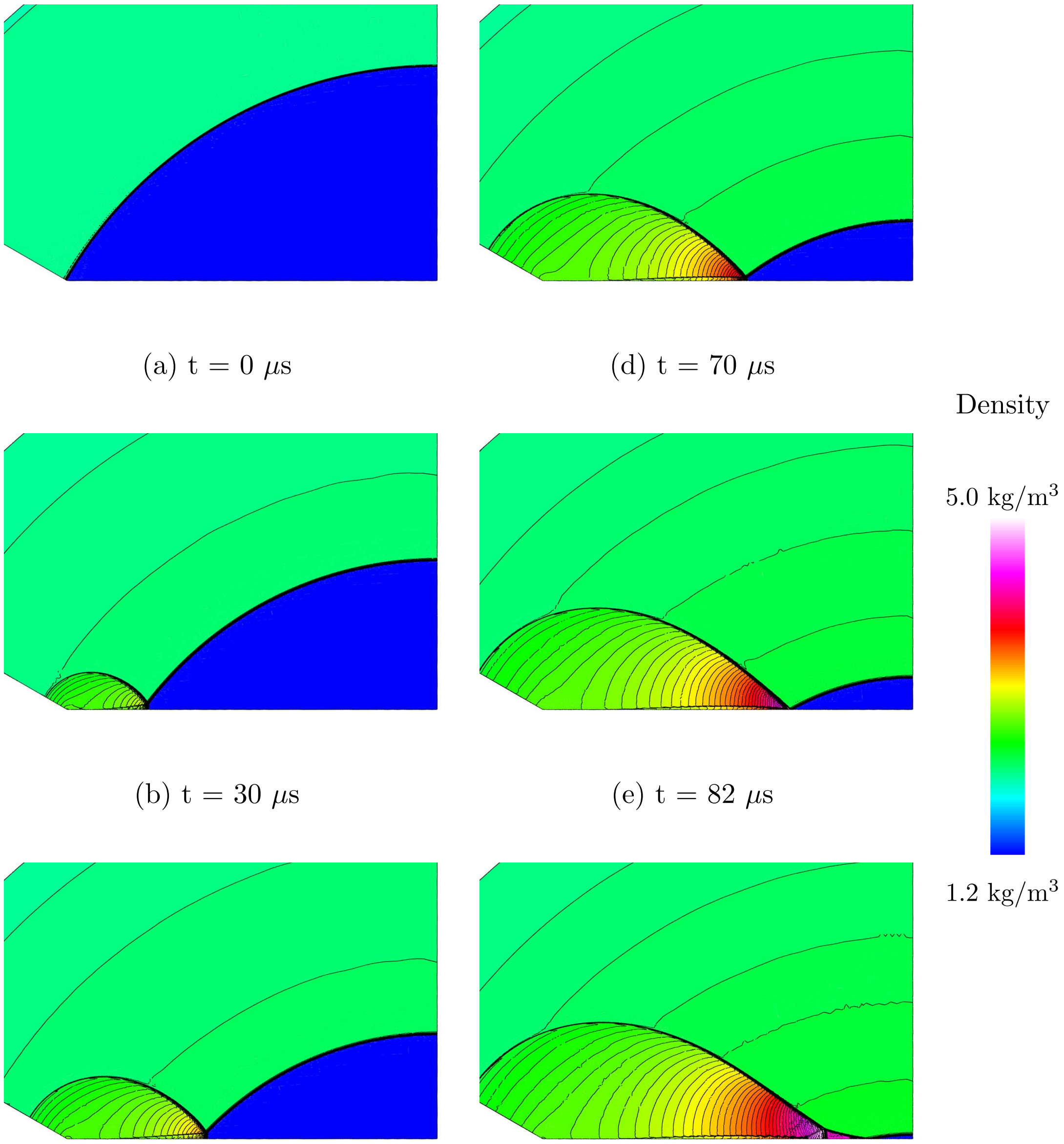

(a) t = 0 μs

(d) t = 70 μs

(b) t = 30 μs

(e) t = 82 μs

(c) t = 50 μs

(f) t = 94 μs

FIGURE 7.20: Contours of constant density for a shock encountering a 30° wedge with a radius of 100 mm and Mach number of 1.46 at the apex

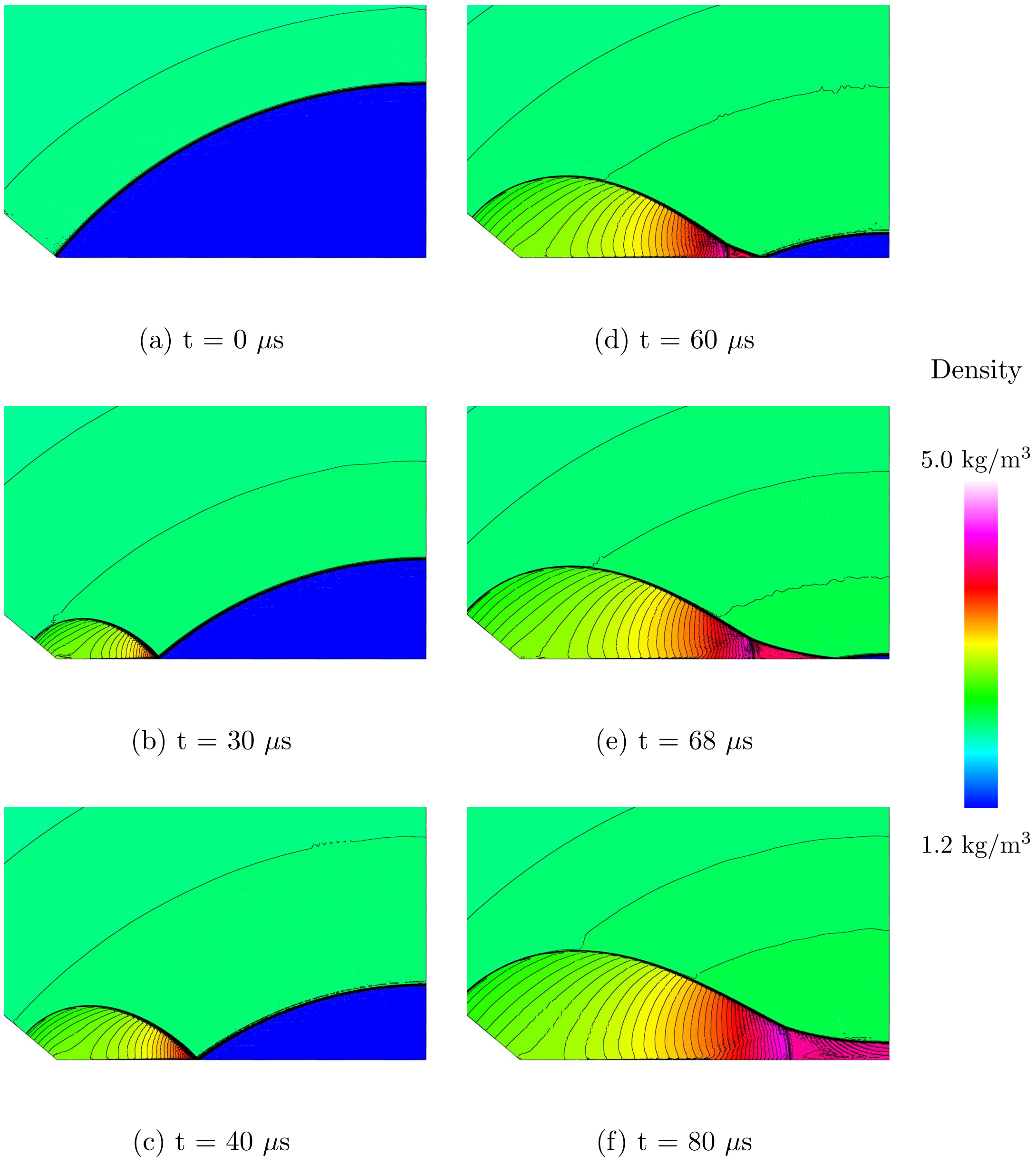

(a) t = 0 μs

(d) t = 60 μs

(b) t = 30 μs

(e) t = 68 μs

(c) t = 40 μs

(f) t = 80 μs

FIGURE 7.21: Contours of constant density for a shock encountering a 40° wedge with a radius of 100 mm and Mach number of 1.46 at the apex

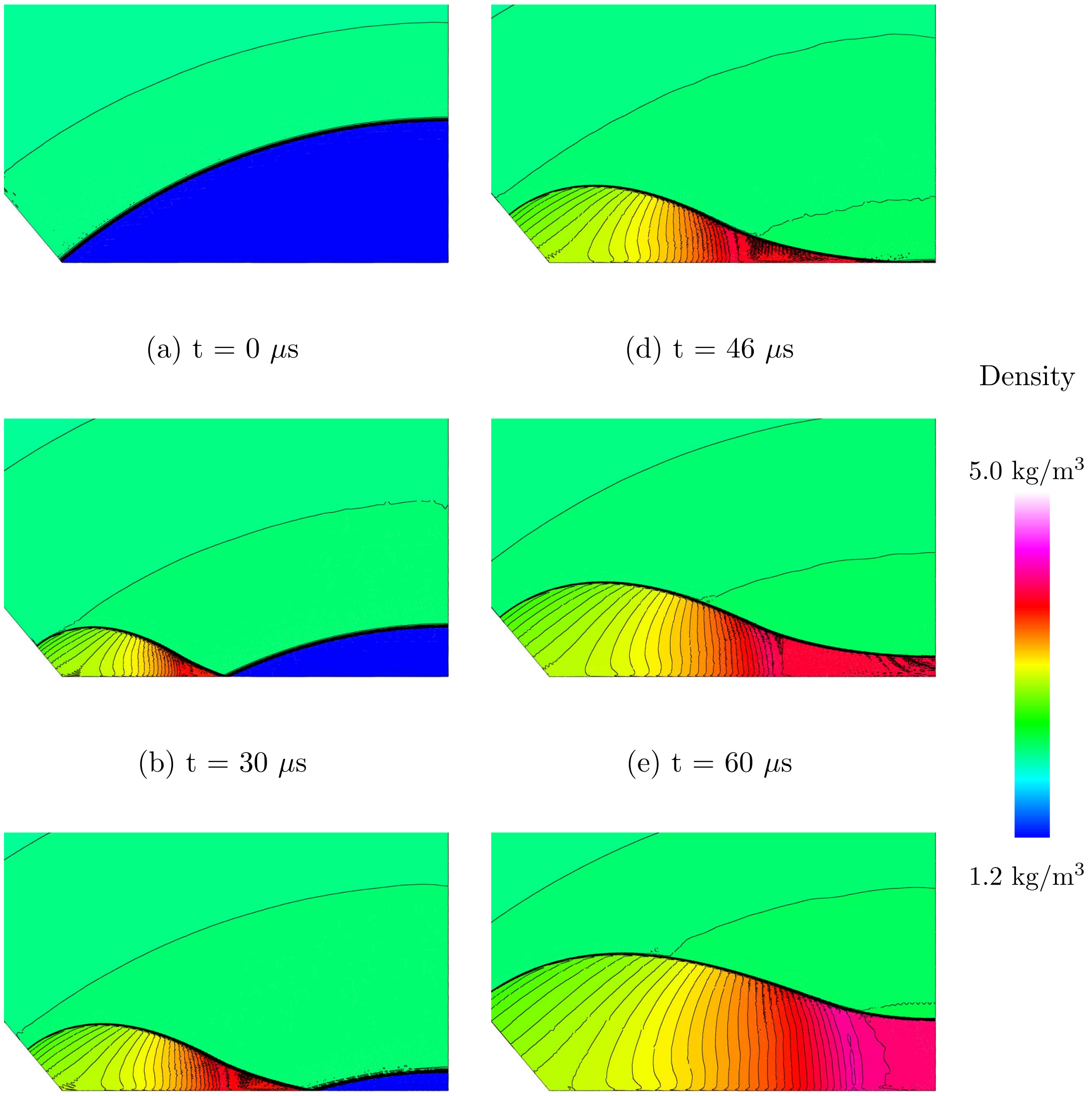

(a) t = 0 μs

(d) t = 46 μs

(b) t = 30 μs

(e) t = 60 μs

(c) t = 40 μs

(f) t = 80 μs

FIGURE 7.22: Contours of constant density for a shock encountering a 50° wedge with a radius of 100 mm and Mach number of 1.46 at the apex

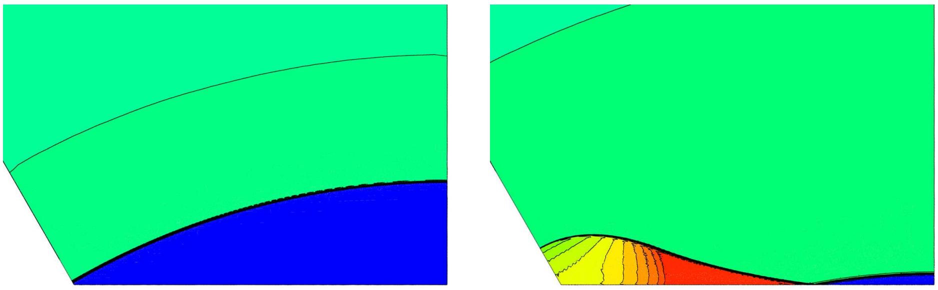

(a) t = 0 μs

(d) t = 24 μs

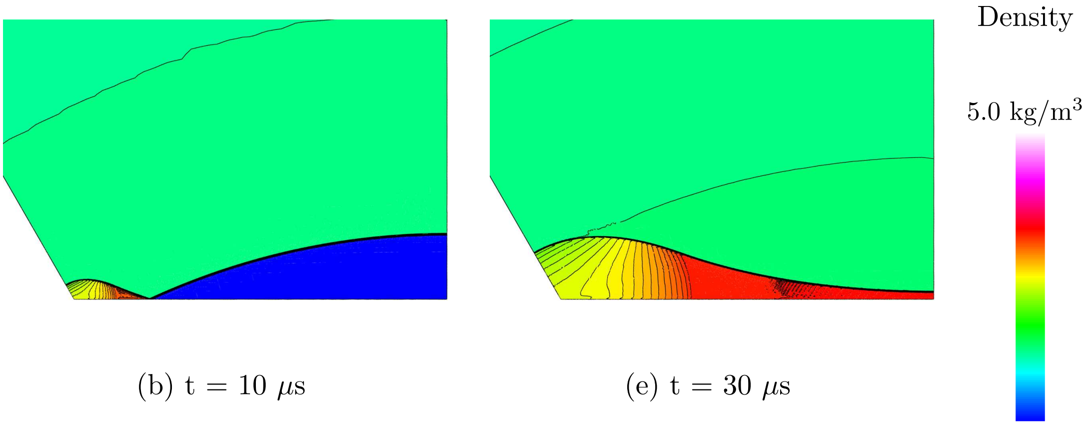

(b) t = 10 μs

(e) t = 30 μs

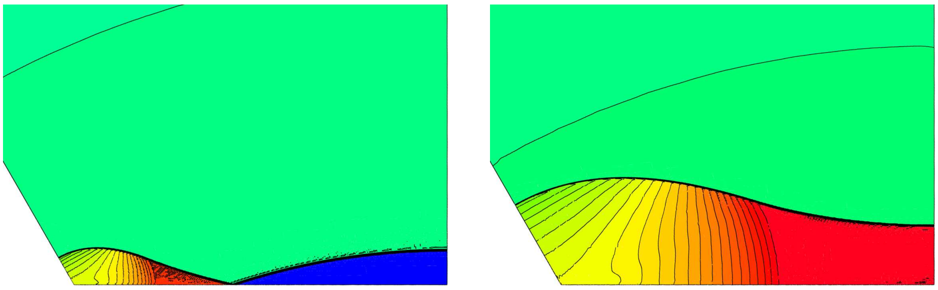

(c) t = 18 μs

(f) t = 50 μs

FIGURE 7.23: Contours of constant density for a shock encountering a 60° wedge with a radius of 100 mm and Mach number of 1.46 at the apex

7.5 Comparison and discussion

A range of results were obtained for the analytical, experimental and computational work described previously. These results will be compared and discussed in this section. This will include an assessment of the quality of the shock waves generated in the experiments, followed by discussions of the initial reflection configuration, transitions that occur along the wedge, the effect of the initial radius on the results, and a brief discussion of the post-reflection behaviour.

7.5.1 Assessment of experimental shock wave quality

Multiple frames of a single converging shock wave were captured using a Photron FASTCAM SA5 high speed camera operating at 42 000 frames per second and a schleiren optical system. This frame rate was reduced from the 100 000 fps used previously in order to obtain a higher resolution and wider field of view. The quality of the shock wave was assessed based on how well the shock wave maintained a cylindrical shape, and the quality of the post-shock flow.

Figure 7.24 shows a qualitative assessment of the shape of the converging cylindrical shock wave segment as it approaches the wedge. The red lines indicate the angle of the walls, and their intersection indicates the focal point of the shock wave. Although the facility was designed so that the centre of the shock would lie on the end of the upper wall (see Figure C.5 in Appendix C), it appears that the actual focal point lies slightly behind this. The reason for this is not clear, but it could indicate a possible slight misalignment of the walls. The green curves are circles centred on the focal point, superimposed over alternate shock positions. These circles adhere closely to the actual shock fronts, indicating that the shock wave is indeed close to circular.

A more quantitative assessment was also carried out. For each photograph, the radius of the shock was estimated by fitting circles to the visible portion of the shock front such that the sum of the squares of the errors for all photographs captured in a single test was minimised. The details of the method developed for this are given in Appendix E. The maximum deviation of any point on a shock front from its circle was less than 0.45 mm, which is equivalent to the uncertainty in the point's location.

Figure 7.25 shows the positions of the shock front for all frames in six tests, and the circles and centres that were fitted to the shock fronts. The geometric centre of the arc that forms the inlet is the point (100 mm, 0), which is marked with a + in the figures. This is the intended centre of the shock wave. The actual centre is marked with an x. For all 30 tests,

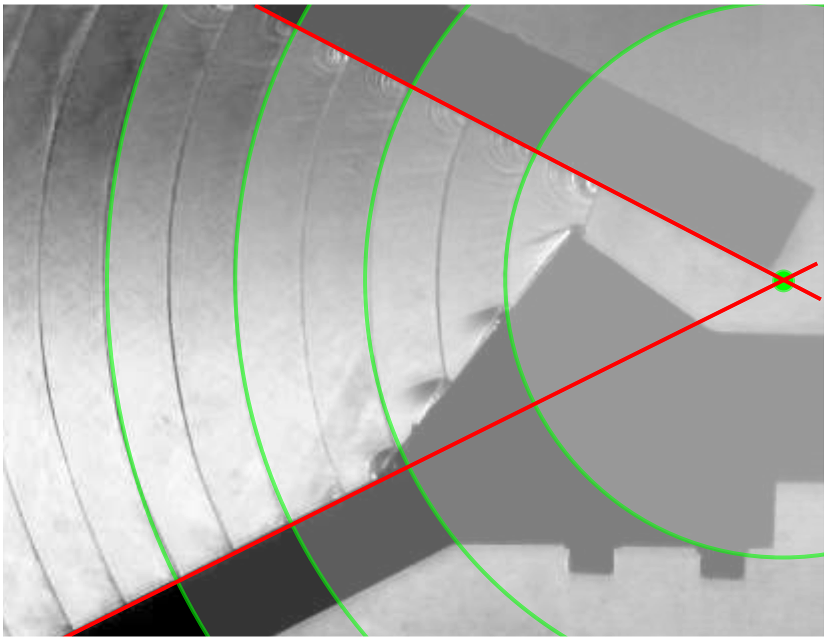

FIGURE 7.24: Successive frames of the same converging cylindrical shock wave segment captured by a high speed camera. The original planar shock entered the facility at Mach 1.37. The green curves are circles superimposed over alternate shock positions

the actual centre lay to the right and slightly below the intended centre. In addition, for every wedge angle tested, the actual centre lay closest to the intended centre for the weakest shocks. Once again, the reasons for this are not clear, but it supports the hypothesis that there may be a slight misalignment in the walls.

In many of the photographs obtained, perturbation waves are visible in the flow behind the shock waves. A large number of these perturbations were caused by a slight indent in the top wall that was incurred during the laser cutting process, and are seen emanating from a point near the top left corner of the photographs shown in Figure 7.11 (d) and (e). Other perturbation waves are visible in regions of the flow, particularly behind the reflected shock. These are generated by small imperfections in the walls of the facility and the gasket material lining the wedge, and appeared to have no noticeable effect on the behaviour of the shock wave.

The facility did show some sensitivity to small disturbances in the slit. For example, a small (approximately 20 mm wide) piece of diaphragm material caught in the slit was enough to cause the formation of a sharp corner in the shock front, and a pair of reflected shocks in the flow behind the shock front. This is in line with the unstable nature of converging cylindrical shocks, as first described by Perry and Kantrowitz (1951). This made it necessary to clear the facility of any diaphragm material before each test.

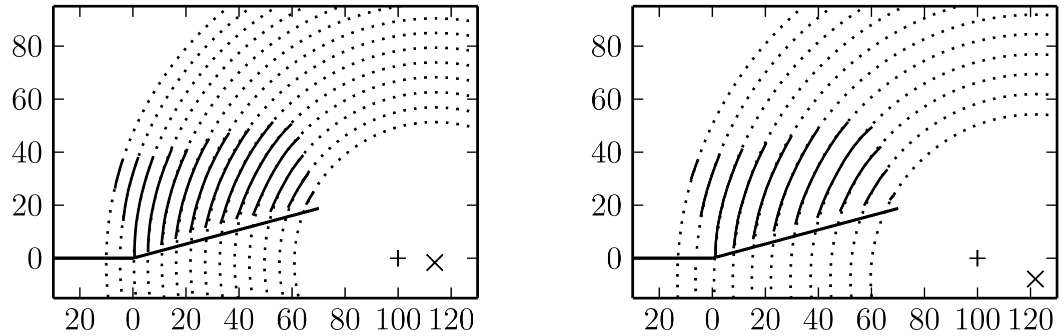

(a) Mach 1.52 shock, 15° wedge (b) Mach 2.03 shock, 15° wedge

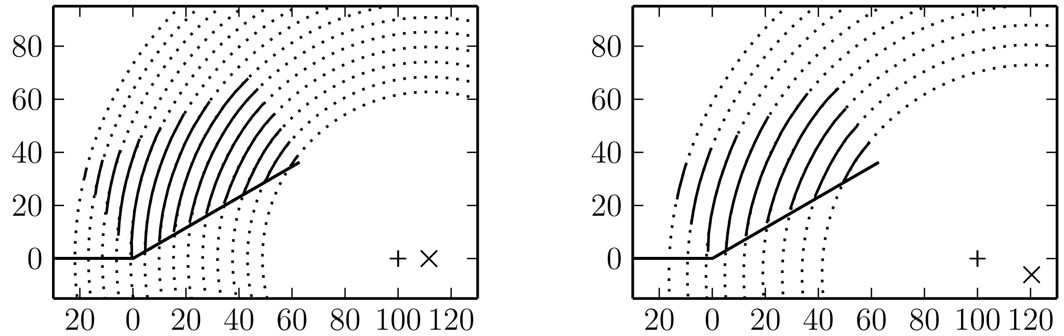

(c) Mach 1.55 shock, 30° wedge (d) Mach 2.05 shock, 30° wedge

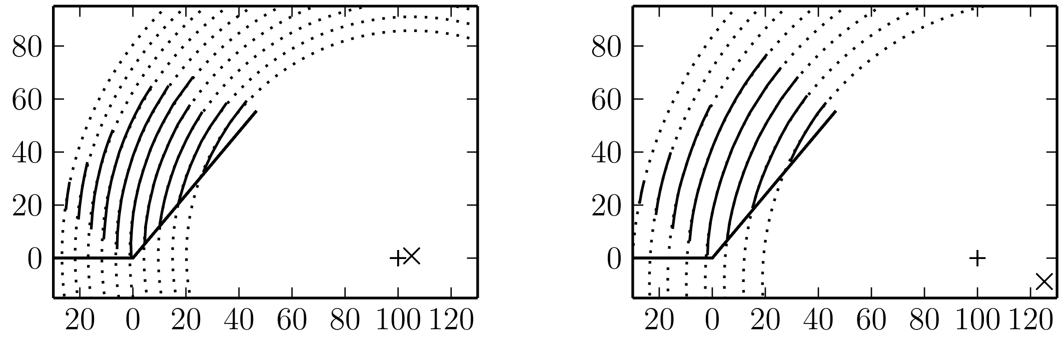

(e) Mach 1.53 shock, 50° wedge (f) Mach 2.08 shock, 50° wedge

FIGURE 7.25: Shock front locations captured from photographs for six tests (solid lines), with circles fitted using a least squares approximation (dotted lines). Dimensions are in millimetres. The geometric centre based on the wedge geometry is shown (+), together with the actual calculated centre (x) for comparison

The final point in assessing the shock quality was to compare the radii and Mach numbers obtained in the facility to those predicted by the CFD simulations. Figure 7.26 shows how these vary with time for a selection of tests. Since the Mach number of the shock in the facility could not be accurately predicted beforehand, there is a slight difference in the conditions between the CFD. Therefore, only cases for which there was close agreement for conditions at the apex are shown. Although the radius-time curve for the Mach 1.52 experiments is shown, the Mach number trend is not, as the relatively large difference in Mach number at the apex (approximately 4%) between the experiment and CFD results makes a direct comparison of Mach number meaningless. The method used to calculate the shock velocity for the experiments is described in Appendix E.

The curvature of the radius-time curves caused by the accelerating shock is difficult to resolve visually, but numerical differentiation of the results show that the Mach number of the shock wave increases with time, as shown in Figure 7.26 (b). In the interest of having a fixed reference Mach number for each test, the Mach number at the instant that the shock passes the wedge apex is taken as the reference Mach number. This is also taken as the time datum. It is important to note that numerical differentiation is sensitive to small uncertainties in the radius measurements, resulting in an amplification of the uncertainty in the Mach number.

Figure 7.27 shows the variation of the Mach number of the shock as it propagates along the wedge surface. The Mach number increases, but the slope of the trend decreases as the shock moves further away from the wedge apex. The Mach number approaches a maximum value, as predicted by equation (7.6).

7.5.2 Classification of reflection configurations

Several different reflection configurations were observed, and have already been described in this chapter. This section discusses the criteria by which these reflection configurations may be classified.

As with planar waves, if the reflected shock wave intersects the incident shock at some distance away from the wedge surface, then the reflection is a Mach reflection (MR). If the incident and reflected shocks intersect on the wedge surface, then the reflection is a regular reflection (RR).

As mentioned in section 2.4.1, an MR may be classified as either a direct Mach reflection (DiMR), or an inverse Mach reflection (IMR) based on whether the triple point trajectory angle (χ) is directed toward or away from the wedge surface. Although the Mach stem of an IMR for a planar shock wave is usually convex, this was not observed in the case of

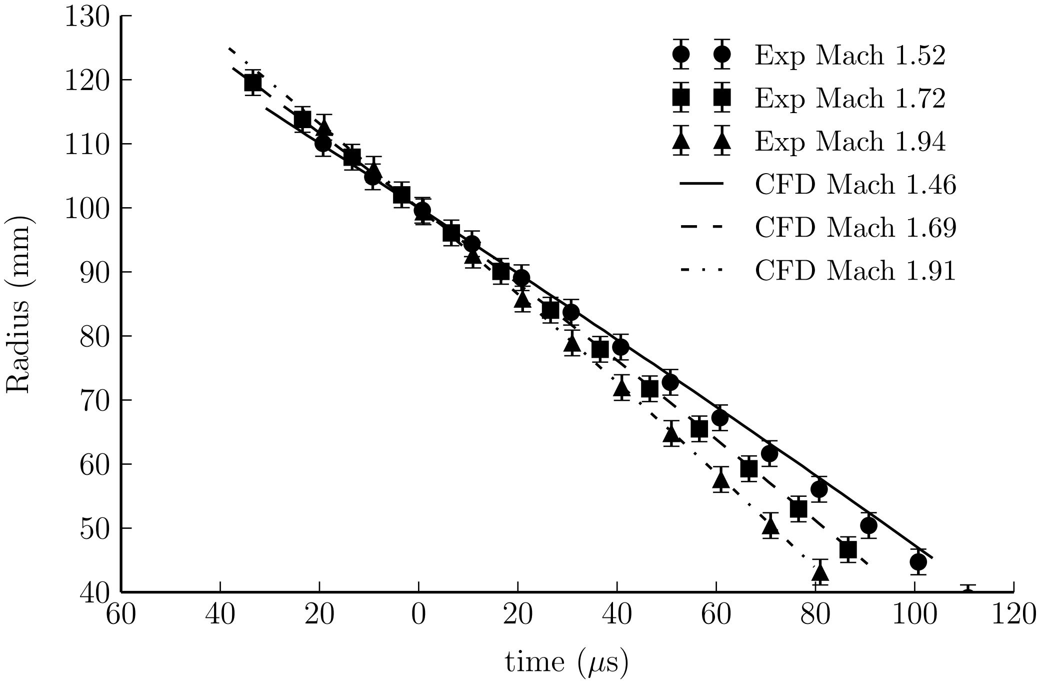

(a) Shock radius vs time

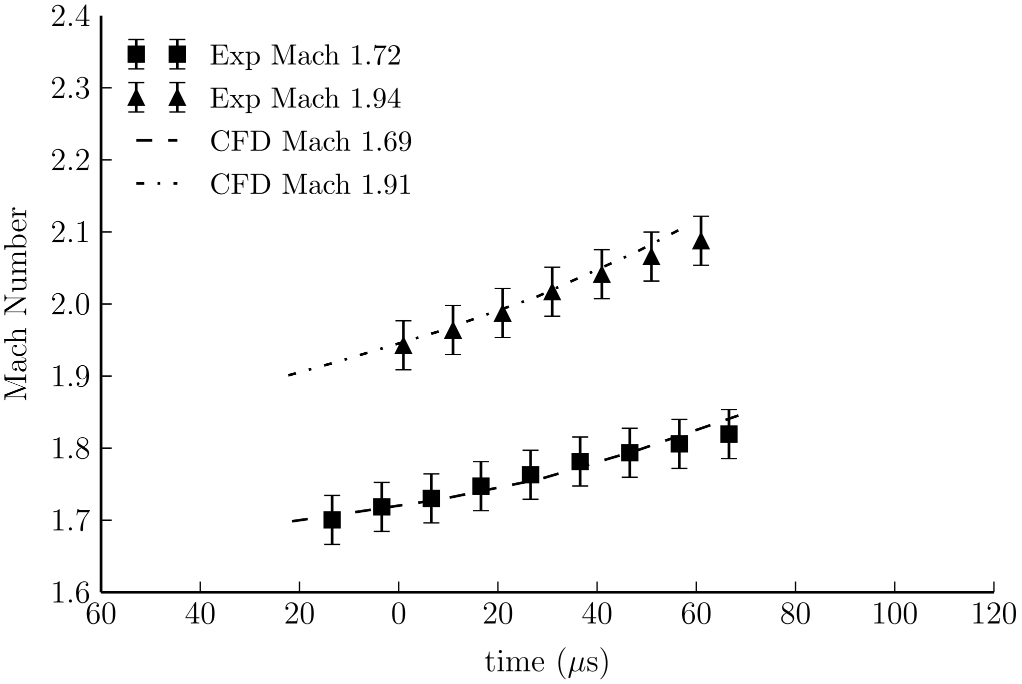

(b) Mach number vs time

FIGURE 7.26: Comparison of the variation of radius (a) and Mach number (b) with time for experimental and CFD results. The time datum is the point at which the shock has a radius of 100 mm, and the reference Mach number is the Mach number at that time

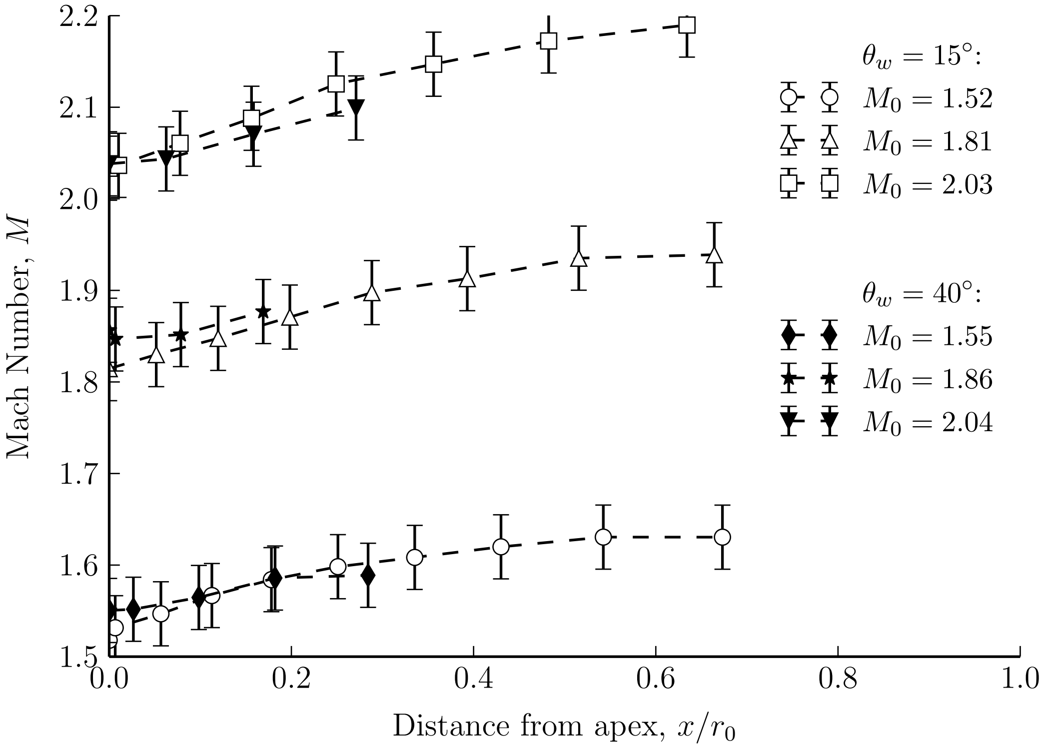

FIGURE 7.27: Variation of the incident shock Mach number with normalised distance along the surface of the wedge

the reflection of a converging cylindrical shock segment. Rather, the shear layer, which is concave for a DiMR, becomes convex, and the Mach stem gradually straightens. There is also an intermediate form, a stationary Mach reflection (StMR), for which the triple point trajectory is momentarily directed parallel to the wedge surface.

Regular reflections may also be further classified based on their history. RRs that are initiated at the wedge apex are distinctly different from those formed after the termination of an MR in that a residual shear layer and Mach stem are still present in the latter configuration. Therefore, RR configurations formed by termination of an MR are classified as transitioned regular reflections (TRRs).

A notable feature of RRs formed by converging cylindrical shock segments is that the reflected shock consists of a convex segment, in which the curvature is caused by the shape of the incident shock wave, and a concave segment, for which compressions generated by the corner govern the shape of the reflected shock. The point at which the curvature of the concave segment begins to reverse coincides with the furthest point reached by signals travelling at the local speed of sound from the wedge apex. In a TRR, the reversal of curvature is instantaneous, and is caused by a shock wave rather than the compressive signals.

Figure 7.28 shows schematic diagrams of these reflection configurations for a converging cylindrical shock wave segment of radius R_1 and incident angle of β, generated by a wedge inclined at an angle of θ_w.

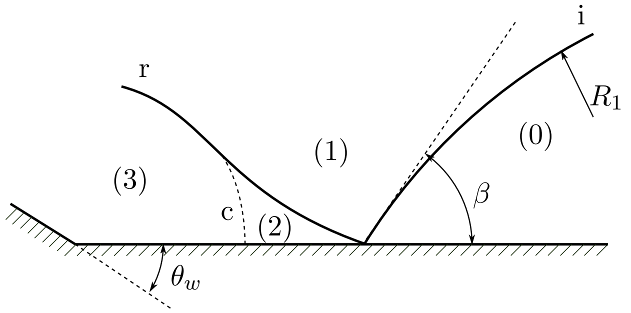

(a) Regular reflection

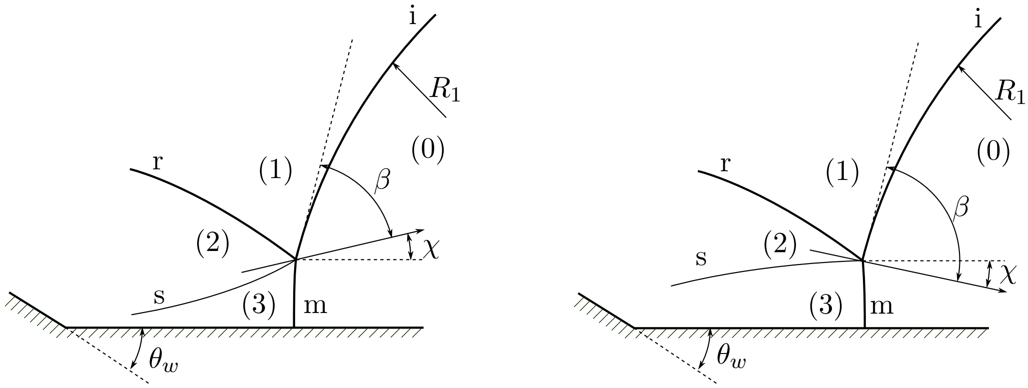

(b) Direct Mach reflection

(c) Inverse Mach reflection

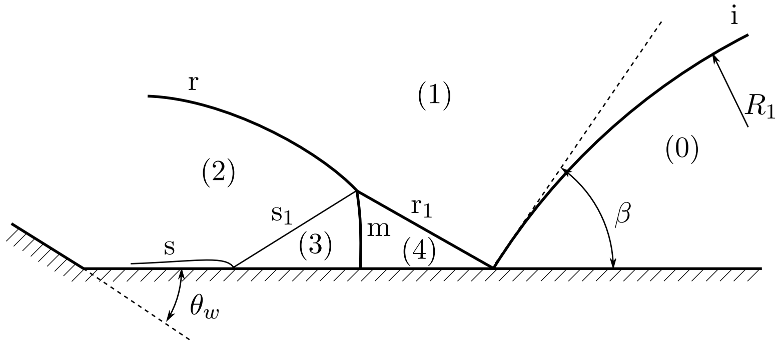

(d) Transitioned regular reflection

Figure 7.28: Schematic illustrations of the reflection configurations observed for converging cylindrical shock waves shock waves over a straight wedge. The labelled discontinuities are (i) incident shocks, (r) reflected shocks, (m) Mach stems, (s) shear layers, and (c) compression waves

7.5.3 Initial reflection configuration

For a planar shock wave encountering a wedge, the reflection configuration may be predicted from the Mach number and angle of incidence by applying the sonic condition. If one considers a cylindrical shock segment with a very large radius, one expects the initial behaviour to begin to resemble that of a planar shock wave. Therefore, for any shock wave that has travelled a distance up the wedge that is very small compared to the radius, yet still very large compared to the shock thickness, there is no reason to expect the reflection configuration to differ from that predicted by the sonic condition under the same conditions.

A shear layer will only form if the initial reflection is an MR, so the presence of a visible shear layer in the flow may be used to classify the initial reflection type. However, it is not always possible to resolve the shear layer of an MR close to transition. Because of this, the best classification that can be made using the current results is to group reflections as either an MR or an indeterminate reflection configuration which could be either an RR or a poorly resolved MR. These indeterminate reflections will be grouped together and referred to as "no visible shear layer" (NVSL) reflections.

Figure 7.29 shows the Mach number and wedge angle for each case in the experimental and CFD results, and indicates whether or not a shear layer was visible. These are compared to the sonic condition. For planar shock waves, one expects MR to occur for conditions lying below the sonic condition curve, and RR to occur for conditions above it.

For all cases lying inside the RR domain for planar shock waves, no shear layers were observed. There were some cases that fell within the MR domain for which there was no visible shear layer, but this does not necessarily mean that these reflections are RR. It could simply mean that the shear layers were too weak to be resolved.

From this, it appears as though the sonic condition does predict the initial reflection configuration for converging cylindrical shock wave segments as well as planar shock waves. However, further investigation is necessary to confirm this.

7.5.4 Mach reflection triple point trajectories and transition

If the initial reflection was regular, then it remained regular throughout the reflection process. However, if the initial reflection was an MR, then transition to TRR occurred at some point along the wedge. The shape and behaviour of the MR before transition to TRR are discussed in this section.

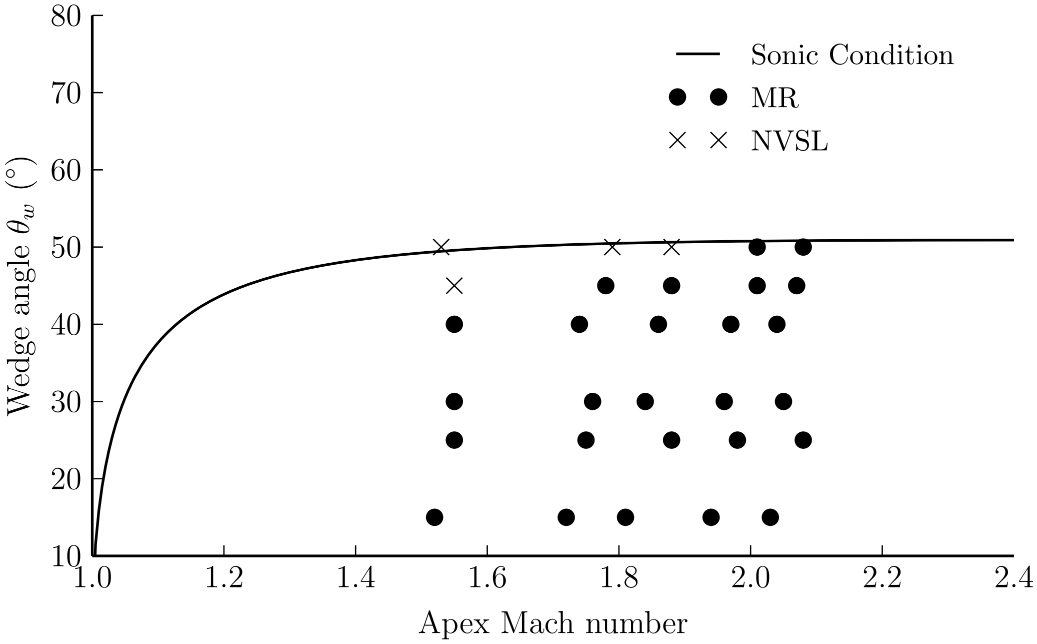

(a) Experimental results

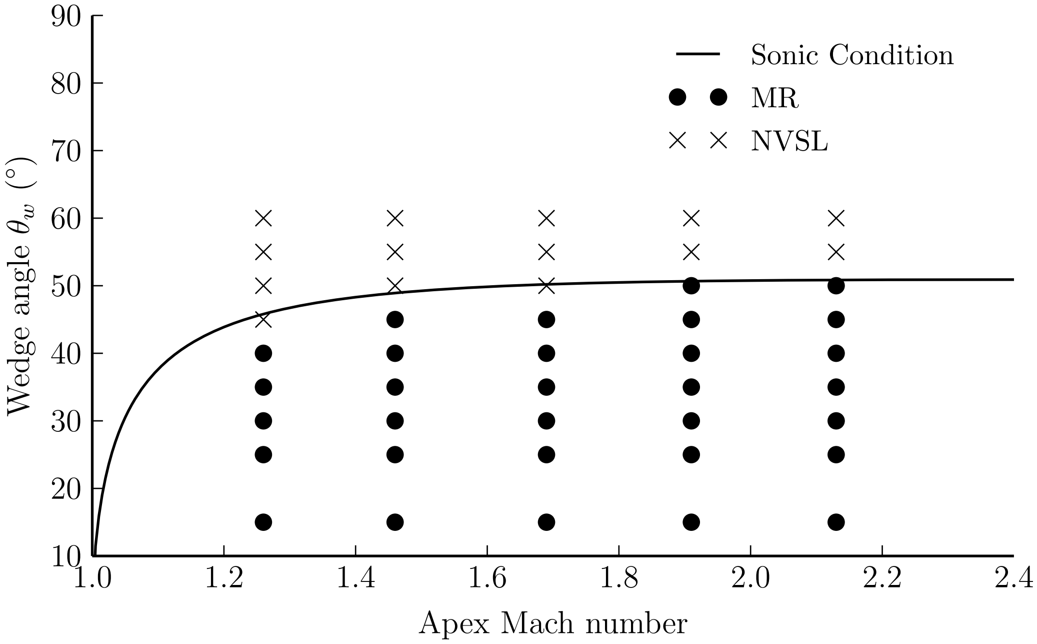

(b) CFD results

FIGURE 7.29: Observed reflection configuration at the wedge apex, classified as either a Mach reflection (MR) or "no visible shear layer" (NVSL)

For those reflections with a visible shear layer, the location of the triple point in the experimental and CFD results was tracked. Figure 7.30 shows the measured triple points for three wedge angles, together with the triple point trajectories predicted by the theoretical model described in section 7.2.

For wedge angles of 30° and below, the initial angle of the triple point trajectory agreed closely with the angles observed for planar shock waves (as in Figure 2.3) for both the CFD and experimental results. The approximate shape of the triple point trajectory in the experiments is captured well by the model, as is the maximum Mach stem height. The transition point predicted by the model for the 30° wedge lies within 5% of the transition point observed in the experiments. For the 15° wedge, however, the end of the model was reached before transition to TRR took place.

The triple point trajectories in the CFD results lie significantly higher than those of the theoretical or experimental results. For the 15° wedge, the disagreement in Mach stem height is approximately 20%, and increases to 60% for the 30° wedge. As a result, the height of the Mach stem reaches a maximum later, and transition to TRR takes place much higher up the wedge than observed in experiments. One possible reason for this could be that the resolution of the CFD was not sufficient to accurately model the flow in the immediate vicinity of the triple point. Because of this, care should be taken when taking quantitative measurements from the CFD results. Qualitatively, however, the general shape of the triple point trajectory measured in the CFD resembles that of the experiments and theoretical model.

For the 40° wedge, the triple point remains very close to the surface, as may be seen in Figures 7.14, 7.15, and 7.21. In the experimental results, this led to the uncertainty in the measured Mach stem height being larger than the Mach stem height itself in some cases.

The trajectory predicted by the theoretical model appears to lie above the actual observed transition point at this angle, and the model overestimates the transition point by between 10% and 20%. For the 45° wedge, the presence of a shear layer in the flow suggests that the initial reflection was an MR, but it is not possible to discern the height of the Mach stem due to the resolution of the results. No comparison with the theoretical model was made for this angle. This is because the model, being based on Whitham's ray-shock theory, predicts a triple point trajectory for all wedge angles, even those for which the initial reflection falls within the RR domain. Therefore, the theory is not applicable for large wedge angles that lie in or close to the RR domain.

The theoretical model made the assumption that the Mach stem would remain straight and perpendicular to the wedge throughout the reflection process. However, the Mach stems

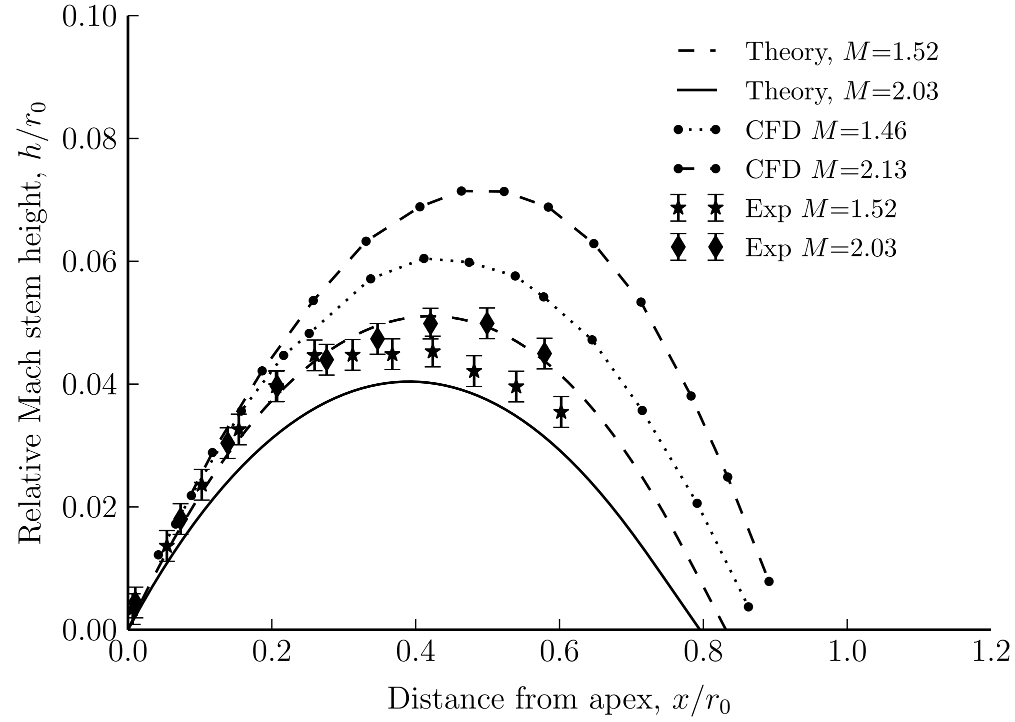

(a) 15° wedge

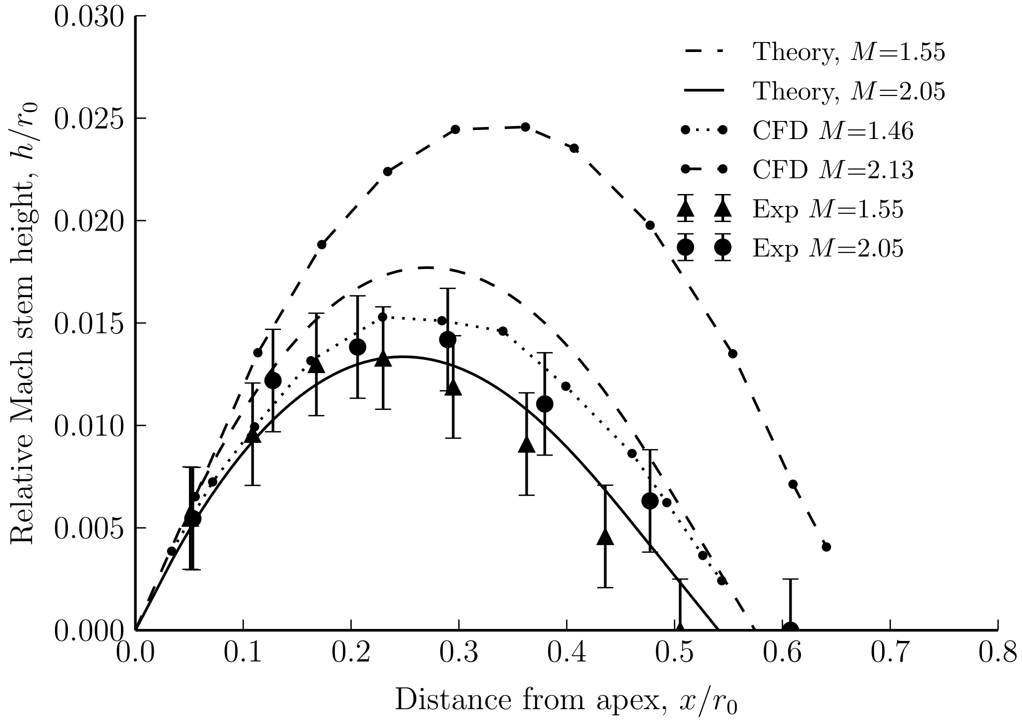

(b) 30° wedge

FIGURE 7.30: Predicted trajectories of the triple points for three different Mach numbers and wedge angles

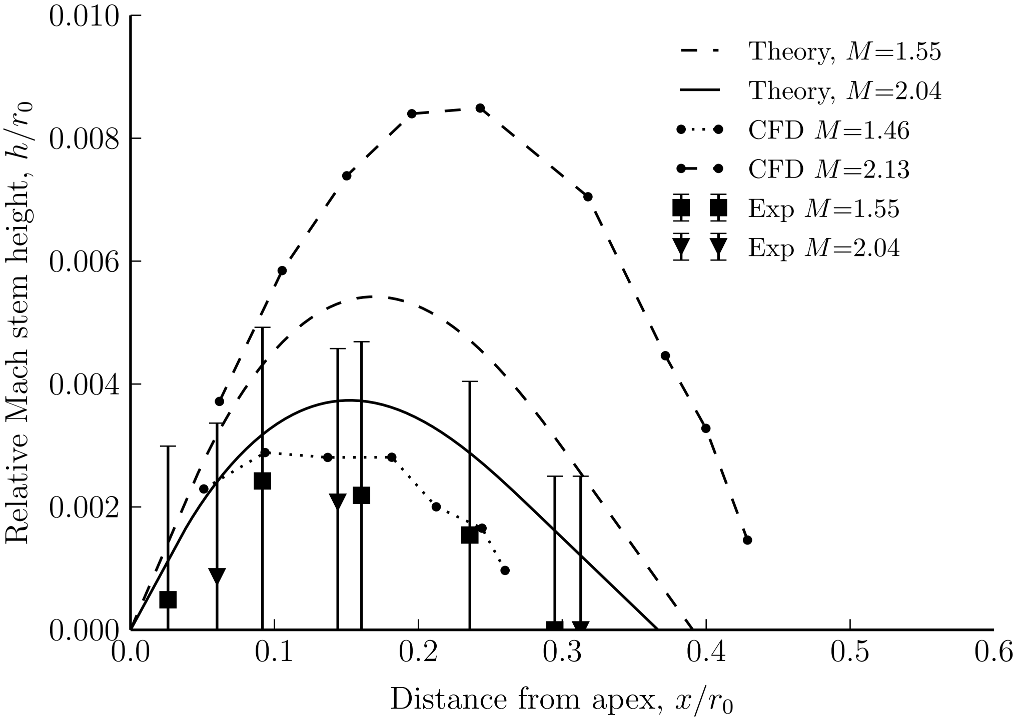

(c) 40° wedge

FIGURE 7.30: *(cont.)* Predicted trajectories of the triple points for three different Mach numbers and wedge angles

observed did begin to tilt forward, particularly as transition was approached. This tilting is clearly visible in Figure 7.10(c) and (d).

7.5.5 Effect of initial radius

When a planar shock wave propagating into stationary air encounters a straight inclined wedge, the reflection pattern is largely independent of the size of the wedge, since there is no way for information from the end of the wedge ahead of the shock wave to reach the flow behind the shock wave. As a result, the reflection pattern that forms remains self-similar, and the scale of the reflection pattern varies linearly with time.

It has already been established that the reflection pattern formed when a converging cylindrical shock segment encounters a straight wedge does not remain self-similar with time. Instead, it varies as the shock wave propagates along the wedge. However, it has not yet been established whether the shape of the reflection depends on the initial radius of the shock wave.

The theoretical models developed in sections 7.2 and 7.1 predict that the shock wave behaviour will depend only on the ratio of the current shock radius to the radius at the apex, and not on the actual values of these radii.

Although only a single radius was tested in the experiments, CFD simulations were carried out at various angles for 50 mm, 100 mm, 200 mm, and 400 mm radii at the wedge apex. Contours of constant density are shown for two times for each of these radii in Figure 7.31.

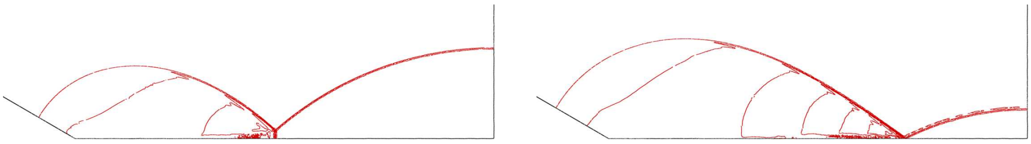

(a) $r_0 = 50$ mm, $t = 70$ μs

(b) $r_0 = 50$ mm, $t = 80$ μs

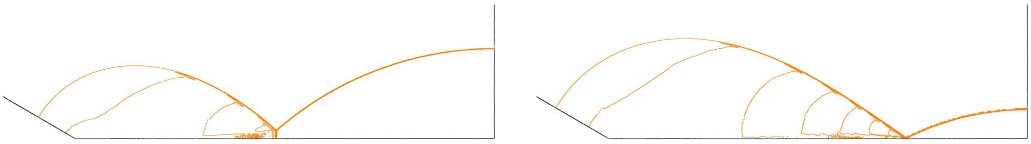

(c) $r_0 = 100$ mm, $t = 140$ μs

(d) $r_0 = 100$ mm, $t = 160$ μs

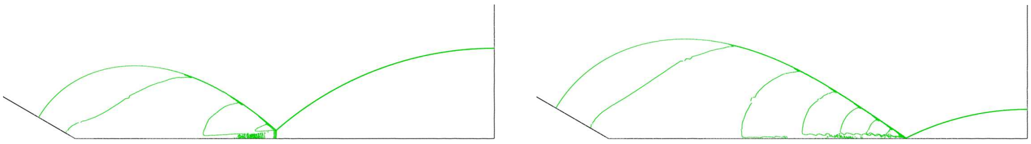

(e) $r_0 = 200$ mm, $t = 280$ μs

(f) $r_0 = 200$ mm, $t = 320$ μs

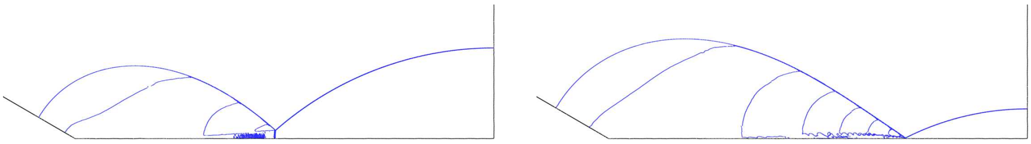

(g) $r_0 = 400$ mm, $t = 560$ μs

(h) $r_0 = 400$ mm, $t = 640$ μs

FIGURE 7.31: Comparison of contours of constant density for a shock encountering a 30° wedge with a Mach number at the apex of 1.69, for various initial radii

The results for the different radii are almost identical, not only in terms of the shock wave positions and angles, but even in terms of the exact location of density contours. This was true for all combinations of apex Mach number and wedge angles simulated. However, the simulations were carried out using an inviscid model, and incorporation of a viscous model may introduce some degree of scale dependence.

In addition, experiments involving a range of apex radii should be carried out under a range of conditions in order to evaluate whether or not the radius at the apex has any effect on the resulting triple point trajectory, or the MR→TRR transition point.

7.5.6 Post-reflection behaviour

Figures 7.32 to 7.35 show contours of constant density from the CFD results for times after the original shock wave is completely reflected by the wedge. Note that the images have been rotated from the position shown in Figure 7.18 so that the wedge lies horizontal and the top wall is the vertical edge on the right of each image.

The flow pattern formed after the reflection of the incident shock off the 60° wedge is shown in Figure 7.32. Since the initial reflection was regular, a single shock wave is present, and there are no curvature discontinuities along the shock front. There are, however, two distinct regions behind this shock. In the first region, the pressure varies as pressure waves generated at the corner travelling at the local speed of sound pass through the flow. The shock wave in this region is convex. The flow in the second region contains flow which the corner signals have not yet reached. The pressure in this region is approximately constant, and the shock wave in this region is concave.

After some time, the corner signals are reflected off the top wall, resulting in compression waves which travel from right to left. The manner in which the concave portion of the shock wave accelerates relative to the convex segment causes the shock to begin to bulge outward. The compression waves begin to collect, forming a sharp “kink” in the shock front. The compressions will eventually form a reflected shock wave, and the bowed shock segment at the top wall will become the Mach stem of an MR. This bears striking similarity to the behaviour of a planar shock reflected from a cavity, as observed by Sturtevant and Kulkarny (1976). In particular, it is remarkably similar to the behaviour shown in Figure 2.11 (d).

For the 40° wedge, a TRR is formed. Therefore, the corner signals are trapped behind the Mach stem, which travels from left to right in Figure 7.33 (a). Ahead of the Mach stem, there is a region of uniform pressure for which the shock front is concave, and behind the Mach stem, the shock is convex and the pressure varies. This Mach stem is reflected off the top wall, producing a region of very high pressure, as seen in Figure 7.33 (b). The pressure in this region dissipates as the shock continues to propagate.

Similar behaviour is observed for the 30° wedge, although the shear layer is more prominent in the high pressure region. This shear layer interacts with the top wall, and eventually meets

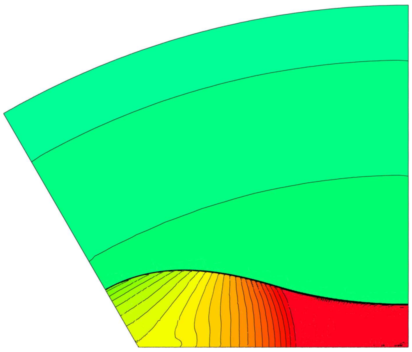

(a) t = 50 μs

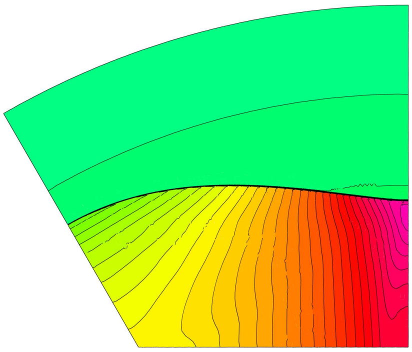

(b) t = 100 μs

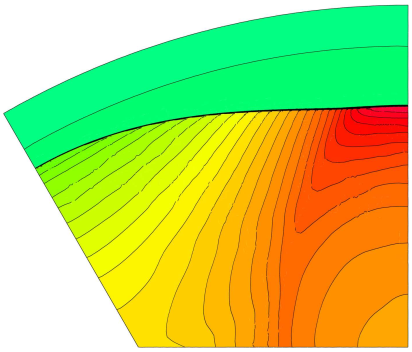

(c) t = 140 μs

FIGURE 7.32: Contours of constant density for a the post-reflection behaviour of a shock wave after encountering a 60° wedge with a radius of 100 mm and Mach number of 1.46 at the apex

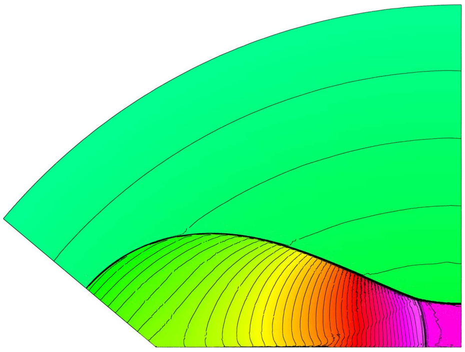

(a) t = 100 μs

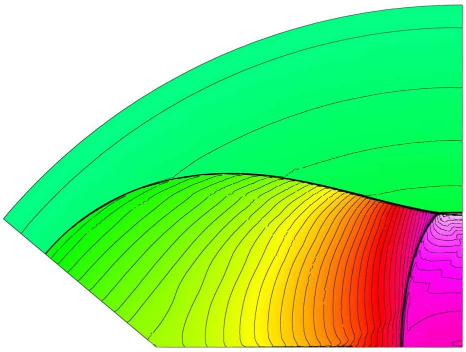

(b) t = 150 μs

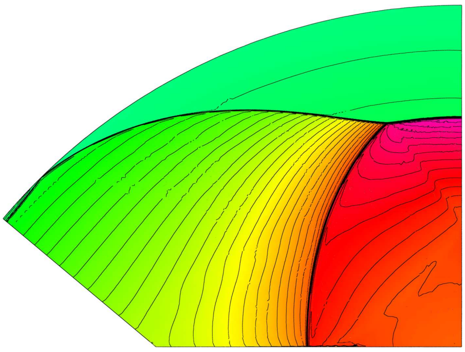

(c) t = 200 μs

FIGURE 7.33: Contours of constant density for a the post-reflection behaviour of a shock wave after encountering a 40° wedge with a radius of 100 mm and Mach number of 1.46 at the apex

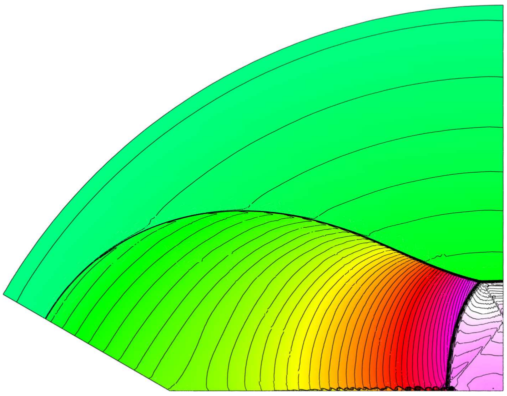

(a) t = 160 μs

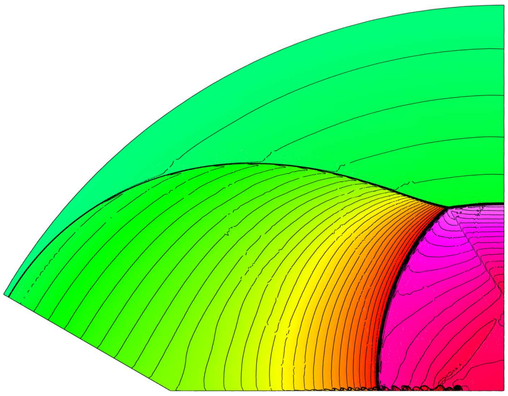

(b) t = 200 μs

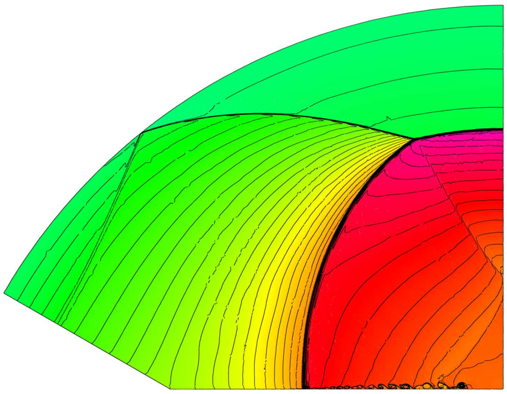

(c) t = 240 μs

FIGURE 7.34: Contours of constant density for a the post-reflection behaviour of a shock wave after encountering a 30° wedge with a radius of 100 mm and Mach number of 1.46 at the apex

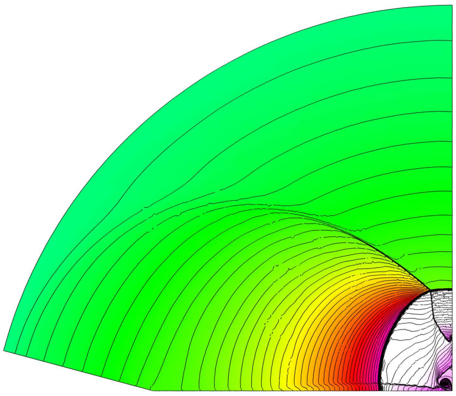

(a) t = 200 μs

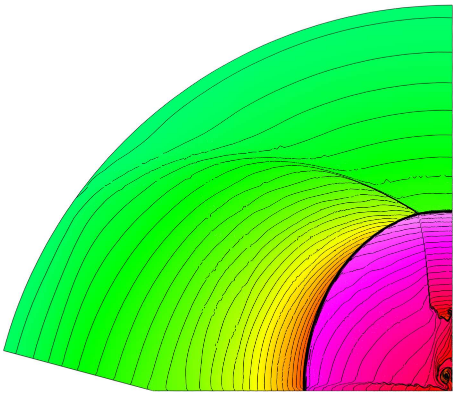

(b) t = 250 μs

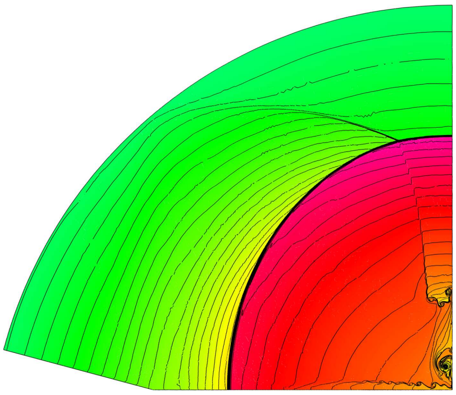

(c) t = 300 μs

FIGURE 7.35: Contours of constant density for a the post-reflection behaviour of a shock wave after encountering a 15° wedge with a radius of 100 mm and Mach number of 1.46 at the apex

the remnants of the original shear layer near the wedge surface, which has decayed into a mature Kelvin-Helmholtz instability, as seen in Figure 7.34 (b) and (c).

The shear layer formed in the reflection of the 15° wedge behaves quite differently. The reflection of the TRR Mach stem off the top wall generates sufficiently high pressures that a portion of the shock front propagates at velocities that are supersonic relative to the velocity of the flow behind it. Both the upper and lower potions of the shear layer begin to wrap up into a vortices. Figure 7.36 shows some of the features that are present in the high pressure region. Over time, the primary reflected shock weakens, and the reflected Mach stem and the new Mach stem approach a single expanding cylindrical shock front.

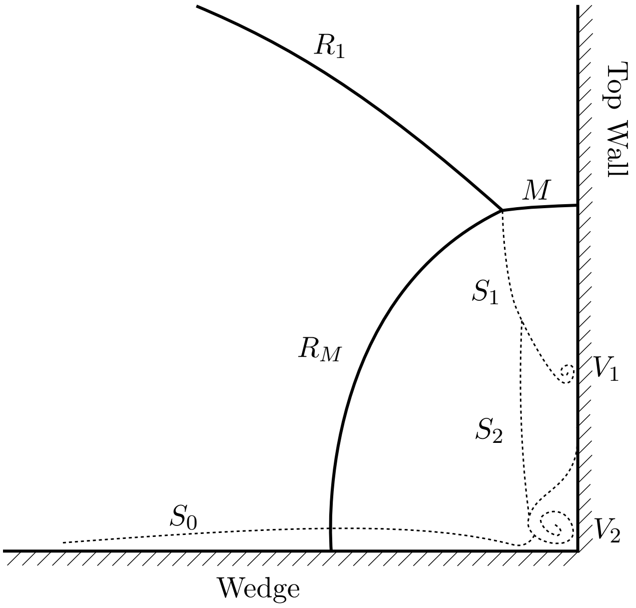

R_1	Primary reflected shock
R_M	Reflected Mach stem
M	New Mach stem
S_0	Original shear layer
S_1	Upper shear layer
S_2	Lower shear layer
V_1	Upper vortex
V_2	Lower vortex

FIGURE 7.36: Schematic diagram of the vortex structures formed behind the reflected Mach stem at low wedge angles

8. Conclusions and Recommendations

A facility that is capable of producing shock waves of arbitrary profile in a controllable and repeatable manner was designed, manufactured, and installed onto an existing shock tube. The facility was used in conjunction with CFD simulations to study the propagation of arbitrarily-shaped shock waves, and the reflection of converging cylindrical shock wave segments. The conclusions drawn from these studies are summarised in this chapter, followed by recommendations for future work.

8.1 Propagation of arbitrarily-shaped shock waves

A brief CFD study looked at the propagation of four shock wave shapes, each consisting of a concave cylindrical arc spanning a set angle, placed between two straight shock segments. Although a concave cylindrical shock segment on its own decreases in radius, it was found that the presence of the straight segments caused the radius to increase along the majority of the shock front. The decrease in radius was limited to the two points at which the straight and curved segments were joined. Over time, a series of compressive waves built up behind these two points, eventually resulting in the formation of a pair of reflected shocks behind the shock front.

The propagation of shock waves consisting of both concave and convex segments was then studied numerically and experimentally. Two profiles were tested — the first consisting of two 90° arcs, one concave and one convex, arranged in an S-shape between a pair of straight segments. The second profile was obtained by replacing the two arcs with sharp 90° corners.

Several difficulties were encountered when modelling the sharp convex corner in the simulations. There is a singularity at the corner which produced numerical artefacts, and in many cases caused the calculation to diverge. This was overcome by using a relatively fine initial mesh, and a very small time step at the beginning of the simulation.

There was excellent agreement for the upper triple point locations obtained in the CFD and experiments at Mach 1.4, but there was a slight discrepancy for the Mach 1.2 shock waves. This may have been caused by the fact that three-dimensional effects from the slit remain significant for longer at the lower Mach numbers. It was noted that the shock appeared to originate at some point inside the slit, rather than at the leading or trailing edge.

For both profiles, the concave segment produced a pair of Mach reflections, and the convex segment expanded, deflecting the triple point of the lower Mach reflection downward, and bringing the Mach stem toward a vertical orientation. Over time, the differences between the two profiles diminished, and both began to tend toward a planar shape.

8.2 Reflection of converging cylindrical shock segments

The behaviour of converging cylindrical shock wave segments encountering a straight wedge inclined at various angles was investigated. Experiments were carried out for shock wave segments with apex radii between 105 mm and 128 mm, apex Mach numbers between 1.52 and 2.08, and wedge angles between 15° and 50°, and schlieren photographs were captured using both single shot and high speed photography. Numerical simulations for apex radii between 50 mm and 400 mm, apex Mach numbers between 1.26 and 2.13, and wedge angles between 15° and 60°.

The sonic condition for planar shock waves appeared to be a reasonable predictor of the initial reflection configuration for the cylindrical shock wave segments. Although there were some reflections in the MR domain that did not have any visible shear layer in both the experimental and numerical results, this may simply be because the shear layer was too weak to resolve.

Those reflections that were initially MR eventually transitioned to TRR at some point along the wedge. A simple method for predicting the triple point trajectory and transition point was developed.

Varying the inital radius had no effect on the resulting reflection in both the theoretical analysis and the CFD. However, this has not yet been tested experimentally, and it is possible that some dependence on the initial radius may be introduced through viscous effects.

8.3 Recommendations for future work

This research has not been exhaustive by any means, and there remains plenty of room for further work in all of fields studied. Some recommendations for improvements to the current work and possible directions for future work are given below.

8.3.1 Facility design

Several improvements may be made to the design of the facility, both to improve its performance, and to expand its capabilities. Some of these are listed here.

- In some of the tests involving converging cylindrical shock wave segments, the very high pressures produced by shock focusing mechanisms caused the walls of the propagation chamber to flex very slightly, allowing a tiny amount of air to leak past the gasket. Although this leakage only occurred after the times of interest in the research for this thesis, it may have a significant effect on studies involving later times after the focus. This problem could be eliminated by reinforcing the walls of the facility.
- Keeping the facility clean and free of trapped diaphragm proved challenging. On at least two occasions, the facility needed to be disassembled in order to removed pieces of diaphragm material that could not be dislodged using compressed air. A diaphragmless driver would help alleviate this issue.
- One way in which higher Mach numbers could be reached would be to modify the end of the facility so that it may be sealed. This would be relatively easy to achieve, and would allow the driven section of the shock tube to be evacuated using a vacuum pump before each test. This would also allow the testing of gases other than air.
- Mounting one of the back outer plate on hinges would make it easier to open the facility. This would allow models to be changed in less time, and make it easier to keep the windows and test section clean.

8.3.2 Curved shock wave propagation

The study into shock wave propagation only investigated a limited range of shock wave profiles, and only two of these were tested experimentally. Suggestions for future work include the following.

- An experimental investigation into the behaviours simulated in section 6.2 needs to be carried out. A wider range of shapes also needs to be tested to isolate the effects of initial radius, convergence angle, and the lengths of the straight segments.
- The compound shock waves tested were for a single angle and step size. These parameters may be varied to determine what effect they have on the shock wave shape.
- The lower wall of the facility may be raised so that it is in view of the windows. Although this would result in a smaller test section, it would allow the interaction between the lower Mach reflection and the bottom wall to be studied. The resulting behaviour could be compared to that observed in the CFD simulations.

8.3.3 Curved shock wave reflection

As with planar shock waves, there is an incredible range of details that may be explored. Some of these are mentioned below.

- While the inviscid CFD and theoretical analysis suggest that the reflection is independent of the radius of the shock at the apex, this still needs to be verified through CFD using an appropriate viscous model, and more importantly, through experiments involving different radii.
- Experiments were mostly carried out at angle and Mach number combinations that put the initial reflection type into the Mach reflection domain. Although the CFD simulations in the regular reflection domain suggest that transition occurs at approximately the same angles and Mach numbers as for planar shock waves. This still needs to be verified by experiment, possibly by testing slightly higher wedge angles.
- Use of shorter exposure times and a higher resolution would improve the accuracy of the results. Use of a circular aperture, particularly for the single shot test, would reduce some of the problems related to sensitivity being direction dependent. Alternatively, the use of shadowgraph instead of schlieren photography could be explored.
- CFD simulations were carried out at fixed 5° intervals, which gives an overview of the reflection domains present. However, this does not allow the transition lines to be located with any meaningful accuracy. A much more detailed parametric study would be needed in order to identify the location of the transition lines, and such a study would likely encounter many of the same difficulties that have been encountered in studying planar shock reflection domains (Ben-Dor, 2007).

- The Mach number range was limited by the capabilities of the shock tube used. Because of this, the strong Mach number range in which planar shocks exhibit transitional and double Mach reflections was barely reached. Also, shock waves weaker than about Mach 1.5 could not be produced. Studies of curved shock reflection in these Mach number ranges would be of great interest.

- A study into the pressures generated in the post-reflection focus at low wedge angles would be of great interest.

- Further two-dimensional shapes, such as the reflection of parabolic or hyperbolic shock waves could be tested. This would be challenging, as the shape of the shock front would vary as it approaches the wedge apex.

- The test facility could easily be adapted to experimentally study shock wave diffraction around corners of various angles, or the reflection of curved shocks off curved surfaces.

- The CFD analysis may be easily extended to study the reflection of converging spherical shock waves off flat surfaces or cones by setting either the top or bottom walls as an axisymmetric boundary.

References

Anderson, JD (1995) Computational Fluid Dynamics: The Basics with Applications. McGraw-Hill, New York.

Anderson, JD (2004) Modern Compressible Flow: with Historical Perspective. McGraw-Hill, New York, 3rd edn.

Anderson, JD (2007) Fundamentals of Aerodynamics. McGraw-Hill, New York, 4th edn.

Apazidis, N, Kjellander, M, and Tillmark, N (2013) "High energy concentration by spherical converging shocks in a shock tube with conically shaped test section." In Bonazza, R (ed.) "Proceedings of the 29th International Symposium on Shock Waves," Springer Berlin Heidelberg.

Ben-Dor, G (2007) Shock wave reflection phenomena. Springer, 2nd edn.

Ben-dor, G and Takayama, K (1985) "Analytical prediction of the transition from Mach to regular reflection over cylindrical concave wedges." Journal of Fluid Mechanics vol. 158, pp. 365–380.

Ben-dor, G, Takayama, K, and Dewey, J (1987) "Further analytical considerations of weak planar shock wave reflections over a concave wedge." Fluid Dynamics Reseach vol. 2, no. 2, pp. 77–85.

Biamino, L, Jourdan, G, Houas, L, Vandenboomgaerde, M, and Souffland, D (2013) "Generation of cylindrical converging shock waves in a conventional shock tube." In Bonazza, R (ed.) "Proceedings of the 29th International Symposium on Shock Waves," Springer Berlin Heidelberg.

Bryson, AE and Gross, RWF (1961) "The propagation of shock waves in a channel of non-uniform width." Journal of Fluid Mechanics vol. 10, pp. 1–16.

Cates, JE and Sturtevant, B (1997) "Shock wave focusing using geometrical shock dynamics." Physics of Fluids vol. 9, no. 10, pp. 3058–3068.

Chester, W (1954) "The quasi-cylindrical shock tube." Philosophy Magazine vol. 45, no. 7, pp. 1293–1301.

Chisnell, RF (1957) “The motion of a shock wave in a channel, with applications to cylindrical and spherical shock waves.” Journal of Fluid Mechanics vol. 2, pp. 286–298.

Dewey, JM, Classen, DF, and McMillin, DJ (1975) Photogrammetry of the shock front trajectory on Dipole West Shots 8, 9, 10 and 11. Tech. Rep. UVIC-PF-1-75, University of Victoria, British Columbia, Canada.

Dewey, JM, McMillin, DJ, and Classen, DF (1977) “Photogrammetry of spherical shocks reflected from real and ideal surfaces.” Journal of Fluid Mechanics vol. 81, pp. 701–717.

Dimotakis, PE and Samtaney, R (2006) “Planar shock cylindrical focusing by a perfect-gas lens.” Physics of Fluids vol. 18, no. 3, p. 1705.

Doyle, KB and Kahan, MA (2003) “Design strength of optical glass.” In “Proceedings of SPIE 5176,” .

Dumitrescu, LZ (1992) “On efficient shock-focusing configurations.” In “Proceedings of the 11th Australasian Fluid Mechanics Conference, University of Tazmania, Hobart,” pp. 723–725.

Duong, DQ and Milton, BE (1985) “The Mach reflection of shock waves in converging, cylindrical channels.” Experiments in Fluids vol. 3, pp. 161–168.

Eliasson, V, Apazidis, N, and Tillmark, N (2007) “Controlling the form of strong converging shocks by means of disturbances.” Shock Waves vol. 17, pp. 29–42.

Eliasson, V, Apazidis, N, Tillmark, N, and Lesser, MB (2006) “Focusing of strong shocks in an annular shock tube.” Shock Waves vol. 15, pp. 205–217.

Ewalds, HL and Wanhill, RJH (1985) Fracture Mechanics. Edward Arnold, London.

Felthun, LT (2002) The modelling of compressible Euler flows with moving boundaries. PhD Thesis, the University of the Witwatersrand, Johannesburg, South Africa.

Grönig, H (1986) “Shock wave focusing phenomena.” In Bershader, D and Hanson, R (eds.) “Proceedings of the Fifteenth International Symposium on shock waves and shock tubes,” pp. 43–56. Stanford University Press.

Guderley, G (1942) “Stärke Kugelige und Zilindrische Verdichtungsstösse in der Nähe des Kugelmittelpunktes bzw. der Zilinderachse (Strength of spherical and cylindrical shock waves in the vicinity of the sphere center and the cylinder axis).” Luftfahrtforschung vol. 199, pp. 302–312.

Henderson, LF (1980) “On the Whitham theory of shock-wave diffraction at concave corners.” Journal of Fluid Mechanics vol. 99, no. 4, pp. 801–811.

Henderson, LF and Lozzi, A (1975) “Experiments on transition of Mach reflexion.” Journal of Fluid Mechanics vol. 68, no. 1, pp. 139–155.

Henshaw, WD, Smyth, NF, and Schwendeman, DW (1986) “Numerical shock propagation using geometrical shock dynamics.” Journal of Fluid Mechanics vol. 171, pp. 519–545.

Hornung, HG (1986) “Regular and Mach Reflection of Shock Waves.” Annual Review of Fluid Mechanics vol. 18, no. 1, pp. 33–58.

Hornung, HG, Oertel, H, and Sandeman, RJ (1979) “Transition to Mach reflection of shock waves in steady and pseudosteady flow with and without relaxation.” Journal of Fluid Mechanics vol. 90, pp. 541–560.

Hu, TCJ and Glass, II (1986) “Blast wave reflection trajectories from a height of burst.” American Institute of Aeronautics and Astronautics Journal vol. 24, pp. 607–610.

Hunter, JD (2007) “Matplotlib: A 2d graphics environment.” Computing In Science & Engineering vol. 9, no. 3, pp. 90–95.

Itoh, S, Okazaki, N, and Itaya, M (1981) “On the transition between regular and Mach reflection in truly non-stationary flows.” Journal of Fluid Mechanics vol. 108, pp. 383–400.

Izumi, K, Aso, S, and Nishida, M (1994) “Experimental and computational studies focusing processes of shock waves reflected from parabolic surfaces.” Shock Waves vol. 3, no. 3, pp. 213–222.

Kambe, M, Ioritani, M, Shirai, S, Kambe, K, and Tezuka, F (1996) “Macroscopic Pores Opened by Shock Wave on Cancer Cell Surfaces: Morphological and Functional Features.” Japanese Journal of Endourology and ESWL vol. 9, pp. 161–167.

Kjellander, M, Tillmark, N, and Apazidis, N (2011) “Experimental determination of self-similarity constant for converging cylindrical shocks.” Physics of Fluids vol. 23, p. 116103.

Kleine, H, Timofeev, E, Hakkaki-Fard, A, and Skews, B (2014) “The influence of Reynolds number on the triple point trajecttories at shock reflection off cylindrical surfaces.” Journal of Fluid Mechanics vol. 740, pp. 47–60.

Lacovig, L (2011) The construction and calibration of a shock tube for largescale diffraction studies. MSc (Eng) dissertation, University of the Witwatersrand, Johannesburg, South Africa.

Liang, SM, Hsu, JL, and Wang, JS (2001) “Numerical study of cylindrical blast-wave propagation and reflection.” American Institute of Aeronautics and Astronautics Journal vol. 39, no. 6, pp. 1152–1158.

Liang, SM, Wang, JS, and Chen, H (2002) “Numerical study of spherical blast-wave propagation and reflection.” Shock Waves vol. 12, no. 1, pp. 59–68.

Lindl, JD, Campbell, EM, and McCrory, RL (1992) “Progress toward ignition and burn propagation in inertial confinement fusion.” Physics Today vol. 45, no. 9, p. 32.

Lock, G and Dewey, JM (1989) “An experimental investigation of the sonic criterion for transition from regular to Mach reflection of weak shock waves.” Experiments in Fluids vol. 7, pp. 289–292.

MacLucas, DA (2012) Shock-wave induced flow features in concave profiles. Ph.D. thesis, University of the Witwatersrand, Johannesburg, South Africa.

Merzkirch, W (1987) Flow Visualization. Academic Press Inc., Orlando, Florida, 2nd edn.

Milton, BE (1975) “Mach reflection using ray-shock theory.” AIAA Journal vol. 13, no. 11, pp. 1531–1533.

Perry, RW and Kantrowitz, A (1951) “The production and stability of converging shock waves.” Journal of Applied Physics vol. 22, no. 7, pp. 878–886.

Ponchaut, NF, Hornung, HG, Pullin, DI, and Mouton, CA (2006) “On imploding cylindrical and spherical shock waves in a perfect gas.” Journal of Fluid Mechanics vol. 560, pp. 103–122.

Prasad, P (1982) “Kinematics of a multi-dimensional shock of arbitrary strength in an ideal gas.” Acta Mechanica vol. 45, no. 3, pp. 163–176.

Präzisions Glas & Optik (2010) “Bk7 optical glass.” `http://www.pgo-online.com/intl/katalog/BK7.html`. [Online; accessed October 2010].

Roark, RJ and Young, WC (1975) Formulas for Stress and Strain. McGraw-Hill, Inc., 5th edn.

Schwendeman, DW (2002) “On converging shock waves of spherical and polyhedral form.” Journal of Fluid Mechanics vol. 454, pp. 365–386.

Schwendeman, DW and Whitham, GB (1987) “On converging shock waves.” Proceedings of the Royal Society of London. Series A, Mathematical and Physical Sciences vol. 413, no. 1845, pp. 297–311.

Settles, GS (2001) Schlieren and shadowgraph techniques: visualizing phenomena in transparent media. Springer-Verlag Berlin Heidelberg New York.

Shigley, JE, Mischke, CR, and Budynas, RG (2004) Mechanical Engineering Design. McGraw-Hill, New York, 7th edn.

Skews, BW and Beharie, M (2009) Experimental Facility for the Study of Focusing of Curved Shock Waves. 4th year project, University of the Witwatersrand, Johannesburg, South Africa.

Skews, BW and Daya, S (2009) Experimental Facility for the Study of Curved Shock Wave Reflection. 4th year project, University of the Witwatersrand, Johannesburg, South Africa.

Skews, BW and Kleine, HH (2007) "Flow features resulting from shock wave impact on a cylindrical cavity." Journal of Fluid Mechanics vol. 580, pp. 481–493.

Skews, BW and Kleine, HH (2009) "Unsteady flow diagnostics using weak perturbations." Experiments in Fluids vol. 46, pp. 65–76.

Smith, LG (1945) "Photographic investigation of the reflection of plane shocks in air."

Sturtevant, B and Kulkarny, VA (1976) "The focusing of weak shock waves." Journal of Fluid Mechanics vol. 73, pp. 651–671.

Taieb, D, Ribert, G, and Hadjadj, A (2010) "Numerical simulations of shock focusing over concave surfaces." AIAA Journal vol. 48, no. 8, pp. 1739–1747.

Takayama, K and Saito, T (2004) "Shock wave/geophysical and medical applications." Annual Review of Fluid Mechanics vol. 36, pp. 347–379.

Takayama, K and Sekiguchi, H (1981a) "Formation and diffraction of spherical shock waves in shock tube." Reports of the Institute of High Speed Mechanics, Tokuhoku University, Sendai, Japan vol. 43, pp. 89–119.

Takayama, K and Sekiguchi, H (1981b) "Triple-point trajectory of a strong spherical shock wave." American Institute of Aeronautics and Astronautics Journal vol. 19, pp. 815–817.

Van Dyke, M and Guttmann, AJ (1982) "The converging shock wave from a spherical or cylindrical piston." Journal of Fluid Mechanics vol. 120, pp. 451–462.

von Neumann, J (1943a) Oblique reflection of shocks. Explosion Research Report 12, Navy Department, Bureau of Ordinance, Washington DC, USA.

von Neumann, J (1943b) Refraction, intersection and reflection of shock waves. NAVORD Report 203-45, Navy Department, Bureau of Ordinance, Washington DC, USA.

Watanabe, M and Takayama, K (1991) "Stability of converging cylindrical shock waves." Shock Waves vol. 1, no. 2, pp. 149–160.

Whitham, GB (1957) "A new approach to problems of shock dynamics. Part 1. Two-dimensional problems." Journal of Fluid Mechanics vol. 2, pp. 145–171.

Whitham, GB (1959) “A new approach to problems of shock dynamics. Part 2. Three-dimensional problems.” Journal of Fluid Mechanics vol. 5, pp. 369–386.

Whitham, GB (1974) Linear and nonlinear waves. John Wiley & Sons, New York.

Wu, JHT, Neemeh, RA, and Ostowski, PP (1980) “Experimental studies of the production of converging cylindrical shock waves.” AIAA Journal vol. 18, no. 1, pp. 47–48.

Zhai, Z, Liu, C, Qin, F, Yang, J, and Luo, X (2010) “Generation of cylindrical converging shock waves based on shock dynamics theory.” Physics of Fluids vol. 22, p. 041701.

Appendix A. Modifications to Existing Shock Tube Driver

The existing shock tube driver was a cylindrical pressure vessel with an internal diameter of 438 mm, and a length of 2000 mm. The ends are sealed by circular plates, one of which has a 100mm wide rectangular cut out across which the diaphragm is placed.

In previous experiments carried out on the shock tube, the entire cylinder was pressurised, and the gas was allowed to expand through the entire volume. The net result was that each test required an excessively large volume of gas, requiring a long time to fill the driver before each test, rapidly draining the reservoir of compressed air. More importantly, there were some safety concerns regarding the energy of such a large volume of pressurised air.

Two possible solutions to this problem were proposed. The first was to manufacture a new rectangular driver with the correct shape; however, this solution was dismissed due to both the cost and the complications of obtaining certification for a rectangular pressure vessel.

The second solution was to manufacture D-shaped “inserts” which would occupy the space inside the driver and reduce its capacity. This has the advantage that the driver does not need to be recertified.

In order to fill the driver at the lowest cost possible, 25 mm thick pine planks with standard widths of 152 mm and 230 mm were cut to width and fitted together with cold glue and 4.0 x 40 mm screws. The planks were then cut to a length of 1990 mm in order to allow some clearance around the ends. The inserts were then sanded into the correct shape, and varnished. Table A.1 gives the widths required to give the correct shape, and a diagram of a cross section through the inserts inside the driver is shown in Figure A.1.

A 0.5mm thick steel sheet was attached with 4.0 x 40 mm screws to cover the inside faces of the driver inserts, in order to prevent the wood from splintering with repeated use. The inserts are held in place by four lengths of L25x25x5mm angle iron which are held in place

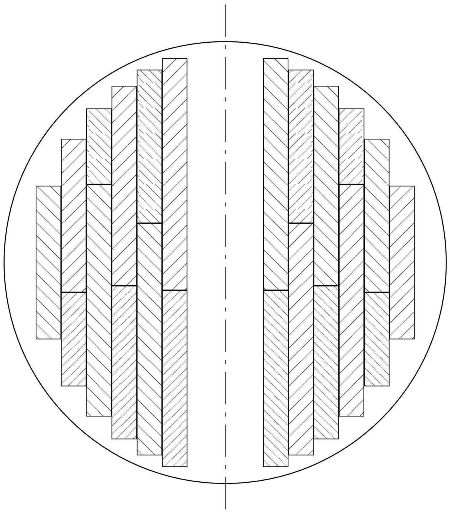

Figure A.1: Cross section of the driver, showing the D-shaped driver inserts

Table A.1: Plank widths for the driver insert.

Planks			(Total)
230 mm	+	175 mm	(405 mm)
152 mm	+	230 mm	(382 mm)
198 mm	+	152 mm	(350 mm)
75 mm	+	230 mm	(305 mm)
152 mm	+	93 mm	(245 mm)
152 mm			(152 mm)

by ten M6 x 12 mm bolts through the end plates of the driver. The angle iron also serves to maintain the 100mm gap between the two inserts.

In addition to these modifications, a 24mm diameter steel tube was attached to the side of the driven section just downstream of the diaphragm. This allows the shock tube to vent after a test, even if the test piece at the end of the shock tube completely closes the end of the shock tube.

Appendix B. Design Sizing Calculations

Sizing calculations were carried out to ensure that the thickness of the profile plate and window would be sufficient to withstand the pressures inside the facility, and that the bolts would be strong enough to hold the facility to the shock tube. These calculations are described in the following sections.

B.1 Profile plate thickness

The deflection of the profile plate needs to be minimized to reduce any deformation of the slit shape. The worst case for the profile will be when it is completely closed. This can be modelled as a rectangular plate with clamped edges, with the pressure behind the reflected shock acting on one side of the plate, and the atmospheric pressure on the other side.

Roark and Young (1975) gives the maximum stresses in a rectangular plate with all edges fixed. The maximum stress in the plate will be along the edge, and is given by

$$\sigma = \frac{-\beta_1 q b^2}{t^2} \tag{B.1}$$

and the maximum deflection in the centre of the plate is given by

$$y = \frac{\alpha q b^4}{E t^3} \tag{B.2}$$

where q is the load per unit area, b is the length of the shorter of the two sides, E is the Young's modulus of the plate, and t is the plate thickness. α and β_1 are constants that depend on the plate's aspect ratio. Values of these constants are tabulated in Table B.1.

If the driver is operated at its maximum operating pressure of 1000 kPa with an atmospheric pressure of 83.5 kPa, equation (2.8) predicts that the generated shock wave will have a Mach

Table B.1: Constants for maximum stress formula in a flat rectangular plate with all edges fixed (Roark and Young, 1975)

a/b	1.0	1.2	1.4	1.6	1.8	2.0	∞
α	0.0138	0.0188	0.0226	0.0251	0.0267	0.0277	0.0284
β_1	0.3078	0.3834	0.4356	0.4680	0.4872	0.4974	0.5000

number of 1.7. Once the shock has reflected off of the profile plate, a shock of this strength will produce a maximum pressure on the profile plate of 850 kPa.

The profile plate is to cover the exit of the existing shock tube, which is a rectangle 100 mm wide, with an aspect ratio of 4.5. Constants corresponding to an aspect ratio of ∞ from Table B.1 were used. These constants would overestimate the maximum stress and deflection, resulting in a conservative design. The plate is made of steel, which typically has a Young's modulus of 200 GPa (Shigley et al., 2004). Substituting these values into equations (B.1) and (B.2) give the maximum stresses and deflections for various plate thicknesses, as tabulated in Table B.2.

Table B.2: Maximum stresses and deflections in the profile plate for various thicknesses

Thickness	Maximum stress	Maximum deflection
5 mm	170.0 MPa	96.6 μm
10 mm	42.5 MPa	12.1 μm
15 mm	18.9 MPa	3.6 μm
20 mm	10.6 MPa	1.5 μm

The stresses in the plate are relatively low for plates of 10 mm and above. For a 10 mm plate, the deflection is approximately 0.1% of plate width, whereas the deflection of a 15 mm plate is just 0.02% of the plate width.

For this reason, and to allow some clearance for the small outer plate to be removed, 15 mm was chosen as the thickness of the profile plate.

B.2 Bolt sizing

The existing end section for the shock tube is attached to the rest of the shock tube by ten M14 bolts. At least three of these bolts would need to be removed in order to attach the apparatus. It is desirable that the same bolts be used, although the existing holes in the shock tube are large enough that M16 bolts may be used if necessary.

Once again, applying a constant 850 kPa pressure in the shock tube will result in a maximum load of 38.25 kN on the profile plate, or a load of 5.46 kN on each bolt. In addition to this, the bolts carry a preload from the initial tightening. This preload may be estimated from the torque applied to tighten the bolt. Shigley et al. (2004) gives the preload as

$$F_i = \frac{T}{Kd} \tag{B.3}$$

where T is the torque applied, K is the torque coefficient, and d is the nominal diameter of the bolt. Using a torque constant of 0.2, bolt diameter of 14 mm, and a rough estimate of the torque of 60 Nm, a preload of 21.4 kN is obtained. The maximum load on each bolt is thus 26.9 kN, and with a tensile stress area of 115 mm^2, this results in a maximum tensile stress of 234 MPa.

Bolts of property class 8.8 are used. These bolts have a proof strength of at least 600 MPa and an ultimate tensile strength of at least 830 MPa (Shigley et al., 2004). This gives a safety factor under static loading of 2.6.

However, the bolts are loaded and unloaded during each test, and thus the effect of fatigue needs to be considered. Shigley et al. (2004) uses the Goodman criterion to calculate the safety factor of a bolt under fatigue loading, producing the following formula:

$$n_f = \frac{2S_e\left(S_{ut}A_t - F_i\right)}{P\left(S_{ut} + S_e\right)} \tag{B.4}$$

where S_e is the endurance strength, S_{ut} is the ultimate tensile strength, A_t is the tensile stress area, and P is the external load applied to the bolt. In this case, this results in a safety factor for fatigue of 3.6.

It was therefore concluded that seven M14 bolts would be adequate for holding the apparatus onto the shock tube.

B.3 Viewing windows

The quality of the viewing windows is a critical factor in ensuring the accuracy of schlieren photographs obtained from the apparatus. Foremost amongst the requirements for the chosen glass are a low dispersion, low refractive index, and good mechanical properties. The borosilicate glass Schott BK7 has the ideal properties for the viewing windows required. A circular window was chosen for the design to avoid stress concentrations in corners. This is especially important considering the brittleness of glasses in general, and their susceptibility to sudden failures, and that in the case of shock focusing, high pressures can be obtained.

For the purposes of sizing, the glass window is modelled as a rigidly supported circular plate with an evenly distributed loading equal to the maximum internal pressure expected in the apparatus. Since the glass will be relatively thick, the shear stress is assumed to be negligible, and bending stress is assumed to play the primary role in fracture. The location of the maximum bending stress depends on the properties of the glass, but will occur either in the centre of the window, or along the edge where the frame clamps the window in place. The magnitudes of the bending moments per unit circumference at these locations in a rigidly supported circular plate under a constant pressure load are given by Roark and Young (1975) as

$$M_c = \frac{pr^2\,(1+\nu)}{16} \tag{B.5}$$

$$M_r = \frac{pr^2}{8} \tag{B.6}$$

where p is the pressure difference across the glass, r is the radius of the window, and ν is the Poisson's ratio. The subscripts c and r denote moments at the centre and edge respectively. The stress due to bending in the glass is

$$\sigma = \frac{6M}{t^2} \tag{B.7}$$

where M is the maximum of M_c and M_r, and t is the plate thickness.

Fracture is assumed to occur by rapid unstable crack growth from a critical crack length, via crack opening due to tensile loading, as is typical for brittle materials. In this case, fracture is governed by the stress intensity factor. The Griffith-Irwin solution for the stress intensity factor is given by Ewalds and Wanhill (1985) as

$$K_I = \sigma\sqrt{\pi a} \tag{B.8}$$

where a is the depth of a crack in the surface of the glass, and failure occurs if

$$K_I > K_{IC} \tag{B.9}$$

where K_{IC} is refered to as the fracture toughness.

Doyle and Kahan (2003) gives the fracture toughness of BK7 glass as 774 psi$\sqrt{\text{in}}$ (0.85 MPa$\sqrt{\text{m}}$) and Präzisions Glas & Optik (2010) gives a Poisson's ratio of 0.206.

The largest window that may be accommodated by the design has an outer diameter of 350 mm. However, a frame would need to overlap this by 10 mm in order to clamp the window in place. This would leave an inner radius of 165 mm.

As in the previous sections, it will be assumed that a constant pressure of 850 kPa acts on the glass, with an atmospheric pressure of 83.5 kPa on the other side. Although it is possible that focussing phenomena may result in pressures higher than this over a small portion of the window, assuming a lower constant pressure is still conservative, as any pressures the glass does experience would be transient and would dissipate quicker than the glass would be able to respond.

Allowing for an initial crack length of 0.5 mm, the minimum thickness of the glass required to prevent rapid unstable crack growth may be found using an iterative method. Glass with a thickness of 28 mm was found to be suitable, although difficulties were encountered when cutting glass to this thickness. Glass with a thickness of 33 mm was available, which would give a maximum stress around the circumference of 14.4 MPa. This would allow the maximum initial crack size to be increased to 1 mm, which would be easier to find during a visual inspection of the glass.

The final window specifications are given in Table B.3.

TABLE B.3: Window specifications

Material	BK7 Glass
Diameter	350 mm
Thickness	33 mm
Chamfer	3 mm

Appendix C. Engineering Drawings

The following pages contain engineering drawings of the apparatus described in chapter 5. They have been divided as follows:

C.1 Assembly drawings

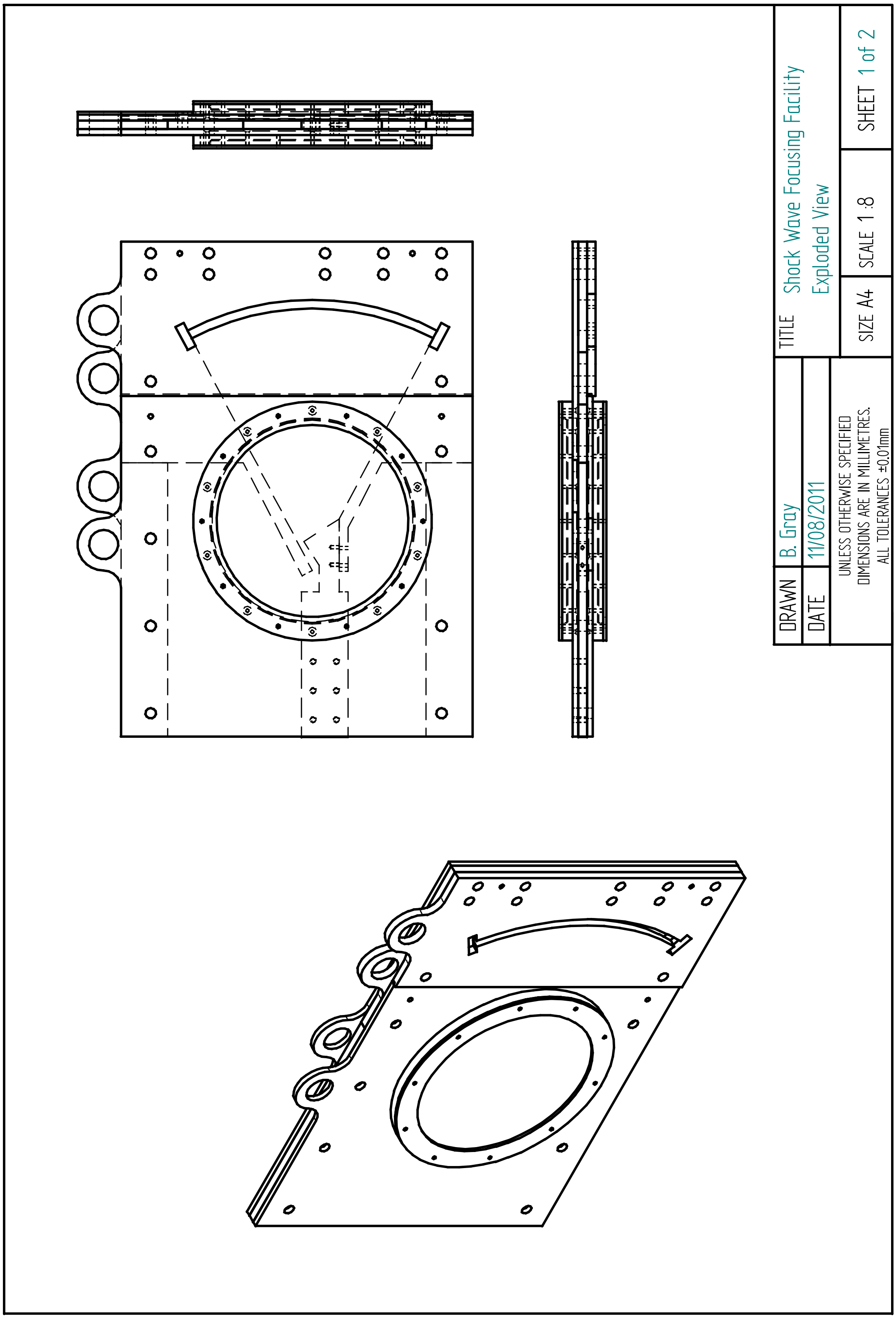

FIGURE C.1: Shock wave focusing facility - Assembly view

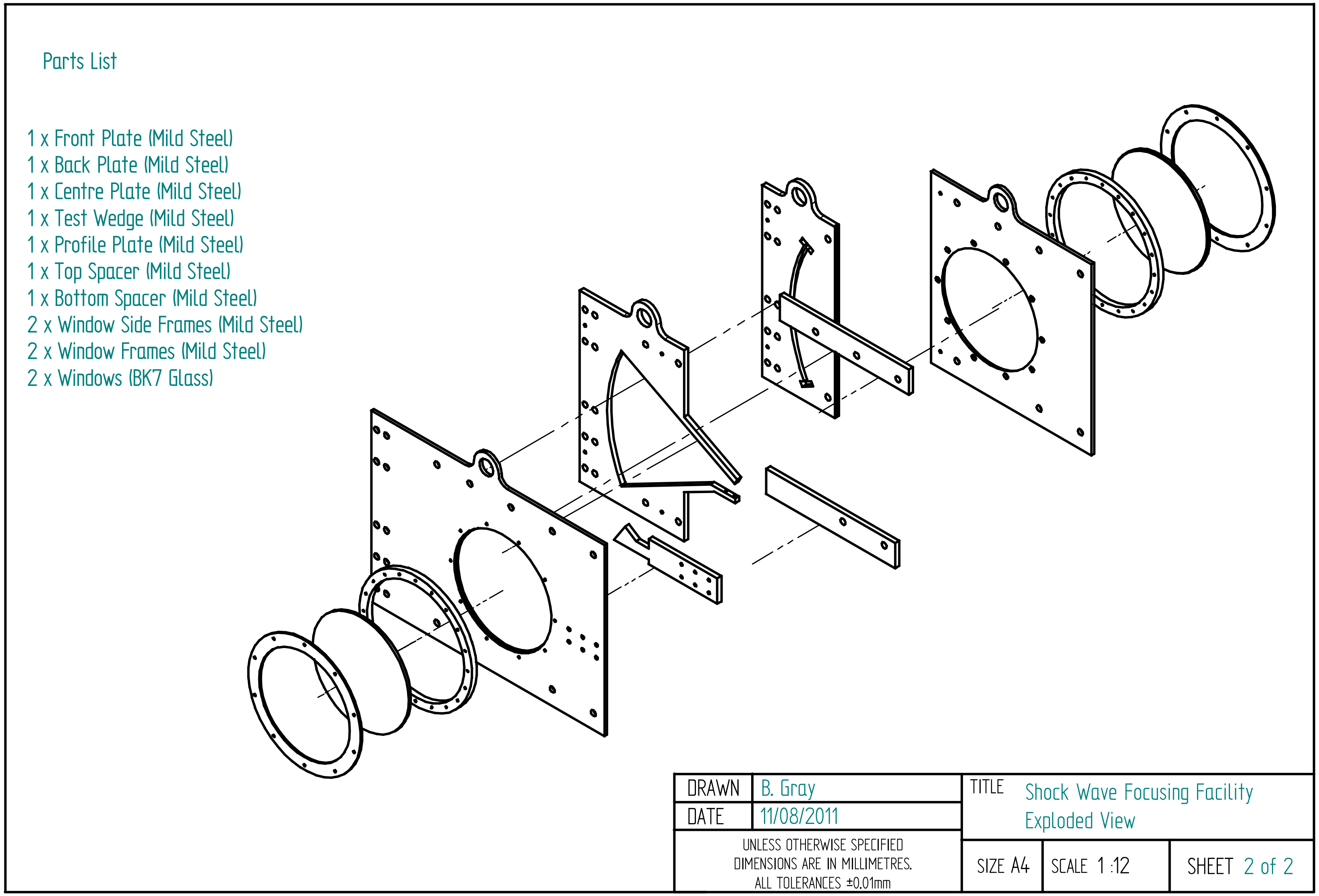

Figure C.2: Shock wave focusing facility - Exploded view

C.2 Part drawings for the converging shock profile

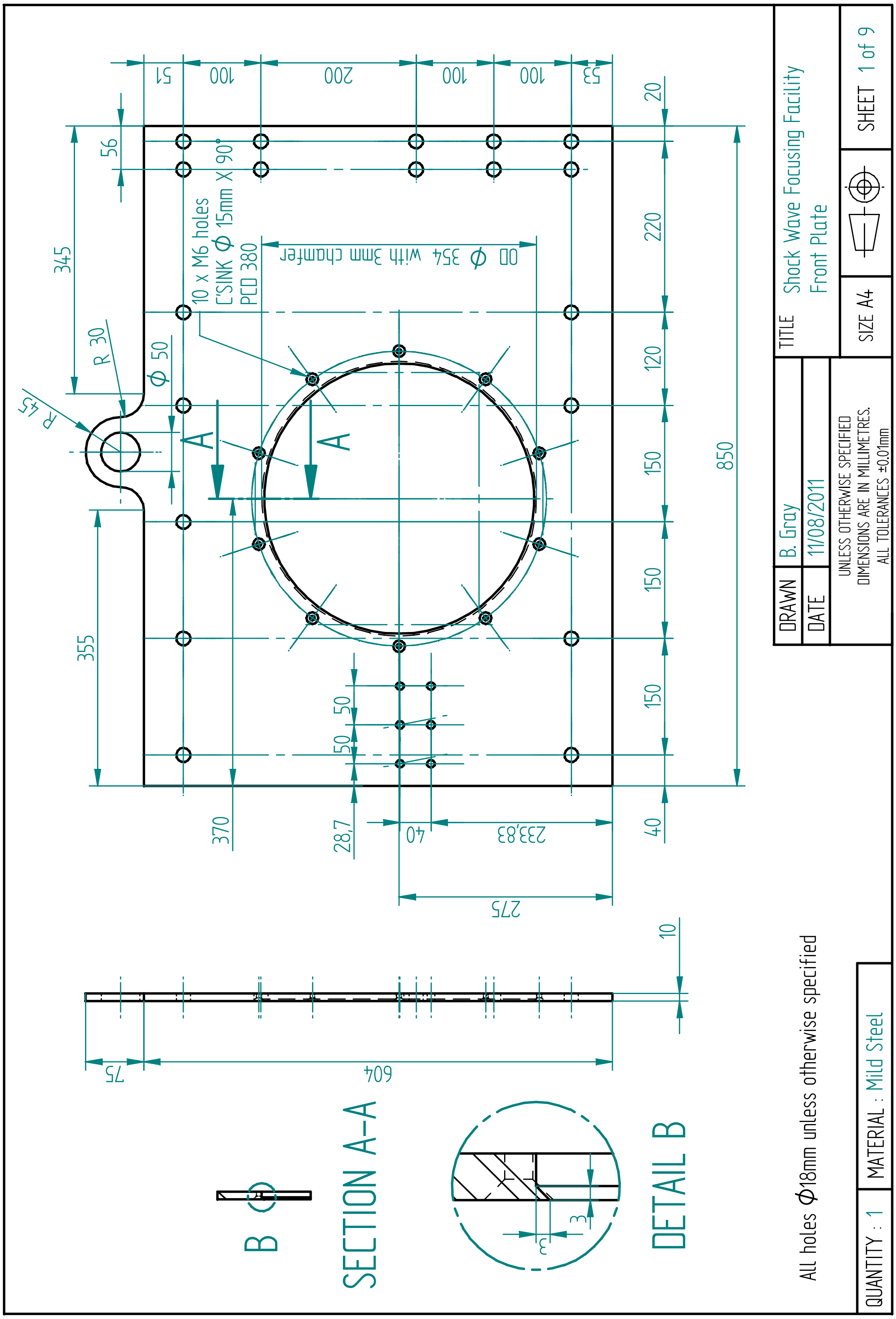

Figure C.3: Engineering drawing of the large window plate

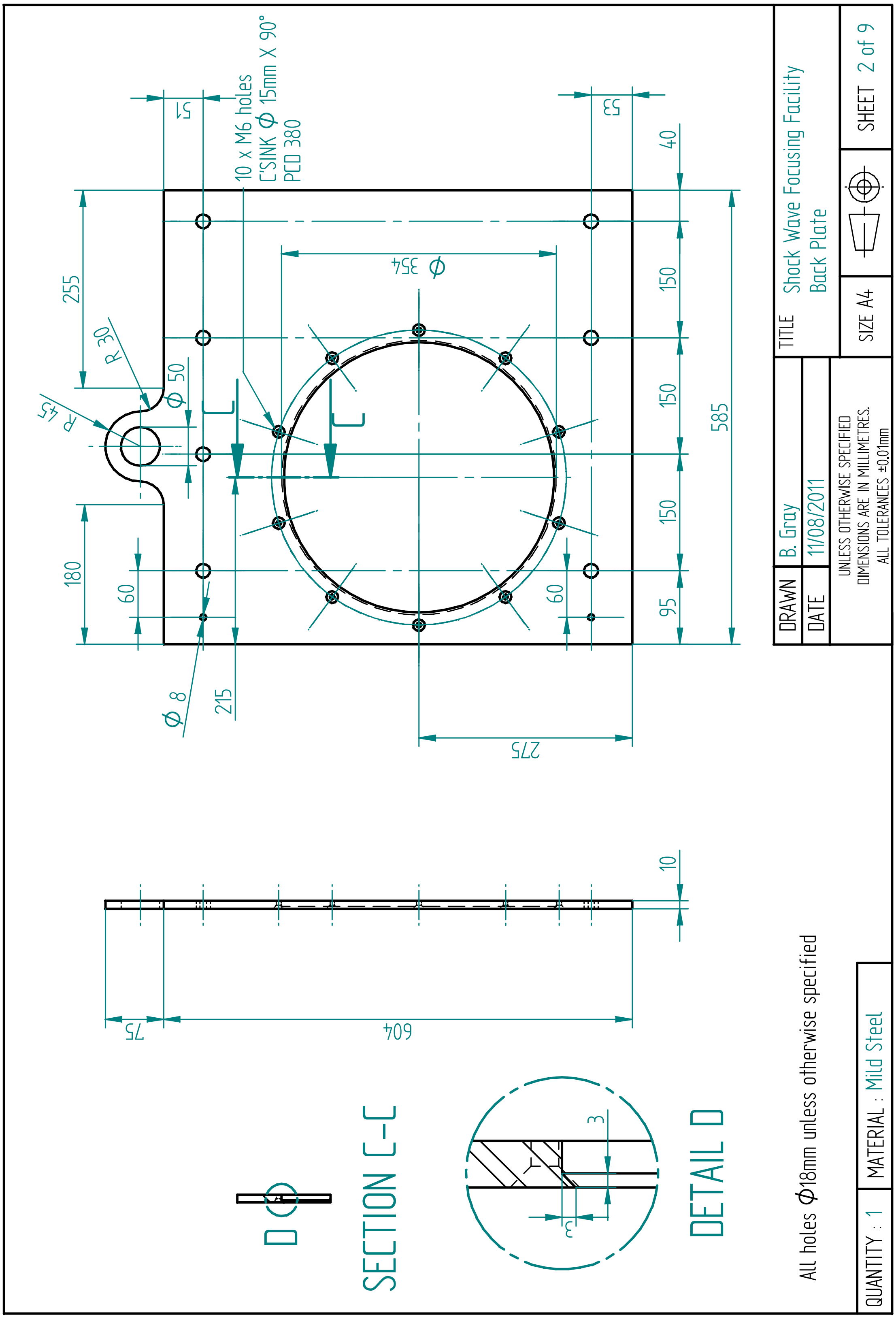

Figure C.4: Engineering drawing of the small window plate

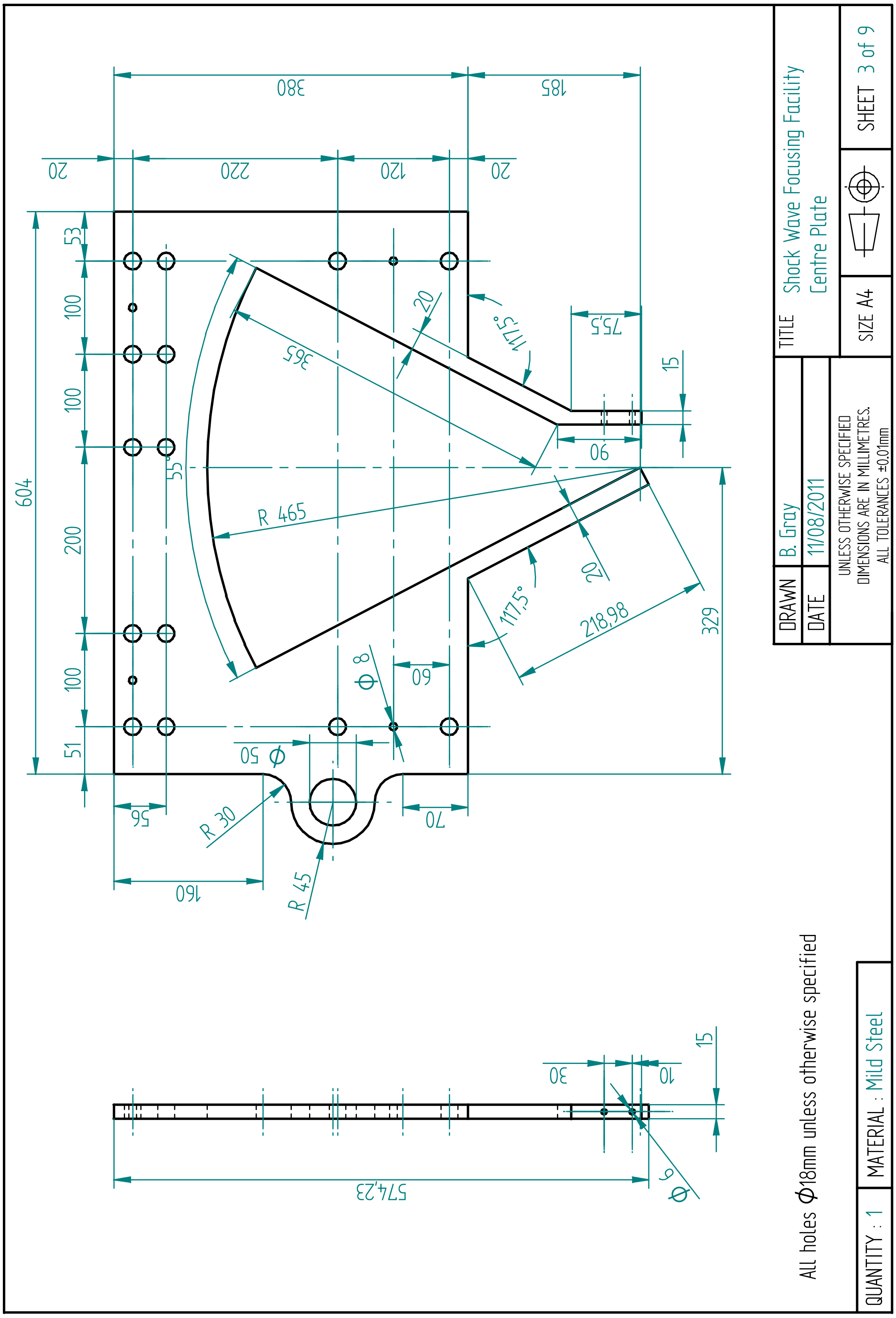

Figure C.5: Engineering drawing of the propagation plate for a 450mm initial radius converging shock

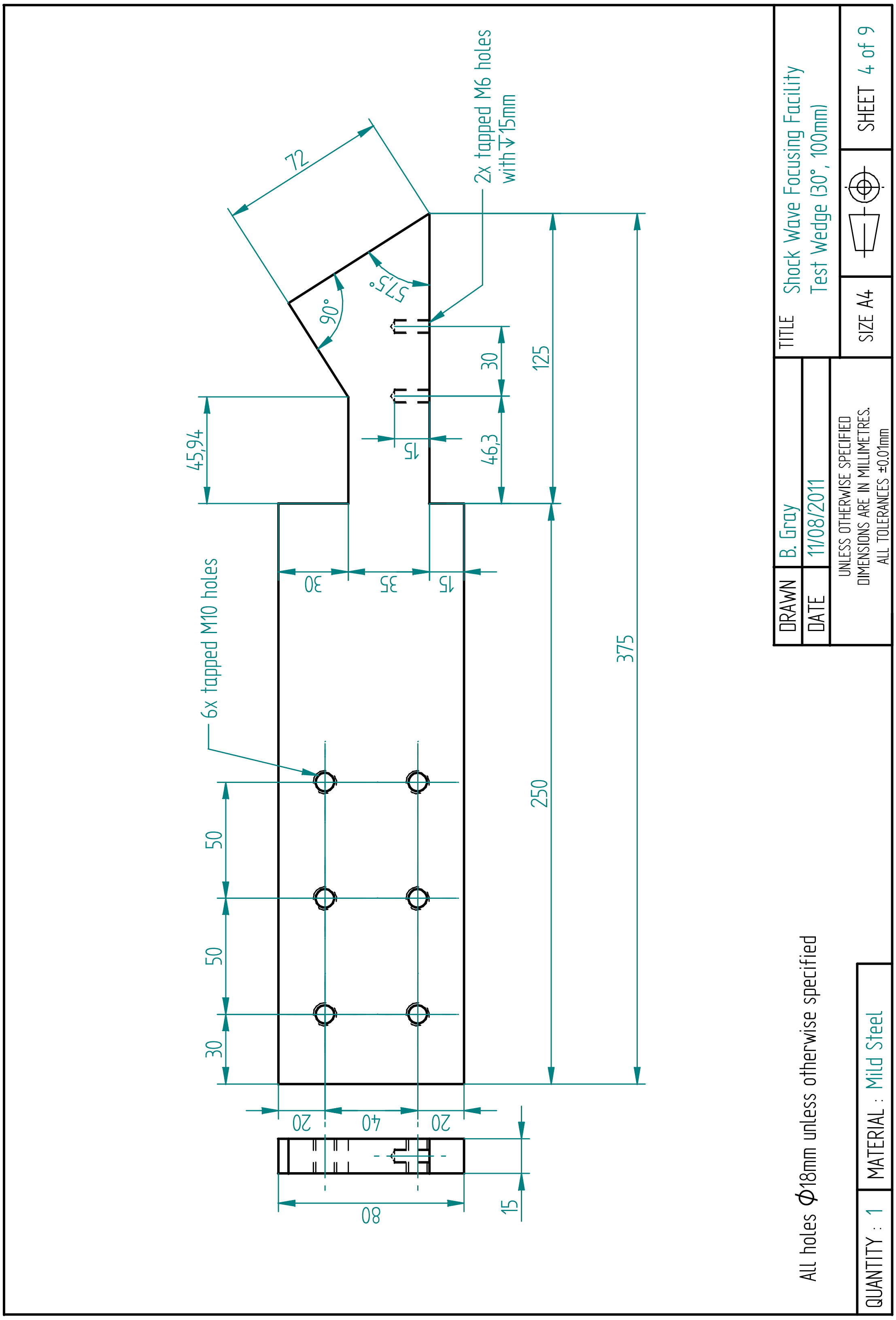

Figure C.6: Engineering drawing of the 30° test wedge

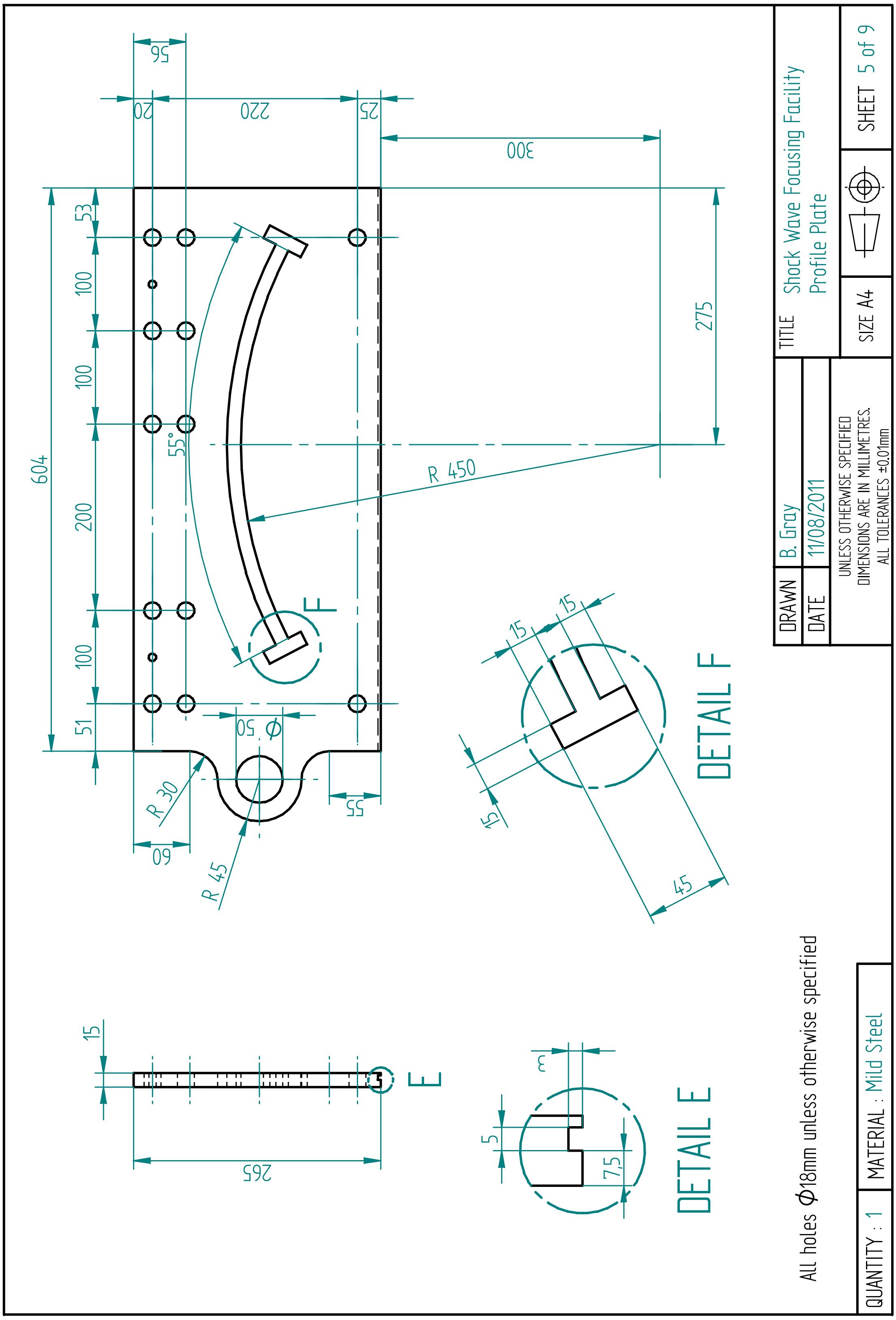

Figure C.7: Engineering drawing of the profile plate for a 450mm initial radius converging shock

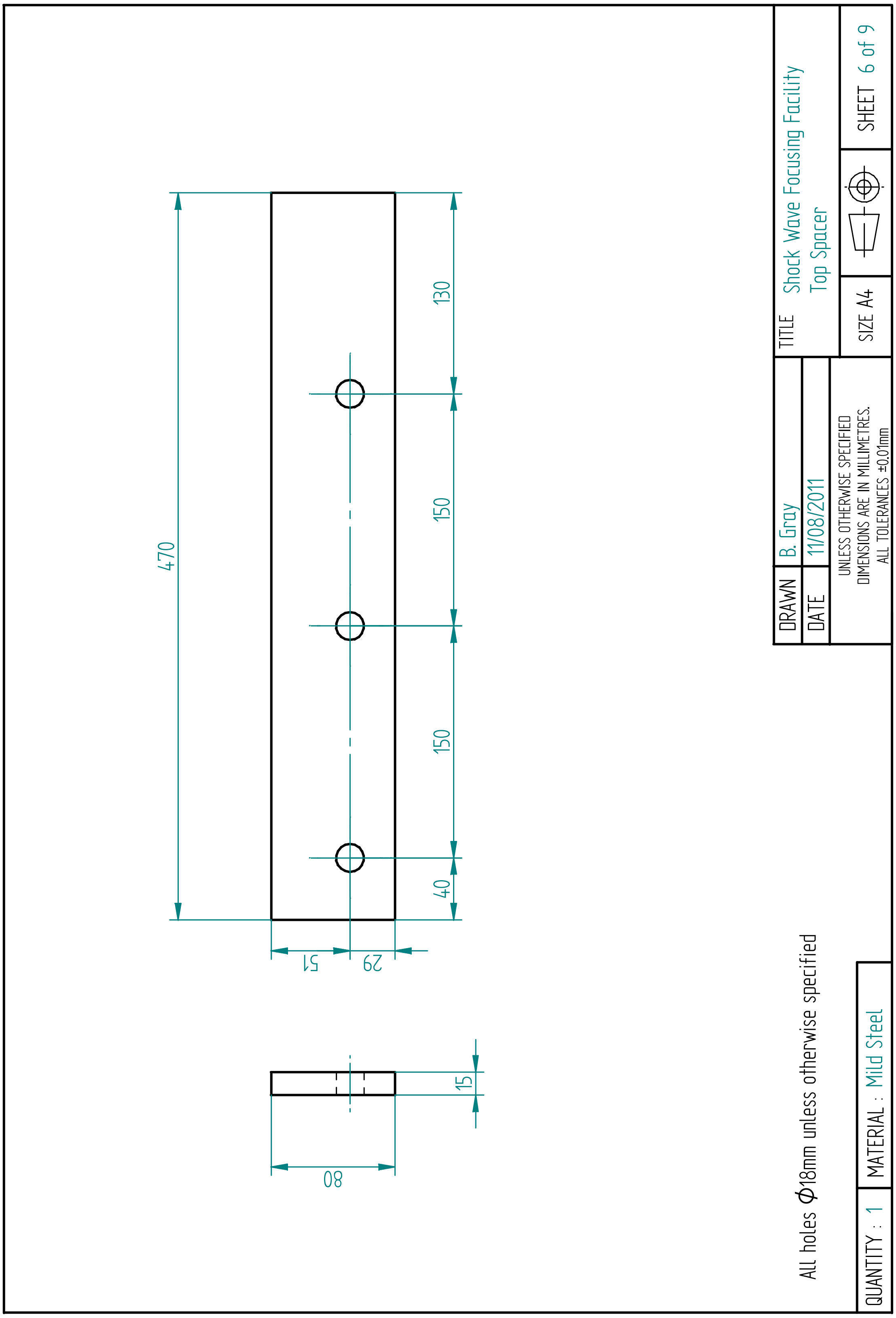

Figure C.8: Engineering drawing of the top spacer plate

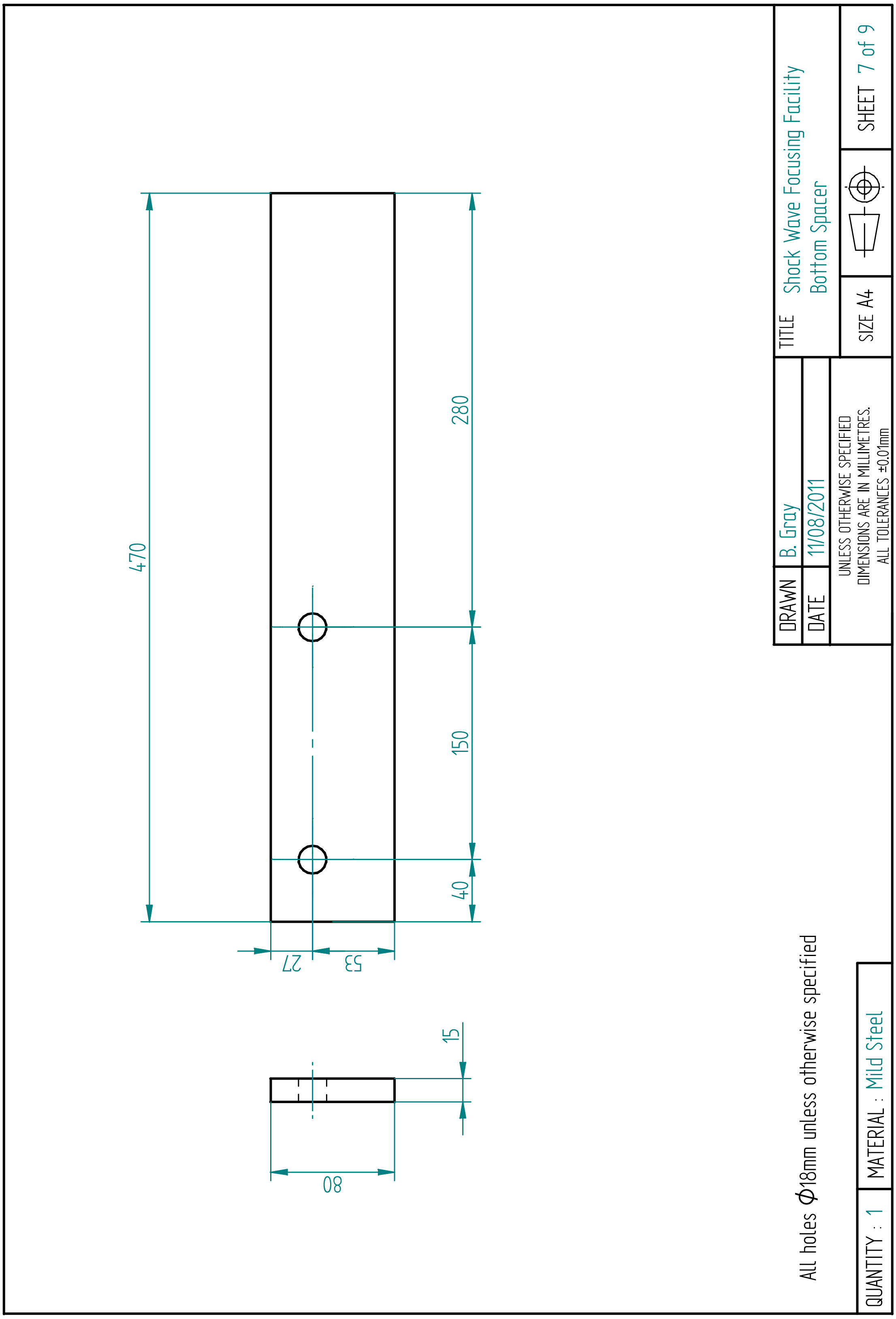

Figure C.9: Engineering drawing of the bottom spacer plate

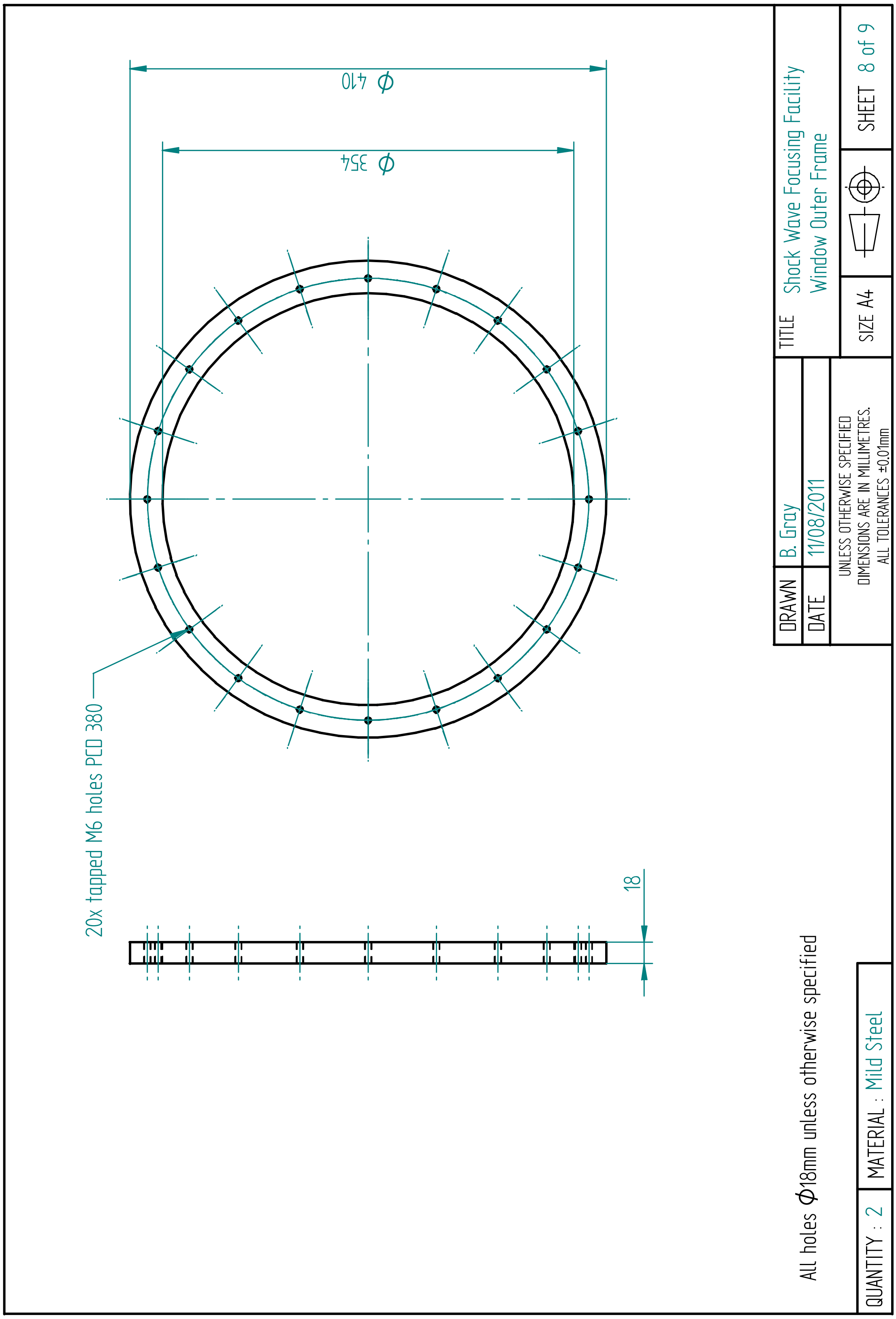

Figure C.10: Engineering drawing of the window frame

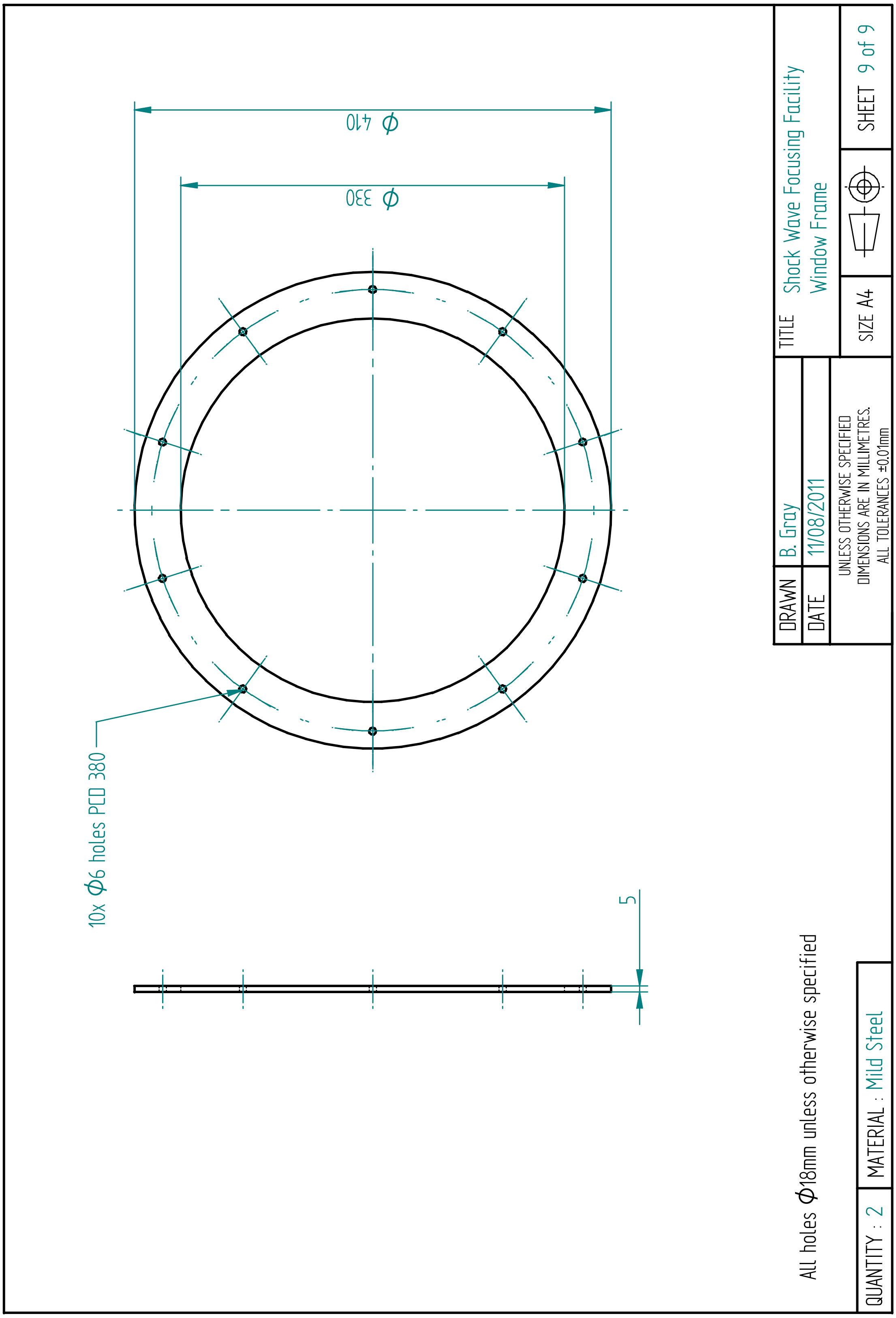

Figure C.11: Engineering drawing of the outer window clamp

C.3 Additional wedges for the converging shock profile

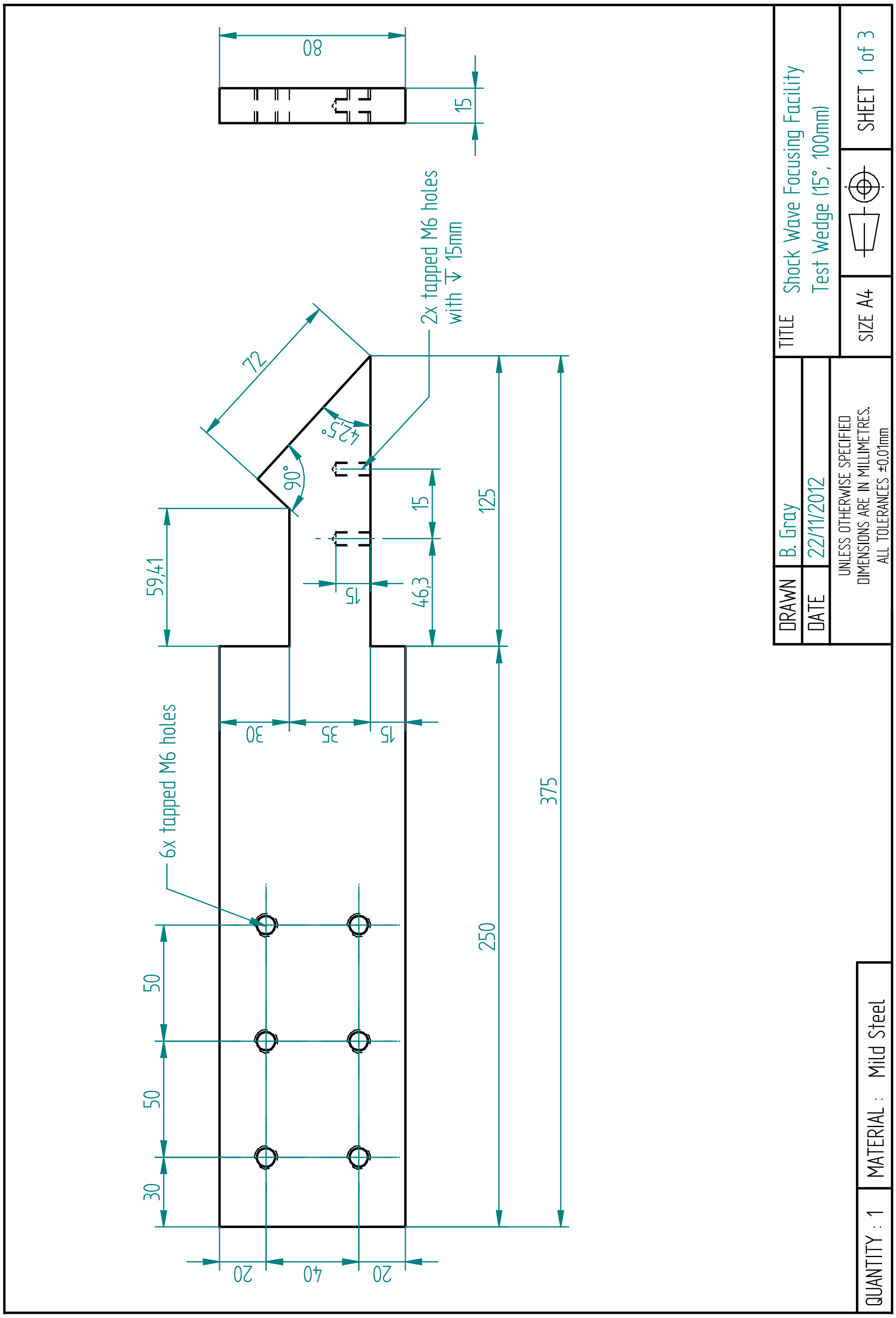

Figure C.12: Engineering drawing of the 15° test wedge

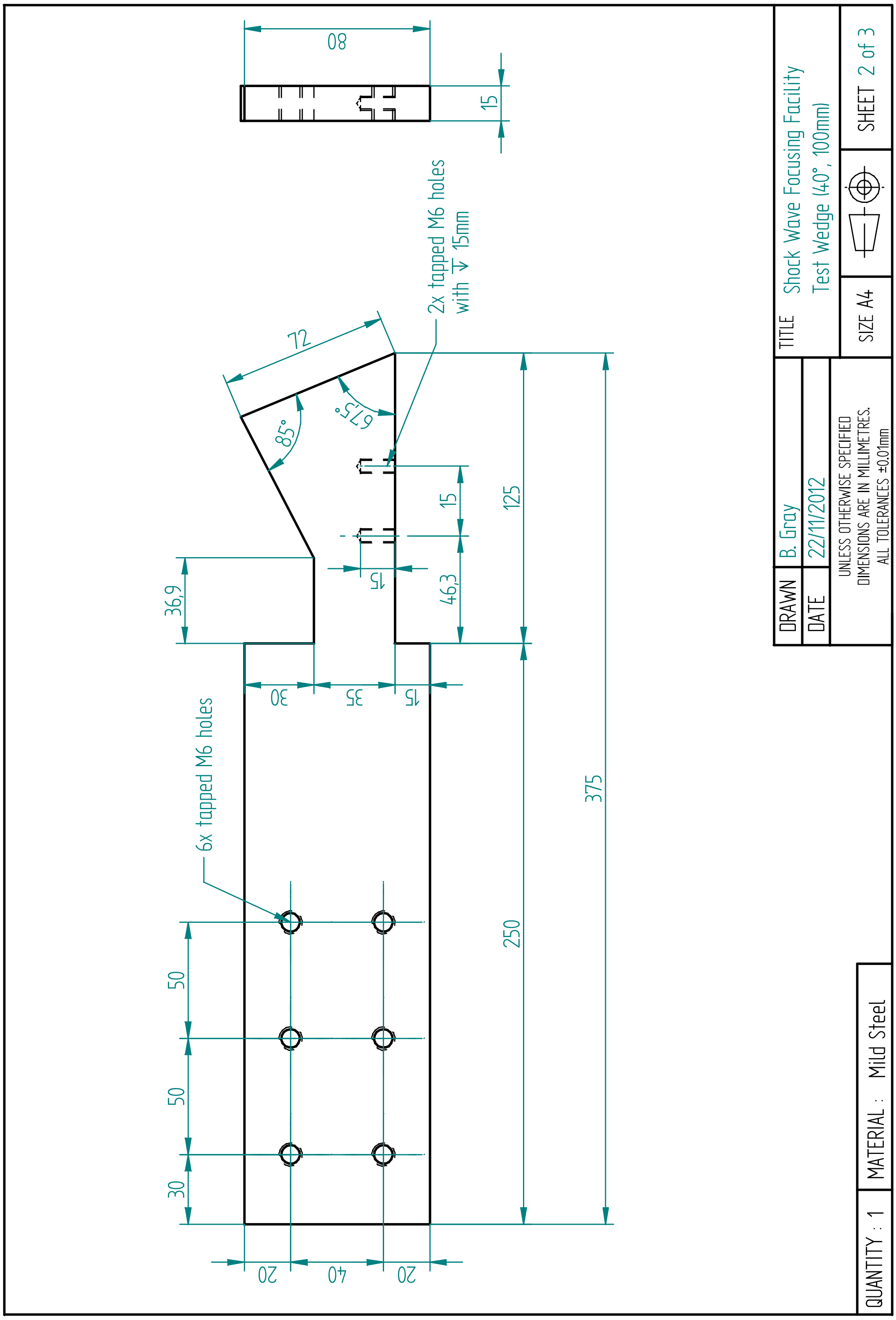

Figure C.13: Engineering drawing of the 40° test wedge

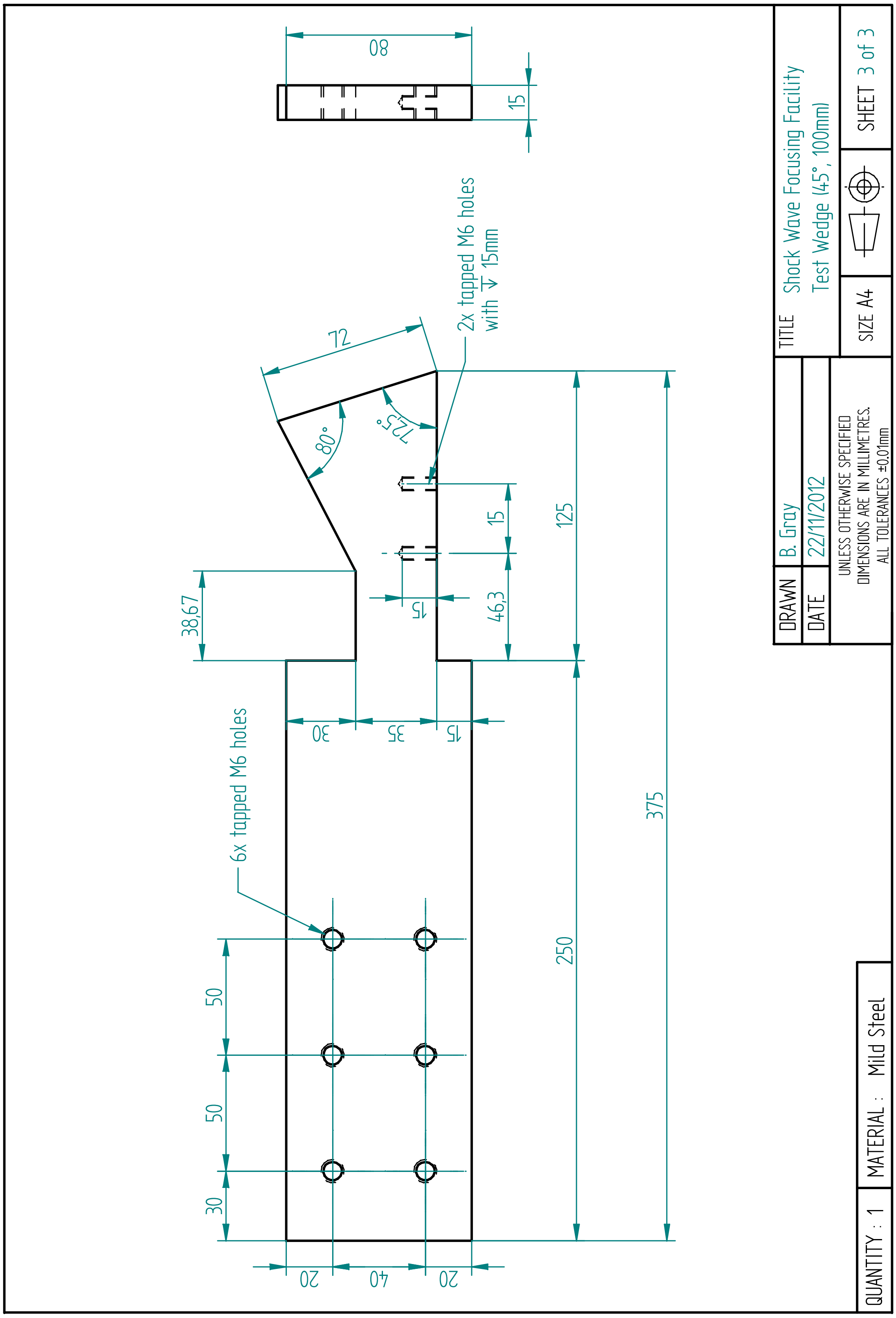

Figure C.14: Engineering drawing of the 45° test wedge

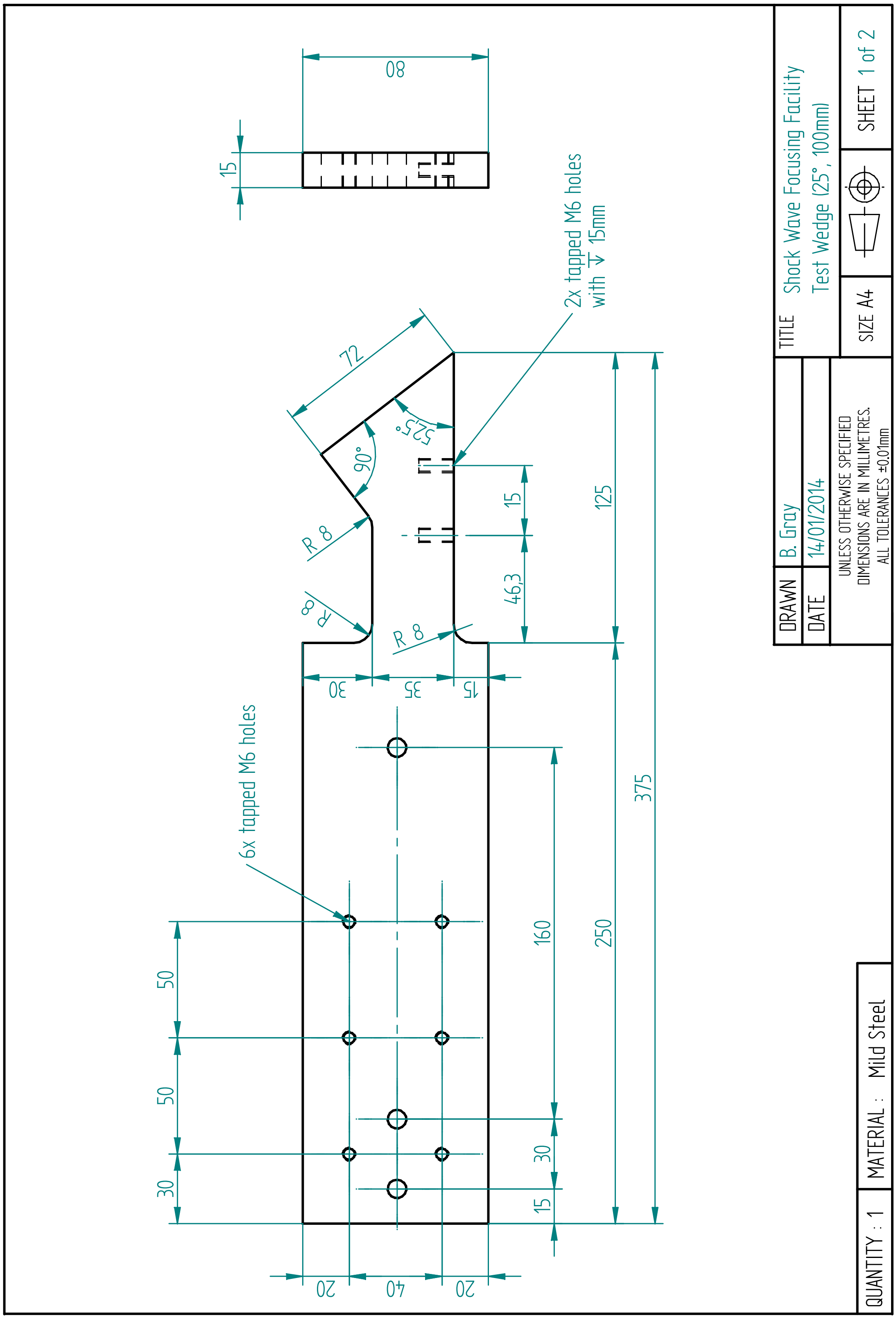

FIGURE C.15: Engineering drawing of the 25° test wedge

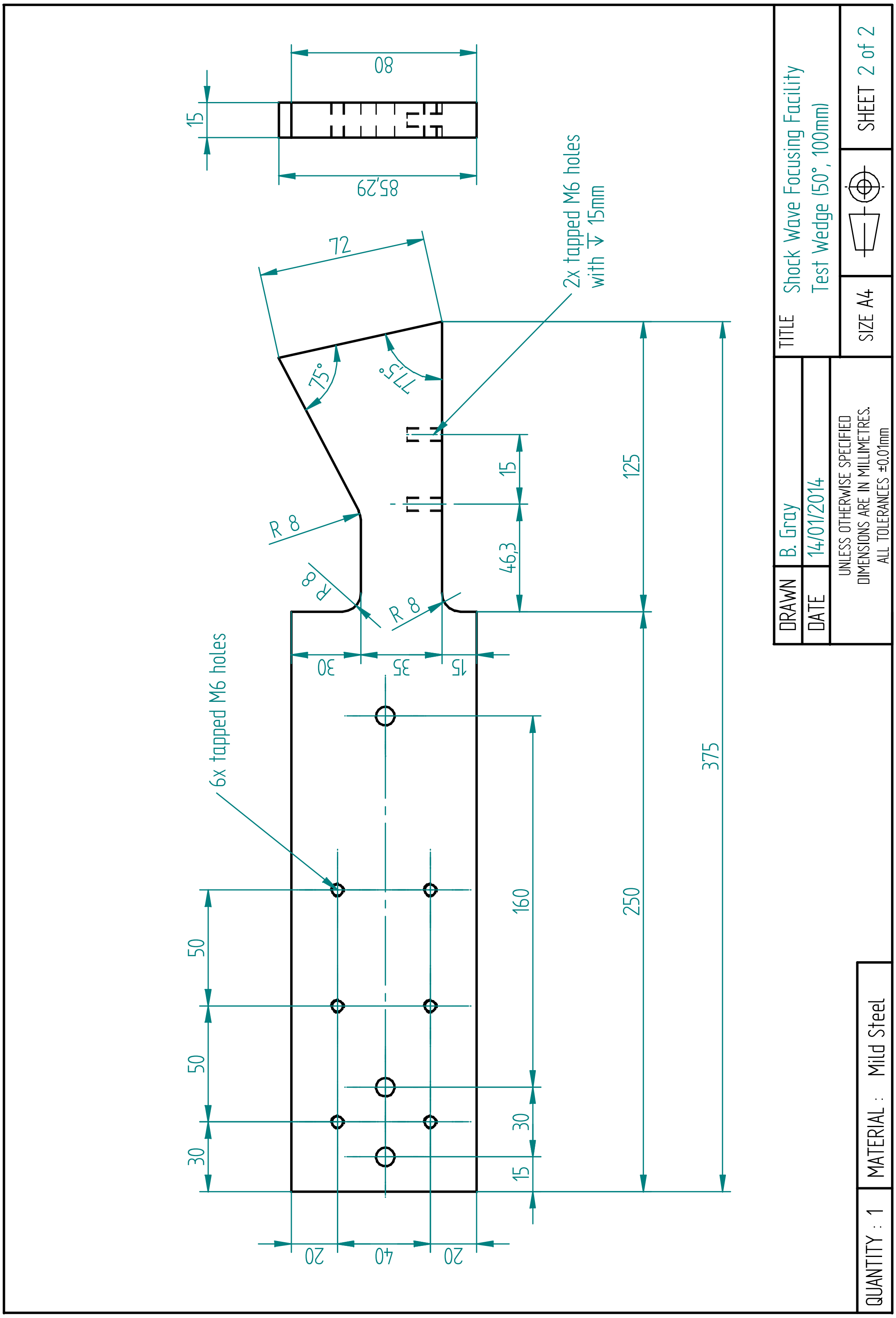

Figure C.16: Engineering drawing of the 50° test wedge

C.4 Part drawings for the compound shock profile

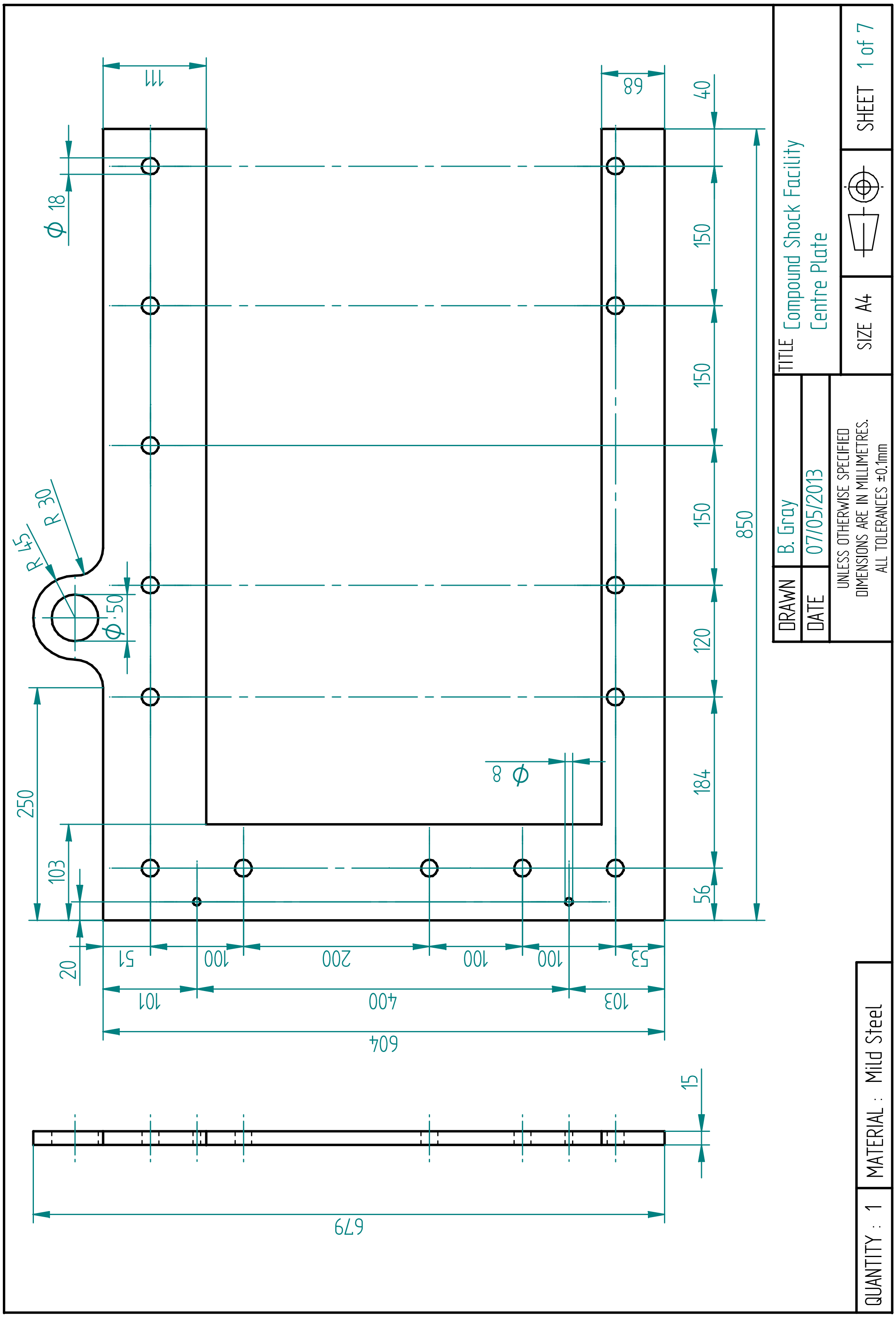

FIGURE C.17: Engineering drawing of the parallel wall propagation plate

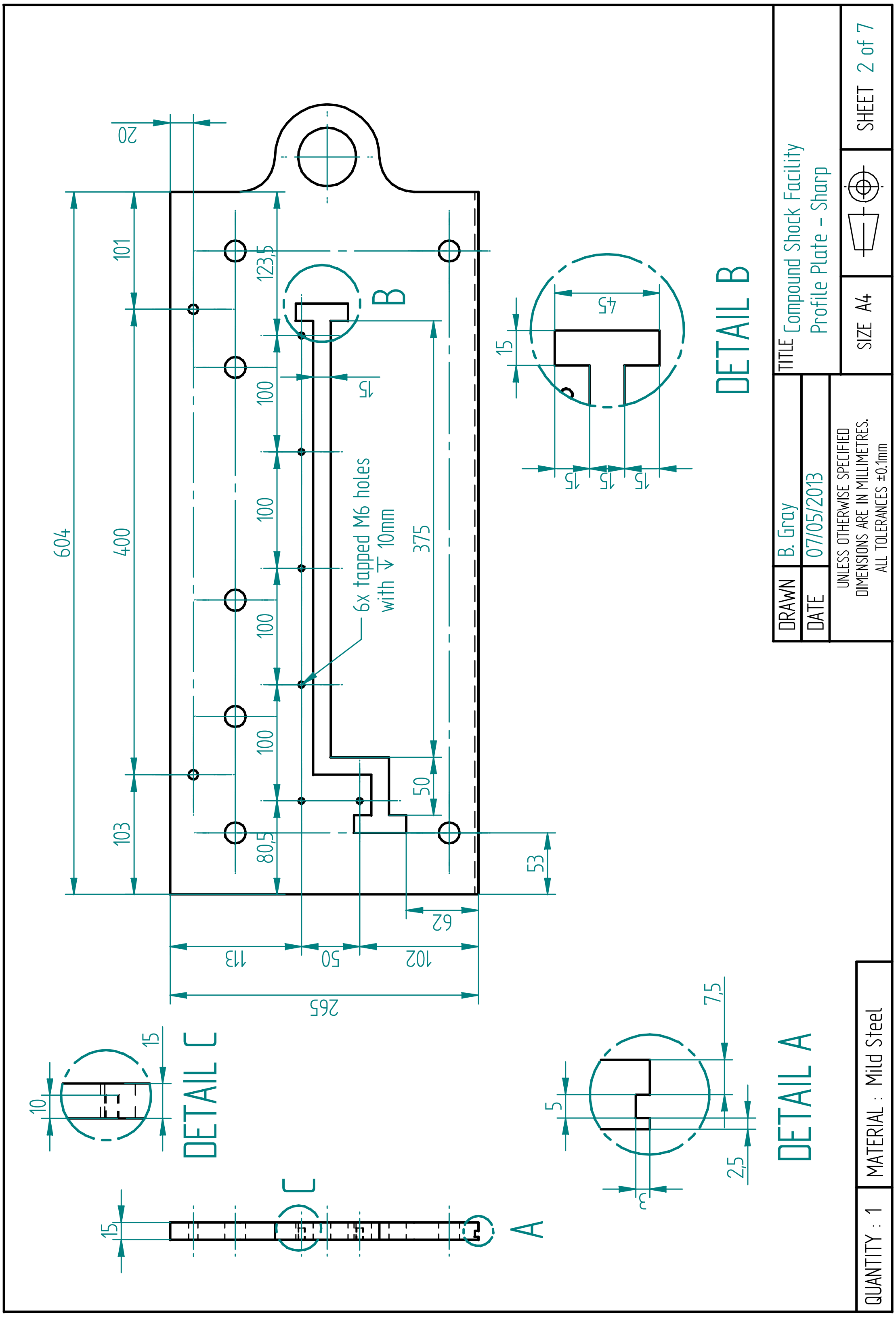

Figure C.18: Engineering drawing of the sharp compound shock profile plate

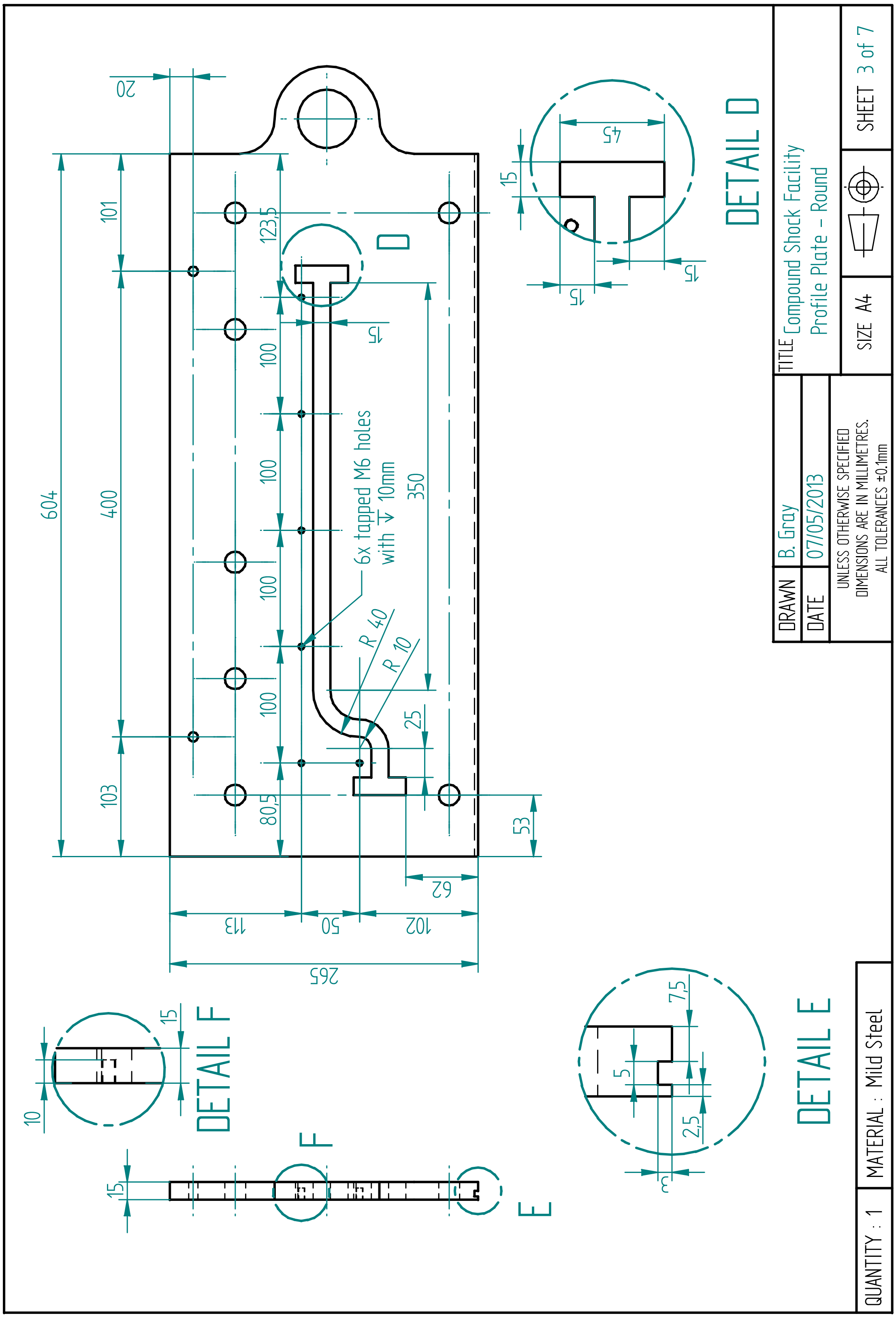

Figure C.19: Engineering drawing of the rounded compound shock profile plate

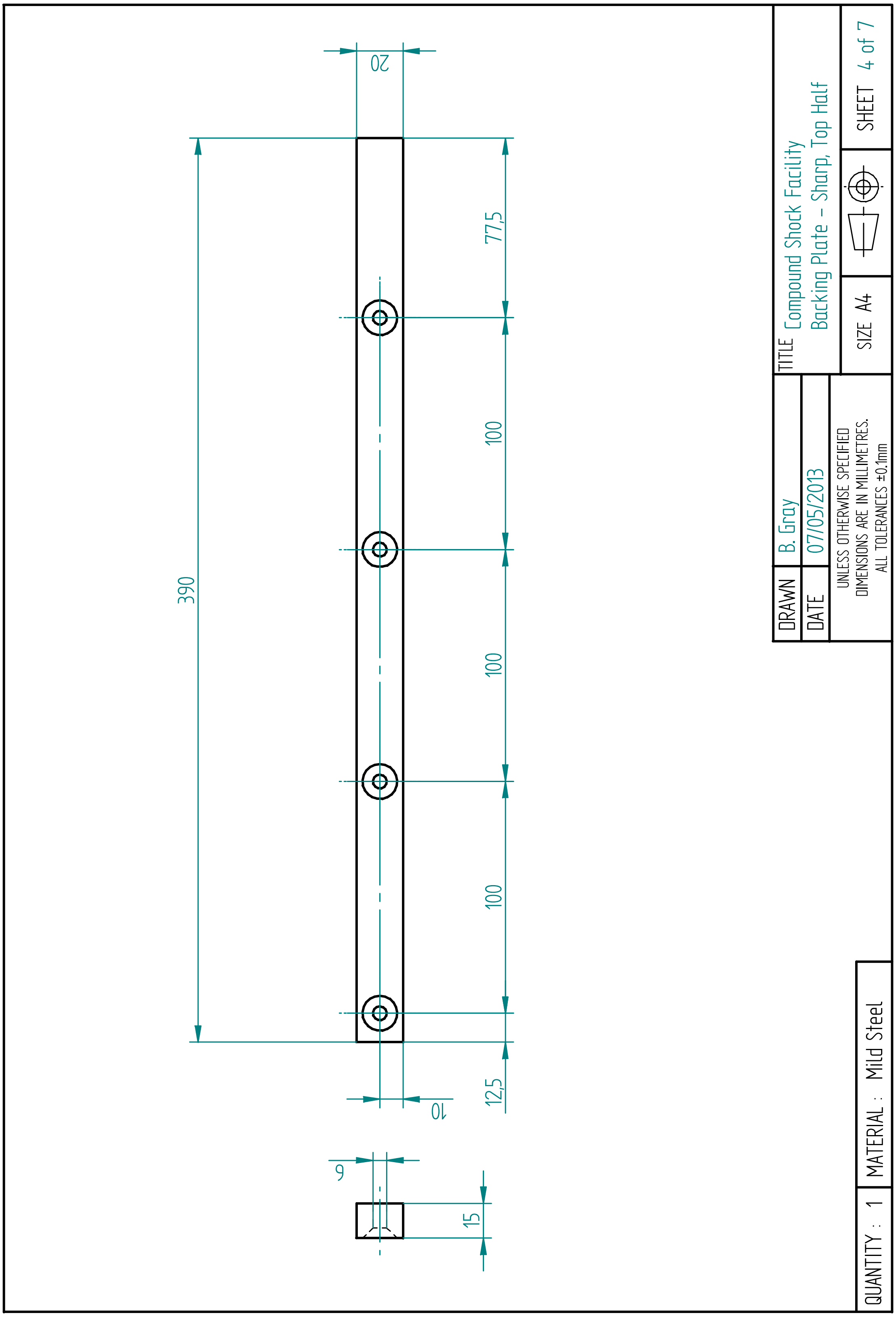

Figure C.20: Engineering drawing of the sharp compound shock backing plate - upper portion

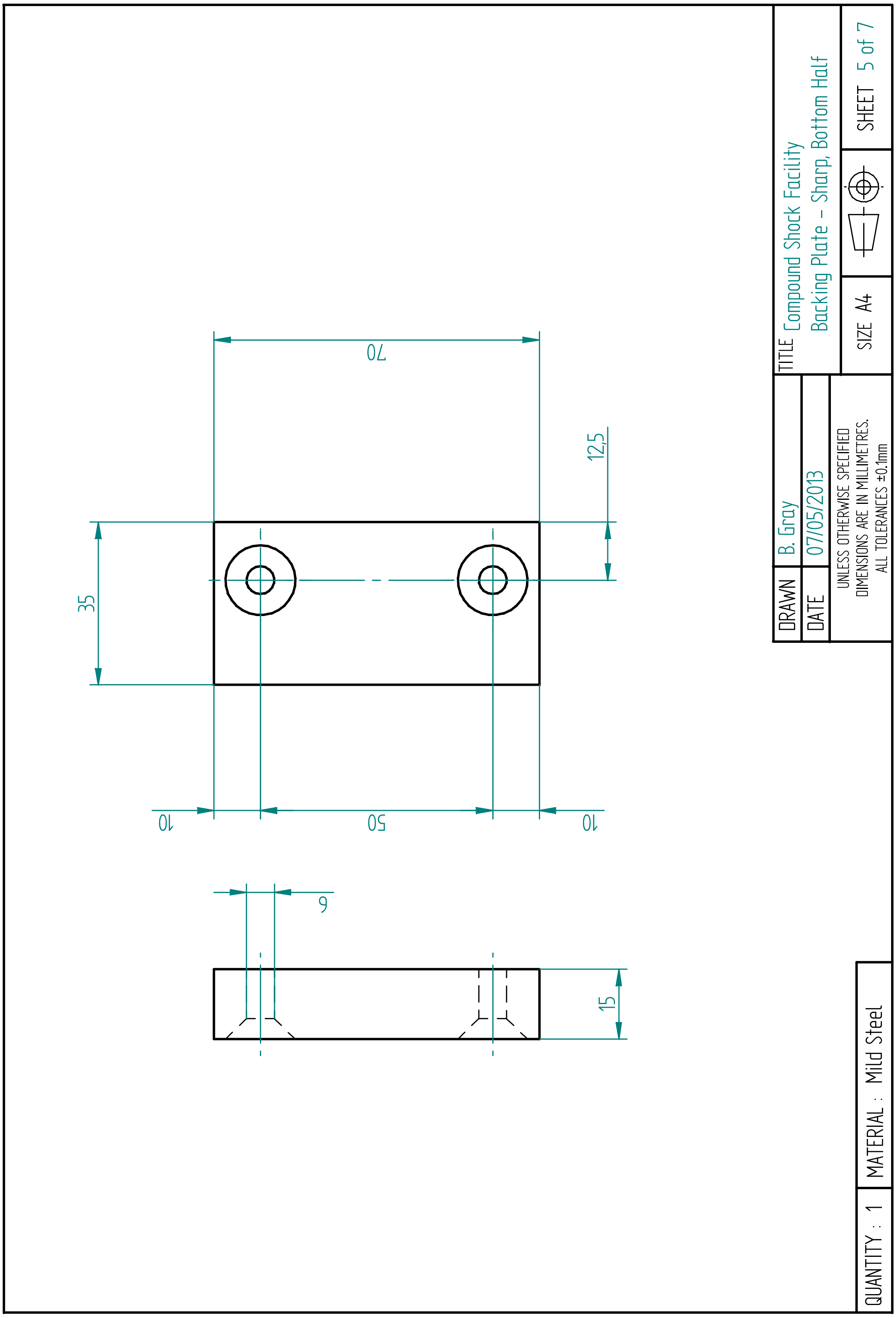

Figure C.21: Engineering drawing of the sharp compound shock backing plate - lower portion

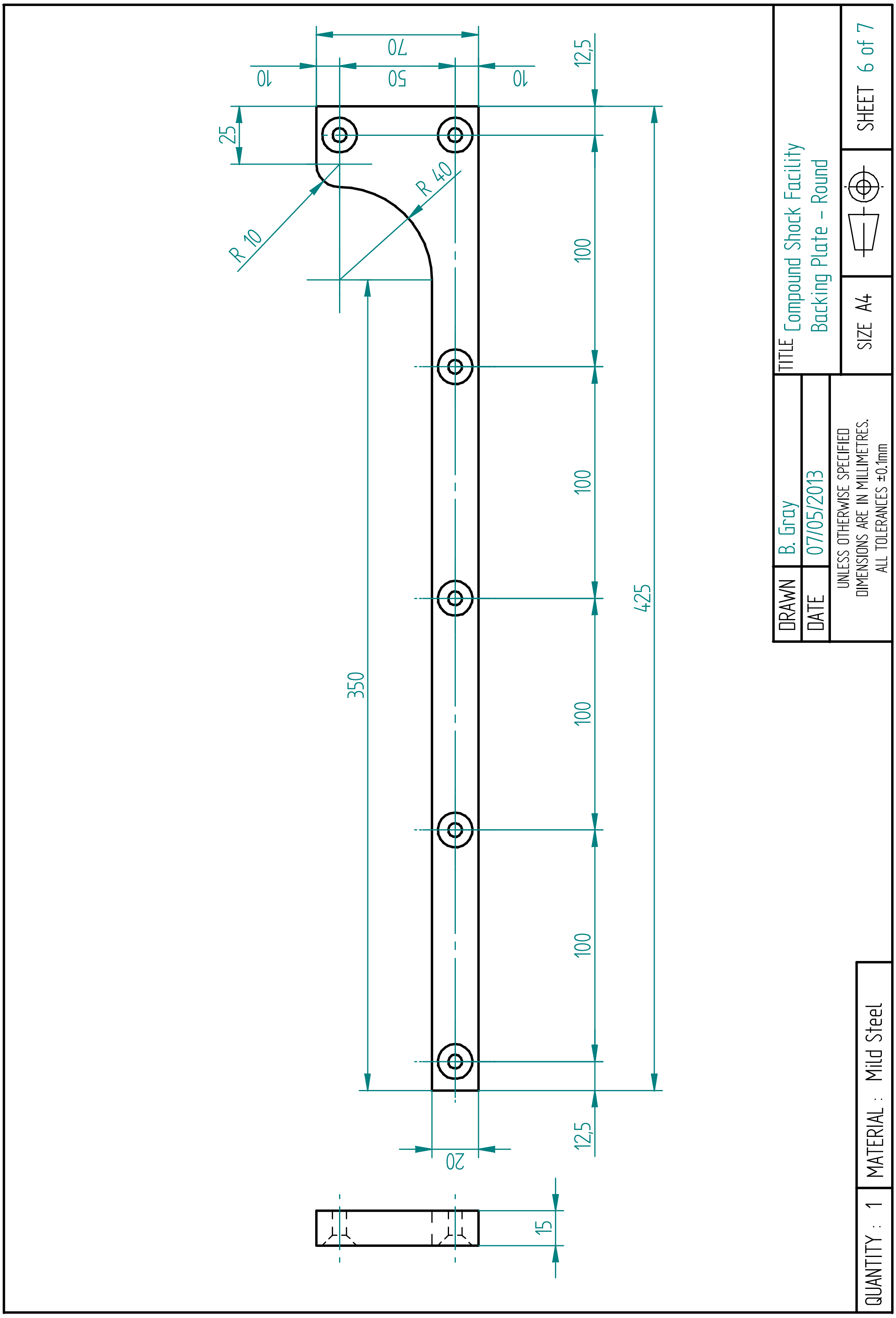

FIGURE C.22: Engineering drawing of the rounded compound shock backing plate

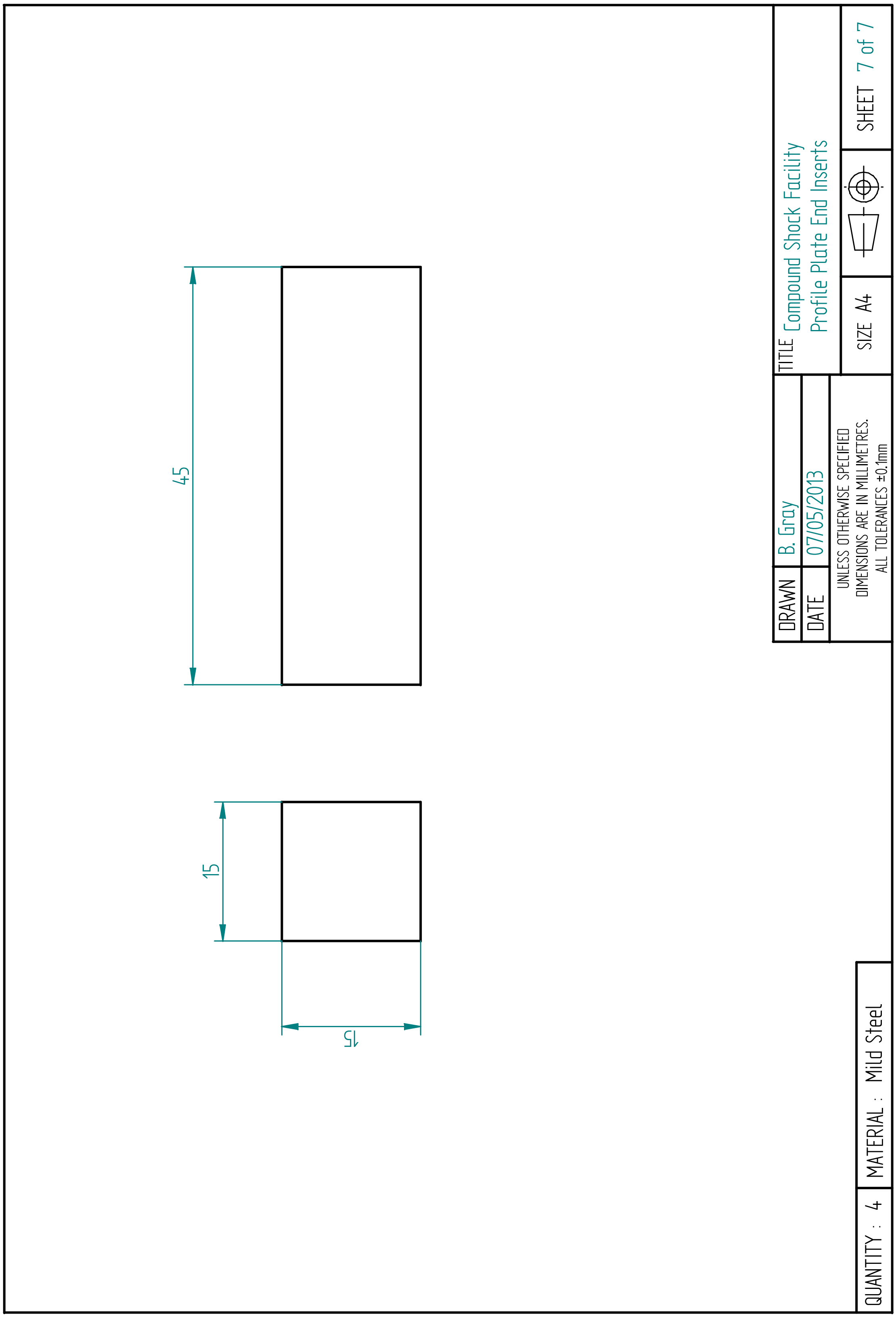

Figure C.23: Engineering drawing of the profile plate end inserts

Appendix D. Changing the Facility Configuration

The facility consists of four plates and an optional test model. The four plates are the smaller and larger outer plates (each fitted with a glass window in a steel frame), a profile plate, and a centre plate. There are three ways in which the configuration may need to be changed - these are, in increasing order of complexity, changing the test model, changing the profile plate, and changing the centre plate.

The procedures for changing the configuration are outlined below. Changing the centre plate requires the complete disassembly of the facility, whereas changing the test model may be done without removing the facility from the shock tube. The profile plate may be changed by following the disassembly procedure up to step 8, and then following the assembly procedure from step 7.

Whenever the facility is open, it is a good idea to take the opportunity to clean away any dust that may have settled on the windows.

D.1 Changing the test model without disassembly

1. Prepare the new test model by lining the sides with paper gasket. Use double-sided wonder tape to ensure that it does not lift along edges exposed to the flow. Trim the edges of the gasket so that it does not protrude into the flow.
2. Connect the hook from the overhead gantry to the tab of the smaller of the two outer plates, and raise it until the chain is only just supporting the weight of the plate.
3. Loosen slightly, but do not remove, the seven bolts holding on the smaller outer plate. The plate should not move, as it should be supported by the gantry.

4. If any spacing plates were used, remove them, taking care to support them while the bolts are being removed so that they do not slip down and scratch the windows.
5. Remove the remainder of the seven bolts, and move the outer plate away from the rest of the facility. Support it so that it doesn't swing.
6. Remove five of the six bolts attaching the test model to the larger outer plate. Loosen the remaining bolt, but do not remove it.
7. Remove any bolts connecting the model to the centre plate.
8. Remove the final bolt, and remove the model from the facility. It is a good idea to clean the windows at this point.
9. Place the new model in the facility, and use a single bolt through the outer plate to hold it in approximately the correct position.
10. Insert and tighten all the bolts connecting the model to the centre plate, Making sure that the edges of model are correctly aligned with respect to the centre plate.
11. Insert and tighten the six bolts connecting the model to the outer plate.
12. If necessary, adjust the O-ring cord, and carefully position the smaller outer plate.
13. Taking care not to scratch the windows or shift any of the gasket material, clamp the smaller outer plate against the profile plate and compress the O-ring. Insert and tighten at least two of the seven bolts to clamp the facility together.
14. If necessary, position the spacer plates (this may need to be done at the same time as the previous step) and then insert and tighten the remainder of the seven bolts.

D.2 Disassembling the facility

1. Prepare a large table. Ideally this table should be located near the end of the shock tube, and an overhead gantry should be positioned such that the facility can be moved from the shock tube to the table.
2. Connect the hook from the overhead gantry to the tab of the larger of the two outer plates, and raise it until the chain is only just taut.
3. Remove the seven bolts connecting the facility to the shock tube. If necessary, insert temporary bolts to clamp the profile plate to the facility.
4. Move the facilty to the table. Position four blocks such that no bolt holes will be obstructed, and lower the facility onto these.

5. Remove the temporary bolts, and the seven bolts holding the smaller outer plate in place.
6. Disconnect the hook from the larger outer plate, and connect it to the tab on the smaller plate. Raise the small outer plate, and place it on the table next to the rest of the facility. Take care not to scratch the windows.
7. Remove the O-ring cord from the groove of the profile plate.
8. Remove the profile plate.
9. Remove the spacer plates, if any.
10. Undo all of the bolts holding the test model in place, and remove the test model.
11. Remove the centre plate.

D.3 Assembling the facility

1. Prepare a large table. Ideally this table should be located near the end of the shock tube, and an overhead gantry should be positioned such that the facility can be moved from the table to the shock tube.
2. Lay the larger of the two outer plates with its smooth inner side facing upward. Use blocks to support it at each corner, making sure that all bolt holes are not obstructed.
3. Prepare the centre plate and the test model (if required) by lining the sides with paper gasket. Use double-sided wonder tape to ensure that it does not lift along edges exposed to the flow. Trim the edges of the gasket so that it does not protrude into the flow.
4. Carefully lower the centre plate onto the outer plate, ensuring that the bolt holes line up. If any part of the centre plate covers the window, take care while moving the plate around to ensure that it does not scratch the window.
5. If a test model is being used, then position it now. Once it is positioned, insert the bolts connecting it to the outer plate, but only tighten any of them until the bolts connecting the test model to the centre plate have been tightened.
6. If any spacer plates are required between the two outer plates, position them now.
7. Lower the profile plate into position. Ensure that the edge of the slit is flush with the back wall of the centre plate, and that all bolt holes are aligned. If necessary, insert dowels to ensure that the profile plate cannot move relative to the centre plate. Use at least two temporary bolts to hold it firmly in position. These temporary bolts will be removed while the facility is being attached to the shock tube.

8. Coat a 604mm long, 4mm diameter O-ring cord with vacuum grease, and insert it into the groove on the side of the profile plate.
9. Lower the smaller of the outer plates into position, ensuring that the bolt holes in all three layers are aligned. This is most easily done using an overhead gantry.
10. Taking care not to scratch the windows or shift any of the gasket material, clamp the smaller outer plate against the profile plate and compress the O-ring. Insert and tighten the seven M14 bolts which clamp the facility together.
11. After ensuring that all parts are either bolted or clamped in place, attach the hook of an overhead gantry to the tab of the larger outer plate, and position the facility at the end of the shock tube.
12. One at a time, replace the temporary bolts holding on the profile plate with bolts passing through the end of the shock tube. Do not tighten these bolts completely until all of the temporary bolts have been removed. If the profile plate was positioned correctly, the O-ring should remain under compression throughout this procedure.
13. Insert the remainder of the seven bolts that connect the facility to the shock tube, and tighten all of the bolts.

Appendix E. Radius and Velocity of a Converging Cylindrical Shock

Each experiment resulted in a series of between 8 and 14 images in which the shock front was visible. The images were captured at 10 μs intervals, with a resolution of 320x192 pixels. The following sections describe the process used to estimate the radius of the shock wave in each image, and obtain the velocity from the change in radii of each frame.

E.1 Converting image coordinates to real coordinates

The location of any point in the image may be specified by the vertical and horizontal distances from the top left corner of the image, measured in pixels. These will be referred to as the pixel coordinates of the point, and may be found using almost any major image editing software. It is important to note that these coordinates are specified in a left-handed coordinate system (that is, the horizontal axis is positive to the right, and the vertical axis is positive downward), as opposed to the conventional right-handed coordinate system (in which the horizontal and vertical axes are positive to the right and upwards). These pixel coordinates need to be transformed into real coordinates, which have a common origin, orientation and scale across all test cases.

The first step is to calculate the scale of the image, which may be used to convert measurements in pixels to measurements in millimetres. Since the length of the wedge is known to be 72 mm for all of the wedges tested, the scale s may be calculated from the pixel coordinates of the apex (x_a, y_a) and end of the wedge (x_e, y_e) in the image.

$$s = \frac{72 \text{ mm}}{\sqrt{(x_e - x_a)^2 + (y_e - y_a)^2}} \tag{E.1}$$

Using this, any measured pixel coordinate may be transformed into a coordinate measured in mm relative to the wedge apex as follows:

$$\begin{aligned} x' &= s(x_i - x_a) \\ y' &= -s(y_i - y_a) \end{aligned} \tag{E.2}$$

where (x_i, y_i) is the pixel coordinate in the image to be transformed. Note the negative sign in the equation for y', which transforms the left-handed coordinate frame used in the image to a more conventional right-handed coordinate frame.

The image is aligned with the wedge, but it is convenient to rotate the coordinate frame such that the centre lies on the x-axis using the transformation

$$\begin{bmatrix} x \\ y \end{bmatrix} = \begin{bmatrix} \cos(\theta_W + \theta_t) & -\sin(\theta_W + \theta_t) \\ \sin(\theta_W + \theta_t) & \cos(\theta_W + \theta_t) \end{bmatrix} \begin{bmatrix} x' \\ y' \end{bmatrix} \tag{E.3}$$

where θ_W is the angle of the wedge, and θ_t is the tilt of the image, which may be calculated from the coordinates of the apex and end of the wedge using

$$\theta_t = \arctan\left(\frac{y_e - y_a}{x_e - x_a}\right) \tag{E.4}$$

The origin of the final coordinate frame (x, y) is located at the wedge apex, and the x-axis is aligned with the bottom wall of the test chamber, as shown in Figure E.1.

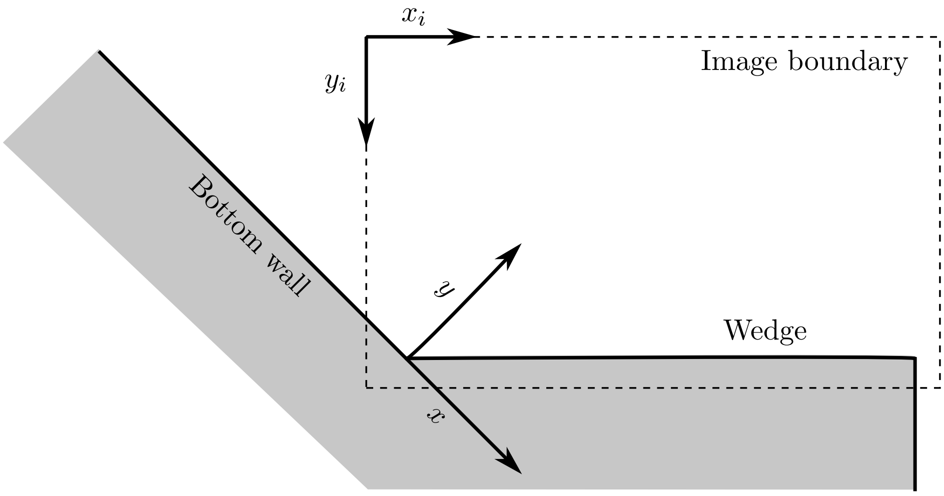

FIGURE E.1: Transformation from the original image coordinates (x_i, y_i) measured in pixels from the top left of the image, to real coordinates (x, y) measured in millimetres from the wedge apex

E.2 Circle fitting and radius estimation

Initially the radius in each image was estimated by fitting a circle to three points taken across the visible shock front. However, due to the uncertainty in the measurements, the results from this method showed some sensitivity to the choice of the three points, particularly for the early and later images in each set, in which a smaller portion of the shock front was visible. A method that used multiple points from all of the available images for each test case was developed, which minimized the sensitivity to the chosen points.

The method makes the assumption that the shock fronts in all images from a particular experiment share a common centre. It uses an iterative process to make gradual improvements to an initial guess of the circle centre until the sum of the squares of the errors in radius estimations for all images of that shock front is minimized. The time required to compute the centre depends strongly on the quality of the initial guess.

E.2.1 Initial guess

A good approximation of the initial guess of the common centre for a particular case is to find the centroid of the centres predicted for each image using a three point method.

The equation for a circle is

$$(x - x_c)^2 + (y - y_c)^2 = r^2 \tag{E.5}$$

where (x_c, y_c) is the centre of the circle, and r is the radius.

Substituting in three points (x_1, y_1), (x_2, y_2), and (x_3, y_3) produces three equations. By eliminating r and expanding, the following expression for the circle centre may be derived:

$$\begin{bmatrix} x_c \\ y_c \end{bmatrix} = \begin{bmatrix} 2(x_2 - x_1) & 2(y_2 - y_1) \\ 2(x_3 - x_1) & 2(y_3 - y_1) \end{bmatrix}^{-1} \begin{bmatrix} x_2^2 + y_2^2 - x_1^2 - y_1^2 \\ x_3^2 + y_3^2 - x_1^2 - y_1^2 \end{bmatrix} \tag{E.6}$$

This will give a different centre for each frame. The initial guess of the centre may then be calculated by averaging all of these centres:

$$\begin{aligned} \overline{x_c} &= \frac{1}{n}\sum_{i=1}^{n} x_{c,i} \\ \overline{y_c} &= \frac{1}{n}\sum_{i=1}^{n} y_{c,i} \end{aligned} \tag{E.7}$$

E.2.2 Radius estimation and error

For any given centre, the radius of the shock in each image may be estimated by minimizing the sum of the squares of the errors of multiple points along the shock front. It is important to choose an optimal number of points at which to evaluate the error. Having too many points inflates the error due to the uncertainty in the measurements, whereas having too few points makes the solution sensitive to which points were chosen. After some trial and error, it was decided that points spaced roughly 20 pixels apart were optimal. Since at least three points per image were necessary to calculate the initial guess, this meant that shock fronts shorter than 40 pixels were excluded from the analysis. However, the shock fronts in some images were long enough to provide as many as 18 points. The varying number of points causes the circle fit to be biased towards images in which a larger portion of the shock front is visible, but this is not necessarily an undesirable property.

Given a circle centre (x_c, y_c), the radius of the shock in a particular image may be found by finding the radius for each image r_i that minimizes the error function $E_i(r_i)$ for that image.

$$E_i(r_i) = \sum_{j=1}^{m} (r_j - r_i)^2 \tag{E.8}$$

where m is the number of points used, and r_j is the distance of a particular point (x_j, y_j) from the centre, given by

$$r_j = \sqrt{(x_j - x_c)^2 + (y_j - y_c)^2} \tag{E.9}$$

The error function $E_i(r_i)$ may be minimised by solving

$$\frac{dE_i(r_i)}{dr_i} = 0 \tag{E.10}$$

where the derivative may be approximated numerically using the central difference formula

$$\frac{dE_i(r_i)}{dr_i} \approx \frac{E_i(r_i + \Delta r_i) - E_i(r_i - \Delta r_i)}{2\Delta r_i} \tag{E.11}$$

The value of r_i that satisfies equation (E.10) may then be calculated using any appropriate numerical scheme. In this case, the bisection method was used to quickly determine r_i to within 10^{-6} mm for each image in a set.

The total of the squared errors for all images in a set for a given centre is then given by

$$E(x_c, y_c) = \sum_{i=1}^{n} E_i(r_i) \tag{E.12}$$

or

$$E(x_c, y_c) = \sum_{i=1}^{n} \sum_{j=1}^{m} (r_j - r_i)^2 \tag{E.13}$$

E.2.3 Improved estimation of the circle centre

The objective is to find the circle centre that minimizes the error function $E(x_c, y_c)$ given by equation (E.13). This may be done using a modified gradient descent method. Any guess may be improved by moving a short distance in the direction of decreasing gradient.

Therefore, given a guess $\vec{x}_i = (x_c, y_c)$, a better guess $\vec{x}_{i+1}$ may be calculated from

$$\vec{x}_{i+1} = \vec{x}_i + \delta\vec{n} \tag{E.14}$$

where δ is the step size, or the distance by which the point is to move, and $\vec{n}$ is a unit vector in the direction of decreasing gradient, and is given by

$$\vec{n} = \frac{-\nabla E(\vec{x}_i)}{|\nabla E(\vec{x}_i)|} \tag{E.15}$$

where $\nabla = \left(\frac{\partial}{\partial x}, \frac{\partial}{\partial y}\right)$ is the gradient operator. The components of the gradient were approximated using a simple central difference scheme as follows:

$$\begin{aligned} \frac{\partial}{\partial x}E(x,y) &\approx \frac{E(x+h,y) - E(x-h,y)}{2h} \\ \frac{\partial}{\partial y}E(x,y) &\approx \frac{E(x,y+h) - E(x,y-h)}{2h} \end{aligned} \tag{E.16}$$

where h is a small step size, in this case taken to be 10^{-8} mm.

Initially, a step size δ of 10 mm was used. If application of equation (E.14) results in an increase in the error function $E(x_c, y_c)$, the time step has overshot the minimum, indicating that the step size was too large. In these cases, the guess is discarded, δ is halved, and a new guess is calculated using the reduced step size.

The process is repeated until δ becomes sufficiently small, or the change in the total squared error becomes negligible over several iterations.

Once the process is complete, the radii of the shock fronts in each image are computed using the final circle centre using the process described in section E.2.2.

E.3 Calculating the shock velocity

The average shock velocity between any two frames is given by

$$\overline{v} = \frac{\Delta r}{\Delta t} \tag{E.17}$$

where Δr is the change in radius between the two frames, and Δt is the time interval between the frames. This average velocity approximates the instantaneous velocity of the shock at the midpoint of the two frames with second order accuracy.

The images are captured at 10 μs intervals, and shock velocities are typically between 400 and 700 m/s. Therefore, in the worst case, the shock moves only 4 mm between frames. The shock wave typically has a thickness of approximately three or four pixels, so the uncertainty in any position measured from the image may be taken as two pixels. With an average image scale of 0.225 mm/px, this corresponds to an uncertainty of 0.45 mm in any measured point. This means that the distance that the shock travels between consecutive frames (and hence the velocity, if it is assumed that the time interval is known exactly) may have an uncertainty that exceeds 10%. However, if two frames separated by 40 μs are used, this uncertainty is reduced to 2.5%.

Therefore, it is necessary to maximize the number of frames across which Δr is measured, in order to minimize the uncertainty in the shock velocity. The experiment that covers the shortest time period covers an interval of 70 μs, so an interval of 60 μs was chosen for calculating the shock velocity. This has two advantages, in that the velocity calculated corresponds exactly to an existing frame (rather than a time in between frames, as for 70 μs), and it allows velocities to be calculated for at least two frames per case, which allows interpolation to estimate the velocity at other points. The uncertainty in the velocity calculated with this method is just 1.7%.